Towards infrared single-photon detection with superconducting magic-angle twisted bilayer graphene

Giorgio Di Battista

München 2024

Towards infrared single-photon detection with superconducting magic-angle twisted bilayer graphene

Giorgio Di Battista

Dissertation
der Fakultät für Physik
der Ludwig–Maximilians–Universität
München

vorgelegt von
Giorgio Di Battista
aus Popoli

München, den 4. November 2024

Erstgutachter: Prof. Dr. Dmitri K. Efetov
Zweitgutachter: Prof. Dr. Preden Roulleau
Abgabedatum: 4. November 2024
Tag der mündlichen Prüfung: 20. Dezember 2024

A mamma, papà, Matteo e Gaia

Contents

List of Figures

Zusammenfassung

Supraleitende Einzelphotonendetektoren gehören zu den fortschrittlichsten verfügbaren Photodetektoren und bieten eine unvergleichliche Empfindlichkeit für Anwendungen, die hohe Präzision erfordern. Hierzu zählen Kommunikation, Radioastronomie, Quantennetzwerke und Spektroskopie. Trotz ihrer zahlreichen Vorteile sind traditionelle supraleitende Materialien durch ihren spektralen Bereich und ihre Empfindlichkeit gegenüber niederenergetischen Photonen begrenzt.

In dieser Arbeit schlagen wir einen neuartigen Ansatz zur Weiterentwicklung der Einzelphotonendetektion vor, indem wir das Potenzial von Moiré-Materialien erforschen. Moiré-Materialien entstehen durch vertikales Stapeln zweidimensionaler Schichten mit einem kleinen Drehwinkel, was zur Entstehung einzigartiger Quantenphasen führt. Insbesondere konzentrieren wir uns auf magisch-winkelverdrehtes Doppelschichtgraphen (MATBG), das aus zwei Grapheneschichten mit einem relativen, sogenannten "magischen" Winkel von 1.1°, besteht. Mit einer Elektronendichte von etwa 10^{11} Ladungsträgern pro cm^2, die um fünf Größenordnungen niedriger ist als bei traditionellen Supraleitern, weist MATBG eine extrem niedrige elektronische Wärmekapazität und eine hohe kinetische Induktivität auf. Diese Eigenschaften positionieren MATBG als bahnbrechendes Material für Quantensensoranwendungen, insbesondere in der thermischen Sensorik und Einzelphotonendetektion.

Unsere Studie markiert den ersten großen Schritt zur Entwicklung eines Einzelphotonendetektors auf Basis von supraleitendem MATBG. Wir demonstrieren erhebliche Fortschritte bei der Herstellung hochwertiger MATBG-Geräre und eine Pionierstudie zur Messung des bolometrischen Effekts unter kontinuierlicher Laserheizung durchgeführt. Dies ermöglichte uns die erste Messung der thermischen Leitfähigkeit im supraleitenden Zustand von MATBG. Der größte Erfolg dieser Arbeit ist ein Durchführbarkeitsnachweis-Experiment, das die Fähigkeit zur Detektion einzelner Photonen demonstriert. Durch die Beleuchtung des Geräts bei Millikelvin-Temperaturen mit einer stark abgeschwächten Laserquelle und Spannungs-Biasing eines MATBG-Geräts nahe seines supraleidenden Phasenübergangs supraleitenden Phasenübergang konnten wir erfolgreich die Nahinfrarot-Einzelphotonendetektion demonstrieren. Unsere Ergebnisse heben die außergewöhnliche Empfindlichkeit von MATBG hervor und liefern wertvolle Einblicke in die Wechselwirkung zwischen MATBG und Photonen.

Diese Forschung ebnet den Weg für die Nutzung von Moiré-Supraleitern als bahnbrechende Plattform zur Entwicklung revolutionärer Quantenbauelemente und Sensoren.

Die Ergebnisse dieser Studie ermutigen nachdrücklich zu weiteren Untersuchungen, um die Einzelphotonendetektionsfähigkeiten auf noch niedrigere Energien mit MATBG und anderen Graphen-basierten Supraleitern mit niedriger Trägerdichte auszudehnen.

Summary

Superconducting single-photon detectors are among the most advanced photodetectors available, offering unparalleled sensitivity for applications requiring high precision, such as communication, radio astronomy, quantum networks, and spectroscopy. Despite their numerous advantages, traditional superconducting materials are limited by their spectral range and sensitivity to low-energy photons.

In this thesis, we propose a novel approach to advance single-photon detection by exploring the potential of moiré materials. Moiré materials are formed by vertically stacking two-dimensional layers with a slight twist angle, leading to the emergence of unique quantum phases. Specifically, we focus on magic-angle twisted bilayer graphene (MATBG), constituted by two graphene layers twisted at the so-called 'magic' angle of 1.1°. With an electron ensemble density of approximately 10^{11} carriers per cm^2, which is five orders of magnitude lower than that of traditional superconductors, MATBG exhibits ultralow electronic heat capacity and large kinetic inductance. These characteristics position MATBG as a groundbreaking material for quantum sensing applications, particularly in thermal sensing and single-photon detection.

Our study marks the first major steps towards developing a single-photon detector based on superconducting MATBG. We have made substantial progress in fabricating high-quality MATBG devices and conducted a pioneering study to measure the bolometric effect under continuous laser heating. This allowed us to perform the first measurement of the thermal conductance in the superconducting state of MATBG. The major achievement of this thesis is a proof-of-principle experiment demonstrating the capability of detecting single photons. By illuminating the device at millikelvin temperatures with a highly attenuated laser source and voltage biasing an MATBG device near its superconducting phase transition, we successfully demonstrated near-infrared single-photon detection. Our findings highlight the exceptional sensitivity of MATBG and provide valuable insights into the interaction between MATBG and photons.

This research paves the way for utilizing moiré superconductors as a groundbreaking platform for developing revolutionary quantum devices and sensors. The results of this study strongly encourage further exploration to extend single-photon detection capabilities to even lower energies using MATBG and other low-carrier density graphene-based superconductors.

Acknowledgments

My deepest gratitude goes to my advisor, Prof. Dmitri Efetov. I sincerely thank you for giving me the opportunity to work on such an interesting topic and for always providing the best tools and collaborations to advance the project. I am especially grateful for our numerous discussions over the years. I deeply appreciate your intellectual honesty and scientific vision. I would not be as proud of my work without your comments and encouragement to improve it. Additionally, I would like to thank you for the responsibilities you entrusted to me from the beginning, always providing guidance and supervision throughout the process. Your mentorship has helped me mature as a young scientist and a person.

I would also like to thank Prof. Dr. Preden Roulleau, Prof. Alexander Urban, Prof. Fabian Grusdt, and Prof. Milan Allan for being part of my PhD committee. Special thanks to Preden for our inspiring and motivating discussions in Venice and Paris.

I extend my gratitude to Prof. Dr. Kin-Chung Fong for his invaluable help over the years. Our collaboration since January 2021 has been crucial for most of the work presented in this thesis. You have taught me how to conduct proper scientific investigations and have pushed me to improve the quality of my work. Thank you for always encouraging me to answer the questions thoroughly. I would also like to thank Prof. Dr. Alessandro Principi for the assistance in the theoretical modeling and interpretation of the data on thermal conductivity. I am also grateful to Paul for the supervision during the first year of my PhD and the friendship over the years.

A big thank you goes to my PhD colleagues Jaime, Rafa, Andres, and Ipsita. Thank you for the physics discussions and journal clubs we had. Looking back, I realize that the value of these discussions was immense, and I learned a lot from all of you. We shared the PhD journey inside and outside of work, and I cherish all the moments we spent together. I also want to thank Alex for being an important scientific role model. The depth of understanding you demonstrated in your work motivated me to conduct deeper investigations in my project.

I would like to express my gratitude to Leon S., Carl, Hajar, and Egor for the work we did in the past year. I am very pleased with the results we have achieved so far and look forward to continuing our work together.

I extend my gratitude to the current group members: Martin, Leon B., Gabriela, Binh, Abdelmajit, Mudit, Shaowen, Jiazhuo, Janos, Danil, as well as the previous group members Roop, Xiaobo, Aamir, Nick, Jose, Petr, Cheng, Elisa, and Prasanna. Although we did not

work together directly, I learned something valuable from each of you. I wish you all the best in your careers and future projects.

I thank Bert, Philipp, Dayse, Christian, and Anton for their technical support, especially during the move from Barcelona to Munich.

Lastly, I would like to thank all my friends from Rome, Barcelona, Munich, and Pescara, as well as my family, for promoting my curiosity and Gaia for her unconditional support.

Author's contributions

In the following, the author's publications, preprints, and patents resulting from the doctoral studies are listed. My contributions to the individual publications are stated below.

Publications in peer-reviewed journals

1. G. Di Battista, K.C. Fong, A. Díez-Carlón, K. Watanabe, T. Taniguchi, and D. K. Efetov, "Infrared single-photon detection with superconducting magic-angle twisted bilayer graphene", *Science Advances* **10**, eadp3725 (2024)

   D.K.E. and G.D.B. conceived and designed the experiments. G.D.B. and A.D.-C. fabricated the devices. G.D.B. performed the measurements. G.D.B., D.K.E., and K.C.F. analyzed the data. T.T. and K.W. contributed materials. D.K.E. and K.C.F. supported the experiments. G.D.B., D.K.E., and K.C.F. wrote the paper.

2. G. Di Battista, P. Seifert, K. Watanabe, T. Taniguchi, K.C. Fong, A. Principi, and D. K. Efetov, "Revealing the thermal properties of superconducting magic-angle twisted bilayer graphene", *Nano Letters* **22**, 16, 6465–6470 (2022)

   D.K.E. and G.D.B. conceived and designed the experiments. G.D.B. fabricated the devices and performed the measurements. G.D.B., D.K.E., and A.P. analyzed the data. A.P. performed the theoretical modeling. T.T. and K.W. contributed materials. D.K.E., P.S., and K.C.F. supported the experiments. G.D.B., D.K.E., and A.P. wrote the paper.

3. S.Y. Yang, A. Díez-Carlón, J. Díez-Mérida, A. Jaoui, I. Das, G. Di Battista, R. Luque-Merino, R. Mech and D. K. Efetov, "Plethora of many body ground states in magic angle twisted bilayer graphene.", *Low Temperature Physics* **49** (6), 631-639 (2023)

   Contribution: sample fabrication, transport measurements and discussion.

4. S. Hubmann, G. Di Battista, I. A. Dmitriev, K. Watanabe, T. Taniguchi, D.K. Efetov, and S.D. Ganichev, "Infrared photoresistance as a sensitive probe of electronic transport in twisted bilayer graphene", *2D Materials* **10**, 015005 (2023)

   Contribution: sample fabrication and transport measurements. Participation to the discussion and writing of the manuscript.

5. S. Grover*, M. Bocarsly*, A. Uri*, P. Stepanov, G. Di Battista, I. Roy, J. Xiao, A. Y. Meltzer, Y. Myasoedov, K. Pareek, K. Watanabe, T. Taniguchi, B. Yan, A. Stern, E. Berg, D. K. Efetov, and E. Zeldov, "Imaging Chern mosaic and Berry-curvature magnetism in magic angle graphene", *Nature Physics* **18**, 885–892 (2022)

   Contribution: design and fabrication of the sample. Participation to the discussion and writing of the manuscript.

6. A. Jaoui, I. Das, G. Di Battista, J. Díez-Mérida, X. Lu, K. Watanabe, T. Taniguchi, H. Ishizuka, L. Levitov, and D. K. Efetov, "Quantum-critical behavior in magic-angle twisted bilayer graphene", *Nature Physics* **18**, 633–638 (2022)

   Contribution: sample fabrication and transport measurements.

7. S. Hubmann, P. Soul, G. Di Battista, M. Hild, K. Watanabe, T. Taniguchi, D. K. Efetov, and S. D. Ganichev, "Nonlinear intensity dependence of photogalvanics and photoconductance induced by terahertz laser radiation in twisted bilayer graphene close to magic angle", *Phys. Rev. Materials* **6**, 024003, (2022)

   Contribution: sample fabrication, transport measurements and discussion.

Publications submitted to peer-reviewed journals

8. J. Díez-Mérida, I. Das, G. Di Battista, A. Díez-Carlón, M. Lee, L. Zeng, K. Watanabe, T. Taniguchi, E. Olsson and D. K. Efetov, "High-yield fabrication of bubble-free magic-angle twisted bilayer graphene devices with high twist-angle homogeneity", *Newton* - in press (2025). *arXiv* 2405.11323.

   Contribution: sample fabrication, transport measurements and discussion. Participation to the writing of the manuscript.

Patents

1. G. Di Battista and D. K. Efetov. Active element for single photon detection, single photon detector and method of manufacturing an active element for single photon detection. *European patent application* **24** 160 614.4 (2024)

   G.D.B. and D.K.E. conceived the idea and wrote the patent.

Introduction

A single photon represents an elementary excitation of the electromagnetic field. This concept was first introduced by Max Planck in 1900 as part of his groundbreaking quantum theory of light[1]. Planck's revolutionary idea suggested that light could be quantized into discrete packets of energy, which were then called 'photons' by Gilbert Lewis in 1926[2]. This intuition, which differs from the classical wave theory of light, profoundly revolutionized our understanding of electromagnetic radiation. Following on Planck's work, Albert Einstein applied the concept of quantized light to explain the photoelectric effect in 1905[3]. He proposed that light consists of individual photons, each carrying a specific amount of energy proportional to its frequency. This explanation provided a clear understanding of how light can eject electrons from a material, a phenomenon that classical physics could not explain. These fundamental works by Planck and Einstein paved the way for the development of modern quantum optics and photonics.

Today, more than one century after the initial theorization of photons, highly sensitive devices known as single-photon detectors (SPDs) have been developed to generate a pulse signal upon the absorption of individual photons[4]. These detectors are indispensable in a myriad of applications, which vary depending on the photon wavelengths they are designed to detect. In the near-infrared range, SPDs are crucial for quantum optics[5–7]. Another significant application of SPDs is in radio astronomy. The far-infrared spectral region, including the Therahertz (THz), constitutes approximately 98% of all photons in the Universe. Detecting faint fluxes of photons emitted by distant stars and celestial objects requires ultra-sensitive detectors of radiation[8, 9]. These instruments are used by astronomers to expand our knowledge about the Universe[10]. Moreover, SPDs have been proposed for use in dark matter searches. Recent theoretical models suggest that dark matter axions could be converted into THz photons, which SPDs could then detect [11, 12].

Single-photon detection is typically achieved using superconducting materials. In a superconductor, electrons are bound in Cooper pairs and are protected from external excitations by the superconducting gap[13]. When a photon with energy higher than the gap impinges on a superconducting device, the deposited energy breaks Cooper pairs and generates quasiparticles, introducing a change in impedance. Harnessing this mechanism, superconductor-based detectors, such as transition-edge sensors[14, 15], superconduct-

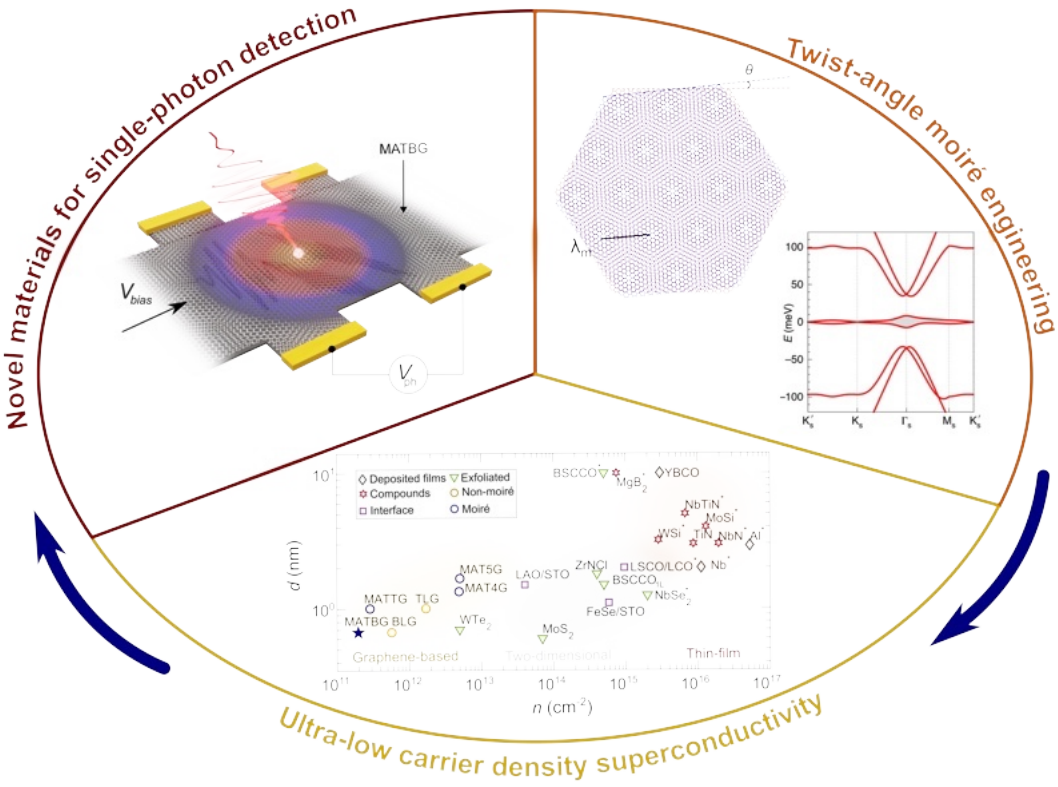

Figure 1: Novel moiré materials for quantum sensing. Moiré superlattices open new avenues for quantum sensing and single-photon detection. By stacking two or more two-dimensional layered materials with a specific twist angle, one can engineer the band structures to achieve novel quantum phases. In the case of MATBG, rotating two graphene layers to the magic angle of 1.1° results in the formation of ultra-flat bands. This leads to a superconducting phase with a carrier density about five orders of magnitude lower than conventional superconductors. These unique properties result in ultra-low heat capacity and high kinetic inductance, making MATBG revolutionary for quantum sensing applications.

ing nanowires[16–19], hot electron bolometers[20], kinetic inductance detectors[21], and Josephson junctions[22–25], offer unrivaled performance in terms of sensitivity, efficiency, spectral resolution and signal-to-noise ratio[4].

However, while SPDs in the visible and near-infrared range are commercially available and achieve excellent performance, extending these capabilities to the mid-infrared and terahertz regions remains a significant challenge due to the extremely low energy of these photons[26]. Extending SPD capabilities to the far-infrared range is an intense area of investigation, focusing on new detector concepts and novel materials. For instance, on the device side, different detector concepts to detect THz photons have been demonstrated using superconducting qubits at microwave frequencies[27, 28], quantum dots[29, 30] and quantum capacitance detectors[31].

In this thesis, we address the challenge of advancing superconducting SPDs from a material science perspective and propose exploring novel material platforms beyond conventional superconductors. As schematically illustrated in Figure 1, we focus on the recently discovered moiré materials. A moiré pattern refers to a new, long-wavelength structural modulation that arises from the interference between two or more periodic templates. In condensed-matter physics, moiré patterns can be generated by vertically stacking two or more two-dimensional layered materials with a relative twist angle, allowing the engineering of the band structure[32, 33]. Over the past few years, moiré material superlattices have exhibited numerous intriguing quantum phases and states that were previously unattainable, making them highly promising for applications in photonics and optoelectronics[32].

For instance, when two graphene layers are twisted relative to each other, the resulting long-wavelength moiré periodic potential can fold the electronic band structure into a mini-Brillouin zone. This folding leads to the formation of flat bands at the magic angle of 1.1°, which in turn give rise to a novel superconducting phase characterized by an exceptionally low carrier density of only 10^{11} electrons per cm^2. This material, known as magic-angle twisted bilayer graphene (MATBG), exhibits an electron density approximately five orders of magnitude lower than that of conventional superconductors (Fig. 1, [P1]), thereby holding great promise for low-energy SPD. In MATBG, even a minute number of quasiparticles generated by a single low-energy photon can induce a substantial perturbation of the superconducting state, thereby opening a promising avenue for extending SPD across a broader spectral range[P1, 34]. In this doctoral work, we have explored for the first time the potential of moiré materials for photodetection and demonstrated SPD using the superconducting state of MATBG.

Outline of the thesis

This doctoral thesis is structured in 7 Chapters. Chapter 1 and 2 are purely introductory, while Chapter 3 and 4 focus on the fabrication and experimental techniques used in this thesis work and the last three Chapters 5, 6, 7 concentrate on the results obtained.

In Chapter 1, we provide the theoretical background on superconducting single-photon detectors. We first introduce the concept of photons and explain the counting statistics for a coherent source (Section 1.1). We then cover superconductivity (Section 1.2) and expand on the non-equilibrium superconductivity resulting from the photon-superconductor interaction (Section 1.2.2). In the last section, we explain how this non-equilibrium state can be exploited to detect single-photons and review the key superconducting photon detector types, focusing on the material properties that determine their sensitivities (Section 1.3).

In Chapter 2, we introduce MATBG, starting from the analytical calculation of the band structure of single-layer graphene (Section 2.1) and describing the emergence of flat bands when two graphene layers are rotated at the magic angle (Section 2.2). Then, we outline the transport characterization measurements typically performed on MATBG samples (Section 2.3) focusing on the ultra-low carrier density superconducting state (Section 2.4).

In Chapter 3, we detail the fabrication protocol developed over the years, starting from

the preparation of the two-dimensional flakes (Section 3.1) to the assembling of the van der Waals heterostructure (Section 3.2). In Section 3.3, we also quantify the twist-angle homogeneity achieved with our fabrication protocol and propose strategies to mitigate twist-angle disorder.

In Chapter 4, we extensively describe the optoelectronic setup employed in our experiments. We discuss how to experimentally ensure low electronic temperature to perform transport measurements of two-dimensional materials (Section 4.1) and the electronic setup used for low-frequency transport as well as the one used for single-photon detection (Section 4.2). Section 4.3 details the optical setup employed to shine radiation at the sample stage and calculate the photon density incident on the MATBG device.

In Chapter 5, we explore the first experiment in which we measured the bolometric response of the superconducting state. We start by presenting our picture of interaction between near-infrared photons and MATBG (Section 5.1) and examine the measurement of thermal conductivity in the superconducting state (Section 5.2), which is a powerful probe of the symmetry of the superconducting gap (Section 5.3).

In Chapter 6 we describe the proof-of-principle experiment performed to demonstrate near-infrared SPD by superconducting MATBG and detail the measurements (Section 6.1, 6.2, 6.3) and analysis conducted (Section 6.4).

In Chapter 7, we outline the first steps towards using the superconducting state of MATBG to detect THz photons, covering both the implementation of a THz millikelvin setup (Section 7.1) and the design of THz antennas for efficient light coupling (Section 7.2).

1

Superconducting single-photon detectors

1.1 Photon counting statistics

In the introduction, we provided a brief historical overview of the quantum theory of light, as introduced by M. Planck and A. Einstein. Their pioneering work predicted that light is composed of discrete packets of energy known as photons. In this section, we derive the statistical properties of a photon stream from first principles. Specifically, we demonstrate through two distinct methods that the photon counting statistics for a coherent light source obeys the Poisson distribution. The first method is based on the derivation by M. Fox[35]. This heuristic approach, that postulates the existence of photons and combines classical electromagnetic equations with combinatorial analysis, provides an intuitive understanding on the photon counting statistics. The second method is based on the derivation by L. I. Schiff[36] and the seminal paper by R. J. Glauber[37]. This more conventional approach, involves the quantization of the electromagnetic field and the use of coherent states. This formalism rigorously derives the Poissonian photon counting statistics from the principles of quantum mechanics. Both demonstrations indicate that, although the average photon flux has a well-defined constant value, the number of photons detected over short time intervals fluctuates due to the discrete nature of photons. These fluctuations, described by Poisson statistics, result in shot noise in photodetectors.

This result is particularly significant for single-photon detection (SPD). By conducting a statistical analysis of detection events triggered by a highly attenuated coherent source at extremely low power levels, ensuring that only single photons are likely to be absorbed by the detector, it is possible to demonstrate the detector's sensitivity to single-photons[5],

35, 38, 39. This method does not rely on single-photon emitters, whose experimental realization presents significant challenges. The chapter concludes by discussing the practical implications of Poisson statistics, demonstrating how the photon counting statistics for a dim, coherent source can be used to verify single-photon sensitivity.

1.1.1 Poissonian statistics for a coherent source

Semi-classical derivation

Classically, a perfectly coherent and monochromatic light beam, for example emitted by a laser source, can be described as:

$$E(x,t) = E_0 \sin(kx - \omega t + \phi) \tag{1.1.1}$$

Where $E(x,t)$ is the electric field associated with the light wave with wave vector $k = \omega/c$. If the source is coherent, the phase ϕ is stable in space and time [35], and therefore the intensity $I \sim |E(t)|^2$ is constant. In this approximation, there will be no fluctuation of the laser intensity. If we postulate that packets of energy $\hbar\omega$ intrinsically constitute the light beam, this implies that the average photon flux (number of photons passing through a cross-section of the beam in unit time) is also constant and can be expressed as:

$$\Phi = \frac{IA}{\hbar\omega} = \frac{P}{\hbar\omega} \quad \text{photons per second} \tag{1.1.2}$$

Where A is the beam's cross-sectional area and P is the power. Therefore, the average number of photons in a time window T is constant and given by $\bar{n} = \Phi T$. In this scenario, it is possible to demonstrate that the Poisson distribution describes the photon statistics for a coherent light source with constant intensity.

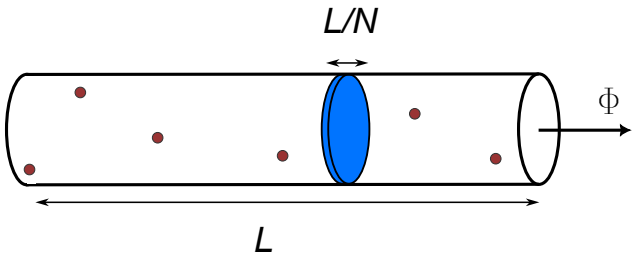

Figure 1.1.1: Ideal light beam segment for a coherent source. Section of a beam light with photon flux Φ, which has $\bar{n} = \Phi L/c$ photons on average. In the limit of $N \to \infty$, the probability of finding n photons within such segment is given by $\mathcal{P}(n) = \frac{\bar{n}^n}{n!} e^{-\bar{n}}$.

To do that, we consider a beam segment of length L, with constant average photon number $\bar{n} = \Phi L/c$ and divide it into N sub-segments of length L/N (see Fig. 1.1.1). We assume L to be sufficiently large to have an integer $\bar{n}$ in the segment. Simultaneously, we

assume N to be large enough that the probability of finding a photon within a particular segment ($p = \bar{n}/N$) is much smaller than the probability of finding zero photons. The probability of finding n photons within such segment $\mathcal{P}(n)$ is then given by the probability of finding n sub-segments containing one photon and $(N - n)$ containing no photons in any possible combination. Using the binomial distribution:

$$\mathcal{P}(n) = \frac{N!}{n!(N-n)!} p^n (1-p)^{N-n} \tag{1.1.3}$$

Which can be rewritten by substituting $p = \bar{n}/N$:

$$\mathcal{P}(n) = \frac{N!}{n!(N-n)!} \left(\frac{\bar{n}}{N}\right)^n \left(1 - \frac{\bar{n}}{N}\right)^{N-n} \tag{1.1.4}$$

Given this expression for the probability, we can take the limit of infinitesimally small sub-segments, i.e. $N \to \infty$. In this limit:

$$\lim_{N\to\infty} \mathcal{P}(n) = \frac{\bar{n}^n}{n!} \underbrace{\frac{N!}{N^n(N-n)!}}_{=1} \underbrace{\left(1 - \frac{\bar{n}}{N}\right)^{N-n}}_{\exp(-\bar{n})} \tag{1.1.5}$$

Specifically, by using the Stirling's formula $\lim_{N\to\infty}[\ln N!] = N \ln N - N$ we obtain:

$$\lim_{N\to\infty} \left[\ln\left(\frac{N!}{N^n(N-n)!}\right)\right] = 0 \tag{1.1.6}$$

From which:

$$\lim_{N\to\infty} \left[\frac{N!}{N^n(N-n)!}\right] = 1 \tag{1.1.7}$$

Moreover:

$$\lim_{N\to\infty} \left(1 - \frac{\bar{n}}{N}\right)^{N-n} = \lim_{N\to\infty} \left[1 - (N-n)\frac{\bar{n}}{N} + \frac{1}{2!}(N-n)(N-n-1)\left(\frac{\bar{n}}{N}\right)^2 + ...\right] =$$

$$= \lim_{N\to\infty} \left[1 - \underbrace{\left(1 - \frac{n}{N}\right)}_{=1} \bar{n} + \frac{1}{2!} \underbrace{\left(1 - \frac{n}{N}\right)\left(1 - \frac{n}{N} - \frac{1}{N}\right)}_{=1} \bar{n}^2 + ...\right] = \exp(-\bar{n})$$

Finally Eq. 1.1.3 can be rewritten as:

$$\mathcal{P}(n) = \frac{\bar{n}^n}{n!} e^{-\bar{n}}, \qquad n = 0, 1, 2, ... \tag{1.1.8}$$

From this derivation, we have demonstrated that for a coherent light source, the probability of finding n photons in a segment of length L follows the Poisson distribution (Fig. 1.1.1).

This implies that while the average photon number in the beam segment is fixed by fixing the laser power $\bar{n} = PL/\hbar\omega c$, the actual photon number n fluctuates above and below the mean value due to the randomness originated from chopping the continuous beam into discrete energy packets (photons)[35]. Statistical fluctuations in photon number around their mean value arise not only in photon counting processes but also in any experiments where the discrete nature of the observable plays a role (electric charge or the particle-like behavior of light, etc.). This "noise" is typically referred to as shot noise.

The mean of the Poisson distribution is given by:

$$\text{Mean}(n) \equiv \mu = \sum_{n=0}^{\infty} n\mathcal{P}(n) = \bar{n} \tag{1.1.9}$$

And the variance:

$$\text{Var}(n) \equiv \sigma^2 = \sum_{n=0}^{\infty} (n-\bar{n})^2\mathcal{P}(n) = \bar{n} \tag{1.1.10}$$

Notably, the Poisson distribution is characterized by having an equal mean and variance.

Quantum-mechanical derivation

In the above section, we derived the photon counting statistics starting from the classical expression for a coherent monochromatic source (Eq. 1.1.1) and assuming that the light is constituted by energy quanta, the photons. In the following, we demonstrate that the same result can be obtained by quantization of the electromagnetic field in vacuum using the formalism provided by quantum mechanics[36, 37]. The main steps of this derivation are finding the Lagrangian expression for the electromagnetic field starting from Maxwell's equations and defining the canonical momenta, which leads to the Hamiltonian. Using this formalism, it is possible to apply the commutation rules by replacing the classical Poisson brackets with commutator brackets. For this purpose, we start by writing the Maxwell equations in empty space:

$$\nabla \cdot \boldsymbol{E} = 0 \tag{1.1.11}$$

$$\nabla \cdot \boldsymbol{H} = 0 \tag{1.1.12}$$

$$\nabla \times \boldsymbol{E} + \frac{1}{c}\frac{\partial \boldsymbol{H}}{\partial t} = 0 \tag{1.1.13}$$

$$\nabla \times \boldsymbol{H} - \frac{1}{c}\frac{\partial \boldsymbol{E}}{\partial t} = 0 \tag{1.1.14}$$

To construct the Lagrangian density $\mathcal{L}$, we make use of the definition of the vector $\boldsymbol{A}$ and scalar potential ϕ[40]:

$$\boldsymbol{H} = \nabla \times \boldsymbol{A} \tag{1.1.15}$$

$$\boldsymbol{E} = -\frac{1}{c}\frac{\partial \boldsymbol{A}}{\partial t} - \nabla\phi \tag{1.1.16}$$

These potentials are not specified completely and can be transformed by changing gauge choice without altering the resulting electric and magnetic field strengths. The Lagrangian density can be constructed using the Euler-Lagrange equations, where we define the four-component vectors $\boldsymbol{\psi} = (\boldsymbol{A}, \phi)$ and $\boldsymbol{x} = (\boldsymbol{r}, t)$:

$$\frac{\partial \mathcal{L}}{\partial \psi_i} - \sum_j \frac{\partial}{\partial x_j}\left[\frac{\partial \mathcal{L}}{\partial(\partial \psi_i/\partial x_j)}\right] = 0 \tag{1.1.17}$$

From which the Lagrangian density reads:

$$\mathcal{L} = \frac{1}{8\pi}\left(\frac{1}{c}\frac{\partial \boldsymbol{A}}{\partial t} + \nabla\phi\right)^2 - \frac{1}{8\pi}(\nabla \times \boldsymbol{A})^2 \tag{1.1.18}$$

As it can be demonstrated that using the Lagrangian density in Eq. 1.1.18 and the definition of $\boldsymbol{A}$ and ϕ provided in Eq. 1.1.17, Maxwell's equations can be obtained[36], this formalism is equivalent to Maxwell's equations. To construct the Hamiltonian, we need to identify the momentum canonically conjugated to $\boldsymbol{A}$ which is:

$$\boldsymbol{P} = \frac{\partial \mathcal{L}}{\partial(\partial \boldsymbol{\psi}/\partial t)} = \frac{1}{4\pi c}\left(\frac{1}{c}\frac{\partial \boldsymbol{A}}{\partial t} + \nabla\phi\right) \tag{1.1.19}$$

Having defined $\boldsymbol{P}$, the Hamiltonian density $\mathcal{H}$ can be constructed as[36]:

$$\mathcal{H} = \boldsymbol{P}\cdot\frac{\partial \boldsymbol{\psi}}{\partial t} - \mathcal{L} = 2\pi c^2|\boldsymbol{P}|^2 + \frac{1}{8\pi}|\nabla \times \boldsymbol{A}|^2 - c\boldsymbol{P}\cdot\nabla\phi \tag{1.1.20}$$

To obtain the Hamiltonian from Eq. 1.1.20, we compute the volume integral:

$$H = \int d^3\boldsymbol{r}\left[2\pi c^2\boldsymbol{P}^2 + \frac{1}{8\pi}(\nabla \times \boldsymbol{A})^2\right] \tag{1.1.21}$$

Where we have eliminated the term $c\boldsymbol{P}\cdot\nabla\phi$ which contributes nothing to the field Hamiltonian. Indeed, by partial integration we get a term $c\int d^3\phi\nabla\cdot\boldsymbol{P}$ which, using the definition of $\boldsymbol{A}$ in Eq. 1.1.16 and Eq. 1.1.11, leads to zero.

Having derived a classical expression for the Hamiltonian in terms of the canonical variables $\boldsymbol{A}$ and $\boldsymbol{P}$, we can convert the classical electromagnetic field into a quantum field by using the commutation rules. As a first step, we find a proper basis to expand the canonical variables, which will then be turned into operators. As in many applications and experiments involving electromagnetic fields, the plane wave approximation is often used, we expand $\boldsymbol{A}$ and $\boldsymbol{P}$ in the basis of plane waves polarized perpendicular to the propagation vectors so that $\nabla\cdot\boldsymbol{A} = \nabla\cdot\boldsymbol{P} = 0$:

$$\boldsymbol{u}_{\boldsymbol{k}\lambda} = \frac{1}{\sqrt{L^3}}\boldsymbol{\epsilon}_{\boldsymbol{k}\lambda}e^{i\boldsymbol{k}\cdot\boldsymbol{r}} \tag{1.1.22}$$

Where $\lambda = 1, 2$. $\boldsymbol{\epsilon}_{\boldsymbol{k}\lambda}$ are two polarization vectors perpendicular to the propagation vector $\boldsymbol{k}$, such that $\boldsymbol{k}\cdot\boldsymbol{\epsilon}_{\boldsymbol{k}\lambda} = 0$ and to each other $\nabla\cdot\boldsymbol{u}_{\boldsymbol{k}\lambda} = 0$. Here, L is the lateral size of a

cubical box which delimits the boundary conditions. Using the plane wave according to Eq. 1.1.22, $\boldsymbol{A}$ and $\boldsymbol{P}$ can be rewritten in terms of $\boldsymbol{u}_{\boldsymbol{k}\lambda}$ as:

$$\boldsymbol{A}(\boldsymbol{r},t) = \sum_{\boldsymbol{k}\lambda}{}' \left[\hat{q}_{\boldsymbol{k}\lambda}(t)\boldsymbol{u}_{\boldsymbol{k}\lambda}(\boldsymbol{r}) + \hat{q}^{\dagger}_{\boldsymbol{k}\lambda}(t)\boldsymbol{u}^{*}_{\boldsymbol{k}\lambda}(\boldsymbol{r})\right] \tag{1.1.23}$$

$$\boldsymbol{P}(\boldsymbol{r},t) = \sum_{\boldsymbol{k}\lambda}{}' \left[\hat{p}_{\boldsymbol{k}\lambda}(t)\boldsymbol{u}_{\boldsymbol{k}\lambda}(\boldsymbol{r}) + \hat{p}^{\dagger}_{\boldsymbol{k}\lambda}(t)\boldsymbol{u}^{*}_{\boldsymbol{k}\lambda}(\boldsymbol{r})\right] \tag{1.1.24}$$

Where $\hat{q}^{\dagger}_{\boldsymbol{k}\lambda}$ and $\hat{p}^{\dagger}_{\boldsymbol{k}\lambda}$ are the hermitian adjoints of the expansion operators $\hat{q}_{\boldsymbol{k}\lambda}$ and $\hat{p}_{\boldsymbol{k}\lambda}$. Here the prime in the summation indicates that the summation extends over half of the $\boldsymbol{k}$ space to avoid double-counting of $\boldsymbol{u}^{*}_{\boldsymbol{k}\lambda}$ and $\boldsymbol{u}_{-\boldsymbol{k}\lambda}$. The commutation relations between the $\hat{q}$'s and the $\hat{p}$'s are:

$$\left[\hat{q}_{\boldsymbol{k}\lambda}(t), \hat{p}^{\dagger}_{\boldsymbol{k}'\lambda'}(t)\right] = \left[\hat{q}^{\dagger}_{\boldsymbol{k}\lambda}(t), \hat{p}_{\boldsymbol{k}'\lambda'}(t)\right] = i\hbar\delta_{\boldsymbol{k}\boldsymbol{k}'}\delta_{\lambda\lambda'} \tag{1.1.25}$$

While all the other pairs commute. Substituting the relations 1.1.23, 1.1.24 into Eq. 1.1.21 and using the commutation relations, the Hamiltonian can be rewritten as:

$$\hat{H} = \sum_{\boldsymbol{k}\lambda}{}' \left(4\pi c^2 \hat{p}_{\boldsymbol{k}\lambda}\hat{p}^{\dagger}_{\boldsymbol{k}\lambda} + \frac{k^2}{4\pi}\hat{q}_{\boldsymbol{k}\lambda}\hat{q}^{\dagger}_{\boldsymbol{k}\lambda}\right) \tag{1.1.26}$$

This Hamiltonian can be further rewritten introducing new operators of the form:

$$\hat{a}_{\boldsymbol{k}\lambda} = \frac{1}{2}\left(\hat{q}_{\boldsymbol{k}\lambda} + \frac{4\pi i c}{k}\hat{p}_{\boldsymbol{k}\lambda}\right) e^{i\boldsymbol{k}ct} \tag{1.1.27}$$

$$\hat{a}'^{\dagger}_{\boldsymbol{k}\lambda} = \frac{1}{2}\left(\hat{q}_{\boldsymbol{k}\lambda} - \frac{4\pi i c}{k}\hat{p}_{\boldsymbol{k}\lambda}\right) e^{-i\boldsymbol{k}ct} \tag{1.1.28}$$

Where we have omitted the similar relations for their respective hermitian adjoints. The commutation relations for these operators are:

$$\left[\hat{a}_{\boldsymbol{k}\lambda}, \hat{a}^{\dagger}_{\boldsymbol{k}'\lambda'}\right] = \left[\hat{a}'_{\boldsymbol{k}\lambda}, \hat{a}'^{\dagger}_{\boldsymbol{k}'\lambda'}\right] = \frac{2\pi\hbar c}{k}\delta_{\boldsymbol{k}\boldsymbol{k}'}\delta_{\lambda\lambda'} \tag{1.1.29}$$

And all the other pairs commute. Substituting the operators $\hat{a}_{\boldsymbol{k}\lambda}$ and $\hat{a}^{\dagger}_{\boldsymbol{k}\lambda}$ in Eq. 1.1.26, we get an Hamiltonian $\hat{H}$ fo the form:

$$\hat{H} = \sum_{\boldsymbol{k}\lambda}{}' \frac{k^2}{2\pi}\left(\hat{a}_{\boldsymbol{k}\lambda}\hat{a}^{\dagger}_{\boldsymbol{k}\lambda} + \hat{a}'^{\dagger}_{\boldsymbol{k}\lambda}\hat{a}'_{\boldsymbol{k}\lambda}\right) \tag{1.1.30}$$

The relations and commutation rules derived here are formally equivalent to the ones of the quantum-mechanical harmonic oscillator, allowing an immediate analogy:

$$\hat{a} = \frac{1}{\sqrt{2m\hbar\omega}}(m\omega\hat{q} + i\hat{p}) \tag{1.1.31}$$

$$\hat{a}^{\dagger} = \frac{1}{\sqrt{2m\hbar\omega}}(m\omega\hat{q} - i\hat{p}) \tag{1.1.32}$$

$$[\hat{a}, \hat{a}^{\dagger}] = 1 \tag{1.1.33}$$

Where $\hat{a}$ and $\hat{a}^\dagger$ are the destruction and creation operators. Therefore, the quantum mechanical properties of the electromagnetic field can be described completely by adopting the commutation relations from independent quantum harmonic oscillators. Adopting the definitions of number operators:

$$\hat{N}_{\boldsymbol{k}\lambda} = \frac{k}{2\pi\hbar c}\hat{a}^\dagger_{\boldsymbol{k}\lambda}\hat{a}_{\boldsymbol{k}\lambda} \tag{1.1.34}$$

$$\hat{N}'_{\boldsymbol{k}\lambda} = \frac{k}{2\pi\hbar c}\hat{a}'^\dagger_{\boldsymbol{k}\lambda}\hat{a}'_{\boldsymbol{k}\lambda} \tag{1.1.35}$$

The Hamiltonian reads:

$$\hat{H} = {\sum_{\boldsymbol{k}\lambda}}' \hbar ck \left(\hat{N}_{\boldsymbol{k}\lambda} + \hat{N}'_{\boldsymbol{k}\lambda} + 1\right) \tag{1.1.36}$$

Where we can identify $\hat{a}'_{\boldsymbol{k}\lambda}$ with $\hat{a}_{-\boldsymbol{k}\lambda}$ and $\hat{N}'_{\boldsymbol{k}\lambda}$ with $\hat{N}_{-\boldsymbol{k}\lambda}$ an extend the summation over the whole $\boldsymbol{k}$ space:

$$\hat{H} = \sum_{\boldsymbol{k}\lambda} \hbar ck \left(\hat{N}_{\boldsymbol{k}\lambda} + \frac{1}{2}\right) \tag{1.1.37}$$

This equation is formally equivalent to Planck's hypothesis discussed in the introduction, which states that discrete pockets of energy constitute light. We got a Hamiltonian H for the electromagnetic field, which is formally equivalent to the sum of the energies of harmonic oscillators. Each plane electromagnetic wave with wave vector $\boldsymbol{k}$ has a energy which is an integer multiple of a fundamental quantum of energy $\hbar\omega = \hbar kc$.

Having established the analogy with the quantum harmonic oscillator, we now aim to derive the photon counting statistics for a coherent source as previously done using the semi-classical method. To achieve this, we introduce coherent states, a convenient set of states that naturally facilitate the discussion of photon statistics and are widely used in quantum optics [37]. First introduced by Schrödinger in 1926, the significance of coherent states in quantum optics was later recognized by R. Glauber in 1963, for which he was awarded the Nobel Prize in Physics in 2005 [37]. These states represent the quantum-mechanical counterpart of a classical monochromatic electromagnetic wave and are essential for describing the output of lasers and other coherent light sources [37]. Specifically, the light emitted by a single-mode laser source can be expressed as a superposition of n-photon states, $|n\rangle$ [39]:

$$|\psi\rangle = e^{-\frac{|\psi|^2}{2}} \sum_{n=0}^{\infty} \frac{\psi^n}{\sqrt{n!}} |n\rangle \tag{1.1.38}$$

Where ψ is a complex number. Here we have also simplified the notation by dropping the mode index $\boldsymbol{k}\lambda$ as a subscript and to the amplitude parameters and operators. By definition, the coherent state is an eigenstate of the destruction operator $\hat{a}$:

$$\hat{a}\,|\psi\rangle = e^{-\frac{|\psi|^2}{2}} \sum_{n=0}^{\infty} \frac{\psi^n}{\sqrt{n!}} \underbrace{\sqrt{n}\,|n-1\rangle}_{\hat{a}|n\rangle = \sqrt{n}|n-1\rangle} = \psi \underbrace{e^{-\frac{|\psi|^2}{2}} \sum_{n=0}^{\infty} \frac{\psi^{n-1}}{\sqrt{(n-1)!}} |n-1\rangle}_{|\psi\rangle} = \psi\,|\psi\rangle \tag{1.1.39}$$

Remembering the definition of number operator $\hat{n} = \hat{a}^\dagger \hat{a}$, we can calculate the average occupation number in the coherent state as:

$$\bar{n} \equiv \langle\psi|\,\hat{n}\,|\psi\rangle = \underbrace{\langle\psi|\,\hat{a}^\dagger}_{\langle\psi|\hat{a}^\dagger = \langle\psi|\psi^*} \;\hat{a}\,|\psi\rangle = |\psi|^2 \tag{1.1.40}$$

Where $|\psi|^2$ represents the average photon number in the coherent state. Therefore, in a coherent state there is not a well-defined number of photons but instead an average number of photons. As the light is constituted by a discrete number of photons with energy $\hbar\omega$, $\bar{n}$ is related to the laser power through the relation: $\bar{n} = P/\hbar\omega \cdot T$. The probability of finding n photons in the state ψ can be calculated as:

$$\mathcal{P}(n) = |\langle n|\psi\rangle|^2 = e^{-|\psi|^2}\frac{(|\psi|^2)^m}{m!} = e^{-\bar{n}}\frac{\bar{n}^n}{n!} \tag{1.1.41}$$

This corresponds to the Poisson distribution previously derived in Eq. 1.1.8, demonstrating that the quantum-mechanical derivation leads to the same result of the semi-classical approach presented above[35, 39].

1.1.2 Single-photon detection with a dim coherent source

Having derived the photon-counting statistics for a coherent laser source, we now explore its implication for SPD. Specifically, we discuss how single-photon sensitivity can be demonstrated by analyzing the statistics of counts of a detector illuminated by a dim coherent source. Similarly to the previous demonstration, we can visualize the SPD experiment with a highly attenuated continuous-wave (CW) laser source as dividing the incoming laser beam into numerous time windows (Fig. 1.1.2). As we continuously measure the device over time for detection events, the number of detected events per bin follows the statistics of photon shot noise or Poisson distribution. The events measured in a time window T have a mean $\mu = \bar{n}$ and a standard deviation $\sigma = \sqrt{\bar{n}}$. In Chapter 6, we measure the 'clicks' recorded by the MATBG detector under illumination with a highly attenuated CW laser source over time. By dividing the traces into time intervals, we demonstrate that the experimentally registered counts are in excellent agreement with the Poisson distribution. However, while this observation is consistent with the quantized nature of light, the fact that the counting statistics follow the Poisson distribution alone does not prove SPD, as multi-photon events (2-photons, 3-photons) would lead to similar observations.

To demonstrate SPD, it is crucial to turn down the incident CW laser power to a regime in which only isolated photons will likely arrive at the detector one at a time. As shown in Fig. 1.1.2a, we can imagine dividing the incoming laser beam into many time windows with a typical timescale given by the detector reset time or dead time, τ_{reset}. In this configuration, if the average number of photons in τ_{reset} is $\bar{n} << 1$, the probabilities of having zero, one, or multiple photons in a time bin will follow the relation:

$$\mathcal{P}(n = 0|\bar{n}) >> \mathcal{P}(n = 1|\bar{n}) >> \mathcal{P}(n \geq 2|\bar{n}) \tag{1.1.42}$$

For instance, considering a time window of 5 ms (which is the typical detector reset time in our device; see Chapter 6), a laser power density of $P_L = 1$ aW/µm^2 corresponds to $\bar{n} = 0.04$ photons incident per µm^2. In Fig. 1.1.2c we plot the probability of detecting n photons for different values of $\bar{n}$ according to the Poisson distribution. We notice that if $\bar{n} << 1$, the highest probability is to have 0 or 1 photon per time bin, while the probability of having multi-photon events is negligible. Specifically, for $\bar{n} = 0.04$, 96% of the time bins contain 0 photons, 3.8% contain 1 photon and less than 0.08% contain 2 or more photons. In this configuration, we can expand Eq. 1.1.8 for $\bar{n} << 1$ and rewrite it as:

$$\mathcal{P}(n) \simeq \frac{\bar{n}^n}{n!}, \qquad n = 0, 1, 2, ... \tag{1.1.43}$$

For single-photon states, $n = 1$ and $\mathcal{P}(n) \sim \bar{n}$. Therefore, the proof of SPD is that in this regime of powers, the detection probability scales linearly with the average photon number, i.e., the incident laser power [5, 23, P1].

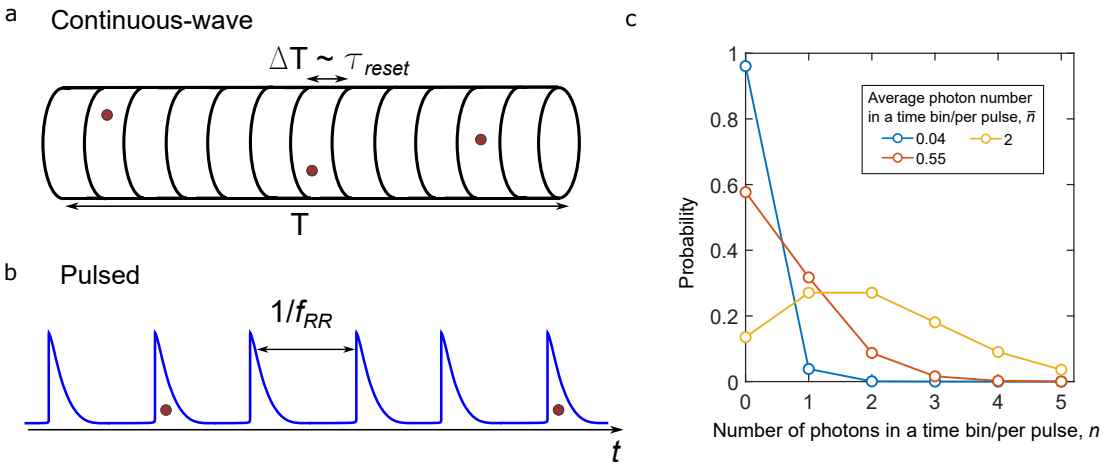

Figure 1.1.2: Poisson distribution for a coherent source. **(a)** The CW experiment is equivalent to divide the time T in small bins of duration comparable to the reset time of the detector $\Delta T \sim \tau_{reset}$. If the average number of photons in ΔT is $\bar{n} << 1$, then all the bins have either 0 or 1 photon with a negligible probability of multiple photons. **(b)** In a pulsed experiment, the laser power is divided into pulses whose temporal separation is given by the laser repetition rate f_{RR}. Analogously to the CW experiment, if the average photon number per pulse is $<< 1$, the pulses will carry mostly 0 or 1 photon, and the probability of carrying 2 photons is negligible. **(c)** Poisson distribution calculated for an average of 0.04 photon (blue), 0.55 (red) and 2 photons (yellow) per time bin or pulse.

A complementary experiment to demonstrate single-photon sensitivity involves measurements with pulsed light excitation (see Fig. 1.1.2b). Unlike the CW experiment, where a continuous stream of photons constitutes the incident beam, the pulsed laser beam is chopped into pulses of short time duration. These pulses are separated by intervals deter-

mined by the inverse of the laser repetition rate, f_{RR}, as schematically illustrated in Fig. 1.1.2b. Each pulse has a probability of containing a certain number of photons within its duration. By employing a pulsed laser source, it is possible to tune the average power and the laser repetition rate to a regime where the average number of photons per pulse, μ is much less than 1:

$$\mu = \frac{P_L}{h\nu} \cdot \frac{1}{f_{RR}} << 1 \tag{1.1.44}$$

Given that the photon counting statistics for a coherent source follow Poisson statistics, this configuration ensures that most pulses carry either zero or one photon, with the probability of a pulse carrying two or more photons being negligible. Similar to the CW experiment, also for the pulsed experiment we calculate the Poisson distributions for $\mu = 0.04$, 0.55, 2 and plot them in Fig. 1.1.2c.

1.2 Detecting radiation with superconductors

Due to their unique properties, superconducting materials are central to modern quantum technologies[41–43]. Superconductivity, first observed in a mercury wire by H. K. Onnes in 1911[44], is characterized by zero electrical resistance and perfect diamagnetism (the Meissner effect) when the material is cooled below its critical temperature, T_c. One of the most promising applications of superconducting materials is the ultra-sensitive detection of light[4]. At cryogenic temperatures, superconductors exhibit extremely low thermal noise and a gap that shields the state from external fluctuations, providing sensitivity down to the quantum limit. The idea of using superconducting materials as photodetectors was first proposed by D. H. Andrews in 1938 [45] and A. Goetz in 1939 [46]. The initial experiment in this field was performed in 1941 when D. H. Andrews utilized a tantalum wire to measure resistance changes caused by incoming infrared radiation [15, 47]. This pioneering work was further advanced in 1949 with the detection of alpha particles [15, 48]. The development of superconducting detectors, which have since become crucial in many scientific and technological applications, started with these seminal studies. In this section, we introduce the fundamental concepts of superconductivity and superconductor-photon interaction, which are necessary to understand the working principles of superconducting photodetectors. The general idea is that electrons in a superconductor are bound in Cooper pairs. When such a device absorbs a photon, it breaks some Cooper pairs, generating free electrons (quasiparticles) above the superconducting gap, leading to a change in impedance. This change in impedance, whether in electrical resistance, kinetic inductance, or other forms, can be used to detect photons.

1.2.1 Superconductivity

When a superconductor is cooled below its critical temperature, T_c it undergoes a phase transition where electrons condense into a coherent quantum state. According to the BCS theory, which successfully describes a large class of superconductors, electrons can form bound states (Cooper pairs) thanks to an effective attractive potential. In the simplest case, the pairs have opposite momenta and spins[4, 13]. As the pairs have zero net spin, they obey the Bose-Einstein statistics and can occupy the lowest energy state with the same center of mass momentum, behaving coherently as a single condensate. As a result, the Cooper pairs form a phase-locked state that can be described by a single macroscopic wave function $\psi(\mathbf{r}, t)$, the order parameter[49]:

$$\psi(\mathbf{r}, t) = \psi_0(\mathbf{r}, t)e^{i\theta(\mathbf{r},t)} \tag{1.2.1}$$

As superconductivity is a coherent phenomenon, the wave function describes the whole ensemble of electrons. In this formalism, the total number of superconducting electrons N_s and the local density of superconducting electrons $n_s(\mathbf{r}, t)$ are given by[49]:

$$\int \psi^*(\mathbf{r},t)\psi(\mathbf{r},t)dV = N_s \tag{1.2.2}$$

$$|\psi(\mathbf{r},t)|^2 = \psi^*(\mathbf{r},t)\psi(\mathbf{r},t) = n_s(\mathbf{r},t) \tag{1.2.3}$$

The formation of a condensate results in a state with zero electrical resistance, allowing electric current to flow unimpeded. The origin of a zero resistance state and, consequently, of a persistent current in a superconductor can be intuitively understood by comparing the scattering processes in a superconductor and a normal metal[49, 50]. Considering the k_xk_y-plane, all the allowed k-states are represented as discrete points (Fig. 1.2.1). Ideally, at $T = 0$, all states within the Fermi sphere are fully occupied, and in the absence of any current, the Fermi sphere is centered in the origin. A finite current applied to the sample, e.g., in the x-direction, results in a shift of the Fermi surface by δk_x along the k_x-direction. In a normal metal, when the Fermi sphere is shifted, it leaves available lower-energy states to which the charge carriers can relax. Due to these scattering processes, the Fermi sphere can rapidly return to its centered position, causing the current to decay (Fig. 1.2.1). On the contrary, in a superconductor, all Cooper pairs are condensed in the lowest energy state with the same center of mass momentum. Consequently, the movement of an electron in a direction results in the movement of another electron in the opposite way, i.e., the scattering processes occur only around the sphere (as depicted in Fig. 1.2.1b). Importantly, this process does not shift the center of the Fermi sphere, resulting in a persistent supercurrent. Other scattering processes become possible only by disrupting the Cooper pairs[49].

Superconducting properties for photodetection

The formation of a condensate leads to a range of unique properties that can be exploited in photodetection[4]. The properties listed here can be utilized for the different detector types described in section 1.3.1.

1. **Sharp resistance vs. temperature transition curve.** The superconducting state vanishes abruptly above the superconducting transition temperature T_c, resulting in a sharp resistance versus temperature transition curve between the superconducting and normal states (Fig. 1.2.2a). The steepness of this transition is particularly useful for bolometric detectors, which operate on the principle that the temperature increase of electrons (ΔT) upon light absorption leads to an increase in electrical resistance (ΔR).

2. **Sharp voltage vs. current (I-V) curve.** The zero resistance state in superconductors can be disrupted if the flowing DC current exceeds a critical value, I_c. Therefore, the typical I-V curve in superconductors is characterized by a flat region ($R = 0$, $V = 0$) when the DC current applied is lower than the critical current ($I_{dc} < I_c$). However, once $I_{dc} > I_c$, the system transitions from the superconducting

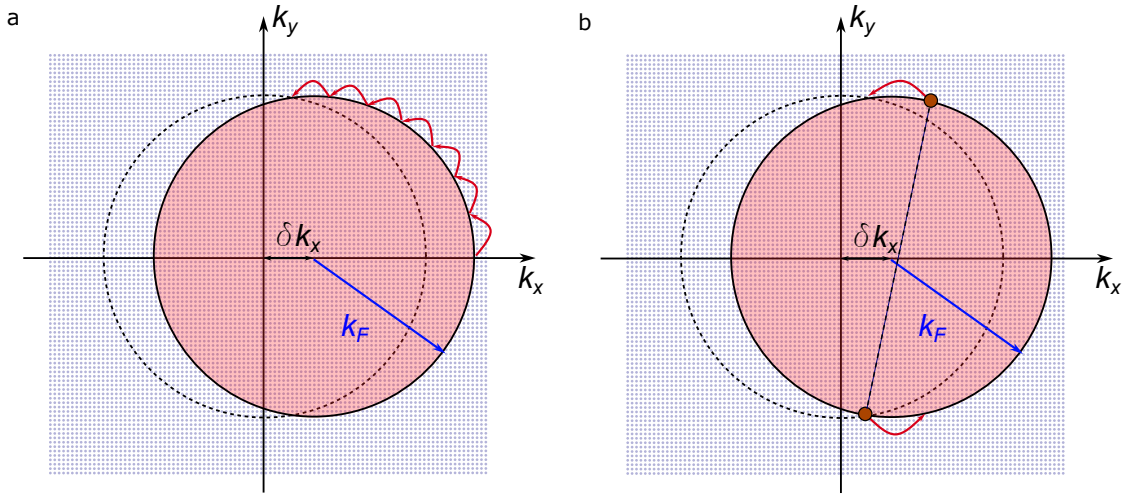

Figure 1.2.1: Schematic picture for the decay of a current in the normal and superconducting state of a metal. (a) In the normal state, the charge carriers can relax to the lower energy states, and the Fermi sphere can rapidly return to its centered position, causing the decay of the current. **(b)** In the superconducting state, the electrons are bounded in Cooper pairs, which have the same center of mass momentum. Since the scattering processes are allowed only around the sphere, this Fermi sphere does not shift back to its origin, resulting in a persistent current. Figure inspired by ref. [50] and [49].

to the normal state, and the I-V characteristic acquires a slope defined by the normal state resistance (Fig. 1.2.2b). The critical current is strongly temperature dependent; therefore, when a superconductor is biased close to I_c, it becomes extremely sensitive, and even a small external perturbation can lead to high voltage output. This property is exploited in superconducting nanowire single-photon detectors.

3. **Kinetic inductance.** Superconductors also exhibit nonzero impedance for AC currents. An electric field applied to a superconductor causes the Cooper pairs to accelerate, allowing energy storage in the form of kinetic energy[4]. This inertia of the Cooper pairs leads to a phase lag between current and voltage, described by the kinetic inductance $L_k = m^*/n_s e^2$, where n_s is the density of Cooper pairs and m^* is the effective mass. The variation in superfluid density induced by external radiation can also be exploited by kinetic inductance detectors[21].

Superconducting gap

While in conventional (or BCS) superconductors, the attractive potential is provided by the lattice deformation induced by the electrons, i.e., the attraction is mediated by phonons[51], in unconventional superconductors, the mechanism of this pairing is still under debate[13]. However, regardless of the pairing mechanism, an attractive potential gives rise to a bound state, which results in an energy gap (Δ) in the density of states around the Fermi level E_F (Fig. 1.2.3). Microscopically, the gap can be interpreted as a binding energy, i.e., the

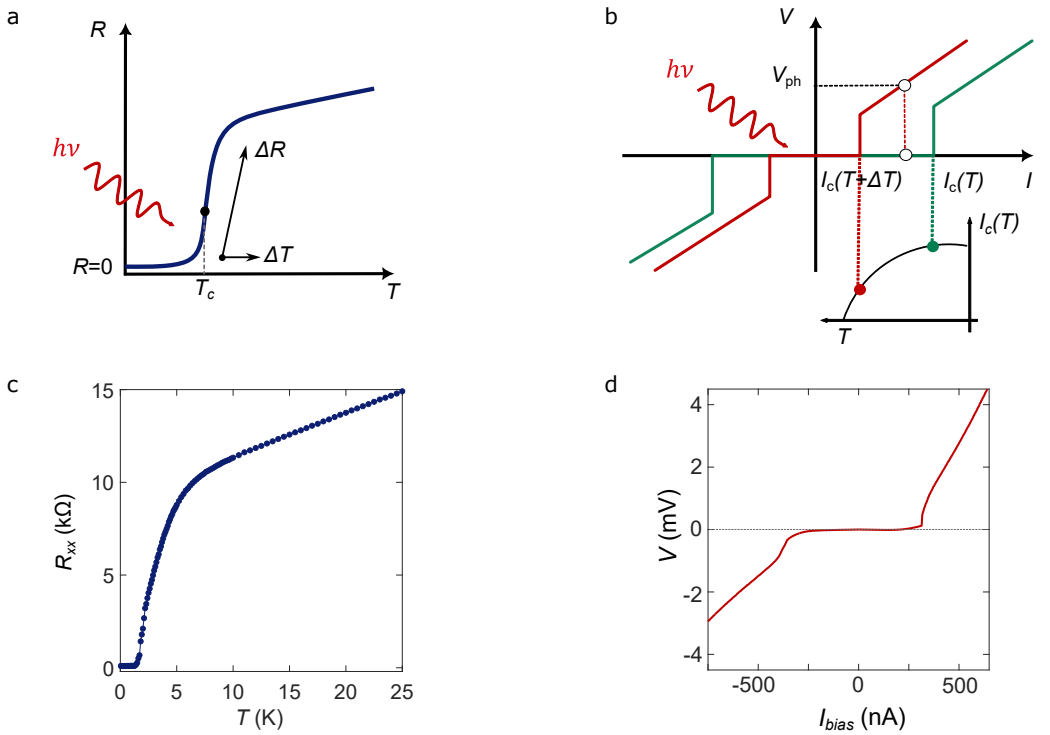

Figure 1.2.2: Superconducting properties for photodetection. **(a)** Sketch of the resistance vs. temperature transition curve for a superconductor. Given the steepness of the superconducting transition, the temperature increase of the electrons induced by the incident photons (ΔT) leads to an abrupt rise in the electrical resistance (ΔR). **(b)** Sketch of the voltage vs. current characteristic for a superconductor. The critical current strongly depends on the temperature; therefore, when a superconductor is biased close to I_c, the incident radiation can reduce the critical current, leading to a high voltage output. **(c)** and **(d)** are the R vs. T and I-V curves measured for a MATBG superconducting sample.

energy required to excite each electron in the Cooper pair. The typical binding energy of Cooper pairs is of the order of $\sim$ meV, which is hundreds to thousands of times smaller than semiconductors ($\sim$ eV)[4]. As we will discuss in section 1.2.2, the superconducting gap is the most important energy scale for superconducting photodetectors. In the most straightforward picture, the photodetection process occurs when the energy of the incident photon is large enough to overcome the binding energy $h\omega > 2\Delta$ and, therefore, therefore to break Cooper pairs, resulting in a measurable change in the superconducting properties[4]. As it is impossible to detect photons with energy smaller than the binding energy, the magnitude of Δ sets the ultimate theoretical limit for superconducting photodetectors.

Thermal quasiparticles

At intermediate temperatures $0 < T < T_c$, due to thermal fluctuations, it is possible to excite some unpaired electrons (quasiparticles) above the superconducting gap. The energy

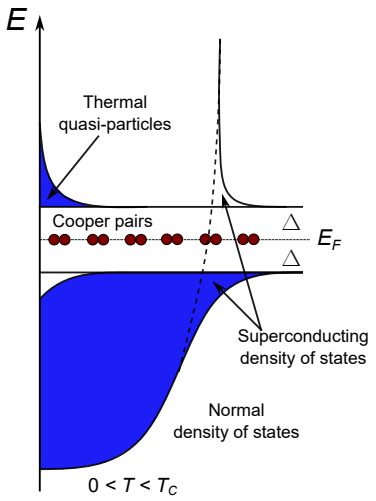

Figure 1.2.3: Superconducting gap. Schematics representation of the superconducting gap. When the superconductor is cooled below T_c the electrons form bound states (Cooper pairs) with a binding energy 2Δ. The binding energy results in a gap in the density of states close to the Fermi level, E_F. Some quasiparticles are thermally excited above the superconducting gap at intermediate temperatures $0 < T < T_c$. The probability of having these excitations depends on the symmetry of Δ and, therefore, of the order parameter. Figure inspired by ref. [4]

of this elementary fermionic excitation of momentum $\hbar\mathbf{k}$ is given by[4, 13]:

$$E_{\mathbf{k}} = \sqrt{\xi_{\mathbf{k}}^2 + |\Delta_{\mathbf{k}}|^2} \tag{1.2.4}$$

Where $\xi_{\mathbf{k}} = \epsilon - E_F$ is the distance in energy from the Fermi level, and Δ_k is the energy gap. Consistently, at the Fermi level $\xi_{\mathbf{k}} = 0$ and $E_k = |\Delta_{\mathbf{k}}| > 0$, indicating that a positive energy $\Delta_{\mathbf{k}}$ is required to generate the quasiparticle excitation. In thermal equilibrium, the probability of a fermionic quasiparticle excitation is given by the Fermi-Dirac distribution:

$$f(E_{\mathbf{k}}) = \frac{1}{e^{\beta E_{\mathbf{k}}} + 1} \tag{1.2.5}$$

Where $\beta = 1/k_B T$. Notably, the excitation probability of a fermion quasiparticle depends on both temperature and $\Delta_{\mathbf{k}}$. Specifically, the symmetry in the k-space of the superconducting gap (and consequently of the order parameter) rules the temperature dependence probability of exciting the quasiparticles. As for a BCS superconductor, the gap is isotropic ($|\Delta_{\mathbf{k}}| = \Delta$), $E_{\mathbf{k}} \geq \Delta$ for all $\mathbf{k}$, and the probability of thermally excited quasiparticles drops exponentially to zero at $T = 0$: $f(E_{\mathbf{k}}) \sim 1/e^{\infty} \sim 0$. On the contrary, for a non-BCS superconductor, the gap is not isotropic (e.g. $\Delta_{\mathbf{k}} = k_x/\mathbf{k}\Delta$ for a p-wave symmetry). The presence of nodal points in the order parameter implies that $E_{\mathbf{k}}$ can be zero along some specific $\mathbf{k}$ directions. As a result, the excitation probability of a fermion quasiparticle, in this case, does not exhibit an exponential decay but rather a power law dependence[51],

52]. As we will discuss in Chapter 5, the quasiparticles thermally excited above the gap are responsible for heat diffusion in the superconducting state. As a result, the temperature dependence behavior of the thermal conductance in the superconducting state is a sensitive probe of the symmetry of the order parameter [52–56].

1.2.2 Superconductor-photon interaction

In this section, we describe a simple picture of superconductor-photon interaction. Understanding the behavior of the superconducting state upon photon absorption is crucial to identify the most important material requirements for SPDs. When a photon with energy ($h\nu > 2\Delta$) is absorbed by the superconductor, it breaks Cooper pairs, creating a certain number of quasiparticles N_{qp}:

$$N_{qp} = \eta \frac{h\nu}{\Delta} \tag{1.2.6}$$

where $\eta \simeq 0.57$ is the down-conversion efficiency, nearly independent of the material [57]. Eq. 1.2.6 indicates that photons with lower energy will generate fewer quasiparticles, making their detection more challenging. The generation of quasiparticles induces a perturbation in the superconductor, driving it into a non-equilibrium state. All superconducting detectors operate on the principle of quasiparticle generation but vary in their methods of utilizing the non-equilibrium state resulting from photon absorption [4]. Thermal dynamics in a superconducting film can be described in terms of three coexisting subsystems: Cooper pairs, electrons (and quasiparticles generated by Cooper pair breaking), and phonons (in the superconductor and the substrate). Without external perturbations, these subsystems are in thermal equilibrium, characterized by equilibrium distribution functions at the same temperature. The external perturbation induced by the incident photon with $h\nu > 2\Delta$, drives the electronic sub-system out-of-equilibrium. The excess energy is then redistributed among the other degrees of freedom to restore thermal equilibrium. This energy down-conversion process (for photons of energy $E_0 = h\nu \sim 1$ eV, which is close to the one used in our experiments) occurs in four distinct stages [4, 58–61]:

1. **Hot electrons.** The absorption of radiation with an energy $E_0 = h\nu$ by the superconductor produces energetic photoelectrons ($\sim E_0$), generating a certain number of secondary photoelectrons. Through electron-electron interactions with timescales $\tau_{e-e} \leq 10^{-15}$ s, the photoexcited electrons thermalize to a hot Fermi-Dirac distribution. These hot electrons have a temperature higher than equilibrium $T_e > T_0$ and therefore will release the excess of energy to the other sub-systems. In this first stage, given the ultra-fast timescale of electron-electron interactions compared to electron-phonon ($\tau_{e-e} << \tau_{e-ph}$), the thermalization process occurs only within the electronic ensemble (in Fig. 1.2.4b the phonon and quasiparticle population is zero). It is also possible that hot electrons interact with optical phonons, which have higher energies than acoustic phonons, and the probability of this process depends on the specific material. As we will discuss in section 5.1, the conversion efficiency of light into hot electrons for graphene is close to 100% (at excitations in the visible and near-IR).

Therefore, all the energy the system absorbs is kept in the electronic ensemble [62, 63].

2. **Phonons.** The first stage ends when the thermal distribution of hot electrons reaches an energy comparable to the Debye energy $E_1 \simeq \hbar\omega_D$, which typically occurs in a few τ_{e-e}. At this point (between the fs and ps range) the electrons start transferring the energy to the phonon sub-system, and the phonon population increases (see Fig. 1.2.4b). At this stage, the electronic distribution passes from an energy $E_1 \simeq \hbar\omega_D$ to an energy $E_2 \simeq 3\Delta$.

3. **Cooper pair breaking.** At this point, the high energy phonons with energies $> 2\Delta$ can be absorbed by the Cooper pairs, creating excited quasiparticles[61] (see Fig. 1.2.4b the abrupt increase in the quasiparticle density). At this stage, there is a mixed distribution of quasiparticles and phonons which approach an energy $E_3 \sim \Delta$. When the energy of the phonons is $< 2\Delta$, no more quasiparticles can be excited through phonon absorption, and the energy of the quasiparticle distribution reaches equilibrium at $\sim \Delta$.

4. **Thermal phonons.** In the last step, the phonon sub-system, constituted only by phonons with energies $< 2\Delta$, equilibrates through phonon-phonon scattering and phonon escape to the substrate[58] restoring thermal equilibrium in all the sub-systems.

We highlight that the general superconductor-photon interaction described here may vary slightly for specific materials. In particular, for moiré superconductors, the details of the down-conversion processes have not yet been investigated and may differ. However, regardless of the details, we emphasize once again that the generation of quasiparticles is determined by the ratio of incident photon energy to superconducting gap energy, as summarized in Eq. 1.2.6 and that the down-conversion efficiency remains unchanged across a wide range of superconductors[57].

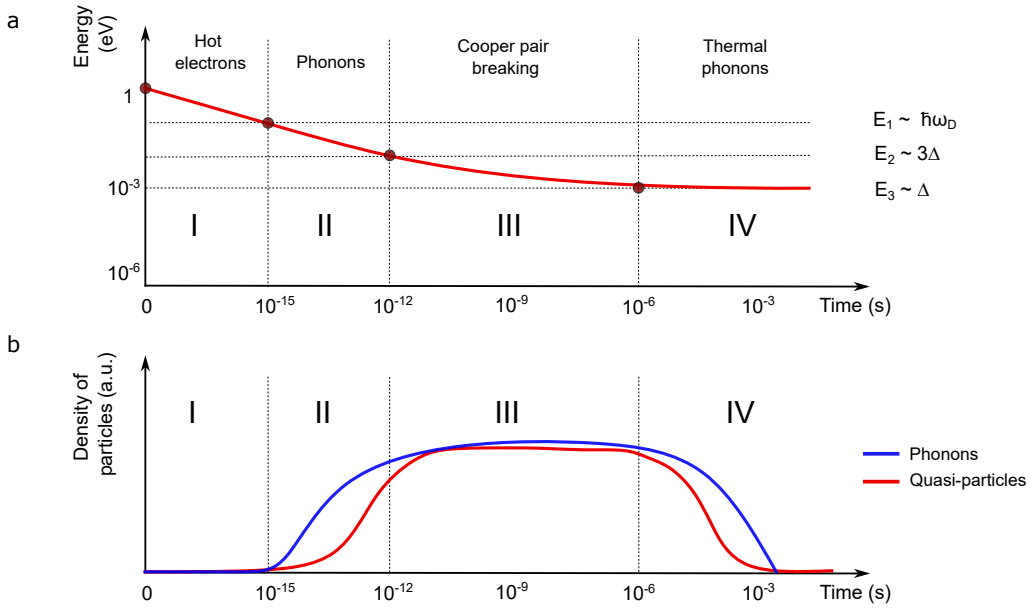

Figure 1.2.4: Schematics of the thermalization process in a superconductor upon photon absorption. (a) Schematics of the energy down-conversion process from the incident photon with energy $E_0 \sim 1$ eV to the equilibrium. The thermalization within the 3 sub-systems (Cooper pairs, electrons and phonons) occurs in four distinct stages. **(b)** Sketch of the sub-system population density for a superconductor that relaxes towards equilibrium. The blue line represents the population of phonons while the red one the population of quasiparticles. Figure inspired by ref. [4].

1.3 Material properties for superconducting photon detectors

As discussed in the introduction of this thesis, our goal is to advance superconducting SPDs from a material science perspective by exploring novel material platforms. To achieve this, it is crucial to understand the material properties that determine SPDs' sensitivities. Therefore, this section reviews some of the main types of superconducting detectors and discusses the key material parameters relevant to their operation.

1.3.1 Review of superconducting detector types

Transition edge sensors

Transition Edge Sensors (TES) exploit the steepness of the superconducting transition[14, 15, 64]. These highly sensitive detectors typically consist of an absorber, thermometer, and thermal link, which can be composed of either the same or different materials (typically tungsten, W). When the TES absorbs a photon, the energy is converted into heat by the absorber, and the superconducting material acts as a sensitive thermometer, i.e., the temperature increase induced by the photon results in a change of its electrical resistance (Fig. 1.3.1). TES devices operate in a voltage bias scheme so that the excess of resistance results in a change of the bias current within the device, which can be accurately measured by a Superconducting Quantum Interference Device (SQUID). The advantage of the voltage bias is using an electro-thermal feedback to stabilize the detector within the superconducting transition and reduce the effective time constant[65, 66]. The TES typically operates in the fourth stage of the energy down-conversion process and relies on detecting equilibrium phonons, making it relatively slow ($\sim$ µs)[67]. The following heat balance equation can describe the dynamics of a TES detector[4]:

$$C(T)\frac{dT}{dt} = P_{opt} + P_{dc} - \int_{T_b}^{T} G(T)dT \tag{1.3.1}$$

Where $C(T)$ is the heat capacity, G the thermal conductance and P_{opt} and P_{dc} are the optical and dc power absorbed by the TES. These equations point out the thermal quantities relevant for the operation of a TES: heat capacity and thermal conductance. The heat capacity, which ultimately depends on the density of states, determines the instantaneous temperature change upon photon absorption, according to $\Delta T \simeq h\nu/C$. Therefore the lower C, the higher the temperature increase for a fixed amount of energy. The heat capacities of TES detectors are carefully engineered to reach extremely low values[15, 68]. The thermal conductance, on the other hand, determines the isolation of the electrons from the thermal bath[69]. This parameter determines the ultimate theoretical performance, Noise Equivalent Power (NEP), achievable by a TES[4, 70]:

$$NEP_{TEF} = \sqrt{\gamma 4 k_B T^2 G} \tag{1.3.2}$$

Where γ is a numerical factor between 0.1 to 1. The ratio between these two quantities gives the time resolution in the linear approximation regime: $\tau = C/G$. TES detectors, as well as hot electron bolometers, give an output signal that is proportional to the energy deposited in the material, enabling photon number resolution[4, 5, 20]. This feature is different from 'clicking' detectors (such as superconducting nanowires) in which the signal does not contain information of the amount of energy deposited. Additionally, TES detectors provide extremely high quantum efficiency[71, 72].

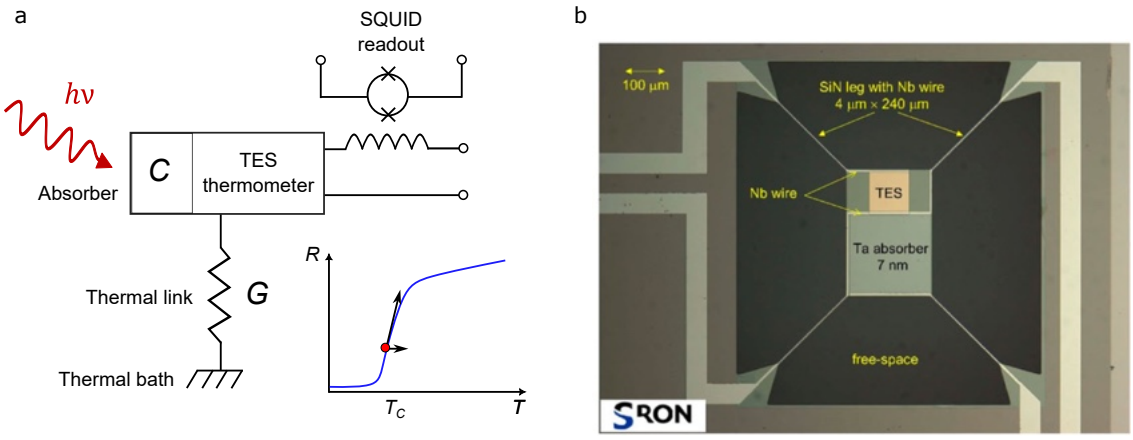

Figure 1.3.1: Transition-edge sensors. **(a)** The incident photon is absorbed by the absorber with heat capacity C. The energy of the radiation is converted into heat and increases the electronic temperature. This temperature increase is readout by the TES thermometer which is a superconducting material operated within the superconducting transition, providing an extremely sensitive temperature readout. The heat is then dissipated to the bath through a thermal link with thermal conductance G. **(b)** Optical image of a SiN suspended TES detector. Adapted from ref. [73].

Hot electron bolometers

A different version of the TES is constituted by the hot electron bolometer[20, 74, 75]. The main difference of this detector type is that it exploits the hot electron effect in thin superconducting films[76, 77]. While TES operates in the fourth stage of the energy down-conversion process, hot electron bolometers operate in the first stage, which makes them much faster than typical TES[78]. In this detector, the thermalization of the hot electrons can be engineered to occur either through the phonon emission or by diffusion through the metallic contacts. Additionally, the absorber, thermometer, and thermal link are all made of the same material. Specifically, the thin superconducting film (in this case, Nb, NbN, Al, Ti) is cooled just below T_c, where electrons and phonons can be treated as two thermal distributions with effective temperatures for each sub-system. In this scenario, the thermalization time within the sub-systems (τ_{th} for the electrons and

τ_{ph-ph} for the phonons) is smaller than the time of exchange between sub-systems (τ_{e-ph}). Therefore, it can be assumed that the temperature is almost uniform throughout the detector[4]. The incoming radiation elevates T_e above the bath, inducing a large increase of the electrical resistance due to the sharpness of the superconducting transition close to T_c[78]. Analogously to the TES, the increase of the electronic temperature is ruled by the heat capacity $\Delta T \simeq h\nu/C$, and the thermal conductance determines the minimum NEP achievable[4]:

$$NEP_{TEF} = \sqrt{\xi k_B T_e G_{e-ph}} \tag{1.3.3}$$

Where ξ is a numerical factor lying between 2 and 4. Notably, G_{e-ph} can be reduced by reducing the volume of the detector. The speed of the detector is given by: $\tau_{e-ph} = C_e/G_{e-ph}$.

Superconducting nanowires single-photon detectors

Superconducting nanowire single-photon detectors (SNSPDs) offer exceptionally high detection efficiency in the visible and near-infrared range, combined with low dark count rates and excellent time resolution. Since G. Gol'tsman's first experimental demonstration in 2001[16], SNSPD's technology has rapidly advanced, making them arguably the most widely adopted type of SPDs. They are constituted by a thin superconducting nanowire (NbN or NbTiN), typically around 5 nm thick and 100 nm wide (see Fig. 1.3.2b), which is cooled below its superconducting critical temperature and biased with a DC current ($I_{bias} < I_c$). Even a single photon can switch the SNSPD to the normal state in this geometry, enabling SPD. Specifically, when a photon is absorbed in the nanowire, it generates a localized non-superconducting region (hotspot) forcing the supercurrent to flow around it[79]. As the nanowire is narrow, this increases the local current density around the hotspot, which exceeds the superconducting critical current and creates a resistive barrier across the nanowire (see Fig. 1.3.2a). Joule heating resulting from the DC bias contributes to the expansion of this resistive region until the current is blocked and a fast voltage pulse is generated[79]. The increase of resistance induced by the absorption event redirects the current to the shunt resistor and allows to reset the detector in a timescale given by the ratio between the kinetic inductance of the material (L_k) and the shunt resistor (R_s) placed in parallel to the device: $\tau \sim L_k/R_s \lesssim 1$ ns[80]. As SNSPDs rely on generating quasiparticles, they operate in the second stage of the down-conversion process. Even though the first demonstration of SNSPDs dates back to 2001, so far, the exact detection mechanism in SNSPDs, which is crucial to identify the key material requirements, is still not fully understood[4, 81]. One of the most accredited models, allows estimating the lower limit on detectable photon energy as[17, 81, 82]:

$$h\nu = \frac{N_0 \Delta^2 w d \sqrt{\pi D \tau_{th}}}{\zeta} \left(1 - \frac{I_{bias}}{I_c}\right) \tag{1.3.4}$$

Where N_0 is the normal metal density of states at the Fermi level, Δ the superconducting gap, D the normal state diffusivity, τ_{th} the electron thermalization time, and ζ the multiplication efficiency of quasiparticles. w and d are the width and thickness of the nanowire.

This model indicates that the material parameters needed to lower the cut-off wavelength and enable low-energy photodetection are primarily the thickness and the normal metal density of states. From the material perspective, two-dimensional superconductors, characterized by a low carrier density and thickness (< 1 nm), could represent a promising pathway to extend the spectral range of SNSPDs. As the output signal of SNSPDs is the normal state resistance across the wire, which is the same regardless of the number of photons absorbed, they do not provide energy resolution. This capability can be achieved using array architectures[83].

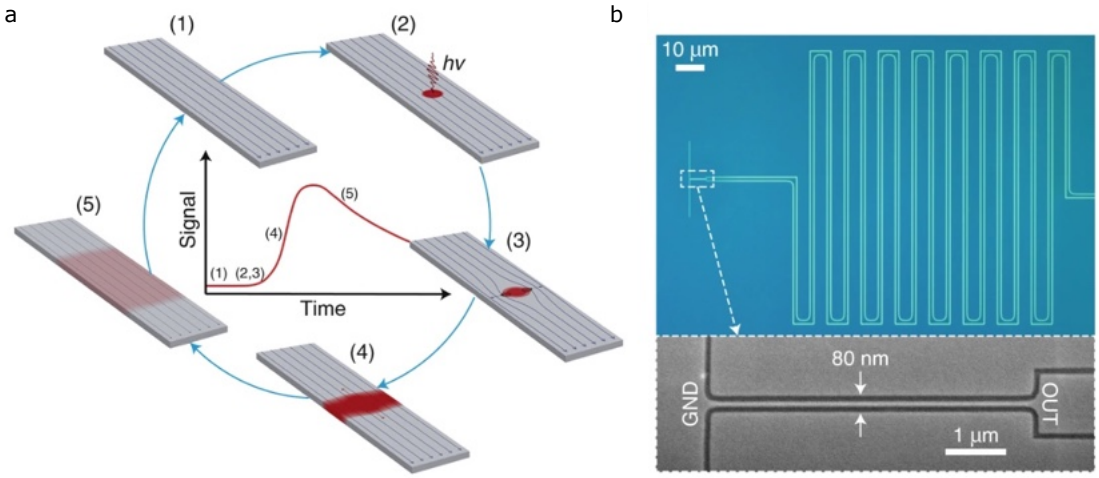

Figure 1.3.2: Superconducting nanowires single-photon detectors. (a) Schematics of the hotspot generation in a SNSPD after absorption of a single photon: (1) a supercurrent flows in the SNSPD; (2) the absorbed photon shares its energy to the other electrons, generating a hotspot of excited quasiparticles; (3) the hotspot grows across the nanowire; (4) the normal domain of quasiparticles breaks down superconductivity across the width of the SNSPD; (5) the current is redirected to the shunt resistor and the SNSPD is reset to the initial state. Adapted from ref. [84]. **(b)** Microscope image of a SNSPD. Adapted from ref. [85, 86].

Kinetic inductance detectors

Kinetic Inductance Detectors (KID) harness the increase of kinetic inductance of a superconducting resonating circuit upon photon absorption and were initially proposed by P. Day in 2003[21]. The incident photon breaks Cooper pairs in the superconductor according to Eq. 1.2.6 (Fig. 1.3.3a). The reduction in the Cooper pair density n_s results in an increase of kinetic inductance $L_k = m^*/n_s e^2$. KID detectors rely on generating quasiparticles and operate in the second and third stages of the down-conversion efficiency, illustrated in Fig. 1.2.4b. As the superconducting material is embedded in a resonator with resonance frequency f_0, the change in kinetic inductance induces a shift of the resonance frequency

(Fig. 1.3.3b) according to the equation[21, P1]:

$$\frac{|\delta f|}{f_0} \approx \frac{\delta L_k}{L_k} \approx \frac{\delta n_{qp}}{n_s} \tag{1.3.5}$$

The sensitivity of this detector ($|\delta f|/f_0$) is therefore proportional to the ratio between the density of quasiparticles generated by the incident photon (δn_{qp}) to the total density of Cooper pairs (n_s). Hence, the key parameters to increase the detector sensitivity and spectral range are the carrier density of the superconducting material (required to be as low as possible) and the resonator's quality factor. Analogously to TES and hot electron bolometers, KIDs intrinsically provide energy resolution[87].

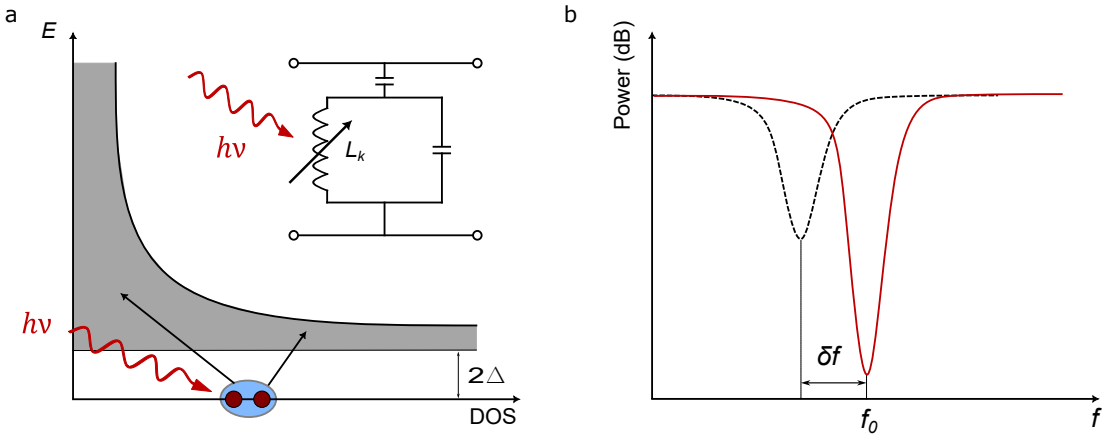

Figure 1.3.3: Kinetic-inductance detectors. **(a)** The incident photon with energy $h\nu > 2\Delta$, breaks Cooper pairs, generating quasiparticles above the superconducting gap. As the kinetic inductance is inversely proportional to the density of superconducting electrons: $L_k \sim 1/n_s$, the suppression of Cooper pair density increases L_k. **(b)** If the superconductor is embedded in a microwave resonating circuit, the change in L_k can be read out as a shift in the resonance frequency δf. The sensitvity of such detector is primarily given by: $|\delta f|/f_0 \approx \delta L_k/L_k \approx \delta n_{qp}/n_s$.

1.3.2 A new platform: magic-angle twisted bilayer graphene

We reviewed the key superconducting detectors in the previous section and highlighted the relevant material parameters for these applications. The key physical quantities for thermal detectors (such as TES and hot electron bolometers) are the electronic heat capacity and the thermal conductance. The first determines the increase of the electronic temperature for a fixed photon energy $\Delta T_e \approx h\nu/C_e$, the second the thermal isolation of the electrons from the thermal bath and consequently the ultimate theoretical performance achievable by the detector[4]. The ratio between the two, sets the detector timescale:

$\tau = C_e/G$. Low heat capacity is desirable for these detectors to induce a measurable increase of electronic temperature even upon absorption of a low-energy photon. Another key parameter, particularly relevant for KID detectors, is the density of electrons contributing to the superconducting state (n_s). As the signal is proportional to the ratio between the density of photo-induced quasiparticles to the total density of superconducting electrons $\delta f \approx \delta n_{qp}/n_s$, materials with low carrier density could be used to extend the spectral range of the detector. As mentioned in the introduction, the technological gap of SPDs in the THz range could be bridged by exploring novel material platforms that increase the sensitivity of the available detector technologies.

From the material perspective, we can compare different superconducting materials in terms of thickness (d) and carrier density (n) in Fig. 1.3.4. The thickness of the material is important as heat capacity and thermal conductance are extensive properties and, therefore, scale with the system's volume. At the same time, the normal state carrier density sets the upper limit of the Cooper pair density ($n_s \leq n$). The conventional materials used for superconducting photodetectors (Nb, NbN, W, Al, Ti) lie on the top right of the graph. These are 3D bulk superconductors, fabricated in thin films ($<$ 10 nm) to reduce heat capacity and thermal conductance. Even though further efforts have been made to develop thinner superconducting films, these bulk superconducting materials often exceed several nanometers in thickness. Indeed, these materials, typically fabricated by sputtering and etching, become strongly disordered and polycrystalline in thin films, which is detrimental to superconductivity[34]. A new perspective is represented by 2D superconductors, which provide intrinsically suppressed thermal properties[34] due to the reduced dimensionality ($\leq$ 1-2 nm) combined with low carrier density and high crystalline quality[88]. Several works have been recently carried out on SPDs based on 2D superconductors[89–93].

Among 2D materials, a new sub-group of superconductors based on graphene has emerged. As anticipated in the introduction and shown in Fig. 1.3.4, most of them are moiré superconductors, i,e. are obtained by stacking different layers of graphene on top of each other and twisting them at the 'magic' angle[94, 95]. However, superconductivity with comparable carrier density has been observed also in non-moiré superconductors based on graphene such as Bernal-stacked bilayer graphene[96] and rhombohedral trilayer graphene[97]. These materials exhibit a record-low electron density, five orders of magnitude lower than the superconductors typically used for photodetection applications [P1, 34]. This unique characteristic makes them particularly interesting for thermal detectors, as their heat capacity is significantly smaller than that of other materials [34, P2]. Additionally, they are promising for KID detectors. The ultra-low carrier density translates into a small density of Cooper pairs and, consequently, a large kinetic inductance. In this material, even a minute amount of quasiparticles generated by a single low-energy photon can induce a substantial change in kinetic inductance, opening a promising avenue to extend SPD across a broader spectral range according to Eq: 1.3.1[P1, P3]. Therefore, in this thesis, we focused on magic-angle twisted bilayer graphene (MATBG) and aimed to exploit its properties for photodetection. In the following chapters, we introduce the

fundamental physical aspects of this novel moiré superconductor, discovered in 2018 [33], discuss the fabrication method, and present the proof-of-concept experiment performed to demonstrate SPD.

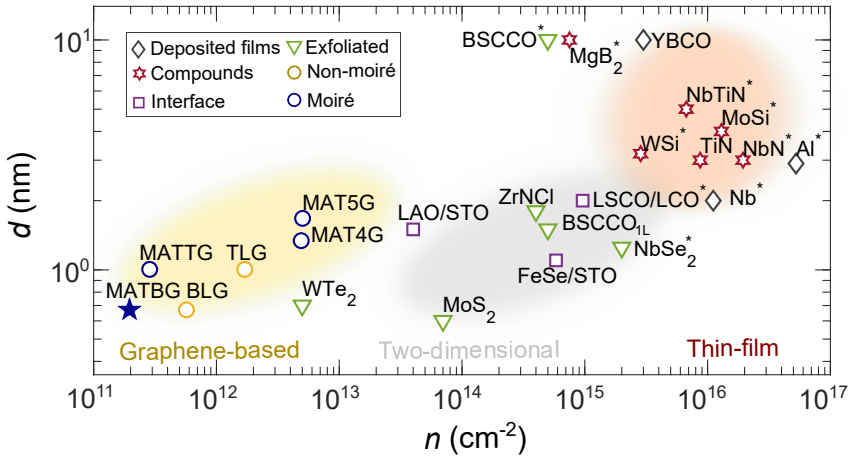

Figure 1.3.4: Superconducting MATBG as an ultra-sensitive material for single-photon detection. Logarithmic plot of film thickness d versus carrier density n for various superconductors. Data are taken from refs. [33, 34, 89, 90, 94–97, P2, 98–102]. The plot includes deposited thin film superconductors (Nb, Al, $YBa_2Cu_3O_{7-\delta}$), compound thin film superconductors (NbTiN, MoSi, WSi, TiN, NbN), interfacial 2D superconductors ($LaAlO_3/SrTiO_3$,$FeSe/SrTiO_3$,$La_{1.55}Sr_{0.45}CuO_4/La_2CuO_4$),exfoliated 2D superconductors (ZrNCl, $Bi_2Sr_2CaCu_2O_{8+\delta}$, $NbSe_2$, MoS_2, WTe_2) as well as moiré (MATBG, magic-angle twisted trilayer graphene, magic-angle twisted four-layer graphene, magic-angle twisted five-layer graphene) and non-moiré (Bernal bilayer graphene, rhombohedral trilayer graphene) graphene-based superconductors. The red, gray and yellow shaded regions serve as rough distinction between thin-film superconductors, two-dimensional superconductors and graphene-based superconductors, respectively. The asterisk indicates the superconducting materials which have been previously used for photodetection applications[4, 81, 89, 90, 93]. In the case of BSSCO SPD was demonstrated but not in the monolayer limit. Adaptd from [P1].

2

Magic-angle twisted bilayer graphene

In this Chapter, we discuss the main electronic properties of MATBG, focusing in particular on its ultra-low carrier density superconducting state. Before showing the transport measurements on MATBG, we first derive the band structure of single-layer graphene with the tight-binding model and then introduce the continuum model to describe the band structure of twisted bilayer graphene.

2.1 Energy bands of single-layer graphene

Graphene was first isolated from thick graphite using adhesive tape in 2004 by A. Geim and K. Novoselov [103]. From that moment, graphene has collected huge attention for its electrical, mechanical, thermal, and optical properties[104, 105]. Graphene is a single atomic layer of carbon atoms arranged in a hexagonal structure (see Fig. 2.1.1a). The basis has two atoms per unit cell and is triangular. The lattice vector in the real space can be written from geometrical considerations and defining a proper reference system (Fig. 2.1.1a) as[106]:

$$\mathbf{a}_1 = \frac{a}{2}(3, \sqrt{3}), \qquad \mathbf{a}_2 = \frac{a}{2}(3, -\sqrt{3}) \tag{2.1.1}$$

While the reciprocal lattice vectors:

$$\mathbf{G}_1 = \frac{2\pi}{3a}(1, \sqrt{3}), \qquad \mathbf{G}_2 = \frac{2\pi}{3a}(1, -\sqrt{3}) \tag{2.1.2}$$

Where $a \approx 0.142$ nm is the carbon-carbon interatomic distance. Each carbon atom has three nearest neighbors, separated in real space by the vectors[106]:

$$\boldsymbol{\delta}_1 = \frac{a}{2}(1, \sqrt{3}), \qquad \boldsymbol{\delta}_2 = \frac{a}{2}(1, -\sqrt{3}), \qquad \boldsymbol{\delta}_3 = -a(1, 0) \tag{2.1.3}$$

Graphene possesses, in total, four valence electrons. Since three of these electrons form covalent bonds in the x-y plane and do not contribute to the conductivity, graphene can be treated as having one conduction electron in the $2p_z$ state [107]. The first Brillouin zone has four high symmetry points: $\mathbf{\Gamma}$, $\mathbf{K}$, $\mathbf{K}'$ and $\mathbf{M}$. As will be discussed in the following, the two inequivalent points located at the corners of the first Brillouin zone, $\mathbf{K}$ and $\mathbf{K}'$ are important in graphene because there electrons behave as massless Dirac particles and are therefore called Dirac points:

$$\mathbf{K} = \frac{2\pi}{3a}(1, \frac{1}{\sqrt{3}}), \qquad \mathbf{K}' = \frac{2\pi}{3a}(1, -\frac{1}{\sqrt{3}}) \tag{2.1.4}$$

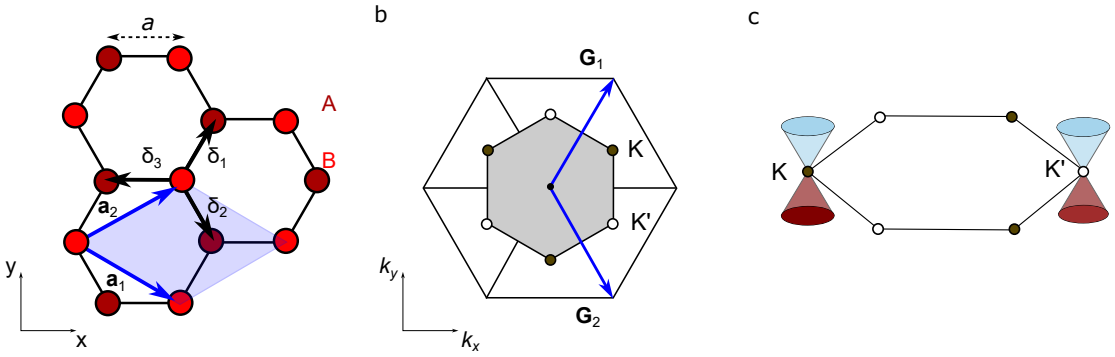

Figure 2.1.1: Band structure of monolayer graphene. (a) Atomic structure of monolayer graphene in real space. The honeycomb graphene lattice features two sublattices, A and B, depicted as red and brown circles. The blue arrows as $\mathbf{a}_1$ and $\mathbf{a}_2$ indicate the lattice vectors. **(b)** The hexagonal Brillouin zone of graphene (marked in grey) includes two non-equivalent corners, $\mathbf{K}$ (solid circles) and $\mathbf{K}'$ (open circles). The blue arrows indicate the reciprocal lattice vectors as $\mathbf{G}_1$ and $\mathbf{G}_2$. **(c)** The low-energy band structure of graphene shows a linear dispersion (Dirac cone) and their corresponding Dirac points at the ($\mathbf{K}$) and ($\mathbf{K}'$) corners of the Brillouin zone.

The first theoretical study of graphene's electronic band structure and Brillouin zones was developed using the tight binding approximation in 1947 by P. R. Wallace [107]. Using this approximation with one p_z orbital on each atomic site [108], the wavefunction has the form:

$$\psi(\boldsymbol{r}) = C_A\phi_A(\boldsymbol{r}) + C_B\phi_B(\boldsymbol{r}) \tag{2.1.5}$$

Where $\phi_A(\mathbf{r})$ and $\phi_B(\mathbf{r})$ are Bloch wavefunctions of p_z orbitals for atoms A and B, while C_A and C_B are the eigenvalues:

$$\phi_A(\mathbf{r}) = \frac{1}{\sqrt{N}} \sum_{\boldsymbol{R_A}} e^{i\boldsymbol{k}\cdot\boldsymbol{R_A}} \phi(r - \boldsymbol{R_A}) \tag{2.1.6}$$

and

$$\phi_B(\mathbf{r}) = \frac{1}{\sqrt{N}} \sum_{\boldsymbol{R_B}} e^{i\boldsymbol{k}\cdot\boldsymbol{R_B}} \phi(r - \boldsymbol{R_B}) \tag{2.1.7}$$

Where $\boldsymbol{R_A}$ and $\boldsymbol{R_B}$ are the positions of the atoms A and B, respectively. Here, the first sum is taken over A and all the lattice points generated from it by primitive lattice translations and the second over the points generated from B. Defining the matrix elements as $H_{ij}(\boldsymbol{k}) = \langle \phi_i(r) | H | \phi_j(r) \rangle$ it is possible to write the 2-by-2 matrix Hamiltonian and then find the eigenvalues:

$$\begin{pmatrix} H_{AA}(\boldsymbol{k}) & H_{AB}(\boldsymbol{k}) \\ H_{BA}(\boldsymbol{k}) & H_{BB}(\boldsymbol{k}) \end{pmatrix} \begin{pmatrix} C_A \\ C_B \end{pmatrix} = E \begin{pmatrix} C_A \\ C_B \end{pmatrix} \tag{2.1.8}$$

As graphene is made up of carbon atoms in a hexagonal structure, the environments around atoms A and B are the same and for the diagonal elements holds: $H_{AA}(q) = H_{BB}(q) = 0$. Assuming only nearest-neighbor interaction, the diagonal elements are constant values independent of $\boldsymbol{k}$. Therefore, just the non-diagonal terms are the non-trivial matrix elements, which can be calculated as:

$$\begin{aligned} H_{AB}(\boldsymbol{k}) = \langle \phi_A(\boldsymbol{r}) | H | \phi_B(\boldsymbol{r}) \rangle = \frac{1}{N} \sum_{\boldsymbol{R_A}} \sum_{\boldsymbol{R_B}} e^{i\boldsymbol{k}\cdot(\boldsymbol{R_B}-\boldsymbol{R_A})} \langle \phi(\boldsymbol{r}-\boldsymbol{R_A}) | H | \phi(\boldsymbol{r}-\boldsymbol{R_B}) \rangle = \\ = \sum_{\boldsymbol{R_A}} e^{i\boldsymbol{k}\cdot(\boldsymbol{R_B}-\boldsymbol{R_A})} \langle \phi(\boldsymbol{r}-\boldsymbol{R_A}) | H | \phi(\boldsymbol{r}-\boldsymbol{R_B}) \rangle = \\ = -t_0[e^{i\boldsymbol{k}\cdot\boldsymbol{\delta_1}} + e^{i\boldsymbol{k}\cdot\boldsymbol{\delta_2}} + e^{i\boldsymbol{k}\cdot\boldsymbol{\delta_3}}] \end{aligned} \tag{2.1.9}$$

Where $\boldsymbol{\delta_1}$, $\boldsymbol{\delta_2}$, and $\boldsymbol{\delta_3}$ are the vectors pointing to the nearest-neighbor atoms from each site defined in Eq. 2.1.3 (see Fig. 2.1.1a). Here, we have used the translational symmetry to get rid of the sum over the B sites and the nearest-neighbor approximation to replace the hopping term $\langle \phi(\boldsymbol{r}-\boldsymbol{R_A}) | H | \phi(\boldsymbol{r}-\boldsymbol{R_B}) \rangle$ with $t_0 \approx 2.8$eV. Substituting $\boldsymbol{\delta_1}$, $\boldsymbol{\delta_2}$ and $\boldsymbol{\delta_3}$ in Eq. 2.1.9 we can rewrite the non-diagonal matrix elements as:

$$H_{AB}(\boldsymbol{k}) = -t_0 e^{-ik_x a}\left[1 + 2e^{i\frac{3a}{2}k_x} \cos\left(\frac{\sqrt{3}a}{2}k_y\right)\right] = \Delta(\boldsymbol{k}) \tag{2.1.10}$$

The matrix Hamiltonian reads:

$$H(\boldsymbol{k}) = \begin{pmatrix} 0 & \Delta(\boldsymbol{k}) \\ \Delta^*(\boldsymbol{k}) & 0 \end{pmatrix} \tag{2.1.11}$$

By solving the equation $\det(H-E) = 0$, one gets the eigenvalues that correspond to upper and lower bands of graphene, respectively:

$$E_\pm(\boldsymbol{k}) = \pm|\Delta(\boldsymbol{k})| = \pm t_0 \sqrt{1 + 4\cos(\frac{3a}{2}k_x)\cos(\frac{\sqrt{3}a}{2}k_y) + 4\cos^2(\frac{\sqrt{3}a}{2}k_y)} \tag{2.1.12}$$

Remarkably, this relation becomes 0 at the Dirac points $\boldsymbol{k} = \mathbf{K}$ or $\boldsymbol{k} = \mathbf{K}'$ as shown in Fig. 2.1.1c and the spectrum is symmetric around zero energy. If we define the vector

$\boldsymbol{q} = \boldsymbol{k} - \mathbf{K}$, we can can expand the expression for $\Delta(\boldsymbol{k})$ around $\boldsymbol{q} = 0$ and find:

$$\Delta(\boldsymbol{q}) \simeq 2t_0 e^{-iK_x a} \boldsymbol{\nabla}_{\boldsymbol{k}} \left(e^{3ik_x a/2} \cos \frac{\sqrt{3}a}{2} k_y \right)_{\boldsymbol{k}=\mathbf{K}} \cdot \boldsymbol{q} = \frac{3at_0}{2} e^{-iK_x a}(q_x + iq_y) \tag{2.1.13}$$

Defining the Fermi velocity as $v_F = 3t_0 a/2$, with a value $v_F \approx 10^6$ m/s, and extracting the phase factor $e^{3ik_x a/2}$, we can write the first order expansion of the function $\Delta(\boldsymbol{q})$ as:

$$\Delta(\boldsymbol{q}) = \hbar v_F (q_x + iq_y) + O\left(\frac{q^2}{K^2}\right) \tag{2.1.14}$$

The Hamiltonian can be rewritten in the form:

$$\hat{H} = \hbar v_F \begin{pmatrix} 0 & q_x + iq_y \\ q_x - iq_y & 0 \end{pmatrix} = \hbar v_F \hat{\sigma} \cdot \boldsymbol{q} \tag{2.1.15}$$

Where $\hat{\sigma}$ are the two-by-two Pauli matrices. Notably, the spectrum depends only on the magnitude of $\boldsymbol{q}$ and not on the direction in the space:

$$E(\boldsymbol{k}) = \pm \hbar v_F |\boldsymbol{q}| \tag{2.1.16}$$

Therefore, the energy bands near the Dirac point have a linear dispersion curve resembling the photon dispersion curve. Recalling the relativistic formula $E = \sqrt{m^2c^2 + q^2c^4}$, it can be noted that this is the same equation provided that the effective mass, m is set to zero. Therefore, electrons near Dirac points can be considered as charged particles with zero-effective mass [106, 108, 109].

2.2 Band structure of twisted bilayer graphene

The band structure of twisted bilayer graphene was first calculated by Lopes dos Santos in 2007 [110], and later by Bistritzer and MacDonald in 2010 [111]. Their pioneering work revealed that for a discrete set of magic angles, the band structure flattens, leading to a vanishing Fermi velocity. The reduction of the Fermi velocity in the flat bands increases the electronic interactions, giving rise to many correlated quantum phases, such as superconductivity and correlated insulating states [112]. The first experimental studies on this system were conducted in the same year by the group of E. Andrei, who employed scanning tunneling spectroscopy to observe Van Hove singularities [113]. Later, in 2018, the transport studies performed by the group of P. Jarillo-Herrero led to the discovery of superconductivity [114]. In this section, we do not provide the complete derivation of the Bistritzer-MacDonald model, but we discuss the main features and provide a phenomenological understanding of the key aspects that lead to the formation of the flat bands. This includes an overview of the conditions under which these flat bands emerge and their implications for the electronic properties of twisted bilayer graphene.

2.2.1 Formation of moiré pattern in twisted bilayer graphene

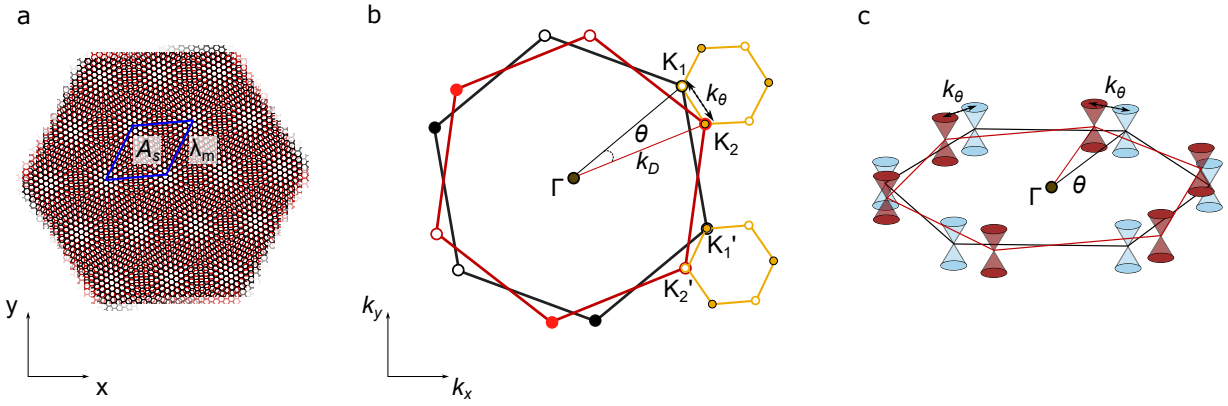

Figure 2.2.1: Moiré pattern and mini Brillouin zone. (a) Moiré pattern is formed in real space by the rotation of two graphene layers. The relative rotation between the layers induces a periodicity with a length scale $\lambda_m \approx a_0/(2\sin(\theta/2))$. For $\theta = 1.1°$, $\lambda_m \simeq 7$ nm. **(b)** The Moiré pattern in real space leads to the formation of mini-Brillouin zones (yellow hexagons) constructed from the difference between the $\mathbf{K}$ and $\mathbf{K}'$ wavevectors of the bottom (red) and top (black) layers: $\mathbf{K}_1 - \mathbf{K}_2$ and $\mathbf{K}'_1 - \mathbf{K}'_2$. **(c)** Dirac cones of the top (light blue) and bottom (red) graphene layers. k_θ is the displacement between the cones, which depends on the twist angle. When the twist angle is small, the Dirac cones of the top and bottom layer get close and hybridize.

As shown in Fig. 2.2.1a, the relative rotation by an angle θ, of two graphene layers stacked on top of each other, generates a moiré pattern with periodicity $\lambda_m \approx a_0/(2\sin(\theta/2))$.

From which the area of the moiré supercell A_s is:

$$A_s = \frac{\sqrt{3}}{2}\lambda_m^2 = \frac{\sqrt{3}}{8}\frac{a_0^2}{\sin^2(\frac{\theta}{2})} \tag{2.2.1}$$

The periodicity in the real space induced by the rotation leads to the formation of new Brillouin zones[115]. These moiré Brillouin zones are defined by the distance between the $\mathbf{K}$ ($\mathbf{K}'$) corners of the Brillouin zones of the top $\mathbf{K}_1 - \mathbf{K}_2$ and bottom layers $\mathbf{K}'_1 - \mathbf{K}'_2$. Defining the Brillouin-zone wave vector for a single layer as $k_D = 4\pi/3a$ (also called Dirac momentum), the size of the mini-Brillouin zone is given by (see Fig. 2.2.1b):

$$k_\theta \approx 2k_D \sin(\frac{\theta}{2}) \tag{2.2.2}$$

Where k_θ defines the side of the hexagon of the moiré Brillouin zone. As expected, there is a large periodicity in the real space for small twist angles, which results in a small size of the Brillouin zone in the reciprocal space, also called the mini-Brilouin zone. The model used to describe twisted bilayer graphene is the continuum model[111, 116–118]. This model considers two layers of graphene described by a Dirac-like dispersion at the $\mathbf{K}$ ($\mathbf{K}'$) corners of the moiré Brillouin zone, each rotated by an angle $\pm\theta/2$, and coupled through a moiré potential $T(\boldsymbol{r})$ that describes the hopping between layers. Within this model, the low-energy Hamiltonian for the $\mathbf{K}$ Brillouin zone reads[117]:

$$H_K = \begin{pmatrix} v_F\boldsymbol{\sigma}\cdot\boldsymbol{p}_1 & T(\boldsymbol{r}) \\ T^\dagger(\boldsymbol{r}) & v_F\boldsymbol{\sigma}\cdot\boldsymbol{p}_2 \end{pmatrix} \tag{2.2.3}$$

The subscripts $i = 1, 2$ indicate the top and bottom layer, respectively, and $\boldsymbol{p}_i = \hbar(\boldsymbol{k} - \mathbf{K}_i)$. As anticipated above, the matrix in Eq. 2.2.3 is formally analogous to that of single-layer graphene. The key difference lies in the off-diagonal terms, which correspond to the interlayer hopping, which is responsible for the hybridization of the bands. The moiré potential can be expressed as $T(\boldsymbol{r}) = \sum_{n=0}^{2} T_{n+1} e^{-i\boldsymbol{q}_{n+1}\boldsymbol{r}}$, where $\boldsymbol{q}_1 = k_\theta(0, -1)$and $\boldsymbol{q}_{2,3} = k_\theta(\pm\sqrt{3/2}, 1/2)$. These $\boldsymbol{q}_{n+1}$ vectors indicate the hopping directions in the first Brillouin zone, which result in three distinct tunneling processes. The interlayer coupling term, according to the symmetry of the system, reads[111, 117]:

$$T_{n+1} = w_{AA}\sigma_0 + w_{AB}[\sigma_x \cos(n\phi) + \sigma_y \cos(n\phi)], \qquad \phi = 2\pi/3; \quad n = 0, 1, 2 \tag{2.2.4}$$

Where w_{AA} and w_{AB} are the interlayer coupling parameters for AA and AB bilayer sites, respectively. The initial calculations of the band structure with the continuum model assumed identical interlayer coupling parameters for the AA and the AB sites, $w_{AA} = w_{AB}$[111]. This ideal assumption, which considers static carbon atoms, leads to a gapless band structure, conversely from experimental observations. In reality, the lattice structure spontaneously relaxes to achieve an energetically favorable configuration. Specifically, twisted bilayer graphene deforms to maximize AB areas while minimizing AA areas[119]. Experimentally, it was found that this lattice relaxation leads to $w_{AA}/w_{AB} \simeq$

0.7-0.8[117]. Including the lattice relaxation into the model enables the opening of a gap between the flat and dispersive bands, as observed in experiments[119]. To summarize, the central concept in the formation of flat bands in twisted bilayer graphene is that the moiré pattern forms a moiré potential, which leads to tunneling between the layers. The interlayer tunneling strongly depends on the twist angle and induces a hybridization of the band structure. At a specific set of angles, called the 'magic' angles, ultra-flat bands emerge[111, 112, 115]. In the following, we phenomenologically introduce the emergence of flat bands, describing how the twisting between the two graphene layers modifies the band structure. We distinguish three different scenarios.

2.2.2 Emergence of flat bands in MATBG

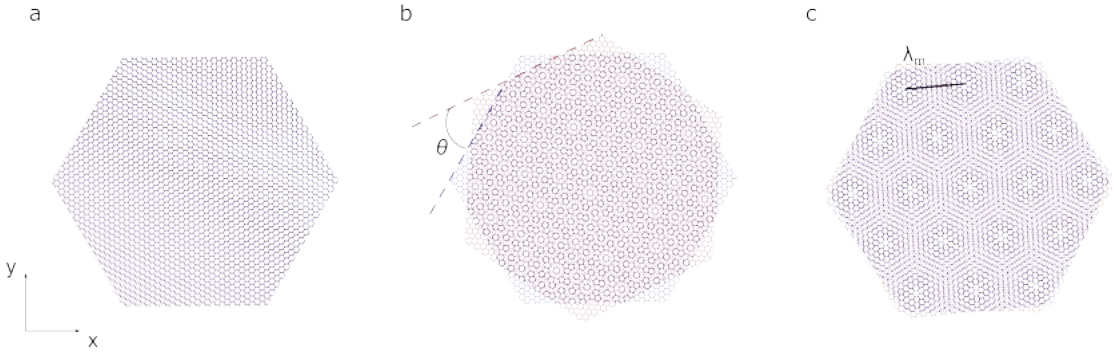

Figure 2.2.2: Twisted bilayer graphene in real space. (a)-(c) Graphene layers in real space rotated at $\theta = 0°$**(a)**, large angles **(b)** and small twist angles **(c)**.

1. No interaction ($w = 0$)

Without interlayer tunneling, the Hamiltonian of the system is simply given by the superposition of two Hamiltonians of single-layer graphene, see Eq. 2.1.15. In this scenario, the effect of the twist angle is just a relative motion of the Dirac cones, which intersect at energy (Fig. 2.2.3a):

$$\Delta E_0 = \frac{\hbar v_F k_\theta}{2} \approx \frac{4\pi}{3a} \hbar v_F \sin(\frac{\theta}{2}) \tag{2.2.5}$$

Notably, at large angles (Fig. 2.2.2b) e.g. $\theta = 10°$, the intersection energy is high, $\Delta E_0 \sim 1$ eV, while at lower angles the intersection occurs at lower energies, e.g. for $\theta = 1°$, $\Delta E_0 \sim 0.1$ eV.

2. Large twist angles ($\hbar v_F k_\theta >> w$)

In presence of interlayer hopping $w \neq 0$, the electrons can tunnel between the two Dirac cones, changing the band structure and generating saddle points in correspondence to

these intersections[115]. The saddle points correspond to peaks in the density of states (DOS), called van Hove singularities (VHSs), measured by scanning tunneling spectroscopy already in 2010 [113]. For large twist angles the energy difference between the VHSs of the conduction band and valence band can be estimated as (Fig. 2.2.3b):

$$\Delta E \approx 2\Delta E_0 - 2w \approx \hbar v_F k_\theta - 2w \tag{2.2.6}$$

From Bernal-stacked bilayer graphene, the interlayer tunneling strength is $w \approx 0.1$ eV[111, 115] (considering $w_{AA} = w_{AB}$ for this phenomenological description[117]). If the twist angle is large, the intersection point of the Dirac cones is located at relatively high energy, e.g. for $\theta = 10°$, $\Delta E_0 \approx 1$ eV $>> w$. As a result, the low-energy band structure is unaffected by this interaction, and the band structure is the same as isolated graphene[113, 120]. As the two competing energy scales that determine the physics of twisted bilayer graphene are the interlayer tunneling strength, w and the intersection energy, $\hbar v_F k_\theta$ a new dimensionless parameter can be introduced:

$$\alpha = \frac{w}{\hbar v_F k_\theta} \tag{2.2.7}$$

3. Low twist angles ($\hbar v_F k_\theta \approx w$)

For low twist angles (Fig. 2.2.2c), the interlayer tunneling strength becomes comparable with the intersection energy, e.g. for $\theta = 1°$, $\Delta E_0 \sim 0.1$ eV $\approx w$. In this scenario, the low-energy band structure is highly affected by electron tunneling and results in a strong hybridization between the layers, leading to the formation of flat bands. The hybridization of the bands at low twist angles results in a strong renormalization of the Fermi velocity v^* , which can be calculated from the continuum model as[111]:

$$\frac{v^*}{v_0} = \frac{1 - 3\alpha^2}{1 + 6\alpha^2} \tag{2.2.8}$$

Where v_0 is the Fermi velocity of single layer graphene and α is a dimensionless parameter given by the ratio between the interlayer tunneling strength and the intersection energy, $\alpha = w/(\hbar v_0 k_\theta)$. If $\alpha = 0$, v^* is the same as single-layer graphene, v_0. In Fig. 2.2.4a we plot the renormalized Fermi velocity as a function of twist angle. Substituting the expression for α and k_θ in Eq.2.2.8 it is possible to calculate the angle for which the Fermi velocity drops to zero ($v^*/v_0 = 0$) as:

$$\theta^{(1)}_{MATBG} \approx 2 \arcsin\left(\frac{3a\sqrt{3}w}{8\pi\hbar v_0}\right) \approx 1.1° \tag{2.2.9}$$

Where we used the values $w = 0.11$ eV, $v_0 = 8.7 \times 10^5$ m/s, and $a = 0.246$ nm[111]. This relation defines the so-called first magic angle[111]. A full sequence of magic twist angles can be derived analytically[117] by the following expression: $\theta_j \approx \theta_0(\alpha_0/\alpha_j)$, where $\alpha_j \approx \alpha_0 + 3/2j$ and $\alpha_0 = w/(\hbar v_0 k_\theta) \approx 1/\sqrt{3}$; $j = 0, 1, ...$

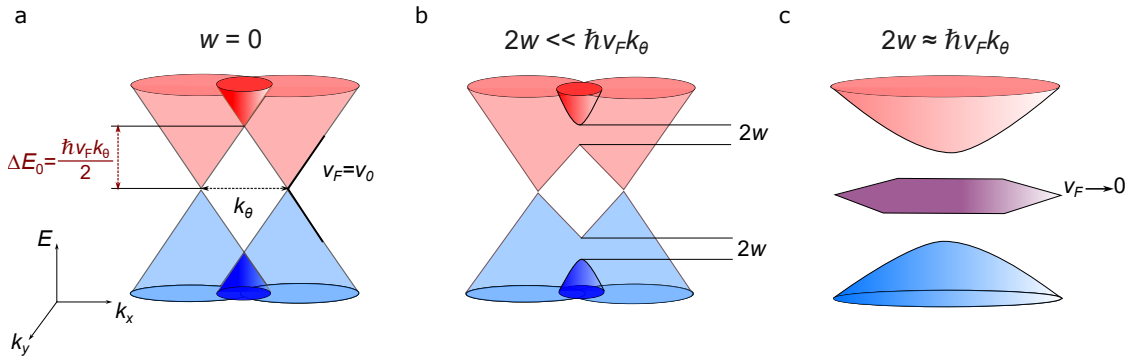

Figure 2.2.3: Engineering of the band structure with a twist. **(a)** Sketch of the band structure of twisted bilayer graphene without interlayer tunneling $w = 0$. In this configuration the Dirac cones of the bottom and top layer intersect at an energy: $\Delta E_0 = \hbar v_F k_\theta/2$. **(b)** In presence of interlayer tunneling, the Dirac cones hybridize and form saddle points in the band structure. For large twist angles the interlayer tunneling strength is much smaller than the intersection energy, and as a result, the low-energy band structure is unaffected by this interaction. **(c)** For low twist angles, the interlayer tunneling strength becomes comparable with the intersection energy: $\hbar v_F k_\theta \approx 2w$, resulting in a strong hybridization of the bands and the emergence of flat bands at low energy. In the flat bands, the Fermi velocity of electrons is strongly renormalized and tends to zero ($v_F \to 0$).

At the magic angles, electrons slow down significantly, forming extremely flat energy bands with a bandwidth of approximately 10 meV[112]. The moiré-periodic potential flattens the electronic bands and separates them from higher-energy dispersive bands, creating an energy gap as shown in Fig. 2.2.4b. As the Fermi velocity approaches zero, the electrons' kinetic energy is greatly reduced, making Coulomb interactions the dominant energy scale[112, 115, P4]. This, combined with the high density of states, leads to strong electronic interactions, resulting in a variety of emergent phases linked to strongly correlated electrons. These phases include correlated insulating states[33], orbital magnetism[122], Chern insulators[123], strange metallicity[P5], and, as anticipated in Section 1.3.2, record-low carrier density superconductivity[34, P2, 114], none of which are present in single-layer graphene.

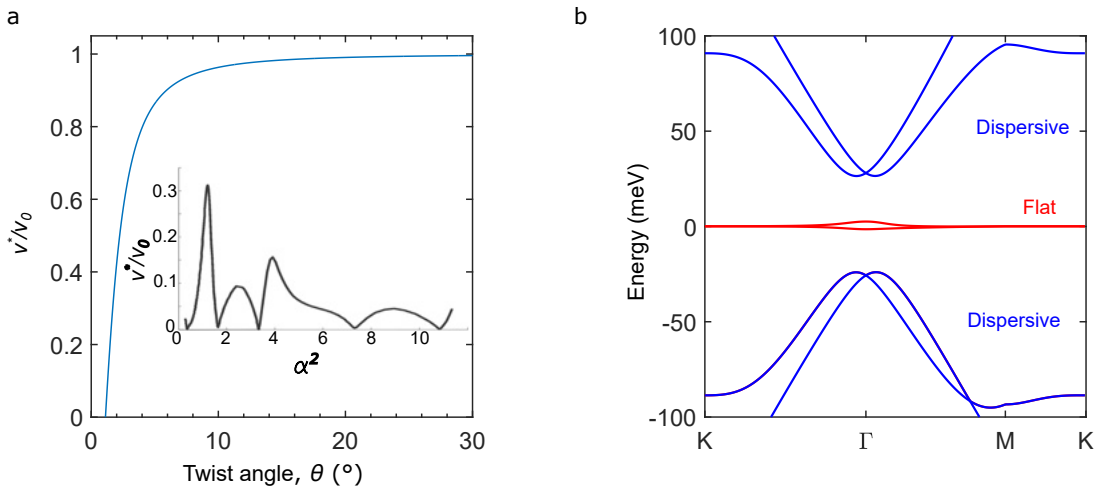

Figure 2.2.4: Renormalization of the Fermi velocity and flat bands in MATBG. (a) Theoretical calculation of the renormalized Fermi velocity v^*/v_0 as a function of twist angle from Eq. 2.2.8, using $w = 110$ meV and $a = 0.246$ nm. **Inset**: Renormalized Fermi velocity as a function of the dimensionless parameter $\alpha = w/(\hbar v_0 k_\theta)$ in the range $0.18° < \theta < 1.2°$. The inset is adapted from Ref. [111]. **(b)** Band structure calculated from the continuum model for a twist angle of $\theta = 1.00°$. The parameters used in the calculations are $w_{AA} = 88$ meV; $w_{AB} = 110$ meV and $v_F = 1.05 \times 10^6$ m/s. The calculation was performed by Marc Currle [121].

2.3 Electronic properties of MATBG

Having discussed the emergence of flat bands at the magic angles from the continuum model, we now turn our attention to the main electronic properties observed in experiments. Electronic properties are typically measured by low-temperature (< 1K) transport experiments. This section provides an overview of the key electronic characteristics observed in high-quality MATBG devices, which include insulating states at integer moiré band fillings and superconducting domes. Detailed descriptions of the low-temperature electrical transport measurements and the fabrication of high-quality MATBG devices can be found in Chapter 3 and Chapter 4, respectively.

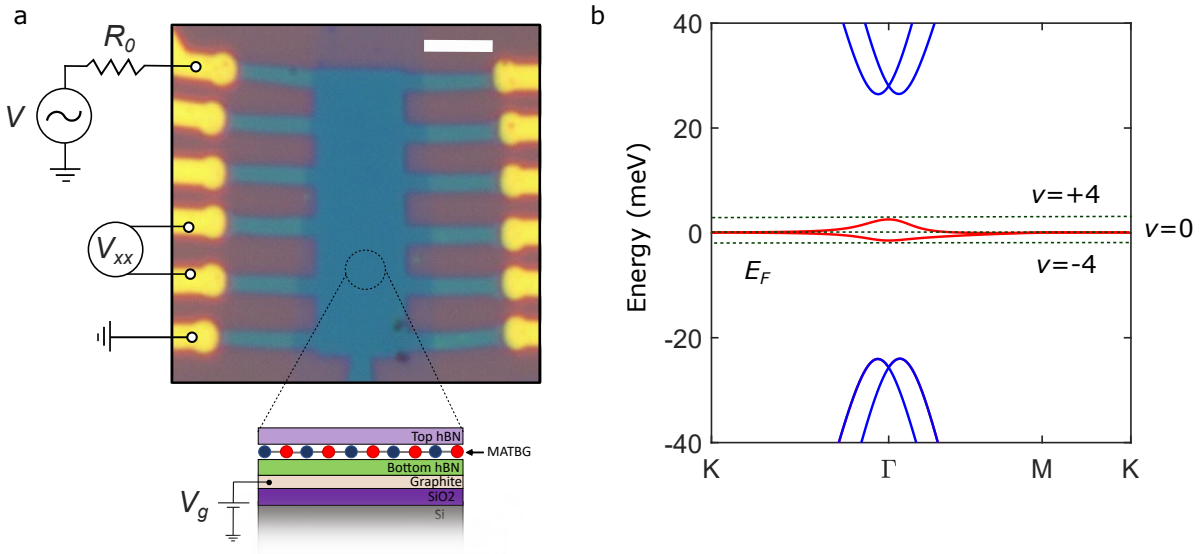

Figure 2.3.1: Transport measurement scheme of a MATBG device. **(a)** A low-frequency AC voltage is applied to the source contact of the device and the voltage is measured in a four-probe scheme with standard lock-in technique (see Section 4.2.1). In our measurements $R_0 = 10$ MΩ . Applying a gate voltage V_g to the graphite gate beneath the sample is possible to tune the carrier concentration in the device according to Eq.2.3.1. **(b)** Zoom in of the band structure calculated from the continuum model for a twist angle of $\theta = 1.00°$. The horizontal dashed lines indicate three different filling factors $\nu = 0, \pm 4$.

In standard transport experiments the four-terminal longitudinal resistance is measured as a function of the carrier concentration in the MATBG and is investigated for different temperatures, magnetic fields, and other experimental parameters. As schematically illustrated in Fig. 2.3.1a, the metallic graphite gate beneath the heterostructure is employed to electrostatically modulate the carrier concentration in the MATBG (n). By applying an external gate voltage (V_g), the electron population across the entire bandwidth of the flat band can be adjusted in situ, allowing the exploration of all correlated phases coexisting in a single device[112]. The relationship between the carrier concentration and the gate

voltage is given by:

$$n = \frac{C_g}{e} V_g \tag{2.3.1}$$

Where C_g is the gate capacitance of the bottom hBN which depends on the material's thickness. Near the magic angle in twisted bilayer graphene, the flat bands exhibit a fourfold degeneracy corresponding to spin and valley degrees of freedom[124, 125]. Therefore, the superlattice density n_s, defined as the density required to fill one band in the superlattice, can be expressed (for small twist angles $1° < \theta < 3°$, [33]) as:

$$n_s = \frac{4}{A_s} \simeq \frac{8\theta^2}{\sqrt{3}a^2} \tag{2.3.2}$$

Where A_s is the superlattice area defined in Eq. 2.2.1. The filling factor (filling of electrons per moiré unit cell) can be derived as:

$$\nu = 4\frac{n}{n_s} \tag{2.3.3}$$

Adjusting the carrier density (filling factor) in MATBG is equivalent to shifting the Fermi level within the band structure as illustrated schematically in Fig. 2.3.1b, according to the relation[126]:

$$n = \int_0^{E_F} DOS(\epsilon) f_{FD}(\epsilon) d\epsilon \tag{2.3.4}$$

While in single-layer graphene, the DOS is linear in energy, in twisted-bilayer graphene, it is non-linear due to the presence of VHSs. By changing the Fermi level, it is, therefore, possible to change the state of the material. In Fig. 2.3.1b, we draw the Fermi level for three filling factors on the calculated single-particle band structure. For $\nu = \pm 4$, we expect the flat bands to be filled and the MATBG to behave as an insulator, while for the filling factor ν=0, we expect a Dirac-like behavior as in single-layer graphene. Fig. 2.3.2a illustrates a typical four-terminal longitudinal resistance R_{xx} vs. moiré filling factor ν for a MATBG device with twist angle $\theta = 1.04° \pm 0.02$ across temperatures ranging from T = 50 mK up to T = 6 K in which we observe a series of high resistive peaks flanked by low-resistive metallic states.

Single-particle picture

As expected from 2.3.1b the most prominent resistance peaks are observed at electrostatic doping levels corresponding to the full filling of the bands (four electrons per moiré unit cell). These states, known as band insulators (BI), correspond to the edges of the flat bands. Gating the system to these doping levels places the Fermi level at the edge of the flat bands. The presence of an energy gap between the flat bands and the dispersive bands (approximately 20-30 meV) manifests in electronic transport as strongly pronounced insulating states at these fillings ($\nu = \pm 4$), as shown in Fig. 2.2.4b. Another feature predicted by the non-interacting picture is the charge neutrality point (CNP), similar to single-layer graphene, which appears as a peak at zero energy.

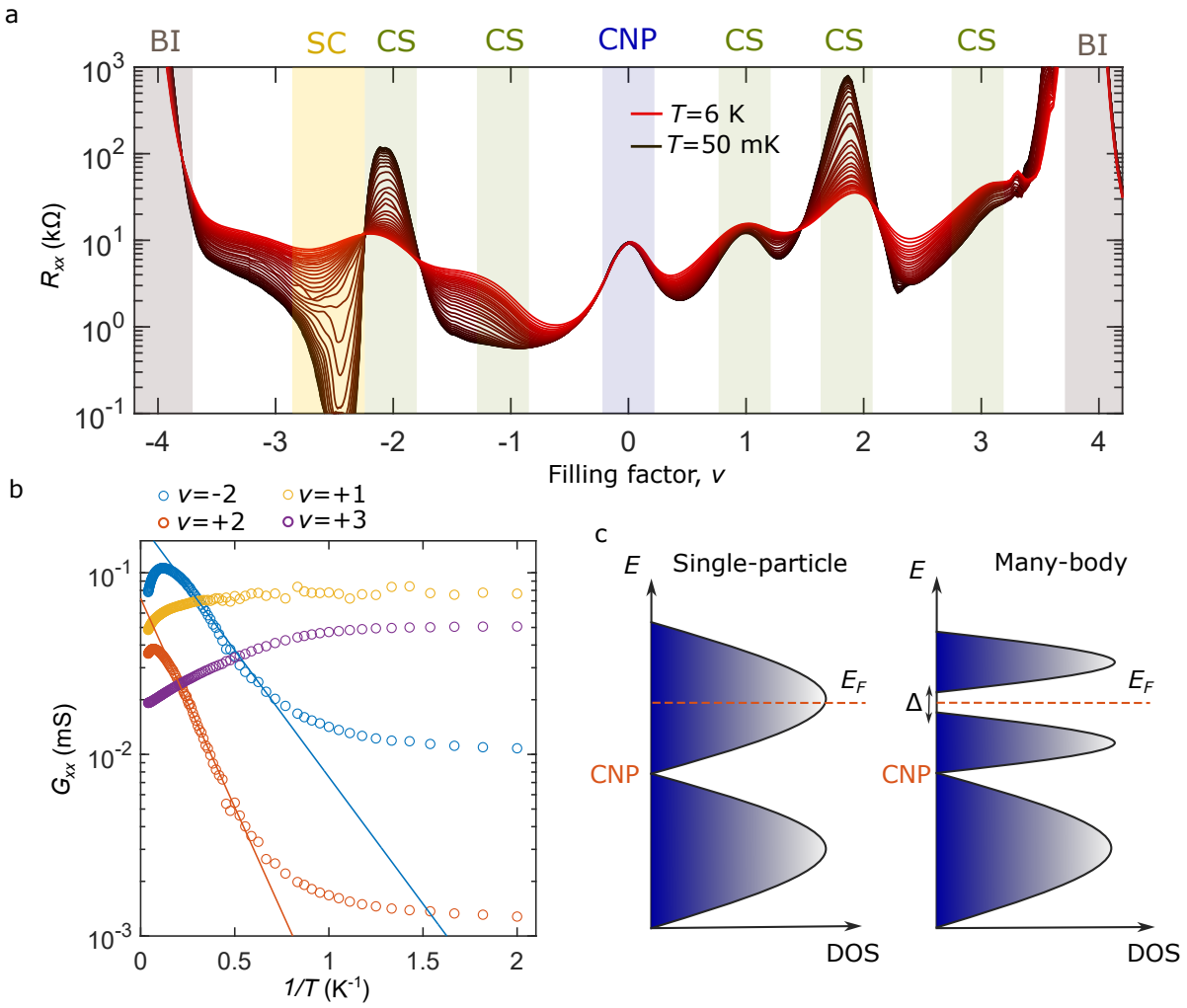

Figure 2.3.2: Transport characterization of MATBG. (a) Longitudinal resistance R_{xx} as a function of filling factor ν for successive temperatures T ranging from 50 mK to 6 K. The charge neutrality point (CNP) and the band insulators (BI) marked in blue and grey respectively are predicted by the band structure obtained in the single-particle picture without including electronic interactions. The states marked in green appearing at the integer fillings of the bands are given by electronic interactions and are not predicted by the single-particle band structure. **(b)** Conductance G_{xx} vs. inverse temperature for $\nu = \pm 2, +1, +3$. The straight lines are fits to the Arrhenius law for temperature-activated behaviour: $G_{xx} \propto \exp(-\Delta/2k_BT)$. From this fit we extract gap values of 0.55 meV for ν = -2 and 0.91 meV for ν =+2. **(c)** Schematic representation of the DOS without considering electronic interactions, i.e. single-particle (left) and many-body (right) picture. The flat bands of MATBG in the single-particle picture are expected to be purely metallic (left). Electronic interactions can split the single particle bands opening up a gap Δ. In the flat bands of MATBG correlated gaps are oberved in correspondence to integer fillings [33, 122, 127].

Integer-filling correlated states

Additional resistance peaks are observed at the integer filling of the moiré unit cell ($\nu = +1, \pm 2, +3$). Unlike band insulators, these peaks are not predicted by the single-particle picture band structure (Fig. 2.3.1b), which predicts metallic states at integer-fillings of the flat bands. These states, emerging at integer fillings of the flat bands, originate from strong electronic interactions[33]. The peaks at $\nu = \pm 2$ exhibit insulating behavior, with resistance increasing as temperature decreases. By analyzing the thermal activation of these gaps (Fig. 2.3.2b), the activated gap sizes for these insulating states are determined to be 0.55 meV (ν = -2) and 0.91 meV (ν =+2) in the shown device. Thermally activated gaps were also reported for $\nu = +3$ and $\nu = +1$ [P4] and are absent for the ν = -3 and ν = -1 states. An intuitive explanation for this phenomenon is that when the moiré lattice sites are fully occupied by an integer number of electrons or holes (integer fillings), no free lattice positions remain, causing resistance to increase significantly[P4]. Conversely, resistance remains low at electron densities between these integer values. In terms of band structure, electronic interactions can split the single-particle flat bands into upper and lower many-body bands, separated by an energy gap Δ (Fig. 2.3.2c). Near the magic angles, the bandwidth W is significantly reduced, making the on-site Coulomb energy U larger than W. Consequently, the gap induced by electronic interactions gives rise to the insulating states observed at the integer fillings of the moiré unit cell, which are referred to as correlated insulators.

2.3.1 Twist Angle Extraction

Transport measurements are also used to determine the relative twist angle between graphene layers. As mentioned earlier, the twist angle θ is related to the superlattice carrier density n_s according to Eq. 2.3.2. By employing transport measurements, n_s can be identified as the carrier density corresponding to the full-filling of the flat bands (band insulators in Fig. 2.3.2a):

$$n_s = \frac{C_g}{e} V_{BI} \tag{2.3.5}$$

Here, V_{BI} represents the voltage at the position of the band insulators (the edge of the flat bands), which can be determined by measuring the R_{xx} vs. V_g traces as shown in Fig. 2.3.2a. The capacitance of the hBN, C_g, can be extracted using various methods, typically through the low-field Hall effect or the quantum Hall effect[33, 122].

Low-field Hall Effect

In a Hall bar geometry (Fig. 2.3.1a), a low external magnetic field < 1 T induces a Hall resistance from which we can extract the Hall carrier density as[33, 122, 128]:

$$n_H = -\frac{B}{eR_{xy}} \tag{2.3.6}$$

Where R_{xy} is the transverse resistance, e the charge of the electron, and B the external magnetic field at which R_{xy} is calculated. Typically, the R_{xy} can be antisymmetrized to eliminate any signal mixing due to geometric effects:

$$R_{xy}^{antisym} = \frac{R_{xy}(+B) - R_{xy}(-B)}{2} \tag{2.3.7}$$

As shown in Fig. 2.3.3a, close to the charge neutrality point, a new Fermi surface forms. Therefore, the Hall carrier density equals the carrier density, from which the gate capacitance can be extracted by a linear fit with the equation:

$$n_H = n = \frac{C_g}{e} V_g \tag{2.3.8}$$

Quantum Hall Effect

The quantum Hall effect provides an independent method to determine the twist angle. When a two-dimensional electron system is cooled to low temperatures and subjected strong magnetic fields ($B > 1$ T), the energies of cyclotron orbits become quantized into discrete values, known as Landau levels. The Hall resistance (R_{xy}) exhibits steps corresponding to these quantized values, while the longitudinal resistivity (R_{xx}) becomes zero. By mapping R_{xx} as a function of gate voltage (V_g) and magnetic field (B), the Landau levels can be identified in this phase space, known as a Landau fan diagram, as a fan of tilted lines with $R_{xx} = 0$ (see Fig. 2.3.3b). The carrier density (n) corresponding to these states can be then expressed as[33, 123, 128]:

$$n = \nu_{LL} \frac{eB}{h} \tag{2.3.9}$$

where ν_{LL} is the filling factor of the Landau levels. As shown in Fig. 2.3.3b, using Eq. 2.3.1, the gate capacitance can be extracted from the slope of the Landau levels as:

$$C_g = \frac{e^2}{h} \frac{\Delta B}{\Delta V_g} \nu_{LL} \tag{2.3.10}$$

In order to properly perform a fitting of the Landau levels, it is important to know the degeneracy of the Landau levels (ν_{LL}). For single-layer graphene, the degeneracy is 4-fold due to spin and valley degrees of freedom. In twisted bilayer graphene, it should be 8-fold, having the additional degeneracy coming from the second graphene layer. However, while the 8-fold degeneracy is observed for devices with large twist angles[129], it was experimentally measured that the degeneracy of Landau levels flanking the charge neutrality point (CNP) in twisted bilayer graphene changes to 4-fold when the twist angle is reduced to values near the magic angle ($\nu_{LL} = \pm 4, \pm 8, \pm 12...$), potentially due to interactions or symmetry breaking[124, 125].

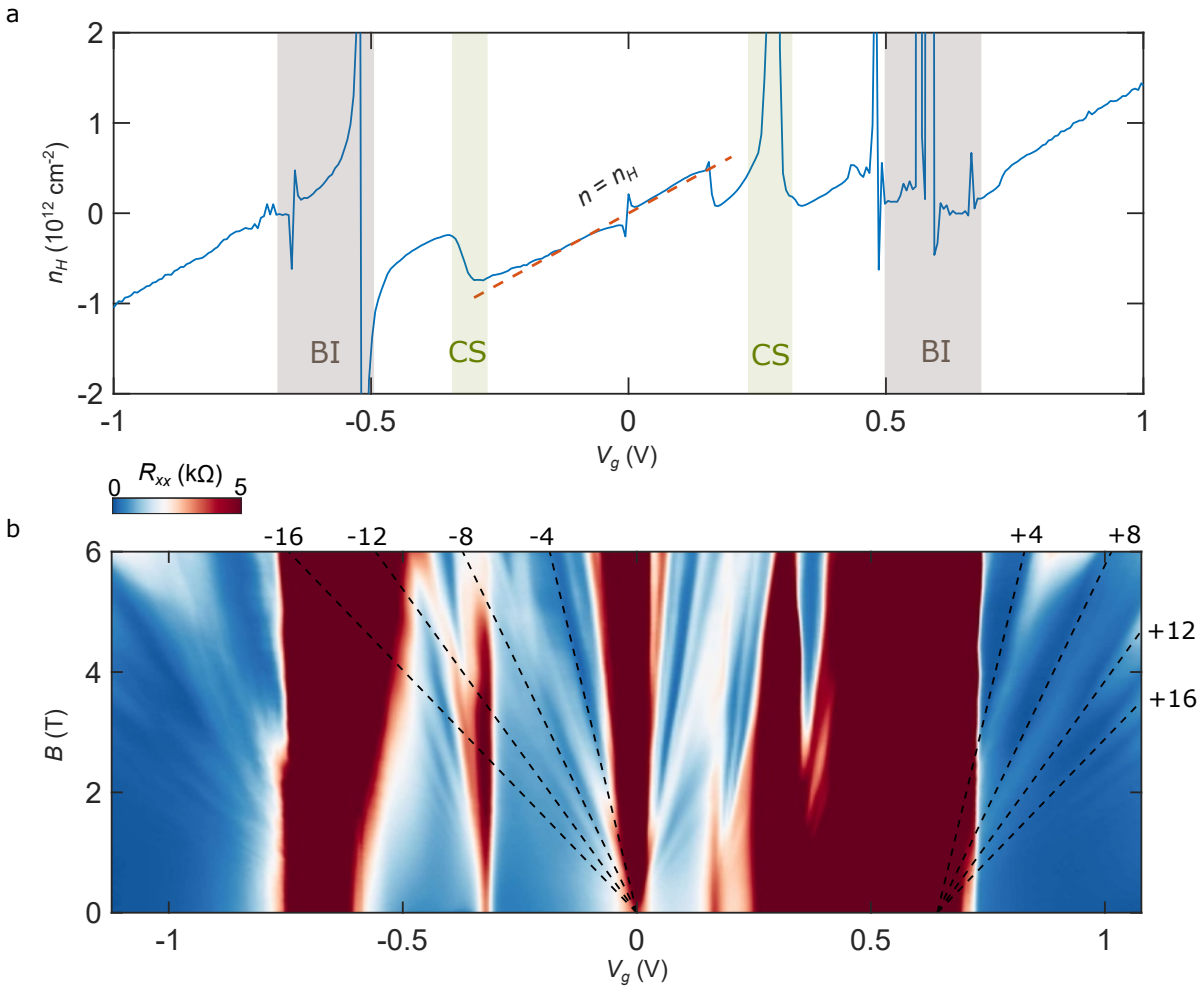

Figure 2.3.3: Twist angle extraction. (a) Twist angle extracted using the low-field Hall effect. Close the CNP a new Fermi surface forms and the gate capacitance can be extracted by a linear fit with the equation: $n_H = V_g C_g/e$. **(b)** Twist angle extracted using the landau fan diagram. The capacitance is obtained by fitting the Landau levels originating from the CNP and the band insulators according to the formula: $C_g = e^2/h \cdot \Delta B/\Delta V_g \cdot \nu_{LL}$. The Landau levels filling factors are: $\nu_{LL} = \pm 4, \pm 8, \pm 12....$ The capacitance extracted with both methods is $C_g = 500$ nF/cm^2 which results in a twist angle of $\theta = 0.93 \pm 0.01°$.

2.4 Ultra-low carrier density superconducting state

The most relevant phase for SPD is the ultra-low carrier density superconducting state observed close to the negative half-filling at $\nu = -2-\delta$. Other studies also reported similar superconducting domes at different filling factors[114, 122, 130]. The color plot in the top panel of Fig. 2.4.1a shows the carrier density, n versus temperature, T. In this phase space, the superconducting region is dome-shaped and flanked by a correlated insulating state. As evidenced by the measurement of the Hall density (n_H) vs. carrier density (n) (bottom panel of Fig. 2.4.1a), in correspondence to the correlated insulator, the Fermi level resets, lowering dramatically the density of free carriers. For optimal doping, we use the low-field Hall effect to extract a carrier density of $n_H = -1.96\times10^{11}$ cm^{-2}. As anticipated in Section 1.3.2, the record-low carrier density of MATBG makes it the most diluted superconducting phase and opens up a promising avenue for low-energy SPD [34, P2]. This peculiar feature also translates into a record low electronic heat capacity, which is another key thermal parameter for superconducting detectors (especially for the TES discussed in Section 1.3.1). In Fig. 2.4.1b we plot the electronic heat capacity (C_e) calculated for MATBG in the non-interacting picture for a carrier density of $n_H = -1.96 \times 10^{11}$ cm^{-2}[P2]. For temperatures below 100 mK, (which is the typical operation temperature for TES) the calculated value is $C_e/A < 10^3\, k_B/\mu\text{m}^2$, which is at the state-of-the-art of TES detectors[68]. However, it is essential to point out once more, that the heat capacity calculated here neglects electronic interactions which in this system are strong. Even though these heat capacity values might not be accurate, they still point out the sensitivity of MATBG for SPD.

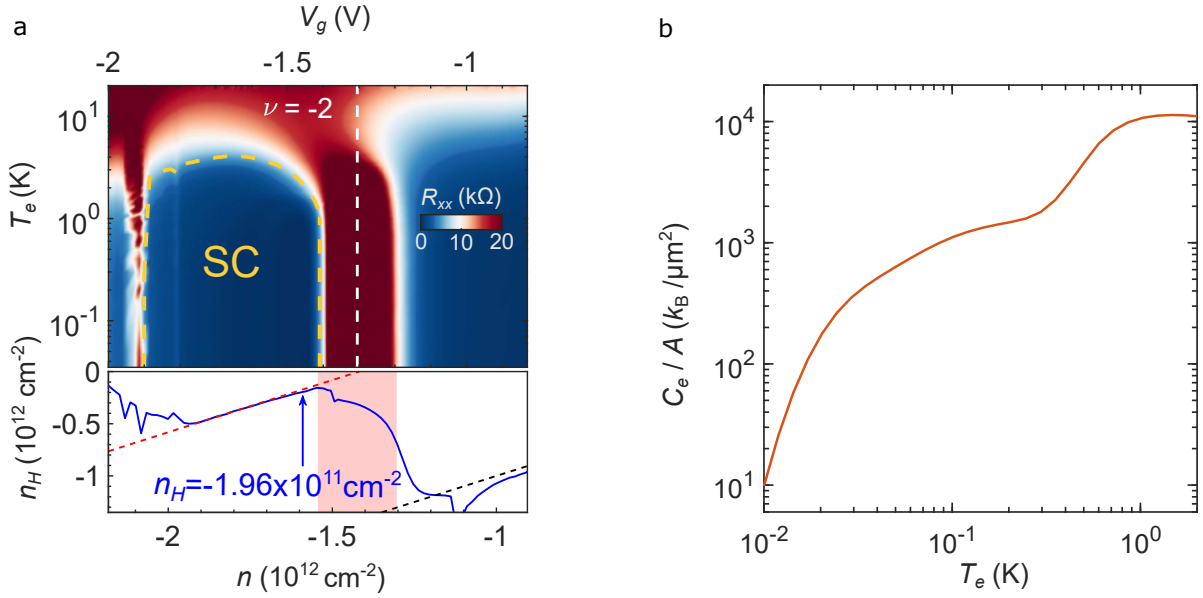

Figure 2.4.1: Superconducting state of MATBG. (a) Top panel: Longitudinal resistance, R_{xx} vs. gate voltage, V_g and temperature, T_e for a MATBG superconducting device. The superconducting region is dome-shaped in the $n - T$ phase space (yellow dashed line) and is flanked by a correlated insulating state at $\nu = -2$ (white dashed line). Bottom panel: low-field Hall effect at $B = 300$ mT, from which we extract the Hall carrier density, n_H as a function of gate-induced carrier density, n. At $\nu = -2$, a Fermi level reset occurs, which reduces the free carrier density to an ultra-low value of $n_H = -1.96 \times 10^{11}$ cm^{-2}. Adapted from [P2]. **(b)** Electronic heat capacity per unit area calculated for MATBG, considering a carrier density of -1.96×10^{11} cm^{-2}. At 35 mK the heat capacity shows ultra-low values of $C_e/A \sim 10^2\, k_B/\mu\text{m}^2$. The heat capacity is calculated in a single-particle picture without including electronic interactions. The theoretical modeling of the heat capacity was performed by Prof. Dr. Alessandro Principi[P2].

3

Fabrication of magic-angle twisted bilayer samples

The work presented in this chapter led to the publication [P6]:
J. Díez-Mérida, I. Das, G. Di Battista, A. Díez-Carlón, M. Lee, L. Zeng, K. Watanabe, T. Taniguchi, E. Olsson and D. K. Efetov, "High-yield fabrication of bubble-free magic-angle twisted bilayer graphene devices with high twist-angle homogeneity", *arXiv* 2405.11323 (2024).
My contribution to this work was device fabrication, transport measurements, discussion, and participation in the writing of the manuscript.

As discussed in Chapter 2, the emergence of flat bands in MATBG gives rise to various quantum phases, including ultra-low carrier density superconductivity, which is particularly advantageous for single-photon detection[P1, 34]. Despite numerous studies conducted since the discovery of this material, significant challenges persist in the device fabrication, which is notoriously tedious and suffers from low yield[P6]. The quantum phases mentioned in Chapter 2, are strongly influenced by several external factors, such as the twist angle[131], the encapsulating layer, [132–134], as well as twist-angle inhomogeneity[135, 136] and strain[137, 138]. Specifically, these last two factors are susceptible to the details of the stacking process[135]. In this chapter, we describe the fabrication protocol implemented and optimized to achieve high-quality assembly of MATBG devices. This protocol, based on a modified dry-transfer technique[139], allows for the production of nearly bubble-free MATBG devices and results in high twist-angle precision and homogeneity[P6]. In section 3.1, we first discuss the exfoliation process and the criteria for selecting flakes to achieve high-quality stacks. In section 3.2, we describe a method developed to lock the

twist angle of MATBG, significantly increasing the fabrication yield. In the final section we quantify the twist-angle disorder obtained with our fabrication protocol (section 3.3).

3.1 Preparation of the 2D crystals

3.1.1 Exfoliation

The exfoliation technique employed for our 2D crystals follows the standard protocol established in 2015 [140]. The crystals are exfoliated using the Scotch tape method on Si/SiO_2 (285 nm) substrates, pre-cleaned with O_2 plasma. Additionally, for graphene and graphite flakes, the chip substrate is heated to approximately 100 °C for a few minutes to enhance the exfoliation yield. Conversely, no heat is applied to hBN chips before the peeling process. Due to the lower density of hBN on the tape compared to graphene, heating the substrate will result in excessive tape residues.

3.1.2 Flake Selection

In our experience, a crucial step for ensuring a successful outcome and achieving high yield and homogeneity of the final stack is the careful selection of 2D crystals from which the heterostructure is assembled. Following the exfoliation process described above, the 2D layers are examined under an optical microscope. We use several criteria for selecting the individual flakes and determining the relationships between the different components in the stack. The primary criterion involves identifying pristine and homogeneous flakes. These should be free of tape residues and step-terraces and well isolated from nearby bulk regions, which typically cause issues during stacking. Additionally, there are specific requirements to consider for the different materials. In the following, we provide a detailed discussion of the selection criteria employed for each stack component.

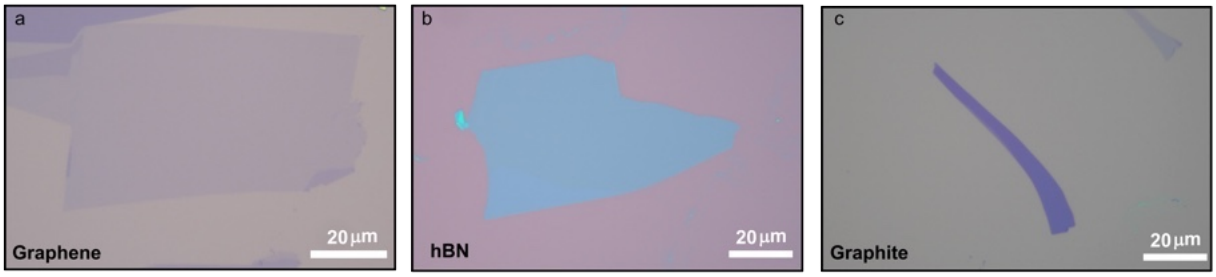

Figure 3.1.1: Flake Selection. **(a)** A suitable graphene flake should be at least twice as large as the desired device size, with an aspect ratio of 2:1. **(b)** The hBN flake should be free of tape residues, step-terraces, defects, or folds. The thickness should be around 10-15 nm, and a sharp edge is needed to lock the graphene. **(c)** A suitable graphite gate is $\sim$ 2-4 nm thick, 3-7 µm wide and 10-15 µm long.

Graphene flakes

As will be discussed in the following, the graphene will be cut into two parts to create two graphene layers with the same crystallographic orientation. Therefore, the graphene flakes should be at least twice as large as the desired device size (aspect ratio of 2:1), so they can be cut into two almost equal parts. The size of the graphene and graphite determines the ultimate device size. The typical active area we aim for has a spatial extension of 10 μm^2 to 50 μm^2. As the usual width of the active area achieved with the graphite gate is in the range from 3 µm-7 µm, graphene flakes which are $\sim$ 10-15 µm $\times$ 15-30 µm are typically desired, such that the final Hall bar devices are $\sim$ 10 µm long. It needs to be considered that not all the twisted bilayer areas will be fabricated, and only the homogenous regions will be used for the final device.

hBN flakes

The complete encapsulation of graphene with insulating hBN layers was crucial to achieve high mobility in transport experiments[141]. Therefore, in our sample, we fully encapsulate the graphene and choose the flakes to be 10-15 nm thick, which is considerably thinner than the ones typically used[33, 114, 130, 134]. We find that the thinner hBN has several advantages. First, thinner hBN flakes are more elastic than thicker flakes, making the stacking process smoother and mitigating the strain within the hetero-structure. This also helps to avoid uncontrolled movements of the stamp's wavefront during stacking, which can give rise to bubble formation[P6]. However, hBN flakes are chosen to be > 5 nm as below this thickness, they are structurally weak and may tear during the stacking process or may give rise to capacitive coupling or current leaking from the gate electrode to the device. As will be discussed in section 3.3.2, using thin flakes is also important to increase the twist angle homogeneity and reduce disorder. Indeed, thin hBN provides higher optical transparency than thicker flakes, crucial to visualizing dirt, defects, folds, or wrinkles in thin hBN flakes under the optical microscope[P3]. Another important criterion is that the hBN, which will be picked up first, should have at least one sharply defined edge. As we will explain in the section 3.2, this is crucial for anchoring graphene during the pick-up process, which helps stabilize and lock the crystallographic orientation of the graphene sheets in the hetero-structure[P6].

Graphite flakes

The desirable parameters for the graphite flakes that serve as gate electrodes are $\sim$ 2-4 nm for the thickness, 3-7 µm for the width, and 10-15 µm for the length. The width is chosen to be smaller than the whole graphene area such that the arms of the Hall bar in the final device can extend beyond its width, allowing independent gating of the central region of the Hall bar and the arms, which enables control over the contact resistance. As superconductivity in MATBG results from a percolation path defined by twist angle inhomogeneities[135], the device width determines the probability of finding a superconducting percolation path within the device active area and, therefore, should not be reduced below

a few µm[P3]. Regarding the thickness, we avoid using graphene with fewer than four layers because this thickness is insufficient to screen the charge puddles in the SiO_2 substrate[142] and can exhibit magnetic properties as shown in the rhombohedral orientation[97]. Thicker flakes are also avoided as they might be difficult to pick up from the stack[P6]. As they are narrower than the twisted graphene regions, they also produce an unwanted height step and curvature in the TBG device, directly proportional to the graphite thickness[143]. The bottom gate needs to be longer than the graphene to be contacted during the lithography process without unwanted connection to the graphene.

3.1.3 Creation of two graphene with the same crystallographic orientation

To ensure that both sheets have the same initial crystallographic orientation before the rotation of the layers, MATBG devices are always assembled starting from a single crystal graphene sheet that is then cut into two halves. The first method of cutting the graphene in two parts was the "tear-and-stack"[129, 144], which consisted of pulling and tearing the graphene sheet during the pick-up process. This method was replaced by the "cut-and-stack" method[132] where the original graphene flake is cut into two pieces with the advantage of not inducing a pulling and tearing motion in the graphene sheet. To cut the graphene, we use two techniques: one with an AFM cantilever mounted on a glass slide and the other with an ultra-strong pulsed laser beam[P6]. The first technique (schematically illustrated in Fig. 3.1.2a) consists of mounting with scotch tape a cantilever on the edge of a PDMS square, which is glued on a glass slide. The glass slide with the AFM cantilever is then placed on the micromanipulator of the transfer stage and lowered towards the chip with the desired graphene flake until contact is made. Once in contact with the chip, the sample stage is moved while the glass slide is fixed. The AFM cantilever passes over the graphene flake, resulting in a 1 µm-wide cut (Fig. 3.1.2b). The second technique (schematically illustrated in Fig. 3.1.2c) uses an infrared pulsed laser (1064 nm) with an average power of 200 mW[145]. The laser path to the sample is focused using a 100× objective, with a beam waist of about 1 µm. By passing the laser across the desired flake, it is possible to cut the graphene analogously to the AFM cantilever (Fig. 3.1.2d). In Fig. 3.1.2b and d, we compare the graphene cutting obtained with the AFM cantilever and the laser. While both techniques give similar results, the laser provides a more controlled graphene-cutting process by inducing less mechanical stress than the AFM cantilever and reducing the chance of breaking a flake while cutting it.

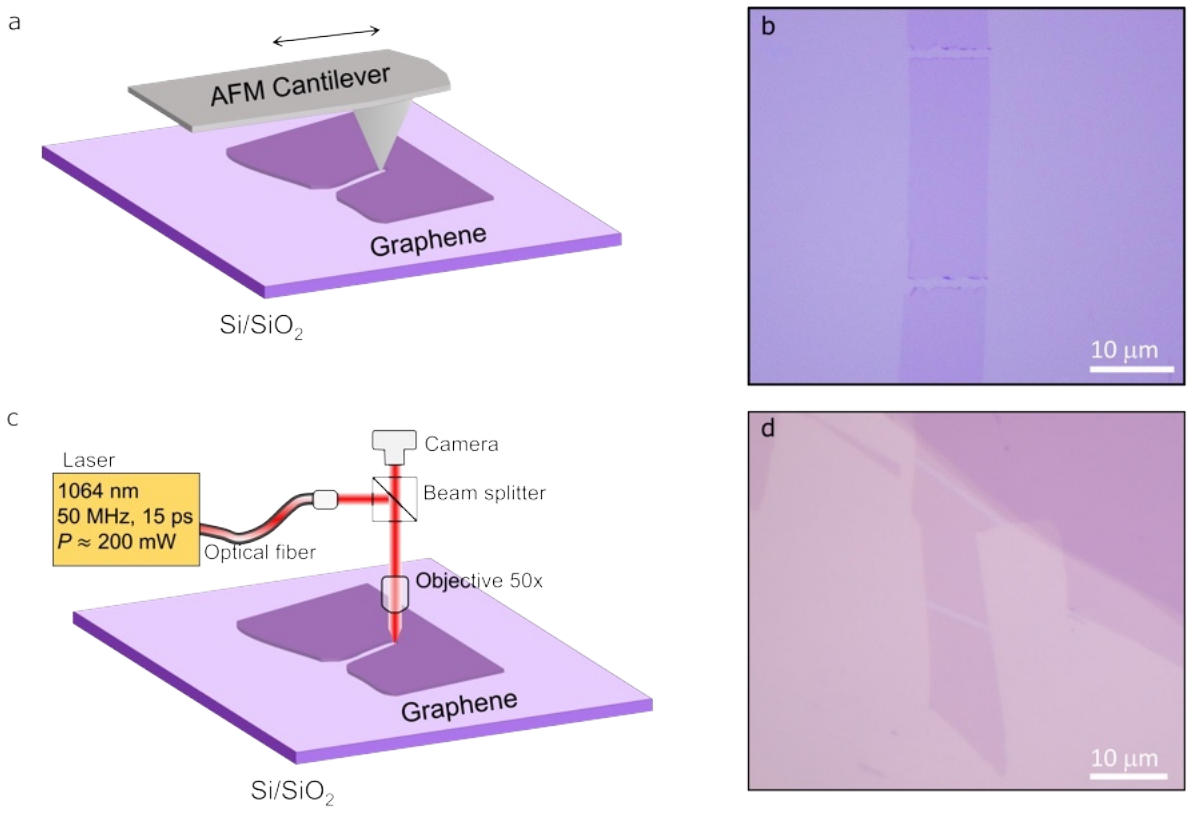

Figure 3.1.2: AFM cantilever and laser cutting. **(a)** Schematic of the graphene cutting technique using the AFM cantilever mounted on the micromanipulator. **(b)** Optical image of the graphene flake cut with AFM cantilever. **(c)** Schematic of the graphene cutting technique employing the infrared pulsed laser. **(d)** Optical image of the graphene flake cut using the pulsed laser. Adapted from [P6].

3.2 Assembly of MATBG devices employing twist-angle locking

3.2.1 Vertical Assembly Technique

After selecting and cataloguing the suitable 2D flakes, we prepare an assembly plan for the stack, ensuring the shape, size, and geometry of the different flakes fit properly. We use a stamp mounted on a glass slide to perform the dry-transfer process, similar to previous works[146]. The stamp consists of a piece of polydimethylsiloxane (PDMS), a few mm^2 in area and 1 mm thick, covered with a polycarbonate (PC) film. The shape can be square, circular or triangular. The PDMS is a viscoelastic material that acts as a cushion during the pick-up process. The PC film is chosen as the adhesive layer due to its high adhesion properties to the 2D materials, and it allows the stacking process to be performed at high temperatures (~ 100 °C), which helps remove impurities from the device during lamination (as discussed in 3.3).

Transfer Stage

The dry transfer stacking technique is performed using a transfer stage, also referred to as a stamping setup. The transfer stage is an optical microscope modified to assemble van der Waals heterostructures[P6]. Below, we list the main components of the transfer stage (shown in Fig. 3.2.1):

- Table to stabilize vibrations.
- X-Y motorized sample stage (b1).
- Manual rotation control with a goniometer (resolution of 0.016°) to twist the two graphene sheets to the desired angle (b2).
- Micromanipulator stage. It consists of a metallic arm (c4) that can move in the X-Y-Z directions and tilt on the X-Y plane (c3). The micromanipulator holds and controls the glass slide with the stamp during assembly. By moving the manipulator in the X-Y direction (c1), we can position the stamp over the sample, and by moving it in the Z direction (c2), we control its height. This allows for making contact or retracting the sample, enabling precise control of the stacking direction and the smoothness of the contact between the stamp and the sample. The tilt angle in the X-Y direction determines the amount of force applied to the PC film.
- Vacuum pumps are used to keep the back of the sample and the stamp in vacuum during the stacking procedure (d).
- Long working distance objectives employed to provide enough space to contact the stamp to the chip while maintaining the proper magnification needed to focus light on the sample.

- Temperature control, which consists of a heater and a thermometer, regulates the temperature of the sample stage during the stacking procedure.

- Camera and imaging software (i).

- Aperture diaphragm control lever. During the stacking process, a large amount of scattered light comes from the glass slide with the PDMS/PC stamp, hampering focus at the sample stage. Closing the aperture diaphragm increases contrast (while reducing brightness) and the depth of field, allowing proper focus of the light passing through the stamp onto the sample.

- Optical filters. Low-pass or band-pass optical filters, which selectively remove certain optical components, help detect defects in the flakes.

- White light source used to image the sample.

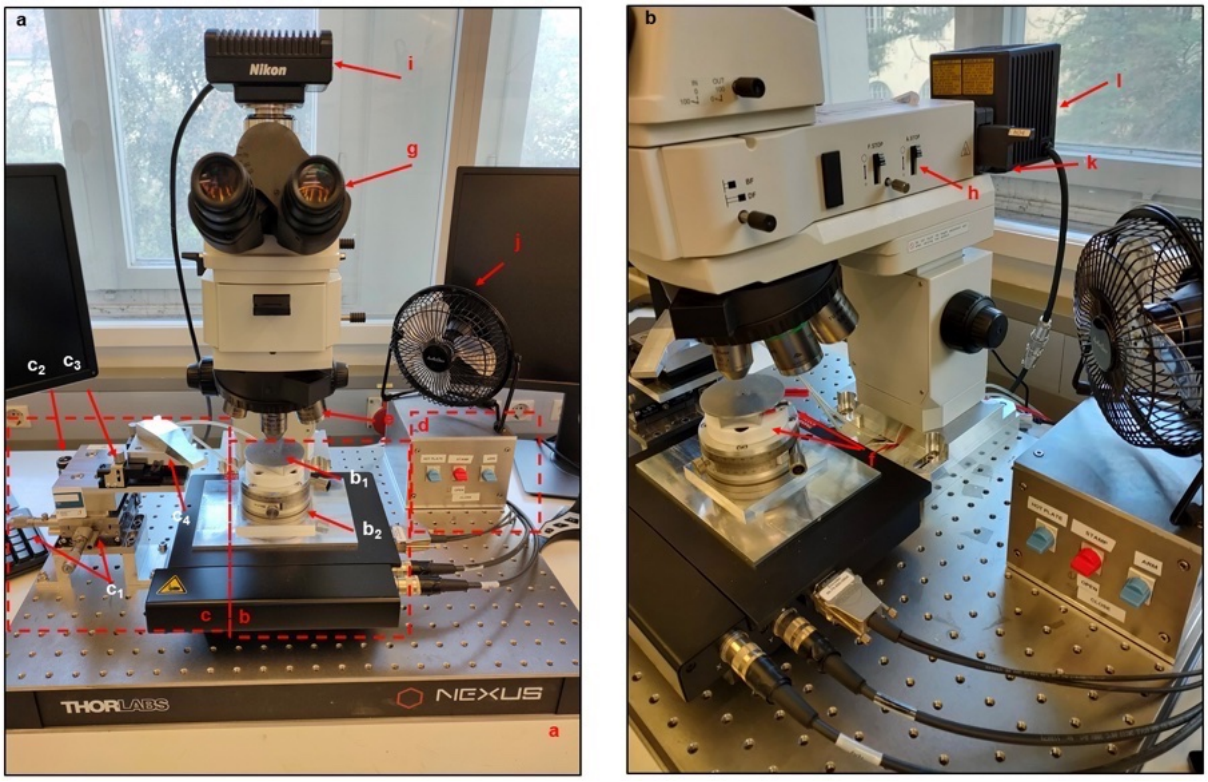

Figure 3.2.1: Vertical assembly setup. (a) Front view of the home-made stamping setup. **(b)** Lateral view of the home-made stamping setup. The specific parts are listed in the text. Adapted from [P6] and [147].

Pick-Up Technique

By manually lowering the z-micromanipulator of the transfer stage, which holds the PDMS/PC stamp, it is possible to approach the 2D layers. The direction in which the PC approaches the crystal determines the relative orientation between the flakes. Therefore, rotating the stamp to the ideal position is crucial. The pick-up process starts by lowering the stamp until it contacts the SiO_2 surface. Once the PC is on the substrate, the contact surface, or 'wavefront', can be easily controlled by moving the z-micromanipulator. The chip with the desired flake is placed on the heated sample stage and held in place by applying vacuum to its back side. The point of contact is easily visible as it is surrounded by Newton's rings (see Fig.3.2.2a, b, c, d, and g). Typically, we tilt the angle of incidence of the glass slide such that the PDMS/PC stamp makes its first contact with the substrate at one of its corners, allowing better control of the wavefront. Since the sudden movement of the PC film can tear, move, or induce bubbles in the heterostructure, once the PC film has fully laminated over the flake, the stamp is retracted slowly. Given the importance of homogeneity in the PDMS/PC stamps, particular care is taken in their preparation. Detailed information on the stamping preparation is provided in the supplementary information of ref. [P6].

3.2.2 Locking the twist-angle of MATBG by anchoring to the hBN edges

The primary challenge in fabricating twisted moiré heterostructures is maintaining the target twist-angle throughout the entire fabrication process. During the pick-up process, lateral and vertical forces applied to the 2D crystals can cause flakes to move and rotate relative to each other, significantly reducing the yield of MATBG devices. Specifically, for MATBG, the configuration where the two graphene layers are rotated at 1.1° is metastable, while the energetically favorable configuration is at a relative angle of zero degrees, causing the layers to revert to an AB configuration[119]. To enhance the yield of MATBG devices, we have developed a clamping technique that interlocks the edges of graphene with hBN, thereby stabilizing the relative twist angle[P6]. Utilizing this technique, we observed a substantial increase in the yield of MATBG devices. The first picked-up hBN is selected for its sharp edge, which serves as an anchor to which the two graphene flakes are clamped. Specifically, the edges of graphene, resulting from the cutting process, fold over the sharp edge of the hBN over a length of approximately 1 µm, as visible in the optical images (Fig. 3.2.2b-d), minimizing any relative motion between them. Crucially, the clamping must be performed using a non-crystallographic axis of both graphene and hBN to avoid unintentional alignment between the layers, which would induce an additional moiré pattern potentially influencing the device's band structure[148, 149].

3.2.3 Stacking Process

After identifying a clean region of the PC film suitable for picking up the entire stack, we assemble the heterostructure. The whole pick-up process is conducted at approximately 100-120 °C. The flakes are laminated at a constant temperature, and the crystals are approached manually using the z-micromanipulator of the transfer stage. The complete stacking process is illustrated in Fig. 3.2.2.

- **Top hBN**. The initial step involves picking up the top hBN with the PDMS/PC stamp. Since the top hBN is used to pick up the other layers, it is crucial to align the sharp edge of the hBN, which will be used to lock the graphene, with the direction in which the PC approaches the crystal (Fig. 3.2.2a).

- **1st Graphene**. To pick up the first graphene layer, the chip is positioned such that the graphene's edge aligns with the top hBN's sharp edge. During this step, the graphene flake is clamped with the top hBN layer (indicated by red arrows in Fig. 3.2.2b,c). The wavefront is approached very slowly to the substrate, and the first graphene layer is fully laminated by the hBN, avoiding any contact between the PC or the hBN with the second graphene flake, which could distort the twist angle. Once hBN fully covers the first graphene, the stamp is slowly retracted and moved a few millimeters above the chip.

- **2nd Graphene**. Before picking up the second graphene sheet, the sample stage is rotated to the target angle of 1.1°. Typically, the target angle is slightly larger than 1.1° to account for the slight twist-angle relaxation often observed during the pick-up process. The second graphene layer is overlapped with the first, and the pick-up procedure is repeated in the same manner as for the first graphene. Similarly, the second graphene layer is clamped to the hBN edge (Fig. 3.2.2d).

- **Bottom hBN**. After picking up both graphene layers, the bottom hBN is picked up. The flake is selected to encapsulate the graphene fully and completely cover the bottom graphite gate (Fig. 3.2.2e,f)[P3].

- **Graphite back gate**. In the final step, the graphite back gate is picked up. Based on our experience, mechanical strain accumulates mainly during this final step of the stacking process while picking up the graphite gate[P3]. This tension can affect the twisted bilayer graphene region, relaxing its twist angle or displacing the position of the graphite gate, potentially destroying the entire stack. Complete encapsulation of the graphite gate with the bottom hBN flakes facilitates the pick-up from the substrate, preventing this from occurring (Fig. 3.2.2g)[P3, P6].

- **Dropping the Stack**. Finally, the complete stack is dropped onto a SiO_2/Si chip with pre-patterned markers used for alignment in the nano-fabrication process. Before dropping, the chips are cleaned with O_2 plasma to improve the adhesion of the

heterostructure. The contact between the PC film and the chip is made at approximately 120-150 °C to enhance bubble mobility. The wavefront is moved slowly over the stack to push away all remaining bubbles[P6]. Once the full stack is in contact, the stage temperature is raised to the melting point of PC, approximately 180 °C. At around 135-140 °C, the PC detaches from the PDMS, and the z-micromanipulator is moved up to detach the entire PC film from the PDMS, and the stamp is fully retracted. At this point, the areas of the PC film in contact with the chip are fully melted and detach from the remaining PC areas on the glass slide (Fig. 3.2.2h).

Throughout the whole process, the stamp's X-Y micromanipulator and sample stage are not moved to avoid tearing the stamp. Once the stack is dropped, the heater is turned off, and the stage temperature is lowered to room temperature. The PC polymer is cleaned by dipping the chip in chloroform for 3 to 5 minutes, then in acetone for 1 minute, and finally in isopropanol for 1 minute. An optical image of the assembled and cleaned stack is shown in Fig. 3.2.2i.

3.2.4 Shaping of the device and electrical contacting

Once the heterostructure is stacked and assembled, it can be fabricated for the specific purpose of the experiment. In our case, we typically opt for a Hall bar geometry as we employ the low-field Hall effect or the quantum Hall effect to extract the twist angle. We shape the sample into the desired nanostructure using electron-beam lithography and reactive ion etching (CHF3/O2 plasma). The heterostructures are then electrically connected through 1D edge contacts[150] using 5 nm of chromium and 50 nm of gold.

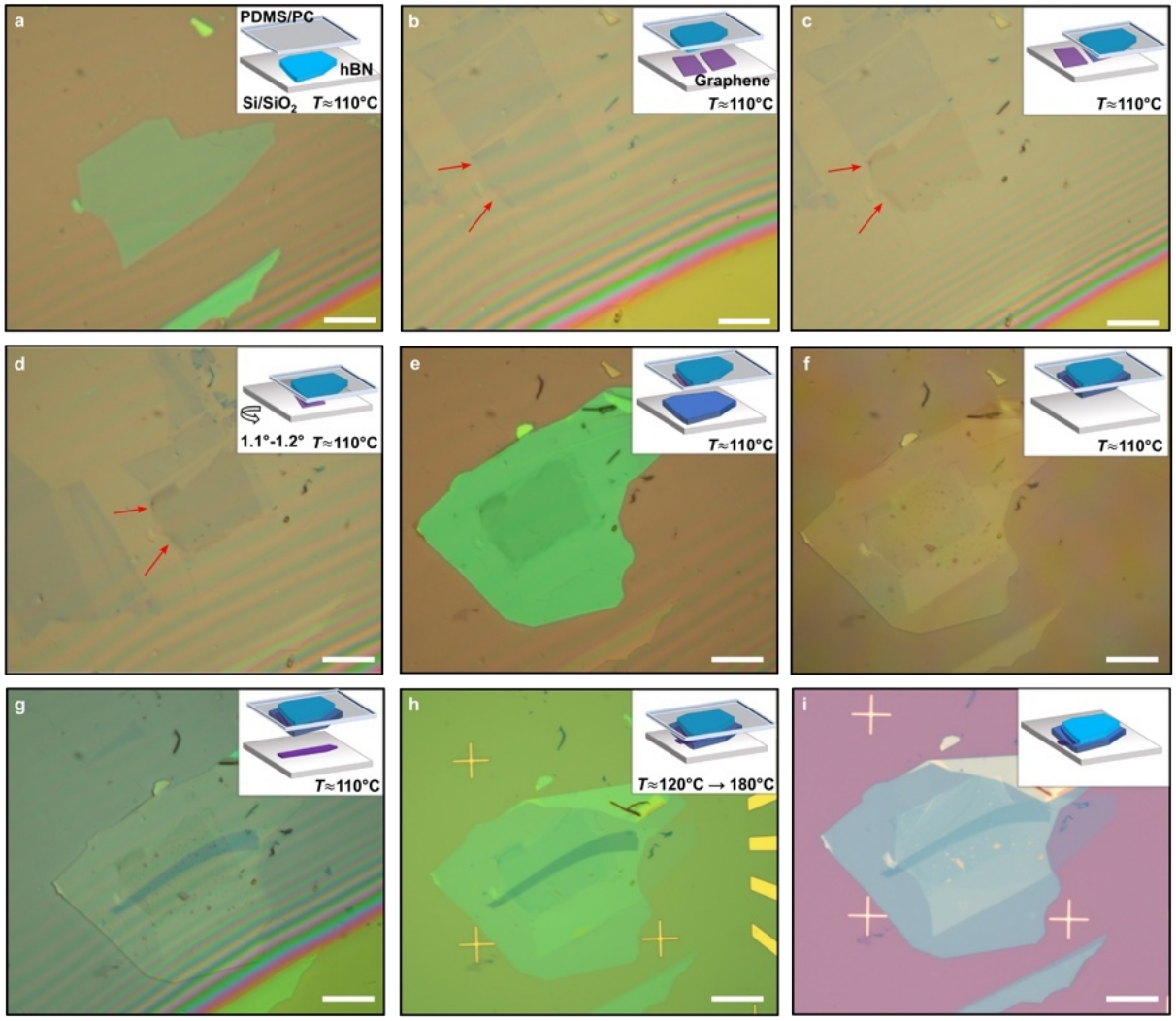

Figure 3.2.2: Stacking process. **(a)** The first step consists in picking up the top hBN with a stamp of PDMS/PC. **(b)** In the second step the top hBN is used to pick up the first graphene which was pre-cut in two halves. The red arrows highlight the part of graphene which sticks out of the hBN and that will anchor to the sharp edges of hBN. **(c)** This image shows successful pick-up of the first graphene layer as indicated by the change of color. **(d)** After rotating the stage at 1.1° with a goniometer the second graphene layer is picked up. **(e)** Once the two graphene layers are successfully picked up, **(f)** The bottom hBN is picked up. **(g)** The stack is carefully aligned over the bottom graphite gate. **(h)** Finally the stack is dropped on a Si/Sio_2 chip by melting the PC at 180°. The chip has pre-patterned markers, used for alignment in the nano-fabrication process. **(i)** The PC layer is removed with clorhoform and the stack can be etcehd in the desired shape and electrically connected. The stack shown here exhibited a twist angle of $1.10° \pm 0.02°$. The scale bar in all figures is 25 µm.

3.3 Twist-angle homogeneity

In this section, we describe the role of bubbles in the twist angle inhomogeneity and detail the bubble removal technique implemented to mitigate twist angle disorder. We also extract the average twist angle between pairs of leads to spatially quantify the twist angle disorder and discuss the yield of this fabrication process.

3.3.1 Strategies to enhance twist-angle homogeneity

The initial studies on MATBG using local probe techniques with nanometer resolution revealed that local twist angle disorder in moiré heterostructures is closely linked to the presence of bubbles. Intuitively, we can imagine that these bubbles distort the crystalline structure, modifying the twist-angle condition in regions up to approximately 0.5 µm around the bubble[135] and inducing significant strain in the device[138]. Therefore, to achieve optimal 2D interfaces and maximize twist-angle uniformity, it is essential to minimize bubble formation during the stacking process. Bubbles typically form due to the accumulation of contaminants on the surfaces of the different 2D materials[151, 152] or rapid movements of the wavefront that trap air along the interface[153]. Therefore, achieving a smooth stacking process, which can be achieved through precise control of the stamp's wavefront, is crucial. We have implemented several strategies to reduce bubble formation over the years, which we summarize in the following.

Using clean stamps and flakes

We ensure that the area of the stamp used for picking up the flakes is clean and free from dust particles or bubbles. As mentioned in section 3.1, we only use flakes with clean interfaces to avoid any dirt or defects that could induce bubbles.

Employing thin hBN flakes

We opt for thin hBN flakes with a 10-15 nm thickness for two main reasons. Firstly, using an optical microscope, thicker hBN would not provide enough optical transparency to visualize the MATBG underneath[P3]. This is crucial for visualizing and identifying cracks or folds in the graphene layers, to avoid during fabrication. As anticipated in section 3.1, optical transparency also aids in identifying step-terraces or tape residues on the hBN interfaces. These residues can trap air or cause abrupt movements in the stamp wavefront during stacking, leading to bubble formation. Secondly, thin hBN flakes are more elastic than thicker ones, facilitating a smoother stacking process and relieving strain within the heterostructure[P6].

High-temperature colamination process

As discussed in previous reports, performing the stack at high temperatures can enhance bubble mobility during pick-up and improve the self-cleaning properties of the van der

Waals interfaces[151, 154]. Following this approach, we conduct the entire stacking process at relatively high temperatures (approximately 100 - 120°C). In particular, when picking up the bottom graphite gate in the final step of the stacking process, we carefully utilize the temperature increase to remove bubbles that may have formed in earlier pick-up steps. To achieve this, we keep the micromanipulator stationary and gradually increase the temperature from 100°C to a maximum of 120°C, allowing the temperature to drive the bubbles away from the sample. The bubble removal process is illustrated in Fig. 3.3.1. The stack shows numerous bubbles before the gate pick-up some of which lie in the twisted bilayer area (Fig. 3.3.1b). During the pick-up, the temperature increase rearranges the bubbles and pushes them away, resulting in a clean graphite region with fewer bubbles forming only at the edges of the graphene (Fig. 3.3.1c).

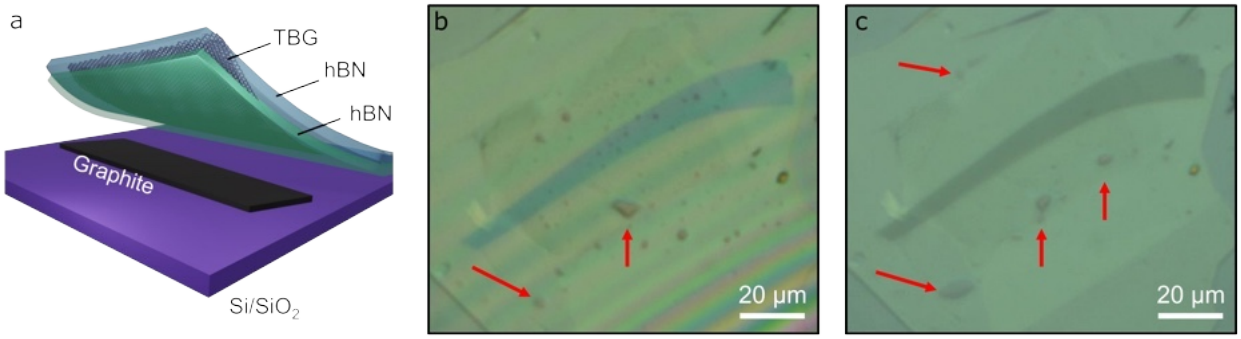

Figure 3.3.1: Bubble removal during the pick-up process. (a) Schematics illustrating the final step of the stacking process, which involves the pick-up of the bottom graphite gate. **(b) Before pick-up**: the stack has numerous bubbles some of which lie in the device area. **(c) After pick-up**: By increasing the from 100°C to a maximum of 120°C, the bubbles are effectively pushed out of the device region and accumulate at the graphene edges. This device exhibited a twist angle of $1.1° \pm 0.02°$. The stack shown here is prepared and assembled by me and the image is adapted from [P6].

3.3.2 Twist-angle homogeneity with our fabrication protocol

This section quantitatively assesses the twist-angle homogeneity achieved through our fabrication protocol. Improvements in the fabrication technique enable the realization of sharp superconducting transitions and hysteresis loops in the I-V characteristics, which are critical for SPD applications, as discussed in section 6.1. To quantify the twist-angle homogeneity, we conduct a two-probe mapping across all the available contacts of the MATBG device. As mentioned in section 2.3.1, knowing the gate capacitance of the hBN insulating layer, we can determine the superlattice carrier density from the voltage of the band insulators (V_{BI}) using the relation: $n_s = C_g V_{BI}/e$ and subsequently the twist angle according to Eq. 2.3.2. By extracting the twist-angles between all of the available contact

pairs in the devices, we typically identify regions of about 6 µm^2 with twist-angle variation $\Delta\theta \leq 0.02°$. Some exceptionally high-quality devices fabricated with this technique exhibit homogeneous areas up to 36 µm^2 [P6], as illustrated in Fig. 3.3.2. However, even in these highly homogeneous devices, we observe regions where the twist angle between neighboring contact pairs changes abruptly, likely due to stacking faults between the two graphene sheets [P6].

In this discussion, it is important to mention that transport measurements probe the electrical properties of the area between two contact pairs spaced approximately a few micrometers apart. Therefore, the twist angle reported in Fig. 3.3.2 should be interpreted as a global twist angle derived from the average carrier density ($\bar{n} \approx C_g V_g/e$) on a micrometer scale. On the nanometer scale (few moiré unit cells), it is expected that there are areas with different twist angles $\theta(\boldsymbol{r})$, which translate into a local carrier density distribution $n(\boldsymbol{r})$ as reported by local probes experiments [135, 136]. Consequently, the phases of matter observed in MATBG and other moiré materials are significantly influenced by local twist-angle inhomogeneities. In section 6.3.4, we discuss the impact of twist-angle inhomogeneities on the efficiency of the observed SPD response.

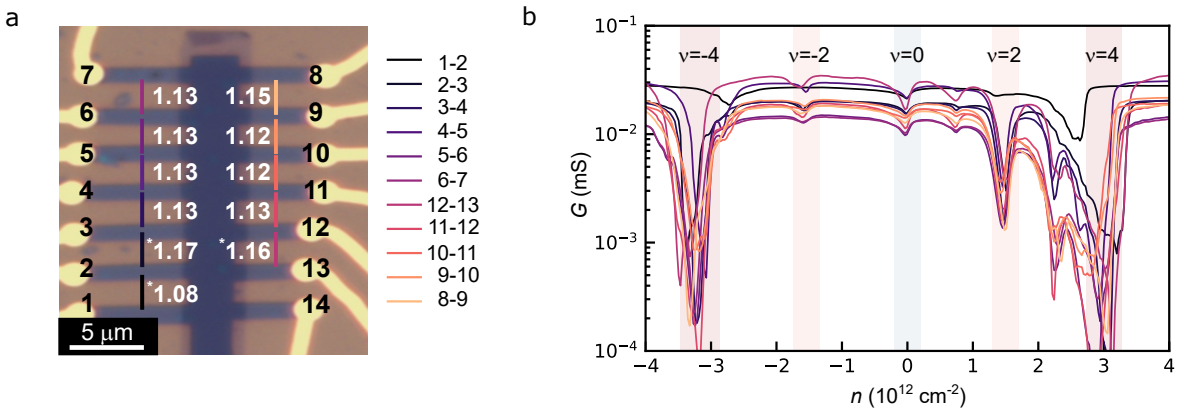

Figure 3.3.2: Characterization of the twist-angle homogeneity across the sample. **(a)** Optical image of a MATBG device with twist-angle homogeneity over 36 µm^2. **(b)** Two probe terminal conductance G vs. carrier density n measurement at $T = 35$ mK for the different contacts in the device shown in **(a)**. The device shown in **(a)** is prepared and measured by me and the image is adapted from [P6].

4

Experimental methods

In this chapter, we describe the experimental setup employed in the experiments. My contributions include the design of the optical setup, the realization of custom-made components, the implementation and characterization of the electronic setup used for single-photon detection, and the development of the software required for data acquisition and analysis.

In the previous chapter, we explored the main aspects of the fabrication of MATBG samples and discussed the methods implemented to mitigate the twist angle inhomogeneity. This chapter focuses on the experimental techniques employed to measure the electronic properties and the photoresponse of MATBG devices. The chapter is divided into three sections: the first introduces the cryogenic setup used to cool down the samples. The second describes the electronic setup employed for low-frequency transport experiments and SPD and the third discusses the optical setup used to illuminate the superconducting state of MATBG.

4.1 Cryogenic setup

Properly cooling down the electrons is a technical challenge for observing and exploring quantum phases. Cryostats can achieve this by reaching extremely low temperatures (down to a few mK). This section introduces the cooling principles of dilution refrigerators and details the main components that constitute this type of cryostat. Understanding these principles is crucial for implementing the optoelectronic setup used to demonstrate SPD and adequately designing the millikelvin terahertz setup discussed in Chapter 7. We discuss

how to ensure proper thermalization of the electronic ensemble using cryogenic filters and measure the resulting bandwidth available in our experiments.

4.1.1 Dilution cooling

Fig. 4.1.1a shows the x-T diagram of liquid ^{3}He-^{4}He mixtures at saturated vapor pressure, where $x = \frac{n_3}{n_3+n_4}$ is the concentration of the ^{3}He isotope and n_3 and n_4 are the molar concentrations of the ^{3}He and ^{4}He isotopes. The phase diagram indicates the values of x and T for which the ^{3}He-^{4}He mixture is in the normal, superfluid, or separated phases. For temperatures below 0.87 K, the liquid separates into two phases, one rich in ^{3}He (concentrated) and the other rich in ^{4}He (diluted). Because of its lower density, the ^{3}He-rich liquid floats on top of the ^{4}He-rich liquid. By cooling down the temperature close to absolute zero, the ^{3}He-rich liquid becomes pure ^{3}He ($\sim 100\%$) while the ^{4}He-rich side reaches a constant concentration of ^{3}He (6.6%) and of ^{4}He (93.4%) even for $T = 0$ K, as sketched in Fig. 4.1.1b.

In this configuration, given the difference in specific heat between diluted and concentrated phases ($C_{3,d}(T) > C_{3,c}(T)$) by transferring ^{3}He atoms at the molar flow rate $\dot{n}_3$ from the concentrated into the dilute phase, cooling will result according to the enthalpy difference ΔH[155]:

$$\Delta H = \int \Delta C dT \tag{4.1.1}$$

Which results in a cooling power, $\dot{Q}$[155]:

$$\dot{Q}(T) = \dot{n}_3[H_{3,d}(T) - H_{3,c}(T)] = 84\dot{n}_3T^2[W] \tag{4.1.2}$$

In our experimental setup the typical flow rate is $\dot{n}_3 = 300$ µmol/s, resulting in a cooling power of $\dot{Q} \simeq 250$ µW at $T = 100$ mK. The finite solubility of ^{3}He is crucial for operating a ^{3}He-^{4}He dilution refrigeration because it permits a high ^{3}He molar flow rate even at temperatures close to absolute zero. This differentiates the operation of a dilution cooling from a pumping cooling[155].

Dilution cooling vs. evaporation cooling

Pumping cooling consists in pumping the vapour above a liquid. In this way, the hottest atoms leave the liquid to fill the vapour, reducing the mean energy of the liquid and cooling it down. The cooling power of an evaporating cryogenic liquid where $\dot{n}$ particles per time are moved to the vapour phase is given by [155]:

$$\dot{Q} = \dot{n}[H_{liq} - H_{vap}] = \dot{n}L \tag{4.1.3}$$

Where $H_{liq} - H_{vap}$ is the enthalpy difference between the liquid and vapour phase, and L is the latent heat of evaporation. In the assumption of pumping with a pump of constant

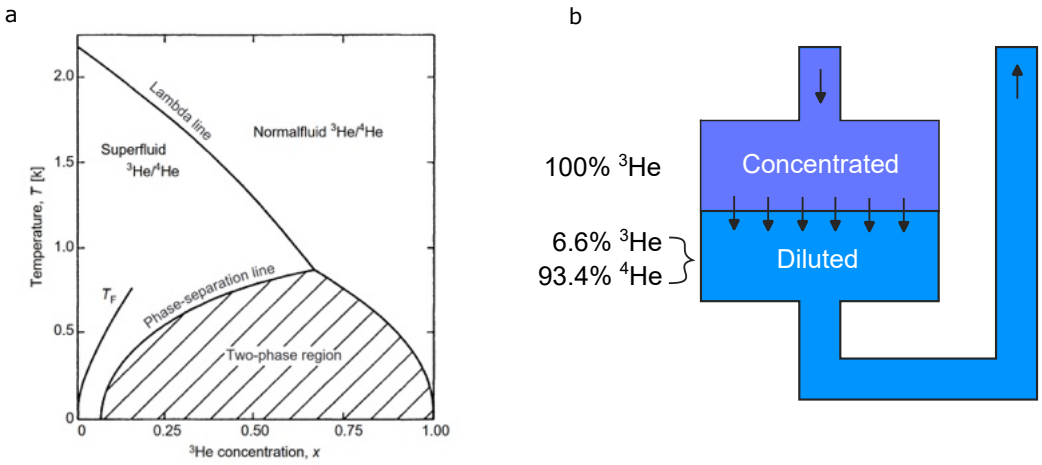

Figure 4.1.1: Phase diagram of liquid ^{3}He-^{4}He mixtures. (a) Phase diagram of liquid ^{3}He-^{4}He mixtures at saturated vapour pressure. For temperatures below 0.867 K the two isotopes are only miscible for certain limiting concentrations which depend on the temperature. Even at $T = 0$ K the concentration of ^{3}He does not approach to zero but remains at $x = 6.6\%$. Adapted from [155, 156]. **(b)** Schematics of the molar flow of ^{3}He atoms from the concentrated to the diluted phase which leads to cooling.

volume rate on a ^{3}He-^{4}He bath with vapour pressure P_{vap}, the cooling power decreases exponentially with temperature:

$$\dot{Q} = \dot{V} P(T) L(T) \propto P(T) \propto e^{-1/T} \tag{4.1.4}$$

As the vapour pressure decreases exponentially with temperature, at low enough temperatures, there is almost no vapour left, resulting in an exponentially decreasing cooling efficiency. This limits the minimum temperatures obtainable by pumping on an evaporating cryoliquid, which are typically around 1.3 K for ^{4}He and 0.3 K for ^{3}He (see Fig. 4.1.2a). On the contrary, dilution cooling allows a high ^{3}He flow rate even at temperatures close to absolute zero, which guarantees a higher cooling power even below 0.3 K (see Fig. 4.1.2b).

4.1.2 Dilution refrigerator principal parts

- **Pulse tube cooling.** The pulse tubes cool the system down to 4 K where the the dilution cycle can start. This cryo-cooler consists of a compressor, a regenerator and pulse tubes (Fig. 4.1.3a). The compressor or piston compresses the working gas, usually helium, at 10–20 bar, moving the gas particles towards the closed end of the pulse tube. The heat of compression (Q_0) is removed by cooling water. This adiabatic compression raises the temperature of the gas particles and generates a temperature gradient from the hot end to the cold end of the pulse tube. At the hot end, the gas conducts its heat to the surroundings through a heat exchanger (Q_h), causing the gas temperature to lower. Then, the piston retracts, and the gas undergoes adiabatic

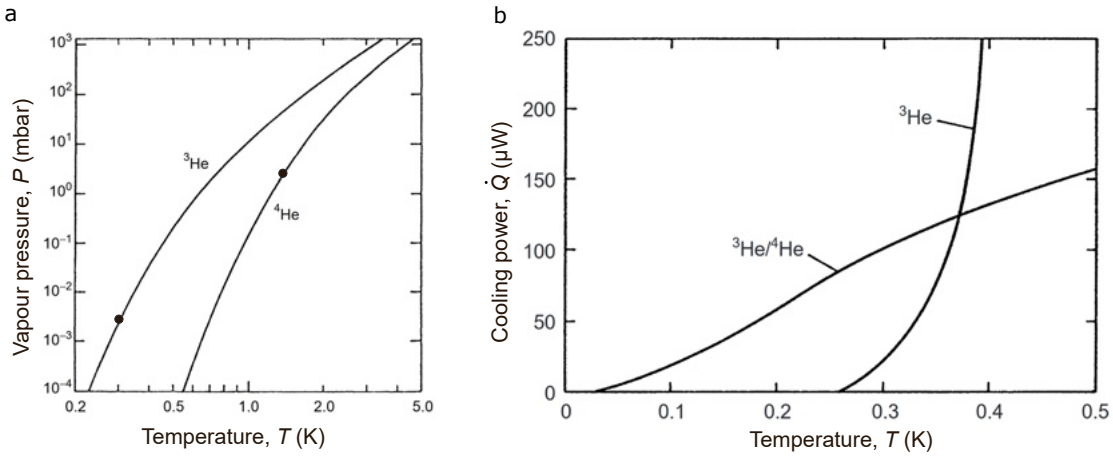

Figure 4.1.2: Dilution cooling vs. evaporation cooling. **(a)** Vapour pressures of ^{3}He and ^{4}He cryoliquids which decrease exponentially with decreasing temperatures. The dots indicate the practical lower temperatures achievable by pumping the vapour pressure. **(b)** Cooling power, $\dot{Q}$ of a ^{3}He evaporation cryostat and of a ^{3}He-^{4}He dilution refrigerator, assuming a helium gas circulation rate of 5 liters per second. Adapted from [155].

expansion, which cools it further. At the cold end of the pulse tube, the gas provides the desired cooling power (Q_c) through a second heat exchanger. Then, the expanding gas passes from the pulse tube into the regenerator, a high heat capacity material. In this step, the gas absorbs heat from the regenerator and the pulse tube walls, cooling them so that the following cycle can start by compressing the gas back through a pre-cooled regenerator. The gas begins at a lower temperature and reaches an even lower temperature after finishing its compression-expansion cycle. In this cycle each element of the gas transports heat against the temperature gradient toward the closed hot end of the pulse tube, where the heat exchanger absorbs it[155].

- **Condensing mixture in the dilution refrigerator.** When the cryostat is cooled at 4 K, the ^{3}He-^{4}He mixture can be condensed into the system. The condensed mixture fills the mixing chamber, the heat exchangers and part of the still plate. At this point, pumping the vapour pressure in the still will cool it down to < 0.8 K, through evaporative cooling.

- **Phase separation.** As the temperature is < 0.8 K the phase separation of the mixture will occur and the liquid separates into a ^{3}He-concentrated phase and a ^{3}He-diluted phase which will accumulate on the bottom of the mixing chamber.

- **Pumping of ^{3}He vapour at the still plate.** As discussed above, in a dilution refrigerator, the cooling occurs when ^{3}He atoms are transferred from the ^{3}He-rich to the ^{3}He-poor side (see Eq. 4.1.2). To enable this circulation, it is important to heat the temperature of the still plate at an appropriately high temperature, e.g. 0.7 K.

This is generally achieved by supplying heat with a heater $\dot{Q}_{st}$ [W] $\approx 40\ \dot{n}_3$ [mol] (in our setup $\dot{Q}_{st} \approx 10$ mW). At this temperature, the vapour pressure of ^{3}He is much larger than the vapour pressure of ^{4}He (see Fig. 4.1.2a). For example, at $T = 0.7$ K and $x = 1.0$ %, we can estimate the pressure of ^{3}He and ^{4}He: $P_3 + P_4 = 22$ µbar and $P_3/(P_3 + P_4) \simeq 90\%$ [157]. Therefore, in the still plate, the vapour is mostly constituted by ^{3}He ($> 90\%$) and by pumping it is possible to selectively pump almost pure ^{3}He. This will result in a pressure difference between the mixing chamber and the still plate, which will continuously drive (through osmotic pressure difference) ^{3}He from the diluted phase to the still.

- **Heater exchange.** The heat exchanger uses the enthalpy of the cold ^{3}He gas, which is pumped away from the still to pre-cool the incoming ^{3}He stream. As the temperature of the incoming stream gets low, the ^{3}He stream can condense and balance the flow.

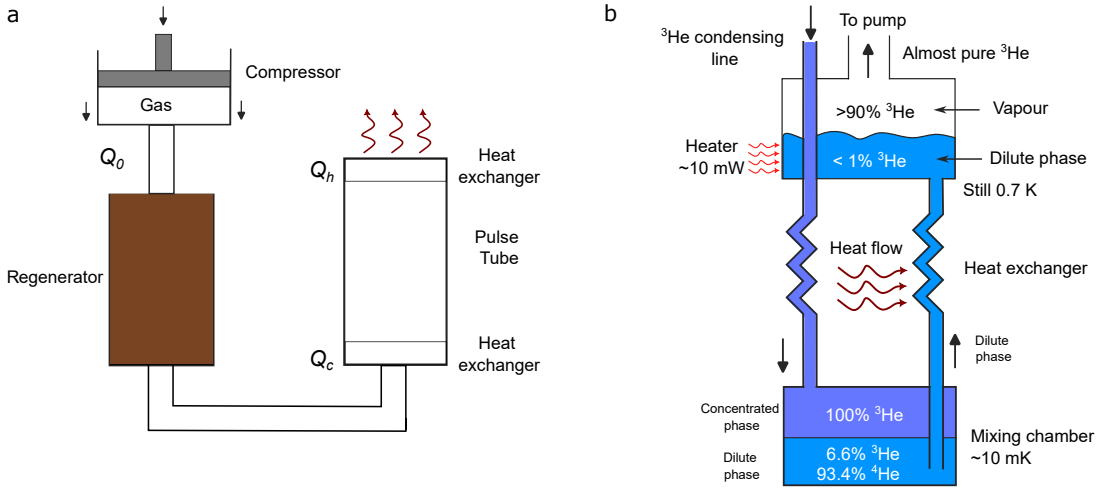

Figure 4.1.3: Dilution refrigerator principal parts. **(a)** Schemtics of the pulse tube cooling. **(b)** Schemtics of the ^{3}He-^{4}He dilution refrigerator.

4.1.3 Cryogenic low-pass filters

Given the suppressed heat capacity and thermal conductivities of 2D materials, the thermalization of the electron gas to the bath temperature (at millikelvin temperatures) is a challenging task which typically requires adequate shielding from high-frequency electromagnetic radiation [158]. This section discusses how thermalization is achieved in our experimental setup. To understand how heat is carried out at low temperatures, we can roughly estimate the temperature dependence of the thermal conductivity, κ for electrons and phonons considering a simple model in which the particles behave as a gas diffusing

through the material[155]:

$$\kappa = \frac{1}{3}\frac{C}{V_m}v\lambda \tag{4.1.5}$$

Where λ and v are the mean-free path and velocity of the particles respectively, C is the heat capacity and V_m is the molar volume. The thermal conductivity relates the rate of heat flow per unit area ($\dot{Q}/A$) to the temperature gradient (∇T) through the Fourier law:

$$\frac{\dot{Q}}{A} = -\kappa\nabla T \tag{4.1.6}$$

The heat conduction through a wire of cross-section A, length L and thermal conductivity κ is given by:

$$\dot{Q} = \kappa(T)A\frac{dT}{dx} \tag{4.1.7}$$

From which integrating in both sides we get[155]:

$$\int_0^L \dot{Q}dx = A\int_0^L \kappa(T)\frac{dT}{dx}dx = A\int_{T_1}^{T_2}\kappa(T)dT \tag{4.1.8}$$

Knowing the temperature-dependence of $\kappa(T)$ for phonons and electrons, respectively, we can predict which of the two ensembles dominates the heat transport at low temperatures.

Lattice thermal conductivity

For the phonon ensemble the thermal conductivity reads[155]:

$$\kappa_{ph} = \frac{1}{3}\frac{C_{ph}}{V_m}v_s\lambda_{ph}(T) \tag{4.1.9}$$

Where v_s is the speed of sound, $\lambda_{ph}(T)$ is the phonon wavelength and C_{ph} the phonon heat capacity. When the temperature is much lower than the Debye temperature ($T << \Theta_D$), there is a small population of thermally excited phonons which are primarily scattered by crystal defects or crystal boundaries resulting in a temperature-independent λ_{ph} (the phonon wavelength is larger than the lattice imperfections). Therefore, in this temperature range the lattice thermal conductivity scales as the lattice heat capacity: $\kappa_{ph} \propto C_{ph} \propto T^3$.

Therefore considering $\kappa_{ph} = bT^3$, we calculate for phonons:

$$\dot{Q} = \frac{Ab}{4L}(T_2^4 - T_1^4) \propto T^4 \tag{4.1.10}$$

In the specific case of copper: $\dot{Q}_{e-ph} \simeq 2\times10^3 V(T_{ph}^5 - T_e^5)$ [W][155].

Electronic thermal conductivity

For the electronic ensemble the thermal conductivity reads:

$$\kappa_e = \frac{1}{3}\frac{C_e}{V_m} v_F \lambda_e(T) \tag{4.1.11}$$

Where λ_e is the mean-free path of electrons, v_F the Fermi velocity, and C_e the electronic heat capacity. As in metals $v_F >> v_s$, the thermal conductivity of electrons is typically larger than the lattice thermal conductivity. At low temperatures, the scattering of electrons with impurities and lattice defects dominates over the one with phonons, resulting in a temperature-independent electronic mean-free path. Therefore, the electronic thermal conductivity scales as the electronic heat capacity: $\kappa_e \propto C_e \propto T$.

Considering $\kappa_e = \kappa_0 T$, we calculate for conduction electrons:

$$\dot{Q} = \frac{A\kappa_0}{2L}(T_2^2 - T_1^2) \propto T^2 \tag{4.1.12}$$

Given these considerations we conclude that at low temperatures (below 1K), most of the thermal transport in solids is carried by electrons ($\propto T^2$) rather than phonons ($\propto T^4, T^5$). Hence, the thermalization of the sample's electron gas to the bath at millikelvin temperatures is obtained via the electrical wires and requires shielding the sample from room-temperature electromagnetic radiation.

In first approximation, the electronic noise at a frequency ν is related to the temperature of the electronic ensemble via the relation $h\nu = k_B T$. Considering a hot (with temperature T_h) and a cold (with temperature T_b) electronic ensemble, we can estimate the spectral attenuation $A(\nu)$ required to shield the cold electronic system from the hot source as [159]:

$$A(\nu) = \frac{e^{\frac{h\nu}{k_B T_h}} - 1}{e^{\frac{h\nu}{k_B T_b}} - 1} \tag{4.1.13}$$

In Fig. 4.1.4a we plot the attenuation required to shield the electronic ensemble at different bath temperatures (T_b) from a reservoir at $T_h = 4$ K according to Eq. 4.1.13. We notice that relatively heavy attenuations are required to thermalize an electron bath at millikelvin temperatures. For instance, to reach $T_b = 35$ mK, it is required a damping of -150 dB at 10 GHz. To achieve such high attenuation factors, a cascade of filters, consisting of different stages, are typically installed at 4 K, 1 K, and at the base temperature of the cryostat [158]. Also, a good thermal anchoring of the wires at the filter stages, which should be well thermalized at their respective bath temperature, is mandatory. In our experimental setup, we mount a two-stage RC low-pass filter (one reactive 7-pole Pi and two dissipative RC filter stages) at the 4-K stage. Additionally, we mount RF filters (three reactive 7-pole Pi) at the mixing chamber stage. The schematic circuit of the filters, as well as expected attenuations, are shown in 4.1.4b and c. In Fig. 4.2.2 we also show a schematic of the complete optoelectronic setup.

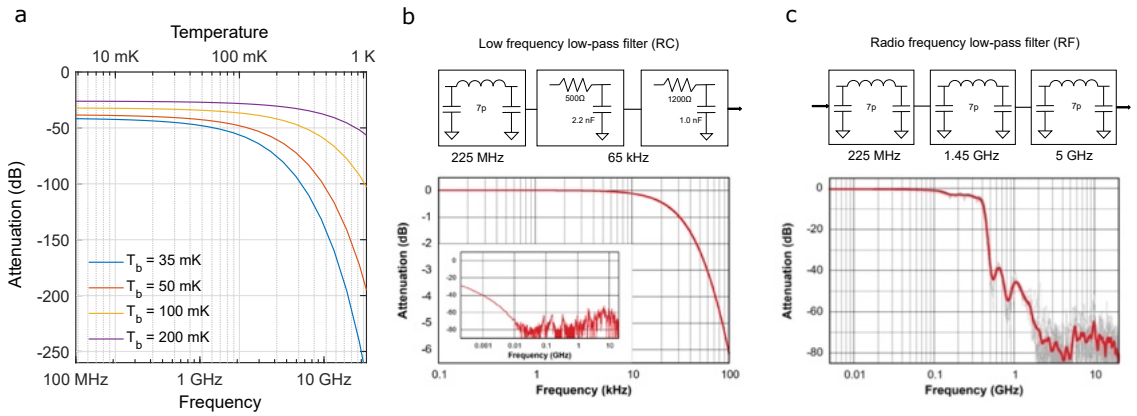

Figure 4.1.4: Cryogenic low-pass filters. (a) Attenuation required to shield an experiment at different base temperatures (T_b) from a 4 K reservoir according to Eq. **(b)-(c)** Schematics and frequency response of the cascade of RC low-pass filter **(b)** and RF low-pass filters **(c)** employed in the experiment. **(b)-(c)** are adapted from the Q-Devil filter manual.

4.1.4 Effective bandwidth of the electrical readout

As discussed in the previous section, the leads in our cryostat are highly filtered with a cascade of cryogenic low-pass filters. While these filters are essential for ensuring proper thermalization of the sample's electrons, they significantly constrain the electrical bandwidth available in the experiment. This constrained bandwidth suppresses some spectral components of electrical signals, leading to distortion of the electrical pulses. In this section, we quantify the overall bandwidth available in our experiment. Assuming our electronic readout behaves as an ideal RC low-pass circuit, we characterize its performance by determining the minimum rise time of electrical pulses and evaluating the available 3-dB bandwidth. To obtain these parameters under conditions resembling our SPD experiment, we place a resistor (10 kΩ) into the sample space and monitor the voltage across the resistor using a 4-terminal configuration.

- **Pulse Rise Time.** To measure the minimum rise time, defined as the time required for a signal to transition from 10% to 90% of the rising edge of the curve, we use an arbitrary waveform generator (AWG) to generate square wave pulses at a frequency of 13.3 Hz (Fig. 4.1.5a). We record the voltage across the 10 kΩ resistor with an oscilloscope. By analyzing the square wave pulse, we extract the minimum rise time $t_r = 422$ µs (Fig. 4.1.5c). This measurement enables to extract the effective 3-dB cut-off frequency as [160]: $f_{3dB} = 0.35/t_r = 830$ Hz.

- **Frequency Response Magnitude.** To measure the 3-dB bandwidth we apply a sinusoidal AC current to the resistor at frequencies ranging from 3 Hz to 100 kHz using a lock-in amplifier. We measure the voltage generated across the 10 kΩ

resistor with a lock-in amplifier in the same configuration (see Fig. 4.1.5d). This measurement shows that the frequency response is flat for low frequencies and drops around 1 kHz. By extracting the 3-dB bandwidth, defined as the frequency at which the initial amplitude drops by 3 dB or 0.707 of its initial value, we obtain $f_{3dB} = 738$ Hz.

Both methods yield compatible results, showing that the bandwidth available in our experiment is less than 1 kHz. This bandwidth determines the electrical pulses' rise time and limits the SPD measurements' maximum operation speed.

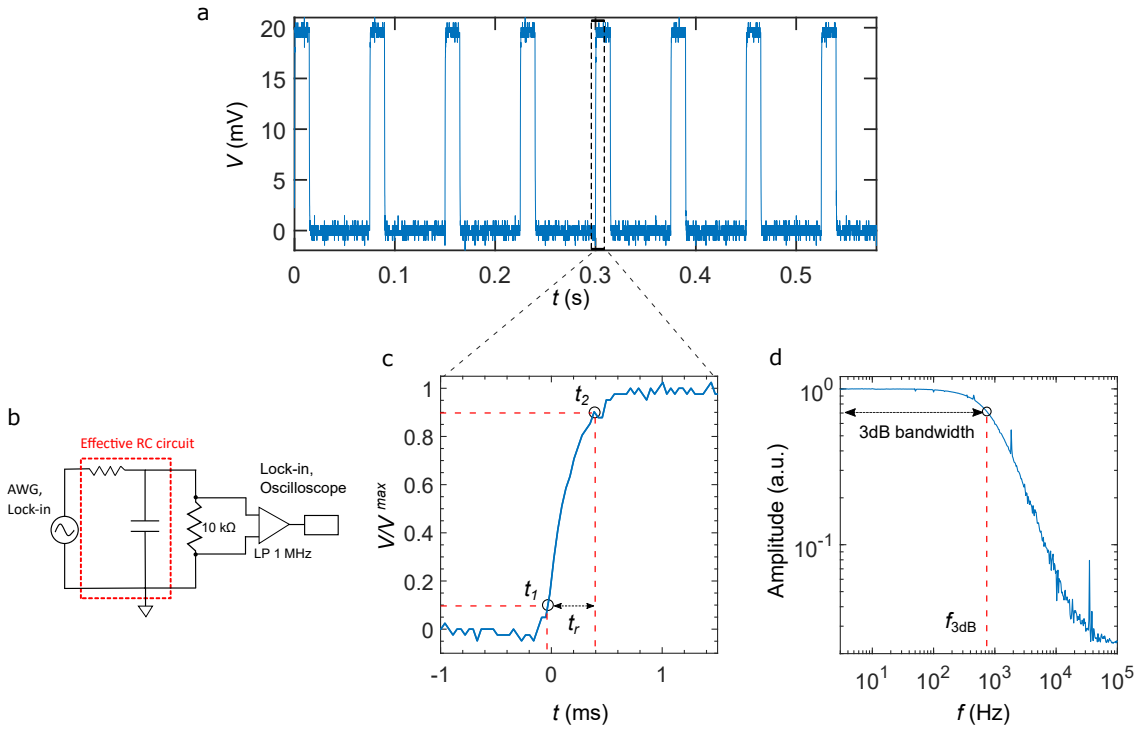

Figure 4.1.5: Minimum rise time and frequency response magnitude of the electrical readout. **(a)** Voltage signal measured with an oscilloscope across a 10 kΩ resistor upon applying a square wave signal with a frequency of 13.3 Hz. **(b)** Circuit schematics employed to measure the frequency response magnitude and the minimum rise time of the pulses. **(c)** Zoom of the voltage traces in **(a)** from which we extract the square wave pulse's rise time, t_r. **(d)** Frequency response magnitude of the electrical readout. The 3-dB bandwidth, f_{3dB} defiend as the frequency at which the initial amplitude of the signal drops by 3 dB is marked by the red dashed line. Adapted from [P1].

4.2 Electronic setup

In this section, we introduce standard low-frequency lock-in techniques used to characterize the electronic transport properties of MATBG devices and describe the electrical readout employed in the SPD experiment.

4.2.1 Low-frequency transport with lock-in technique

Lock-in amplifiers use the knowledge of a signal's time dependence to isolate it from a noisy environment. The device multiplies the input signal with a reference signal, internally generated by the lock-in amplifier or externally supplied, and then applies an adjustable low-pass filter to the resulting output as illustrated in the schematics of Fig. 4.2.1a. This technique, referred to as demodulation or phase-sensitive detection, effectively isolates the signal at the desired frequency from other frequency components. Therefore, the typical experiment involves applying an AC current at a reference frequency to the sample and measuring the voltage signal in a two or four-probe scheme at the same reference frequency.

Signal mixing

The reference signal is usually a sine wave but can also have other forms, such as square wave etc. Considering a purely real (zero imaginary part) sinusoidal input signal $V_s(t)$ [161]:

$$V_s(t) = \sqrt{2}R \cdot cos(\omega_s t + \theta) = \frac{R}{\sqrt{2}} e^{-i(\omega_s t+\theta)} + \frac{R}{\sqrt{2}} e^{+i(\omega_s t+\theta)} \tag{4.2.1}$$

And a complex reference signal $V_r(t)$:

$$V_r(t) = \sqrt{2} e^{-i\omega_r t} \tag{4.2.2}$$

The complex signal after mixing $Z(t)$ can be calculated as:

$$Z(t) = \mathrm{X}(t) + i\mathrm{Y}(t) = V_s(t) \cdot V_r(t) = R[e^{i[(\omega_s-\omega_r)t+\theta)]} + e^{-i[(\omega_s+\omega_r)t+\theta)]}] \tag{4.2.3}$$

This signal has two frequency components at $\omega_s - \omega_r$ (slow or DC component) and $\omega_s + \omega_r$ (fast component). The goal of the low-pass filter is to suppress the fast component so that the signal after demodulation becomes:

$$Z(t) = R \cdot e^{i[(\omega_s-\omega_r)t+\theta)]} \tag{4.2.4}$$

Typically the experiment is designed in such a way that the signal frequency is the same as the reference frequency, $\omega_s = \omega_r$ so that the signal simplifies as:

$$Z(t) = R \cdot e^{i\theta} \tag{4.2.5}$$

In this way the in-phase and out-of-phase components of the demodulated signal $Z(t)$ can be extracted as:

$$X = \mathrm{Re}(Z) = R\cos\theta \tag{4.2.6}$$
$$Y = \mathrm{Im}(Z) = R\sin\theta \tag{4.2.7}$$

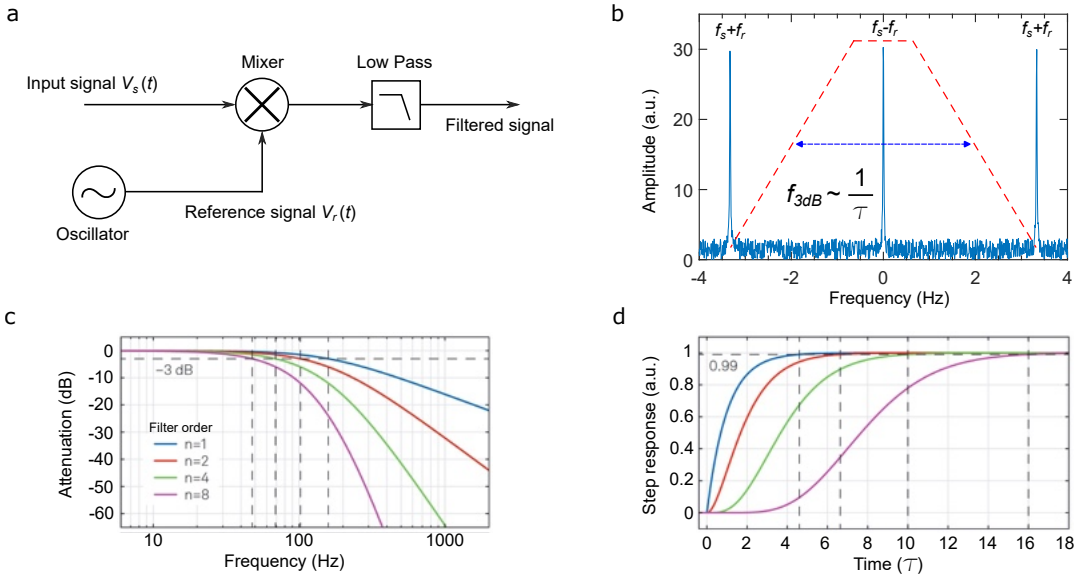

Figure 4.2.1: Lock-in technique. **(a)** Schematic of the lock-in amplification. The signal mixer combines the input $V_s(t)$ with the reference $V_r(t)$. The resulting signal is then low-pass filtered. **(b)** In the frequency domain the mixed signal (in the assumption of a sinusoidal input signal) features two components at $f_s + f_r$ and $f_s - f_r$. The red dashed line represents an ideal "brick-wall filter" which rejects the noise and the fast component $(f_s + f_r)$. The filter time constant τ is inversely proportional to the 3dB bandwidth f_{3dB}. Hence, increasing the time constant is possible to narrow the bandwidth to suppress the noise. **(c)** Transfer function $H(\omega)$ against frequency of an RC filter for different filter orders (n = 1, 2, 4, 8). The dashed horizontal line indicates the 3dB attenuation and the vertical dashed lines define the corresponding f_{3dB}. High-order filters feature a narrower bandwidth. **(d)** Step response functions in the time domain for different filter orders (n = 1, 2, 4, 8). High-order filters lead to a large increase in the signal settling time. The dashed vertical lines define the settling time (in units of τ) needed to reach the 99% of the final value (horizontal dashed line). **(c)** and **(d)** are Adapted from [161].

Low-pass filtering in the frequency domain

Once the signal is mixed with the reference, adjusting the low-pass filter to the specific experiment is crucial to isolate the signal at the desired frequency from other frequency components. Generally speaking, in the frequency domain the low-pass filter can be ideally pictured as a "brick-wall filter" which cuts off the frequencies $f > f_{cut-off}$ and keeps

unchanged the frequencies $f < f_{cut-off}$ (red dashed line in Fig. 4.2.1b). In a simple formalism, the relation between the incoming signal $Q_{in}(\omega)$ and filtered signal $Q_{out}(\omega)$ is given by[161]:

$$Q_{out}(\omega) = H(\omega) \cdot Q_{in}(\omega) \tag{4.2.8}$$

Where $H(\omega)$ is the transfer function of the filter. For a RC filter, $H(\omega)$ can be approximated as[161]:

$$H(\omega) = \frac{1}{1 + i\omega\tau} \tag{4.2.9}$$

Where $\tau = RC$ is the filter time constant with resistance R and capacitance C. As discussed also in section 4.1.4, for an RC filter the cut-off frequency f_{3dB} can be defined as the frequency at which the initial signal amplitude is reduced by 3 dB and is given by: $f_{3dB} = 1/(2\pi\tau)$. Therefore, the choice of the time constant primarily determines the filter's cut-off frequency. Another important parameter is the roll-off, i.e. the rate at which a filter attenuates the signal beyond its cutoff frequency. For this case, the roll-off is 6 dB/octave (or equivalent to 20 dB/decade). This means that for every tenfold increase in frequency beyond the cutoff frequency, the filter's output signal is attenuated by 20 decibels, or equivalently, the signal is attenuated by 6 dB (half of the power) for each doubling of the frequency (see Fig. 4.2.1c)[161]. A filter with such roll-off is typically a first-order filter. To increase the roll-off steepness it is possible to cascade several RC filters. For every filter added, the order n is increased by 1 and the resulting attenuation has a total roll-off of n $\times$ 20 dB/dec (see Fig. 4.2.1c)[161]:

$$H_n(\omega) = H_1(\omega)^n = \left(\frac{1}{1 + i\omega\tau}\right)^n \tag{4.2.10}$$

For a high-order filter, the 3dB bandwidth reads[162]:

$$f_{3dB} = \frac{\mathrm{FO}}{2\pi\tau} \tag{4.2.11}$$

Where FO is a factor that depends on the filter order, e.g., for a first-order filter, FO = 1; for a second-order filter, FO = 0.6436, etc. (see Table 4.1). Hence, increasing the filter order reduces the 3dB bandwidth, according to Eq. 4.2.11.

Low-pass filtering in the time domain

The filter time constant τ and order n are, therefore, the most important parameters that can be externally tuned in the lock-in amplifier. However, since the applied filters cut some spectral components, particular care is required to avoid distortion of the original signal. Specifically, external fixing of τ and n results in a constrained electrical bandwidth and a subsequent modification of the rise time of the electrical signal in the time domain.

As shown in the time-domain response in Fig. 4.2.1d, given the constrained bandwidth, a certain amount of time is needed for the signal to settle to the actual value. To accurately measure a filtered signal, it is crucial to wait for the signal to settle before taking the measurement. In the Table 4.1, we list the waiting time needed to reach some percentage of the final value for filters of different orders but the same time constants.

Filter Order	Roll-off	FO	Settling times in units of τ			
			63%	90%	95%	99%
1	6 dB/oct	1.0000	1.0	2.3	3.0	4.6
2	12 dB/oct	0.6436	2.1	3.9	4.7	6.6
3	18 dB/oct	0.5098	3.3	5.3	6.3	8.4
4	24 dB/oct	0.4350	4.4	6.7	7.8	10.0

Table 4.1: Properties and settling times for n-th order RC filters. Adapted from [162] and [161].

4.2.2 Electrical readout for single-photon detection experiment

As discussed in the previous section, the lock-in amplifier uses low-pass filtering in the frequency domain to isolate the signal at a reference frequency from a noisy background. This measurement technique is used for most of the transport characterization reported in this thesis (Chapter 2 and 3) and for measuring the bolometric response presented in Chapter 5. However, the electrical readout used for the SPD measurements differs from the standard lock-in technique. In the proof-of-concept experiment presented in Chapter 6, we use a highly attenuated coherent source that stochastically provides photons incident on a superconducting MATBG device biased close to the superconducting transition. In this scenario, there is no reference signal, and the voltage must be monitored over time to detect photodetection events, which will define the 'clicks' of the detector. Also, photodetection events can potentially lead to ultra-fast photoresponses in the nanosecond or even the picosecond range, as discussed in Fig. 5.1. The voltage readout should have the highest possible bandwidth to avoid cutting any spectral components. By definition, the lock-in amplifier filters out part of the input signal by applying a narrow-band low-pass filter. Therefore, instruments capable of recording voltage over time with broader bandwidths are needed. Our experiment uses a sampling oscilloscope with variable bandwidth up to 600 MHz (UHF-Scope Zurich Instrument) or a 100-kHz-bandwidth analog-to-digital converter (UHF-Aux In Zurich Instrument). However, as discussed in section 4.1.4, the available bandwidth in our experiment (< 1 kHz) represents a limiting factor for the speed of the readout mechanism. A step forward would be implementing radiofrequency cables that provide large bandwidth while not hampering the electronic temperature. In section 6.4.3 we analyze the timescale of the pulses generated by MATBG and discuss possible strategies to improve the detector's speed.

In Fig. 4.2.2, we schematically illustrate the setup employed to perform SPD measurements. We place the device on the cold finger of a dilution refrigerator (BlueFors-SD250), housed in a gold-coated oxygen-free copper box (custom-designed to have optical access). We apply a bias voltage at the source contact of the device with a voltage generator (Keithley 2400) in series with a 1/1000 voltage divider. The voltage probes are connected to a room-temperature 1-MHz-bandwidth low-noise amplifier (SR-560). We also use a room-temperature low-pass filter with a sharp cut-off of approximately 1-10 kHz to reject white

noise outside the readout bandwidth. As mentioned above, the amplified signal is fed to either the sampling oscilloscope or the analog-to-digital converter (UHF-Aux In Zurich Instrument) to record photovoltage time traces over time. The optical excitation is provided by a cryo-compatible single-mode optical fiber.

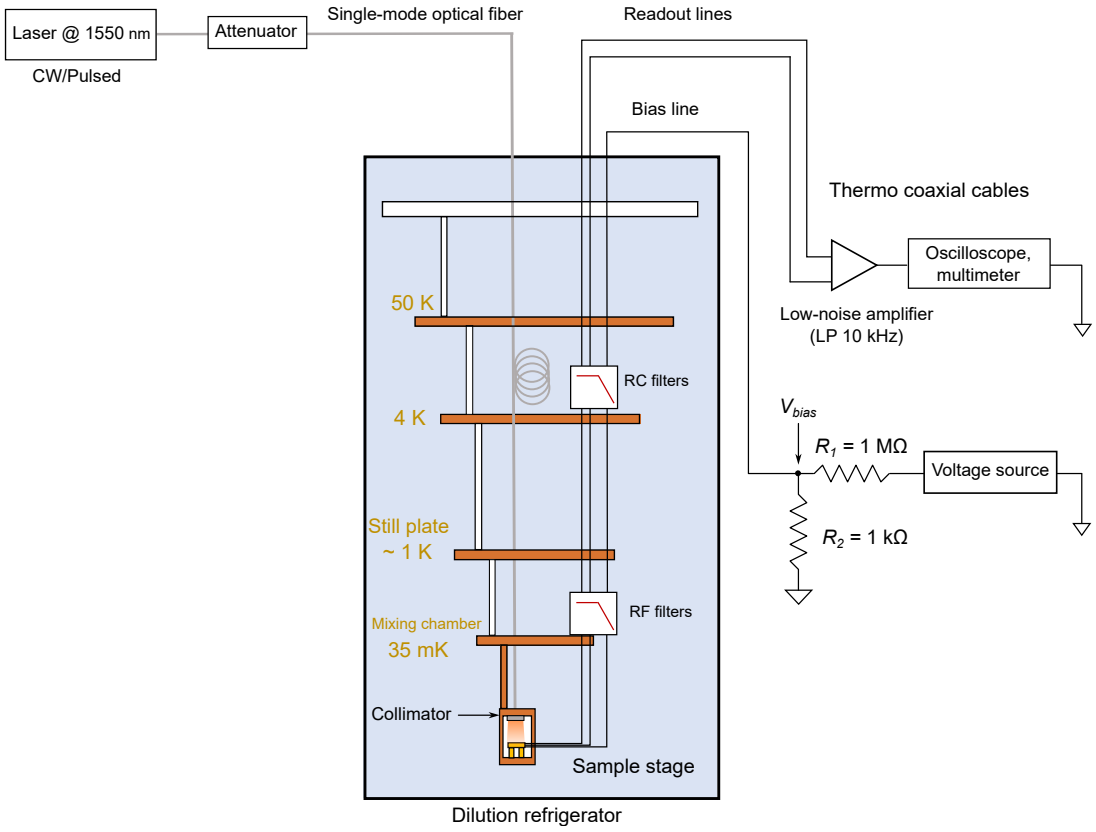

Figure 4.2.2: Optoelectronic setup. Schematics of the optoelectronic setup employed to measure the SPD response by the MATBG superconducting detector. Adapted from [P1].

4.3 Optical setup

In Section 1.1, we derived the photon statistics for a coherent source and discussed how single-photon sensitivity can be demonstrated by analyzing the count statistics of a detector illuminated by a highly attenuated coherent source. In this section, we describe the optical setup used in our experiment and calculate the density of near-infrared photons incident on the MATBG device. We utilize a 1550-nm laser diode (Taiko PDL M1) as the coherent source. The light is transmitted into the dilution refrigerator to the MATBG detector via a single-mode optical fiber, which is coupled with a collimator positioned a few centimeters above the sample space, enabling illumination of the entire device area (approximately 4 mm spot diameter). The incident laser power is regulated through a programmable optical attenuator (JGR OA5), allowing for attenuation of the optical power by several orders of magnitude and precise adjustment of the average photon number incident on the device. The schematic of the optoelectronic setup used in our experiment is shown in Fig. 4.2.2.

4.3.1 Beam profile at the sample stage

As shown in detail in Fig 4.3.1, in our setup, the output power P_{out} emitted by a telecom laser is coupled into the cryostat with a single-mode optical fiber. The fiber is then connected to a laser beam coupler, providing a collimated output with beam radius $w_0 \sim 2$ mm and Rayleigh range $z_R = \frac{\pi w_0^2}{\lambda} \sim 8$ m. To quantitatively describe the amount of light and the rate of photons incident on the MATBG detector, we consider a Gaussian beam profile. Using the Gaussian approximation, we can express the intensity profile I in terms of the distance from the beam center, r and the propagating distance z[163]:

$$I(r,z) = I_0 \left(\frac{w_0}{w(z)}\right)^2 e^{-2(\frac{r}{w(z)})^2} \tag{4.3.1}$$

Where $w(z)$ is the value of the radius at a certain distance z given [163] by $w(z) = w_0\sqrt{1+\left(\frac{z}{z_R}\right)^2}$ and $I_0 = \frac{2P_{out}}{\pi w_0^2}$ is the total irradiance of the laser source, given by the Gaussian normalization condition. As in our experiment, z is the distance away from the end of the fiber coupler, we simulate $w(z)$ up to 1 m (4.3.1c,). Given the position of the device, located around $z_0 \approx 3$ cm away from the fiber coupler $\left(\frac{z_0}{z_R} = 0.0037 \ll 1\right)$, we can consider the beam to be collimated and replace in $w(z) \approx w_0 = 2$ mm. Since we align the device to be roughly at the center of the beam, it reads $I(r=0,z_0) = \frac{2P_{out}}{\pi w_0^2}$.

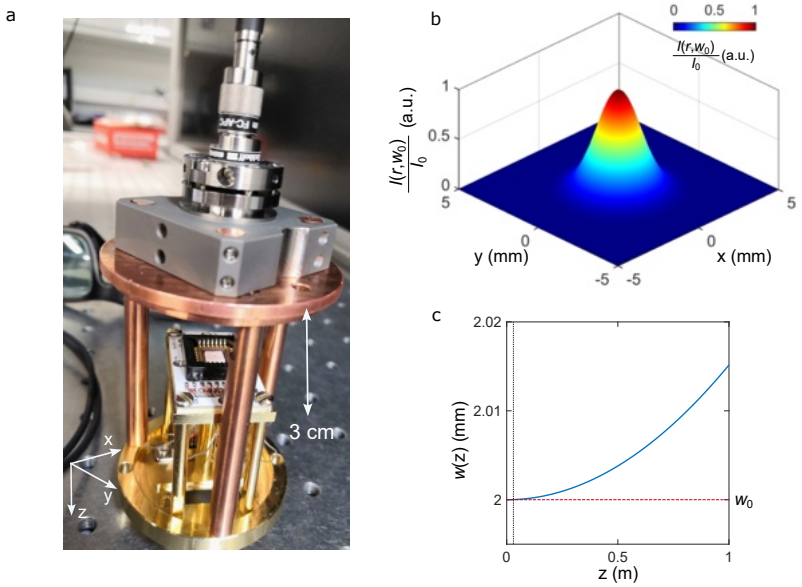

Figure 4.3.1: Beam profile at the sample stage. (a) Optical image of the experimental scheme. The single-mode optical fiber designed for 1550-nm transmission is connected to a laser beam coupler which provides a collimated output. The sample is located approximately 3 cm away from the fiber coupler. Every component shown in the optical image was custom-designed by me. **(b)** 3D plot of the normalized beam intensity in the Gaussian beam approximation. **(c)** Simulation of the Gaussian beam radius $w(z)$ at a distance z from the fiber coupler, given by $w(z) = w_0\sqrt{1+(z/z_R)^2}$. The black vertical line indicates the position of the sample $z_s = 3$ cm. Adapted from [P1].

4.3.2 Calculation of the power density incident on the MATBG device

With the considerations made in the previous section, we can calculate the power density P_L incident on the MATBG as follows:

$$P_L = 10^{-\eta/10} \cdot T_{fiber} \cdot \frac{P_{out}}{\frac{\pi}{2} w_0^2}\,, \tag{4.3.2}$$

Where P_{out} is the total power output coming out of the laser, $T_{fiber} = 0.021$ the effective transmission of the fiber (including all the optical connections and vacuum feed-throughs), and η the variable attenuation (in dB) used to control the power incident on the device. In the SPD measurements with the CW laser source, we keep the laser power constant ($P_{out} = 11$ µW) and scan η between several orders of magnitudes from 70 dB to 4 dB. For device A, a typical attenuation of 40 dB results in $P_L = 3.7$ aW/µm^2.

Given P_L, the average incident photon rate per unit time τ per µm^2 $\langle N_{photon}\rangle$ reads:

$$\langle N_{photon}\rangle = \tau \cdot \frac{P_L}{h\nu}\,, \tag{4.3.3}$$

Where $h\nu = 1.28 \times 10^{-19}$ J is the energy of a single photon at $\lambda = 1550$ nm. For an attenuation of 40 dB and $\tau = 5$ ms (which is the typical reset time of the MATBG detector), we expect $\langle N_{photon} \rangle = 0.14$.

In pulsed experiments, by changing the laser repetition rate (f_{RR}), we can control the number of photons carried on average by each pulse μ as:

$$\mu = \frac{1}{f_{RR}} \cdot \frac{P_L}{h\nu} \cdot \int_{-l_1/2}^{l_1/2} dx \int_{-l_2/2}^{l_2/2} dy \, e^{-2(x^2+y^2)/w_0^2} \,, \tag{4.3.4}$$

Where l_1 and l_2 are the length and width of the measured area. Since we assume the sample to be located at the center of the beam and l_1, $l_2 \ll w_0$, we can simplify (0.4) to:

$$\mu = \frac{1}{f_{RR}} \cdot \frac{P_L}{h\nu} \cdot l_1 \cdot l_2 \,. \tag{4.3.5}$$

In the SPD experiment described in Chapter 6, we set the output power to $P_{out} = 3$ nW and the laser repetition rate to $f_{RR} = 100$ Hz. Considering the spatial dimension of the sample $l_1 = 3$ µm, $l_2 = 5.3$ µm, for an attenuation of 13 dB, we obtain $\mu = 0.62$.

It is worth noticing that the calculated values are only an upper-bound estimation because the optical alignment is not controlled accurately in the cryogenic experiment. In particular, it is possible that the sample is not perfectly located in the center of the beam and that the effective incident power is lower.

5

Measuring the bolometric response of superconducting MATBG

The work presented in this chapter led to the publication [P2]:
G. Di Battista, P. Seifert, K. Watanabe, T. Taniguchi, K.C. Fong, A. Principi, and D. K. Efetov, "Revealing the thermal properties of superconducting magic-angle twisted bilayer graphene", *Nano Letters* **22**, 16, 6465–6470 (2022).
My contribution to this work was conceptualizing and designing the experiment, fabricating devices, measuring, analyzing data, and writing the manuscript.

As the first experimental exploration of the sensitivity of the superconducting state of MATBG, we measure its bolometric response upon illumination with telecom wavelength. This measurement is particularly interesting for photodetection applications as it reports the first measurement of the thermal conductivity in the superconducting state, which, as discussed in section 1.3.1, is important to determine the performance of thermal detectors. In addition, we find that the thermal conductance exhibits a power law dependence in the low-temperature limit, similarly to what was observed in nodal superconductors [52]. In this Chapter, we perform an optoelectronic experiment in which we monitor the 4-terminal transport properties of the MATBG device upon illumination with laser light at a wavelength of $\lambda = 1550$ nm (see schematics in Fig. 5.1.1a). Operating with steady-state illumination, the electronic temperature T_e can be extracted by measuring the critical current I_c, which has a pronounced temperature dependence. Using this thermometry, we can probe the heating induced by the laser light and measure the electronic thermal conductance of the superconducting state of MATBG.

5.1 Light-matter interaction in MATBG for near-infrared photons

Given the novelty of the material, a comprehensive description of the light-matter interaction in MATBG is still lacking. Considering the energy scales involved in the experiment, i.e. the energy of the incident photons (0.8 eV), which is significantly larger than the width of the flat bands ($\sim$ 10 meV [33]) and the typical size of the superconducting gap ($\sim$ 1 meV [164]), we consider the absorption properties of MATBG to be similar to those of AB bilayer graphene for near-IR photons [P2, 165]. We assume that the absorbed photons excite electrons from the valence bands to the high-energy conduction bands (Fig. 5.1.1b). Since the k-space of the flat bands does not extend far from the Dirac points [166], there is a vanishing joint density of states for vertical transitions from and to the flat bands [P2]. Therefore, as a first approximation, we exclude processes in which photons are absorbed within the flat bands and induce inter-band transitions from the flat bands to the higher energy conduction bands. Additionally, given that the moiré unit cell ($\sim$ 13 nm) is considerably smaller than the wavelength of the incident photons, we consider the effect of the superlattice negligible for the absorption process.

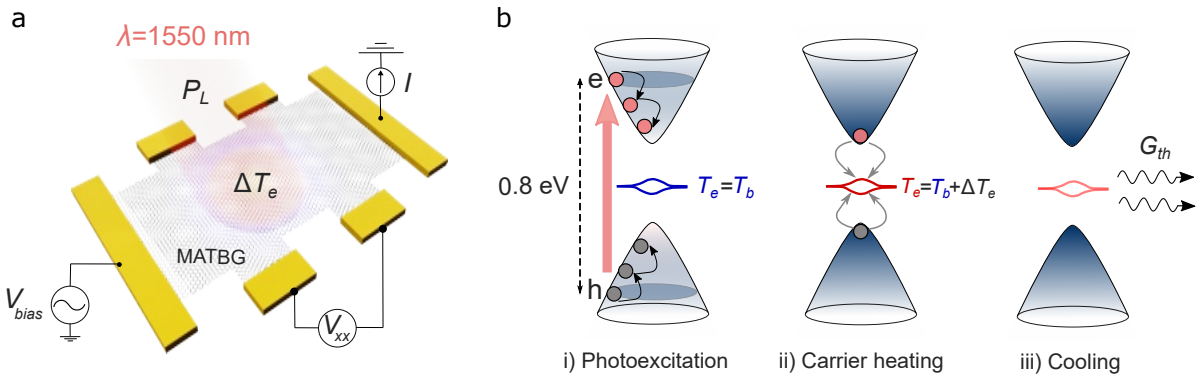

Figure 5.1.1: Schematic of the light-matter interaction in MATBG. (a) We illuminate a superconducting MATBG with CW laser light (λ = 1550 nm) and monitor the light-induced change in resistance with a four-terminal transport scheme. **(b)** Schematics of the photoexcitation-thermalization-cooling process in MATBG. The absorbed photons generate electron-hole pairs in the high-energy dispersive bands. Then, the photoexcited carriers efficiently thermalize by electron-electron interactions to a hot carrier distribution with electronic temperature T_e in the flat bands. The electronic thermal conductance, G_{th} rules the cooling process of these thermal electrons. Adapted from [P2].

Following the analogy to AB-stacked bilayer graphene, we expect that the photoexcitation-thermalization-cooling processes well-studied for graphene will be qualitatively applicable to MATBG. As illustrated in the schematics in Fig. 5.1.1b, absorbed photons excite

electron-hole pairs in the higher energy dispersive bands. These photo-excited carriers relax on ultra-fast timescales through electron-electron interactions, ultimately reaching the flat bands and forming a thermal distribution. Consequently, the photo-absorption process effectively raises the electron temperature, T_e, above the device temperature, which is determined by the lattice and the metallic leads and is in thermal equilibrium with the bath temperature, T_b. Another crucial aspect is the energy conversion efficiency from photoexcitation to a thermal hot carrier distribution. Previous studies on graphene have demonstrated near-unity conversion efficiency for near-IR photons [62, 63, 167], with negligible optical phonon emission due to the ultra-fast electron-electron scattering time (less than 100 fs, ref.[168]) compared to the electron-phonon scattering time. Given the similarity to graphene for these excitation energies, we assume that the energy conversion from photoexcitation to a thermal hot carrier distribution in MATBG is highly efficient [P2]. Once the carriers are heated above the bath temperature, $\Delta T_e = T_e - T_b$, they dissipate the additional heat to reach thermal equilibrium. The electronic thermal conductance, G_{th}, defines this final cooling process.

5.1.1 Estimation of the optical absorption in the experiment

The considerations regarding the absorption of MATBG discussed above assume a suspended two-dimensional layer [169]. However, in our experiment, MATBG is deposited on a substrate and embedded in a heterostructure. These additional layers can affect the local electric field, leading to wave interference, ultimately altering the absorption[170]. To account for this, we employ the optical transfer matrix formalism to evaluate the impact of the additional layers on the absorption of the MATBG layer. As schematically illustrated in Fig. 5.1.2b, we assume the 1550 nm radiation to be linearly polarized and at normal incidence[170]. The transfer matrix depends on the layers' complex refractive indices and thicknesses. The refractive index values used are from the literature (https://refractiveindex.info/) for these materials. The thicknesses of the 2D layers constituting the heterostructure are measured using an Atomic Force Microscope, as shown in Fig. 5.1.2a. For the main MATBG device investigated in this experiment, the thicknesses are:

- Top hBN=10 nm
- MATBG=0.69 nm
- Bottom hBN=15 nm
- Graphite=3 nm
- SiO2=285 nm
- Si=1 mm

To perform these calculations, we use the MATLAB code provided by ref. [170]. Using these input parameters, we estimate the absorption of MATBG to be $\sim$ 6.4 %, which is only slightly enhanced compared to the one expected for suspended MATBG (4.6%). Engineering the substrate with cavities[171] or photonic crystals[172] can enhance MATBG's absorption, similar to what was previously done in graphene. As discussed in section 4.3,

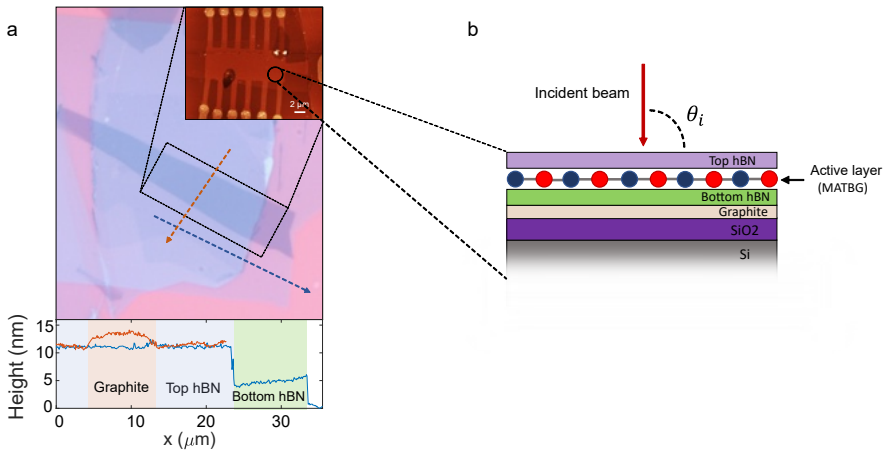

Figure 5.1.2: AFM and optical micrographs of a MATBG sample. **(a)** The main panel is the optical image of the final hBN/MATBG/hBN/Graphite stack. The inset shows an AFM scan of the final device etched into a Hall bar geometry. The dashed square indicates the area imaged with the AFM. The lower panel shows the height profiles along the blue and red dashed lines from which we extract the hBNs and graphite thicknesses. **(b)** Schematic cross-section of the stack used in the optical transfer matrix calculations. The second layer of the heterostructure (MATBG) is the active layer in our calculations. Adapted from [P1].

the laser beam in our experiment is of millimeter size. As a result, the radiation is absorbed not only by MATBG but also by the other layers of the heterostructure, the substrate, and the gold electrodes. Given the larger band gap compared to the excitation energy of 0.8 eV, the absorption by Si/SiO_2 and hBN layers is negligible[P2]. Conversely, the gold electrodes and the local graphite gate underneath the heterostructure can absorb part of the radiation. However, we qualitatively argue that even though these materials absorb radiation, they do not constitute an additional heating source for the MATBG layer [P2]. Indeed, gold and graphite are both bulk 3D materials with thermal conductivities much higher than 2D materials like MATBG. In a steady state, the increase in electronic temperature (ΔT_e) depends on the ratio between optical absorption (α) and thermal conductivity (κ): $\Delta T_e \sim \alpha/\kappa$. Therefore, we can consider the electronic temperature increase of these materials to be negligible compared to that of superconducting MATBG. In the modeling performed in section 5.3.2, we estimate the temperature increase of the gold electrodes to be approximately 10^{-8} mK. Furthermore, the electronic thermal conductivity of a superconductor is strongly suppressed below the critical temperature, and its thermal conductivity is dominated by electron diffusion, where only thermally excited quasiparticles conduct heat, while Cooper pairs do not (see section 1.2.1). This results in a much lower thermal

conductivity than non-superconducting metals within our investigated temperature range. In addition, the bottom hBN layer, which separates the MATBG from the graphite local gate, provides additional thermal isolation. Therefore, even if the graphite is slightly heated by the radiation, it would not perturb the temperature of the MATBG. Based on these arguments, we can neglect the heating effects from materials other than MATBG and assume that the measured temperature increase in our experiment is primarily due to the light-induced heating of the MATBG electrons [P2].

5.2 Bolometric response of superconducting MATBG

5.2.1 Critical current thermometry

Considering the model of photoexcitation-thermalization-cooling described above, we measure the increase in the electronic temperature ΔT_e upon illumination with the external laser power by using the temperature dependence of the critical current $I_c(T)$. In order to provide a sensitive measurement of I_c, we perform nonlinear resistance measurements $\mathrm{d}V_{xx}/\mathrm{d}I$ vs. source-drain current (I_{dc}). The $\mathrm{d}V_{xx}/\mathrm{d}I$ trace is the first derivative of the current-voltage I-V characteristic. As anticipated in section 1.2.1, in superconductors, the I-V curve exhibits a flat region ($R = 0, V = 0$) when the applied DC current is lower than the critical current ($I_{dc} < I_c$). As I_{dc} equals I_c, the system transitions from the superconducting to the normal state and the I-V characteristic recovers the slope given by the resistance of the device's normal state (Fig. 5.2.1a). The superconducting-normal state transition at I_c manifests as a pronounced peak in the $\mathrm{d}V_{xx}/\mathrm{d}I$ characteristic. Identifying the maxima in the $\mathrm{d}V_{xx}/\mathrm{d}I(I_{dc})$ traces, we can carefully extract the critical current of the MATBG superconductor (inset of 5.2.1c).

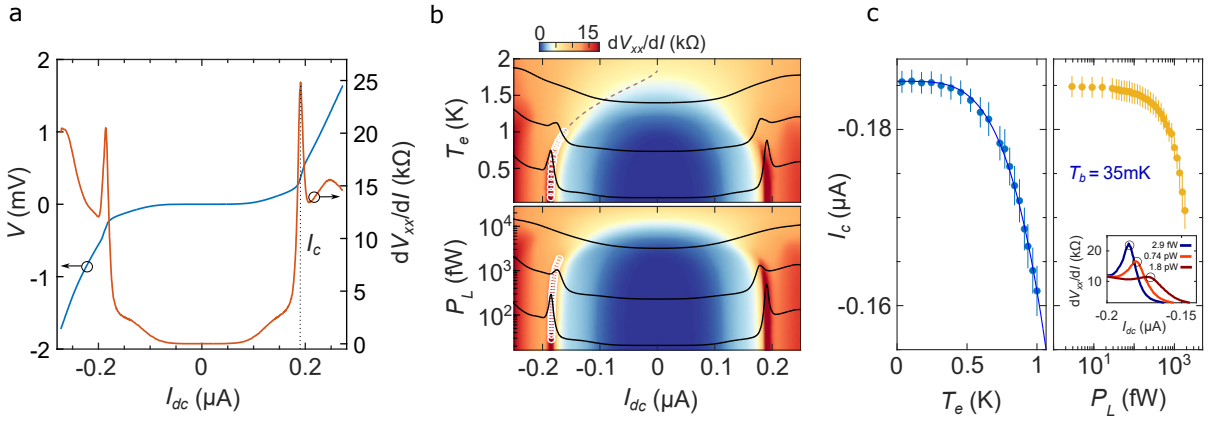

Figure 5.2.1: Critical current thermometry. **(a)** I-V (blue) and $\mathrm{d}V_{xx}/\mathrm{d}I$ (red) characteristic for the MATBG superconductor at 35 mK. The transition from the superconducting to normal state occurs when the applied DC current equals the critical current I_c. This manifests as a pronounced peak in the $\mathrm{d}V_{xx}/\mathrm{d}I$ trace. **(b)** Top panel: color plot of the longitudinal $\mathrm{d}V_{xx}/\mathrm{d}I$ vs. source-drain current (I_{dc}) and T_e. In black, the $\mathrm{d}V_{xx}/\mathrm{d}I$ line cuts measured at 3 different temperatures. The white dots are the extracted values of I_c, fitted with the empirical formula $I_c(T_e) = I_c(T_e = 0)[1 - (T_e/T_c)^4]^{3/2}$ (dashed line). Bottom panel: color plot of the longitudinal $\mathrm{d}V_{xx}/\mathrm{d}I$ vs. I_{dc} and laser power (P_L). In black, the $\mathrm{d}V_{xx}/\mathrm{d}I$ line cuts measured at 3 different temperatures and in white, the extracted values of I_c. **(c)** I_c vs. T_e (left panel) and P_L (right panel) with errorbars. Critical current vs. temperature values are fitted according to the empirical formula used in **(b)**. In the bottom inset the method used to extract I_c by taking the peak of the $\mathrm{d}V_{xx}/\mathrm{d}I$ traces. **(b)** and **(c)** are adapted from [P2].

To perform critical current thermometry, we first calibrate MATBG's critical current as a function of temperature. For this purpose, we measure I_c at different bath temperatures (T_b) by heating the cryostat. As T_b is in equilibrium with the T_e of the MATBG, this measurement directly provides $I_c(T_e)$ (Fig. 5.2.1c). Then, we measure I_c, as a function of the laser power P_L, while keeping T_b constant at 35 mK (Fig. 5.2.1b). By measuring I_c as a function of both electronic temperature $I_c(T_e)$ and absorbed laser power $I_c(P_L)$, we can relate ΔT_e with the P_L and measure the bolometric response of MATBG according to the formula derived in section 5.2.2. By looking at the colormaps in Fig. 5.2.1b, we notice that the measurements of $\mathrm{d}V_{xx}/\mathrm{d}I$ vs. T_e are similar to the measurements of $\mathrm{d}V_{xx}/\mathrm{d}I$ vs. P_L, further confirming our assumption that the incident radiation is primarily absorbed by the electrons, which are heated above the bath temperature, $T_e > T_b$.

5.2.2 Derivation of the thermometer calibration formula

In this section, we derive the analytical expression used to relate ΔT_e with the P_L. To calibrate our thermometer, we use the empirical relation for the superconducting electron density, discussed in ref. [173]:

$$N_s(T) = N_s(0)\left[1 - \left(\frac{T_e}{T_c}\right)^4\right] \tag{5.2.1}$$

Using that the critical current density (J_c) of a superconductor is proportional to the product of the superconducting gap (Δ) and the local density of superconducting electrons (N_s): $J_c \sim N_s\Delta$, combined with the definition of the order parameter, $N_s \sim \Delta^2$, we can write: $J_c \sim N_s^{3/2}$. From this equation, we derive an analytical expression to relate the critical current and the electronic temperature T_e in a broad range of temperatures:

$$I_c(T_e) = a\left[1 - \left(\frac{T_e}{b}\right)^4\right]^{3/2} \tag{5.2.2}$$

Here a is the fitting parameter that estimates $I_c(T_e = 0)$ and b is the fitting parameter that estimates T_c. Reverting Eq. 5.2.2 we obtain an analytical expression relating T_e and P_L:

$$T_e(P_L) = b\left[1 - \left(\frac{I_c(P_L)}{a}\right)^{\frac{2}{3}}\right]^{\frac{1}{4}} \tag{5.2.3}$$

By inserting the measured $I_c(P_L)$ into Eq. 5.2.3, we obtain the electronic temperature, T_e induced by a specific laser power, P_L. As the critical current strongly depends on temperature, when calibrating the thermometer at different bath temperatures (T_b), we express the critical current as: $I_c(P_L) = \Delta I_c(P_L) + I_c(T_b)$. Here, $I_c(T_b)$ represents the critical current extracted from Eq. 5.2.2 at a certain T_b. Since I_c remains constant at the lowest powers, we define $\Delta I_c(P_L)$ as the variation of I_c from the average at low powers:

$\Delta I_c(P_L) = I_c(P_L) - \langle I_c \rangle_{lowP}$. Finally, we obtain the thermometer calibration from the formula:

$$T_e(P_L) = b\left[1 - \left(\frac{\Delta I_c(P_L) + I_c(T_b)}{a}\right)^{\frac{2}{3}}\right]^{\frac{1}{4}} \tag{5.2.4}$$

Similarly, as T_e is constant for the lower powers, we extract the increase in the electronic temperature ΔT_e by subtracting the average at low powers: $\Delta T_e(P_L) = T_e(P_L) - \langle T_e \rangle_{lowP}$.

5.2.3 Extraction of the thermal conductance in the superconducting state

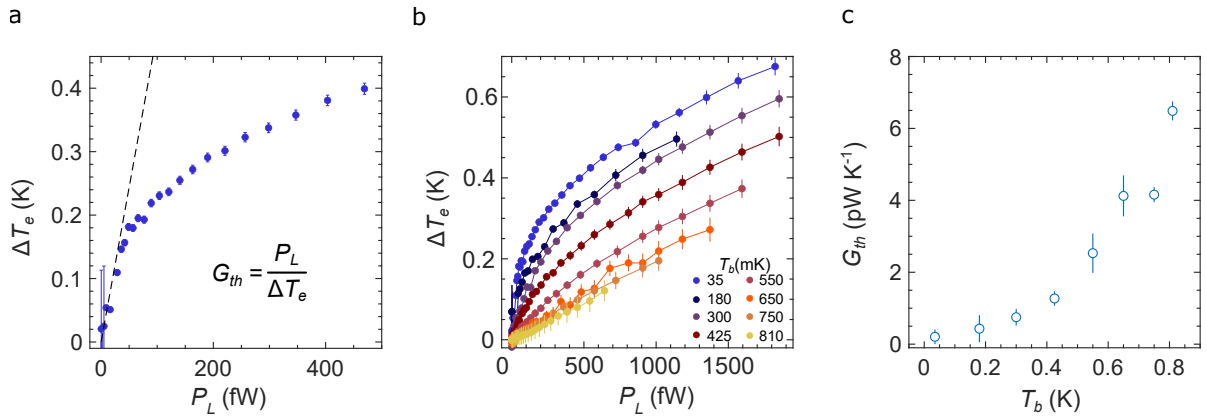

Figure 5.2.2: Extraction of thermal conductance from the bolometric response. **(a)** Increase of electronic temperature, ΔT_e vs. P_L for $T_b = 35$ mK. The black dashed line is a linear fit in the linear approximation regime, $\Delta T_e/T_b < 1$. From the fit, we extract $G_{th} = P_L/\Delta T_e$. **(b)** ΔT_e vs. P_L measured at different bath temperatures, T_b ranging from 35 to 810 mK. **(c)** Performing linear fits for all the bath temperatures in the low heating regime, we extract the thermal conductance in the superconducting state. **(b)** and **(c)** are adapted from [P2].

Having derived in Eq. 5.2.4 an analytical expression which relates the electronic temperature with the measured change in critical current, we can extract ΔT_e versus P_L for the MATBG superconductor, as shown in Fig. 5.2.2a. We observe that for low powers, ΔT_e increases linearly before saturating at higher P_L. From the bolometric response, we can experimentally determine the electronic thermal conductance, G_{th}. For low heating powers and small ΔT_e such that $\Delta T_e/T_b < 1$, the linear response regime holds and we can define the electronic thermal conductance using the Fourier Law: $G_{th}(T_b) = P_L/\Delta T_e$ [174, 175]. Performing a linear fit at low heating power where the linear approximation is valid (black dashed line in Fig. 5.2.1a), we extract $G_{th} = 0.2$ pW/K for $T_b = 35$ mK. As G_{th} is a function of T_b, we measure ΔT_e vs. P_L at different T_b between 35 and 810 mK, which is the highest temperature at which we can extract I_c (Fig. 5.2.2b). From these

measurements, we can extract the temperature dependence of the thermal conductance in the superconducting state as reported in Fig. 5.2.2c.

We notice that for temperatures 35 mK $< T_b <$ 810 mK, G_{th} ranges from 0.2 pW/K to 7 pW/K. Therefore, a minute laser power of 0.2 pW applied in the steady state, increases the electronic temperature of MATBG by 1 K (at $T_b = 35$ mK). These low numbers indicate an excellent thermal isolation of MATBG electrons from the thermal bath and reveals the high sensitivity of the MATBG detector [P2]. In addition, the extraction of G_{th}, is independent on the cooling mechanism (electron diffusion or phonons) and does not assume any microscopic model to describe the cooling of the electrons. The fact that we operate at small heating powers allows us also to provide a considerably simplified model to describe the cooling mechanism in MATBG. Indeed, by restricting our experiment to the linear response regime, we can neglect, to the first order, the spatial-temperature dependence of the thermal conductance when solving the differential equation that describes the thermal diffusion in MATBG, as discussed in section 5.3.2.

5.3 Thermal conductivity as a probe of superconducting gap structure

As anticipated in section 1.2.1, the order parameter of superconductors can exhibit various symmetries. These symmetries range from the conventional s-wave to the more exotic p- or d-waves. Specifically, s-wave superconductors feature an isotropic superconducting gap, while p- or d-wave superconductors exhibit nodes in their gap function. Heat transport is a powerful probe of the superconducting gap structure[52, 53]. While superconductors allow charge flow without dissipation, they are extremely poor heat conductors. As anticipated in section 1.2.1, in a superconductor, the quasiparticles thermally excited above the superconducting gap carry heat, whereas the Cooper pairs forming the condensate do not. Consequently, the temperature activation behavior of the thermal conductivity in the superconducting state, $\kappa(T)$ strongly depends on the gap symmetry. For low enough temperatures, well below the critical temperature ($T << T_c$), the thermal conductivity in an s-wave superconductor is exponentially suppressed compared to the normal state because of the isotropic symmetry of the superconducting gap. In contrast, nodal p- and d-wave superconductors exhibit a power-law temperature dependence as the presence of nodes in their gap structure allows thermal excitations even for $T << T_c$. In the case of nodal superconductors, the thermal conductivity also shows residual terms at zero temperature given to impurity scattering that broadens the nodes and produces a residual density of states at zero energy[52].

Given the novelty of the material, the investigation of the MATBG's order parameter is still under lively debate[164, 176–178]. In our study, we theoretically model the contribution of electron diffusion to the thermal conductance to infer information on the symmetry of the superconducting gap. In this model, based on a simplified device geometry, the heat diffusion is dominated by the quasiparticles thermally excited above the superconducting gap[P2]. In the following section, we perform an analytical calculation of the thermal conductance for a simple device geometry 5.3.1. The simple model we solve analytically captures the basic physics of the problem. Then, we describe the actual model used to fit our experimental data, in which we consider a Hall bar geometry and calculate the thermal conductance for both isotropic and nodal superconducting gap.

5.3.1 Analytical solution of the heat transfer equation for a simple geometry

We start considering a two-dimensional electron gas connected with two electrodes in which uniform heating with power P is applied (Fig. 5.3.1a), for instance by an external laser source. In this simplified scheme, the electrodes are anchored at the base temperature T_0, acting as a thermal reservoir and a thermal gradient is generated across the sample by the applied heating. The heat can be dissipated through two primary channels: electronic diffusion (G_{diff}) and electron-phonon coupling (G_{e-ph}), as schematically illustrated in Fig.

5.3.1c. The spatial distribution of the electronic temperature can be calculated according to the two-dimensional heat transfer differential equation[179]:

$$p = -\nabla \cdot (\kappa_{diff} \nabla T_e(x,y)) - \Sigma_{e-ph}(T_e^{\delta} - T_0^{\delta}) \tag{5.3.1}$$

Where p is the applied heating per unit volume, Σ_{e-ph} and δ are the electron-phonon coupling constant and temperature power law constant, respectively, and $T_e(x,y)$ is the elevated electron temperature at position (x,y) of the sample from the base temperature T_0. κ_{diff} is the thermal conductivity according to the electronic diffusion. At low enough temperatures (the electron-phonon coupling scales as power law), we only consider the experimental conditions in which the heat transfer by the electron diffusion is much larger than the electron-phonon coupling contribution[180]. For a typical metal the electronic contribution of thermal conductivity due to diffusion is given by the Wiedemann-Franz law and can be expressed as: $\kappa_{diff} = \kappa_{WF} = \mathcal{L}T\sigma$, where $\mathcal{L}$ is the Lorenz number [175, 179].

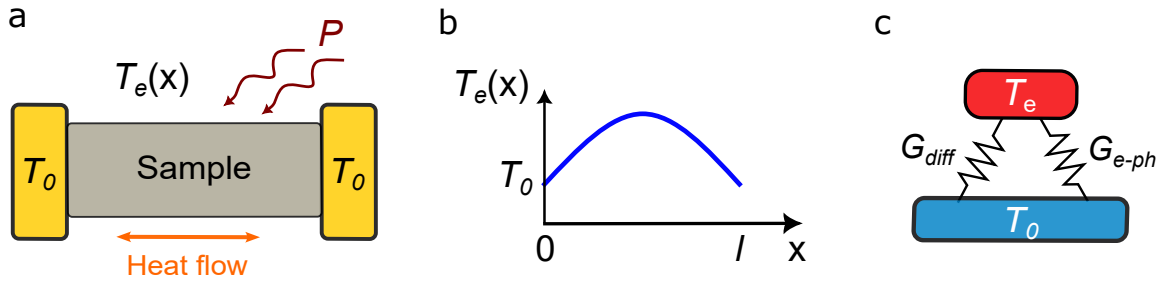

Figure 5.3.1: Heat equation for a simple sample geometry. **(a)** Schematics of a two-terminal geometry in which a sample is connected with two electrodes anchored at base temperature T_0 and uniform heating P is applied. **(b)** Sketch of the temperature profile $T_e(x)$ calculated analytically from the two-dimensional heat equation. **(c)** According to the thermal model heat from the electrons can flow out through two different channels: electronic diffusion to the electrodes (G_{diff}) and electron-phonon coupling (G_{e-ph}).

Neglecting the electron-phonon coupling contribution and considering the one-dimensional case, the heat diffusion equation can be simplified as[180]:

$$P = -\frac{\mathcal{L}}{2R} l^2 \frac{d^2}{dx^2} T_e^2(x) \tag{5.3.2}$$

where R and l are the electrical resistance and distance between the two terminals, respectively, and P is the total heating applied on the two terminal device. We can now formulate the boundary conditions needed to solve the differential equation. Since in our model, we consider that the metallic contacts are thermalized at the bath temperature, we can write: $T_e(x=0) = T_e(x=l) = T_0$. In this geometry, the heat flows from the middle of the sample to the contacts, which act as thermal reservoirs: $\frac{dT_e}{dx}|_{x=l/2} = 0$. By solving analytically 5.3.2 we get an expression for $T_e(x)$:

$$T_e(x) = \sqrt{-\frac{PR}{\mathcal{L}}\left(\frac{x}{l}\right)^2 + \frac{PR}{\mathcal{L}}\left(\frac{x}{l}\right) + T_0^2} \cong T_0 + \frac{1}{2}\frac{PR}{\mathcal{L}T_0}\left(\frac{x}{l} - \frac{x^2}{l^2}\right) \tag{5.3.3}$$

Here the approximation in Eq. 5.3.3 is done considering the linear regime of small temperature increases: $\Delta T_e = T_e(x) - T_0 << T_0$. The temperature profile derived in Eq. 5.3.3 and sketched in Fig. 5.3.1b shows that the electronic temperature peaks at the center of the sample and decays to the two metallic contacts, because of the uniform heat provided.

In steady-state experiments we typically measure the average electronic temperature $\langle T_e \rangle = \frac{\int_0^l dx T_e(x)}{\int_0^l dx}$ across the sample, from which:

$$\langle T_e \rangle = T_0 + \frac{1}{12}\frac{PR}{\mathcal{L}T_0} \tag{5.3.4}$$

Defining $\Delta T_e = \langle T_e \rangle - T_0$ and using the expression for the thermal conductance in the linear response regime, $G_{th} = \frac{P}{\Delta T_e}$, we get:

$$G_{th} = \frac{1}{12}\frac{\mathcal{L}T_0}{R} = \alpha \kappa_{diff} \tag{5.3.5}$$

Where α is a numerical prefactor is due to the integration of the temperature profiles across the sample. For this simple sample geometry, we obtain $\alpha = 12$ (as reported in ref. [175, 179, 180]). κ_{diff} is the electronic diffusion to the thermal conductivity, which is described by the Wiedemann-Franz law for the simple metal we are considering.

To extend this model to our experiment, we need to estimate α for our specific geometry (Hall bar) and κ_{diff} for the MATBG superconductor. Specifically, we calculate the $\kappa_{diff}(T)$ for an isotropic, s-wave gap and for a nodal gap, in the scenario that the thermal conductance is dominated by the electron diffusion of the quasiparticles excited above the superconducting gap and that the electron-phonon contribution is negligible ($G_{e-ph} \ll G_{diff}$).

5.3.2 Simplified model of the MATBG superconducting channel

In the previous section, we solved analytically the one-dimensional heat transfer equation and extracted the thermal conductance assuming that electronic diffusion (Wiedemann-Franz law) constitutes the primary channel of heat dissipation. Here, we briefly describe the heat transfer equation, considering a geometry similar to the one used in our experiment.

The optical image of the device is shown in Fig. 5.3.2a. Based on this image, we model heat diffusion in the measured region using a geometry closely resembling the sample (Fig. 5.3.2b). The model consists of a channel (made of superconducting MATBG) with length L and width W. The channel is surrounded by four metallic leads: two on the upper side

and two on the lower side of the Hall bar. The Hall bar is composed of gold electrodes and MATBG arms, which are gated close to charge neutrality in a metallic state (Fig. 5.3.2a). The distance between the centers of two consecutive metallic leads is denoted as d_c, and they all have the same width w_c. The entire device is illuminated by laser light, and the injected power into the channel is P. Analogously to section 5.3.1, we consider the two-dimensional heat equation for electronic diffusion [P2]:

$$\kappa_{diff}\nabla^2\delta T_e(x,y) + \frac{P}{WL} = 0 \tag{5.3.6}$$

where κ_{diff} represents the thermal conductivity of MATBG, and $\delta T_e(x,y) = T_e(x,y) - T_b$ represents the temperature increase of the channel relative to the temperature of the bath (T_b). In Eq. 5.3.6, we neglect the spatial-temperature dependence of thermal conductivity. This approximation is valid at the first order because the thermal conductance is experimentally extracted at low heating powers, satisfying the condition $\frac{\Delta T_e}{T_b} < 1$. Consequently, the local temperature variation $\delta T_e(x,y)$ can be considered smaller than the equilibrium value T_b [P2].

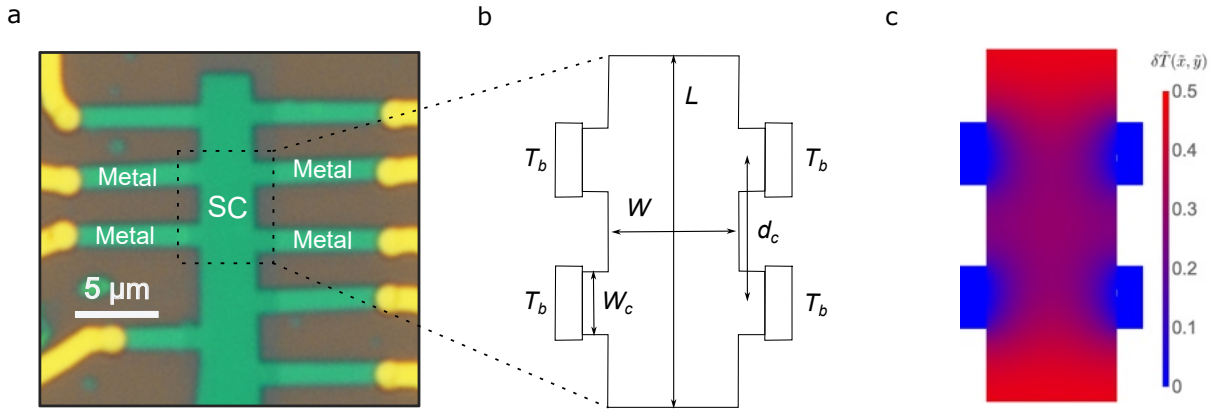

Figure 5.3.2: Simulation of the heat diffusion equation on the Hall bar geometry. **(a)** Optical image of the measured MATBG device. The middle channel is gated in the superconducting state, while the arms of the device are gated in a metallic region. **(b)** Simplified geometry used to model the heat diffusion. Since the arms are gated in a metallic state they act as a "cooling fin" for the superconductor [77]. We fix the MATBG arms and electrodes at $T_b = 35$ mK. **(c)** Eq. 5.3.6 solved on the geometry in **(b)**. The temperature raise $\delta\tilde{T}(\tilde{x},\tilde{y})$ is given in units of $PW/(\kappa_{diff}L)$. The simulation shown in **(c)** was performed by Prof. Dr. Alessandro Principi [P2].

Given this equation we define appropriate boundary conditions [P2]:

- Since the metallic leads are situated along the left or right side of the Hall bar, we assume that no heat current flows through either the upper and lower edges

$\left.\frac{\partial \delta T_e}{\partial y}\right|_{y=\pm L/2} = 0$. Conversely, a heat current flows through the metallic leads.

- The second boundary condition assumes that, given the small heating the gold electrodes and MATBG arms are thermalized at the bath temperature T_b. Indeed, considering the laser intensities for which the condition $\frac{\Delta T_e}{T_b} < 1$, (approximately 10^{-4} W/m^2), we estimate a temperature increase of approximately 10^{-8} mK for the gold electrodes at $T_b = 35$ mK (the area close to the arms is ~ 2 µm^2 and $G^{Au}_{WF} = \frac{\mathcal{L}T}{R^{Au}} \sim T \times 1.1 \cdot 10^{-4}$ W K^{-2} where $R^{Au} \sim 2.2\ 10^{-4}\ \Omega$ is estimated from ref. [181]). Regarding the arms (which are gated in the normal metallic state), we model them based on the idea that they can act as a "cooling fin" for the superconductor, as demonstrated in ref. [77]. The cooling is efficient because the hot quasiparticles in the superconductor could diffuse into the normal conductor but not in the reverse direction because of the superconducting gap. This allows us to set the boundary condition of unidirectional heat flow and fix the temperature of the arms to be at the base temperature: $\delta T_e(\pm W/2, y) = 0$.

To perform the numerical calculation, we introduce dimensionless quantities. We rescale lengths with W, temperatures with $PW/(\kappa_{diff} L)$, and heat currents with P/L. The parameters used in the simulation are: $d_c = 1.1\ W$, $L = 2.7\ W$, $w_c = 0.5\ W$ and $W = 3.7$ µm. The numerical solution of the heat diffusion equation on the geometry described above is shown in Fig. 5.3.2c. Similarly to the previous section, we define the channel thermal conductance as $G_{th} = \mathcal{N}\kappa_{diff} d_c/W$, where the dimensionless numerical factor $\mathcal{N}$:

$$\mathcal{N}^{-1} = \frac{\kappa_{diff} L}{P d_c^3} \int_{-\frac{d_c}{2}}^{\frac{d_c}{2}} dy \int_{-\frac{W}{2}}^{\frac{W}{2}} dx\, \delta T_e(x, y) \tag{5.3.7}$$

Importantly, we verify that Eq. 5.3.2 reproduces the result derived in section 5.3.1 $\mathcal{N}$=12, for a channel of length d_c and width W in contact with two thermal baths at positions $y = \pm d_c/2$, and no current flowing through other edges [180]. Calculating Eq. 5.3.2 for our specific geometry we obtain $\mathcal{N} \approx 5.2$. As anticipated above, the two geometries (in Fig. 5.3.1 and in Fig. 5.3.2) differ only for a scale factor (~ 2) in the calculation, which does not substantially change the model. Similarly to Fig. 5.3.1, the heated electrons diffuse from the center of the sample to the metallic leads which constituted the thermal bath.

Having calculated the geometrical factor for our Hall bar geometry, we can estimate the temperature dependence of the thermal conductance considering the two different superconducting gap symmetries. The theoretical calculations are detailed in the supplementary information of ref. [P2] and were performed by Prof. Dr. Alessandro Principi. Here, we only report the final expression obtained for the quasiparticle thermal conductivity κ_{diff}:

$$\kappa_{diff}(\Delta(T), T) = \frac{e^2}{\rho} \frac{D^2(\Delta(T), T)}{I(\Delta(T), T)} \tag{5.3.8}$$

where $D^2(\Delta(T),T)$ and $I(\Delta(T),T)$ are two integrals dependent on the superconducting gap Δ defined as:

$$D(\Delta(T),T) = \int_0^\infty d\xi \int \frac{d\phi_k}{2\pi} \left[4k_B T \cosh^2\left(\frac{\sqrt{\xi^2+\Delta_k^2}}{2k_B T} \right) \right]^{-1} \left(\frac{\xi^2+\Delta_k^2}{T} - \Delta_k \frac{\partial \Delta_k}{\partial T} \right) \tag{5.3.9}$$

and:

$$I(\Delta(T),T) \approx \frac{1}{2} \int_0^\infty d\xi \int \frac{d\phi_k}{2\pi} \left[4k_B T \cosh^2\left(\frac{\sqrt{\xi^2+\Delta_k^2}}{2k_B T} \right) \right]^{-1} \left(\frac{\xi^2+\Delta_k^2}{T} - \Delta_k \frac{\partial \Delta_k}{\partial T} \right) \frac{\xi}{\sqrt{\xi^2+\Delta_k^2}} \tag{5.3.10}$$

Finally, the expression for the thermal conductance considering the electron diffusion of thermally excited quasiparticles reads:

$$G_{th}(\Delta(T),T) = \mathcal{N} \frac{e^2}{\rho} \frac{d_c}{W} \frac{D^2(\Delta(T),T)}{I(\Delta(T),T)} \tag{5.3.11}$$

5.3.3 Comparison with the experimental results

We finally compare the model described above with the experimental data. Fig. 5.3.3b shows the fit of the modeled $G_{th}(T_b)$ for isotropic and nodal superconducting gaps to the experimentally measured thermal conductance. Here, the size of the superconducting gap Δ_0 is the only fitting parameter, while we fix $T_c = 2.1$ K and normal state resistivity $\rho = 15$ kΩ from independent measurements [P2]. As expected, the two different gap symmetries lead to significantly different heat diffusion for the limit of $T_e \ll T_c$. Specifically, for $T_b < 0.8$ K, the thermal conductance modeled for an isotropic superconductor is exponentially suppressed. Conversely, the thermal conductance modeled for a nodal superconductor decays with a power-law dependence. Comparing the model and experiment in Fig. 5.3.3b, we observe that our measurements are incompatible with an exponential temperature activation behavior, and that the power-law dependence provides a much better fit to the experimental data. The best fit for the isotropic case gives $\Delta_0 \sim 0.33 \pm 0.05$ meV, while for the nodal case, we obtain $\Delta_0 \sim 0.47 \pm 0.07$ meV. Notably, the value extracted for Δ_0 is in agreement with the measurements on the gap size of MATBG performed with Scanning Tunneling Microscopy (STM) [164]. This quantitative agreement with STM measurements confirms the soundness of the theoretical model and strengthens the validity of the assumptions made to reach this result. In the hypothetical scenario where the contribution to the thermal conductance is dominated by electron diffusion of quasiparticles thermally excited above the superconducting gap, our results suggest that the obtained $G_{th}(T_b)$ aligns more closely with a nodal p- or d-wave symmetry rather than an isotropic s-wave symmetry [P2].

As previously mentioned, this model is conceived with the assumption that electron diffusion plays a more dominant role in thermal conductance than electron-phonon scattering.

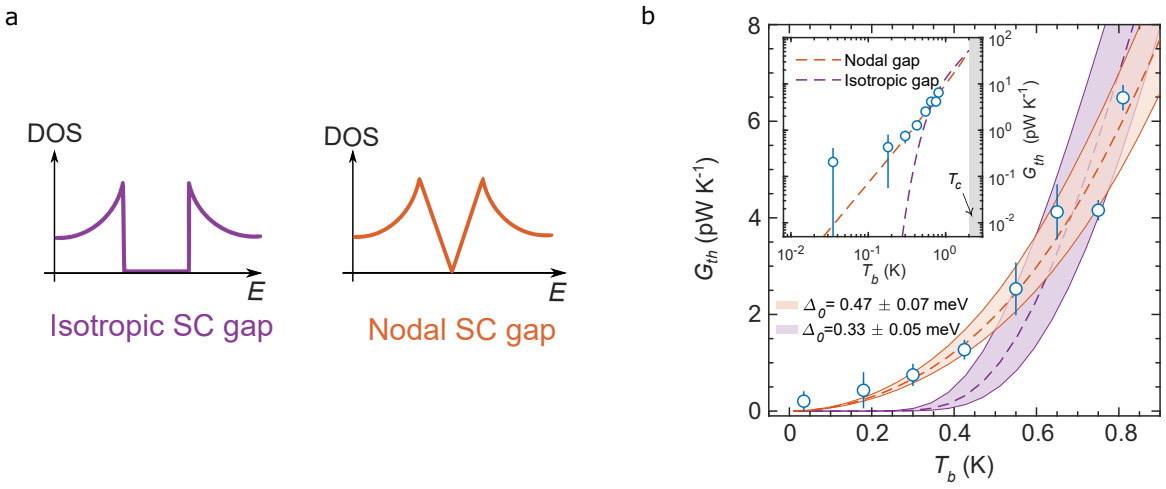

Figure 5.3.3: Fit of the experimental thermal conductance. **(a)** Sketch of the density of states (DOS) for an isotropic s-wave superconducting gap (violet) and for a nodal, V-shape superconducting gap (orange). **(b)** G_{th} vs. T measured in the superconducting state. The dashed lines with the shaded regions are the best fit with errorbar to the experimental data. By fixing fix $T_c = 2.1$ K and $\rho = 15$ kΩ we extract from the fit $\Delta_0 \sim 0.33 \pm 0.05$ meV (for the isotropic gap) and $\Delta_0 \sim 0.47 \pm 0.07$ meV (for the nodal gap). Here G_{th} is modeled considering electron diffusion for the two different superconducting gap symmetries. In the inset the same data and fit are plotted in logarithmic scale. Adapted from [P2].

As discussed in section 4.1.3, in metals the electron-phonon cooling mechanism typically scales as a high-order power law with temperature ($\sim T^{\delta}$). In contrast, the electron diffusion mechanism scales linearly ($\sim T$) and dominates at low temperatures. Notably, the crossover temperature in graphene occurs around 1 K [175]. Given that our experiments are conducted at temperatures below 1 K, we can draw an analogy to graphene and argue that this assumption is also valid for MATBG. However, no studies so far have deeply investigated electron-phonon interactions in MATBG at such low temperatures. Recent reports utilizing time- and frequency-resolved photovoltage measurements have demonstrated that the electron-phonon scattering in MATBG is substantially different from that in graphene, possibly because of the combined effect of low-energy moiré phonons and a reduced superlattice Brillouin zone [182]. An additional factor that complicates the interpretation of the thermal conductivity data is the local twist angle inhomogeneity intrinsic in MATBG samples [135]. This source of disorder can lead to the coexistence of regions in both the superconducting and the normal states, which could affect the dynamics of thermal quasiparticles. In summary, while our observations on the symmetry of the superconducting gap are not conclusive, we hope that our experimental results will inspire further theoretical investigations and new experiments to explore low-temperature thermal transport in MATBG.

5.4 Photovoltage generation by superconducting MATBG

Having verified the small values of MATBG's thermal conductance, we measure the photovoltage response of the superconducting state, to explore the possibility of using MATBG as an ultrasensitive photodetector. Specifically, we measure the differential photovoltage $V_{\rm ph}$ vs. I_{dc} as a function of absorbed laser power, as is shown in Fig. 5.4.1. To perform differential photovoltage experiments, we bias the laser diode with a sinusoidal current with frequency f_0. In this way, the applied AC current induces a sinusoidal modulation of the laser power (Fig. 5.4.1a). We then measure the photovoltage generated in the MATBG with a lock-in referenced at the frequency of the modulation f_0. We find that the photovoltage is minimum at $I_{dc} \sim 0$ and monotonically increases as I_{dc} approaches I_c. When the critical current is reached the photovoltage shows a pronounced maximum. Fig. 5.4.1c shows the power dependence of the voltage peaks $V_{\rm ph}^{\rm max} = V_{\rm ph}(I_c)$ taken at $T_b = 35$ mK. Its value is almost constant for the lowest powers, however as P_L is increased it follows a linear dependence, which indicates that the detector operates in a linear response regime. Performing a fit in the linear region we can extract the detector responsivity: $S = \frac{dV}{dP_L} = 4.2 \times 10^7$ V/W.

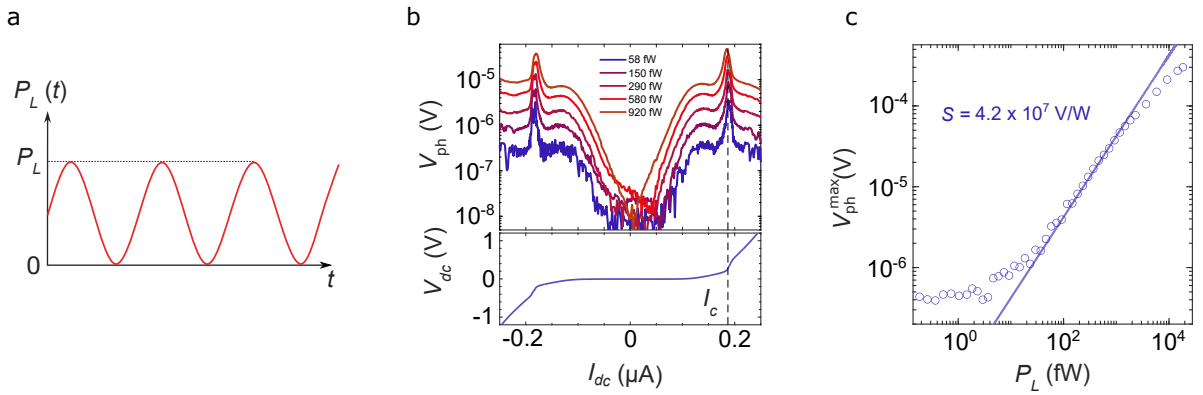

Figure 5.4.1: Photovoltage generation by superconducting MATBG. (a) Sinusoidal modulation of the laser power induced by the external current bias of the laser diode. **(b)** Top panel: differential photovoltage $V_{\rm ph}$ as a function of DC current bias (I_{dc}), measured at different laser powers. Bottom panel: Current-voltage characteristic I-V as a function of DC current bias (I_{dc}). $V_{\rm ph}$ shows pronounced peaks at the critical current. **(c)** Extracted photovoltage peaks $V_{\rm ph}^{\rm max}$ as a function of P_L. The blue line is a linear fit from which we extract the detector responsivity, $S = 4.2 \times 10^7$ V/W.

To investigate whether the differential photovoltage signal arises from a light-induced change in resistance (i.e. a bolometric effect), we calculate the photoresponse from the transport measurements of MATBG (Fig. 5.2.1b) and compare it with experimental data. Since the laser power oscillates with frequency f_0 between a maximum value (P_L) and

zero (as sketched in Fig. 5.4.1a), the generated photovoltage, V_{ph} can be approximated as the difference between the voltage at maximum power and the voltage at zero power: $V_{\mathrm{ph}}(P_L, I_{dc}) \approx V(P_L, I_{dc}) - V(P_L = 0, I_{dc})$. If the differential photovoltage signal is generated by a bolometric effect ($\Delta V = \Delta R \cdot I_{dc}$), we can rewrite:

$$V_{\mathrm{ph}}(P_L, I_{dc}) \approx V(P_L, I_{dc}) - V(P_L = 0, I_{dc}) \approx \left[\left. \frac{dV}{dI} \right|_{P_L, I_{dc}} - \left. \frac{dV}{dI} \right|_{P_L = 0, I_{dc}} \right] \cdot I_{dc} \qquad (5.4.1)$$

Using the $\frac{dV}{dI}$ traces measured as a function of I_{dc} for different powers (Fig. 5.2.1b), we can then use this expression to calculate the expected V_{ph}. In Fig. 5.4.2 we compare the measured V_{ph} with the calculated values obtained from Eq. 5.4.1. Even though there are slight discrepancies in the exact photovoltage values between measurements and calculations, the calculated traces reproduce well the overall behavior, in particular the monotonic increase of V_{ph} as I_{dc} approaches I_c and the peak at $I_{dc} \sim I_c$. The good agreement between the two suggests that the observed photovoltage generation is primarly due to a bolometric response of the MATBG superconducting state. As expected, the strongest photoresponse is observed close to the superconducting transition. Therefore, in the following chapter, where we aim to detect single photons, we bias our MATBG device close to the superconducting-to-normal state transition, where the device shows the highest responsivity.

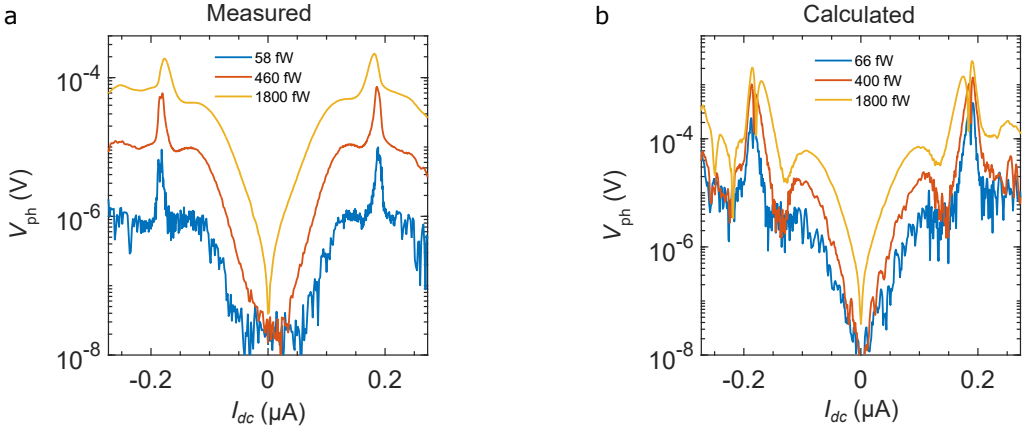

Figure 5.4.2: Comparison between the measured and calculated photovoltage. (a) Measured photovoltage traces V_{ph} as function of DC current bias I_{dc}, at three different laser powers. **(b)** Photovoltage traces calculated from the measured $\mathrm{d}V_{xx}/\mathrm{d}I(I_{dc})$ traces, assuming a bolometric effect (Eq. 5.4.1).

6

Detecting single near-infrared photons with superconducting MATBG

The work presented in this chapter led to the publication [P1]:
G. Di Battista, K.C. Fong, A. Díez-Carlón, K. Watanabe, T. Taniguchi, and D. K. Efetov, "Infrared single-photon detection with superconducting magic-angle twisted bilayer graphene", *Science Advances* **10**, eadp3725 (2024).
My contribution to this work was conceptualizing and designing the experiment, fabricating devices, measuring, analyzing data, and writing the manuscript.

In this chapter, we present the proof-of-concept experiment conducted to demonstrate near-infrared single-photon detection with superconducting MATBG. First, we discuss the importance of a hysteresis loop in the I-V characteristics for enabling SPD. Next, we detail the experimental circuit used to reset the detector and to obtain the photovoltage time traces observed. Following this section, we describe the measurements and analysis carried out to confirm single-photon sensitivity. Finally, in the last section, we perform a deeper analysis of the self-reset circuitry. This allows us to speculate on the microscopic mechanism leading to the photoresponse and suggest possible ways to improve the detector's performances.

6.1 Hysteretic *I-V* characteristics in MATBG superconductors

As discussed in Chapter 3, our group has developed a protocol to produce high-quality MATBG devices [P6], in which the intrinsic disorder due to the twist angle inhomogeneities is mitigated. Thanks to this fabrication protocol, we can produce MATBG devices featuring a switching behavior in the *I-V* characteristic, where the change in resistance from superconducting to normal state is approximately 10 kΩ. These attributes, combined with the thermal properties of MATBG, are crucial for photodetection applications [P1, P3].

The optical image (inset of Fig. 6.1.1b) shows a high-quality MATBG device. As explained in section 2.3, the van der Waals stack consists of two graphene sheets rotated at a global twist angle of approximately 1.1°, encapsulated within insulating hBN layers. By applying an external gate voltage to the metallic graphite gate underneath the heterostructure, we can control the carrier concentration in the MATBG layer. In Fig. 6.1.1, we plot the four-terminal transport characterization of a high-quality MATBG device with a twist angle $\theta = 1.04° \pm 0.02$. In Fig. 6.1.1a, the plot of the longitudinal resistance R_{xx} versus the moiré filling factor ν for temperatures ranging from $T = 50$ mK up to $T = 6$ K shows a pronounced superconducting state, which lies in proximity to the correlated insulating state at half-filling (ν = -2). In the bottom panel of Fig. 6.1.1a, we plot the R_{xx} vs. T trace measured at the optimal doping of ν = -2.45. From this, we extract a normal state resistance of approximately 10 kΩ and a critical temperature T_c of approximately 2.8 K.

At the same doping level, we measure the *I*–*V* characteristic of the superconducting state in a four-terminal current-biased scheme at $T = 35$ mK (Fig. 6.1.1b). Performing a linear fit of the slope in the *I-V* curves (Fig. 6.1.1c), we extract a normal state resistance for the MATBG film of $R_N = 17.8$ kΩ and a resistance right before the superconducting transition of $R_{SC} = 1.7$ kΩ. Therefore, the MATBG superconductor exhibits a large change in resistance (~ 16 kΩ) when transitioning from the superconducting to the normal state. We also observe a pronounced hysteresis loop when sweeping the direction of the bias current I_{bias}, characterized by $\Delta I = I_c - I_r \approx 15$ nA. Here, I_c and I_r are the switching and retrapping currents, respectively [P1]. Such hysteresis loops have already been observed in MATBG samples [127]. They are potentially due to a current-induced self-heating hotspot when the MATBG is in the normal state, similar to other superconductors [51, 183]. Specifically, sweeping the DC current across the superconducting state in a current-biased scheme results in minimal Joule heating dissipation across the sample ($P_J = I^2 R_{SC}$), leading to the largest switching current, I_c. Conversely, when sweeping the DC current across the normal state, non-zero Joule heating ($P_J = I^2 R_N$) increases the electronic temperature, causing a reduction in the current at which the system reverts to the superconducting state (retrapping current, I_r).

We have produced several MATBG superconducting devices for this experiment with the procedure described in Chapter 3. Among all the superconducting MATBG, we have measured 3 high-quality devices that featured sharp superconducting transitions with hys-

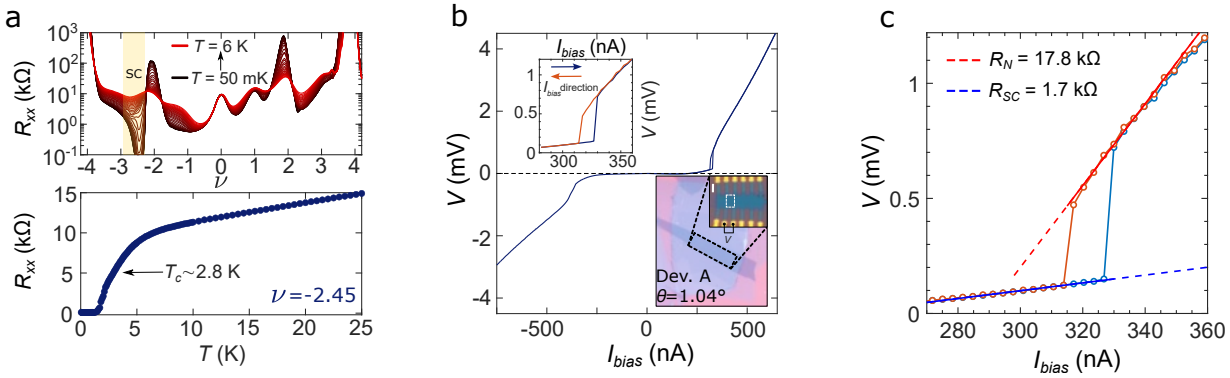

Figure 6.1.1: Transport characterization of high-quality superconducting MATBG devices. **(a)** Top panel: longitudinal resistance R_{xx} of a MATBG device, with twist angle θ = 1.04°, as a function of filling factor ν. The resistance traces are measured for temperatures ranging from 50 mK to 6 K. The device exhibits a pronounced superconducting state for -3 < ν < -2. Bottom panel: superconducting transition, R_{xx} vs. T measured at the optimal doping (ν = -2.45). **(b)** The current-biased *I-V* curve measured at the same doping (ν = -2.45) shows a hysteresis loop when sweeping direction of the bias current. In the top inset we plot a zoom *I-V* curve close to the transition, to highlight the hysteresis loop. The optical image of the MATBG device is in the bottom inset. Scale bar: 3 µm. **(c)** Zoom of the hysteresis loop in the *I-V* characteristic. The dashed lines are linear fits from which we extract the normal state resistance of MATBG R_N = 17.8 kΩ and the resistance in the superconducting state right before the transition R_{SC} = 1.7 kΩ. **(a)** and **(b)** are adapted from [P1].

teretic *I-V* characteristic. In Fig. 6.1.2, we show the optical images of devices A, B, and C as well as the *I-V* curves at different temperatures and gate voltages. Consitently for all the three devices, the hysteresis loop disappears when the temperature approaches 1 K. As visible from the optical image of Fig. 6.1.2, devices A and C have a single bottom graphite back-gate, while device B has an additional graphite top gate, which was picked up at the first step of the stacking process. The global twist angles measured from transport data for devices A, B, and C are $\theta = 1.04°$, $\theta = 1.03°$, and $\theta = 1.16°$, respectively [P1].

We argue that the presence of a hysteresis loop in the *I-V* characteristic is closely tied to the sample's homogeneity [P3]. In MATBG, intrinsic twist angle disorder leads to localized regions with different critical currents [135]. In highly disordered samples, numerous small areas become resistive at different critical currents, resulting in a smeared superconducting transition. Conversely, in highly homogeneous MATBG, where a significant portion of the device shares the same twist angle, the transition from superconducting to normal state occurs sharply at the same critical current, exhibiting a switching behavior with a significant resistance change (∼ 10 kΩ). In the presence of such switching behavior, we also observe the hysteresis loop in the *I-V* curves described above.

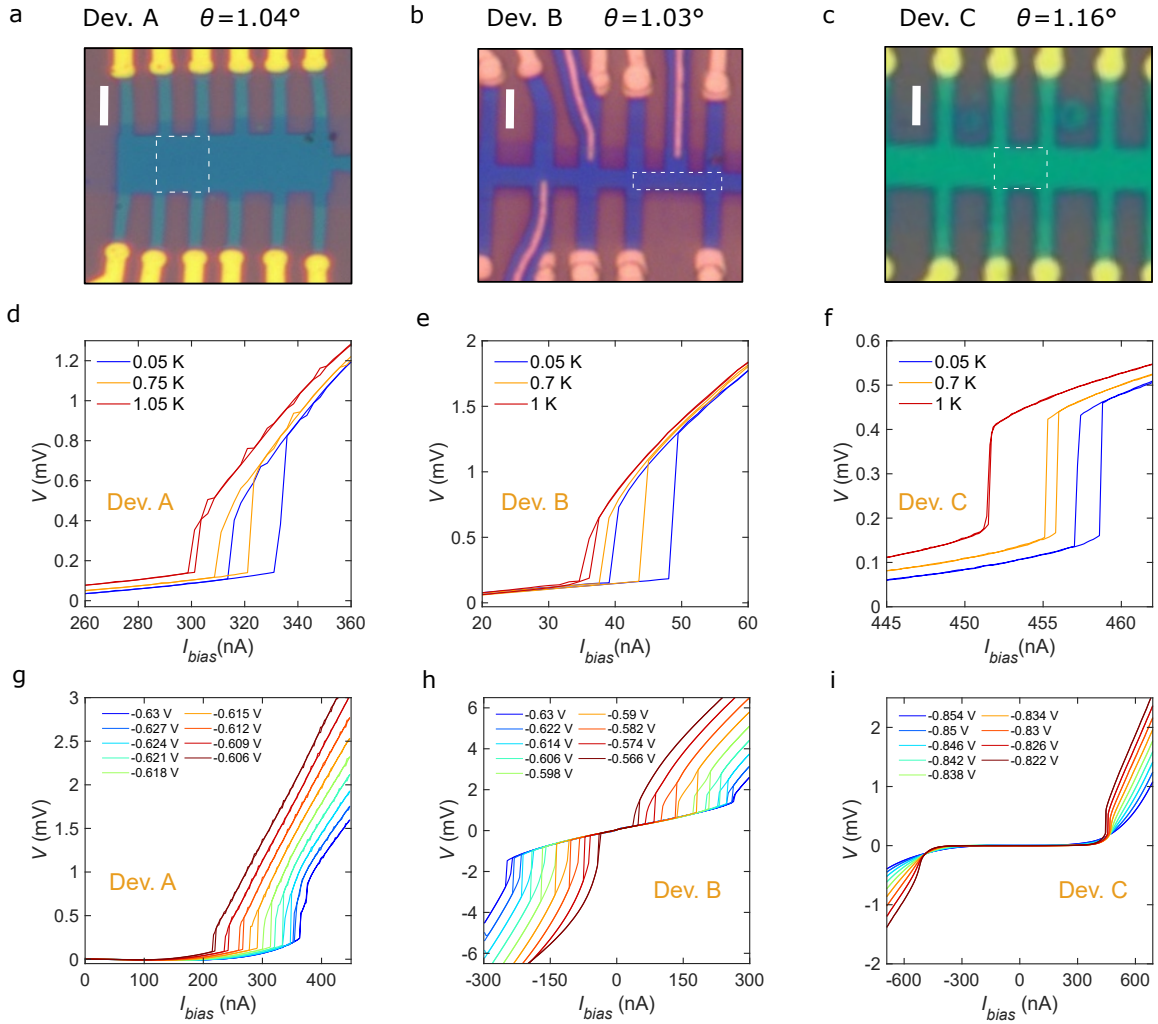

Figure 6.1.2: Current-biased *I-V* curves at different temperatures and gate voltages. (a)-(c) Optical images of the measured devices. The scale bar is 3 µm in all the images. Device A and C have a single bottom graphite back-gate, while device B has a double graphite gate. **(d)-(f)** Zoom of the hysteresis loop in the *I-V* characteristic, measured in a current-biased scheme at 3 different temperatures for devices A, B, and C. These measurements are performed at the same gate voltages used for the photodetection experiment: V_g =-0.620 V for device A, V_g =-0.566V for device B, and V_g =-0.8257 V for device C. Notably the observed hysteresis loops disappear when the temperature approaches 1 K, consistently for all the 3 devices. **(g)-(i)** *I-V* characteristic measured in a current-biased scheme at T = 35 mK for different gate voltages within the superconducting region for device A, B and C respectively. Adapted from [P1].

6.2 Photoresponse measurements

6.2.1 Implementation of the self-reset circuitry

The hysteresis in the I-V characteristic observed in the current-biased scheme is useful for enabling SPD. Similarly to SNSPDSs, the heating induced even by a single photon can generate a resistive hotspot that expands through Joule heating, triggering an avalanche effect and leading to the complete breaking of superconductivity across the whole device. This process gives rise to a large voltage output which can be easily measured. However, in a purely current-biased scheme, the detector would not be able to return to the superconducting state after photoabsorption due to the presence of a hysteresis loop in the I-V curve. When this phenomenon, known as "latching," occurs, the detector stabilizes in the resistive state and no longer detects photons[P1, 80]. To prevent "latching", and enable continuous detection of photons, we implement the self-reset circuitry sketched in Fig. 6.2.1a, b.

The circuit is constituted by a voltage divider with load resistor $R_2 \ll R_{res} + R_{MATBG}$. Here R_{res} is a residual resistance (arising from the contact resistance and the metallic leads) and R_{MATBG} is the 4-terminal resistance of the device's active region, sketched as a variable resistor[P1]. In this scheme, most of the current flows across the load resistor, I_2 and a small part of it through the device, I_d. The divider induces a voltage bias (V_{bias}) across the source and drain contacts of the MATBG. In this way, the increase of resistance ($\Delta R_{MATBG} \sim 16$ kΩ) induced by the transition of the MATBG detector into the normal state increases the current into the load resistor and reduces the current flowing in the detector, which in turn reduces the Joule heating[P1]. The reduction of I_d when the MATBG is in the normal state closes the hysteresis loop and allows the detector to return to the superconducting state after the detection event. We provide a detailed investigation of the reset circuit in section 6.4.1.

Fig. 6.2.1c plots the I-V curve measured in the voltage bias scheme as a function of the externally applied voltage V_0. As expected, the hysteresis loop present in the current-biased scheme is completely closed in the voltage-biased configuration (inset of Fig. 6.2.1c). We also measure the voltage applied by the divider (V_{bias}) across the source and drain contacts of MATBG (Fig. 6.2.1d). Importantly, V_{bias} is linearly proportional to V_0 even when the MATBG undergoes a phase transition from the superconducting to the normal state. This implies that the additional voltage introduced in the circuit by switching to the normal state ($\Delta R_{MATBG} \sim 16$ kΩ) is compensated by a reduction of the current flowing in the device. In Fig. 6.2.2, we plot the I-V curves of devices A, B, and C measured in the current-biased scheme (top) and in the voltage-biased scheme (bottom).

6.2.2 Photovoltage time traces

Having implemented the self-reset circuitry, we can bias our device near the normal-superconductor transition to enable SPD. When the Cooper pairs break upon photon absorption, they produce a voltage output. As discussed in section 6.2.1, after detecting

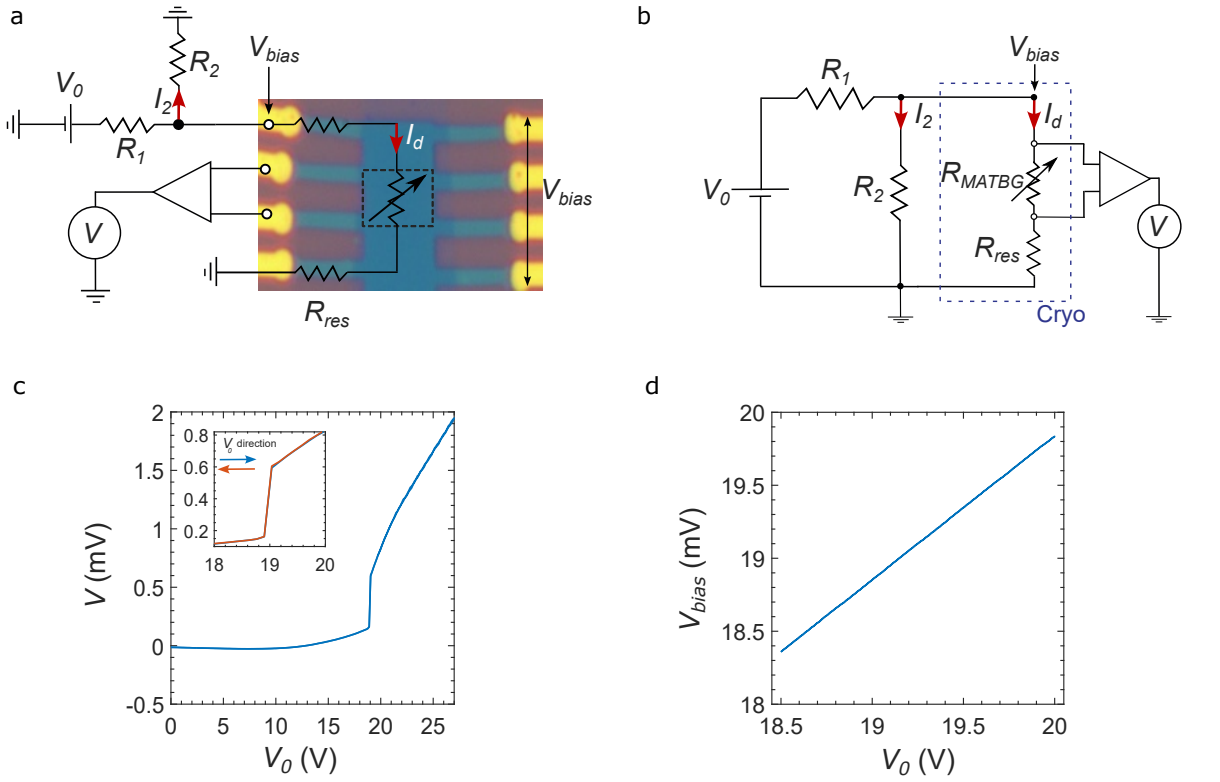

Figure 6.2.1: Implementation of the voltage-bias circuit. (a)-(b) Simplified circuit diagram used to measure the I-V characteristic in a voltage-biased scheme. The voltage divider ($R_1 = 1$ MΩ, $R_2 = 1$ kΩ for device A) provides a voltage bias (V_{bias}) across the source and drain contacts of the MATBG device, which is depicted as a variable resistor. $R_{res} \sim 54.5$ kΩ is the residual resistance (arising from the contact resistance and the metallic leads). In this scheme, most of the current flows across the load resistor, I_2, and a small portion of it through the device, I_d. The MATBG resistance increase induced by the transition in the normal state increases I_2 and simultaneously reduces I_d, suppressing the Joule heating. **(c)** I-V curve measured in the voltage bias scheme as a function of the externally applied voltage V_0. The reduction of I_d when the MATBG is in the normal state closes the hysteresis loop present in the current-biased I-V characteristic. **(d)** Measurement of the voltage applied by the divider (V_{bias}) across the source and drain contacts of MATBG. V_{bias} is linearly proportional to V_0 even when the MATBG undergoes a phase transition from the superconducting to the normal state, indicating that the additional voltage introduced in the circuit by the switching to the normal state is compensated by a reduction of I_d.

a photon, the self-reset circuitry reduces the current flowing in the detector and prevents "latching" into the normal state. The photovoltage time traces, $V_{\mathrm{ph}}(t)$ are recorded by connecting the voltage probes, in the 4-terminal scheme, to a room-temperature low-noise amplifier, as illustrated in Fig. 6.2.3. The voltage output is then fed to an oscilloscope or an analog-to-digital converter, which measures the voltage over time induced by the

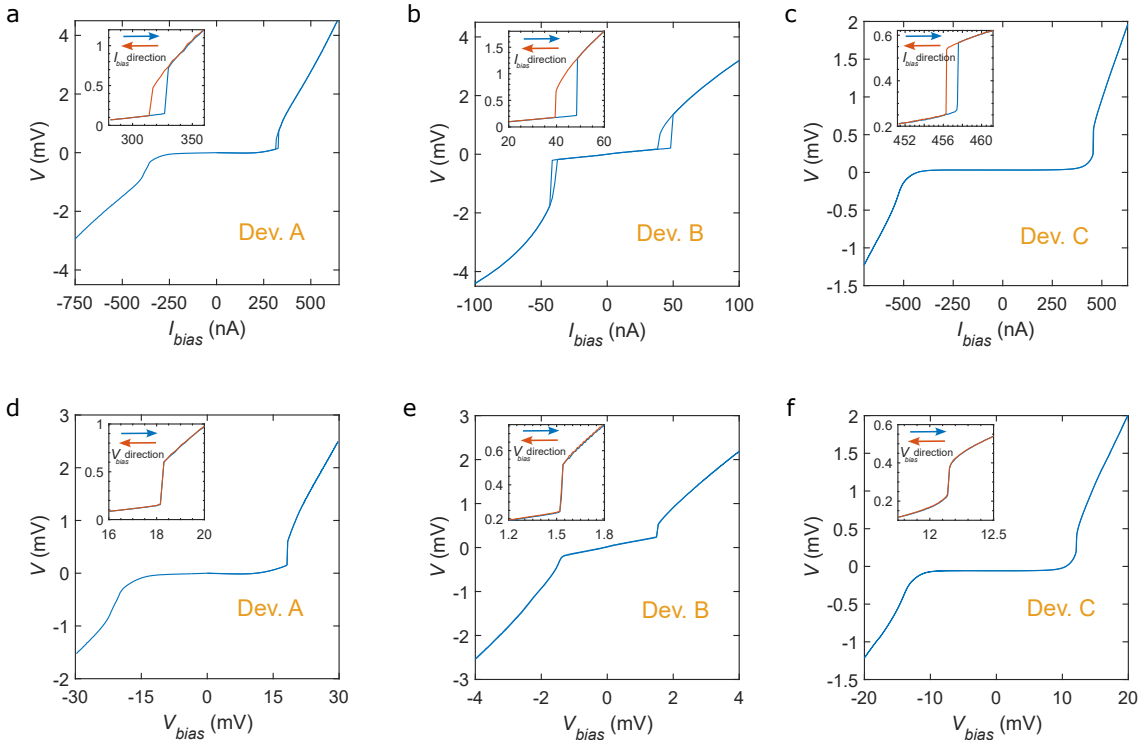

Figure 6.2.2: Current-biased and voltage-biased *I-V* curves. **(a)-(c)** *I-V* curves measured for device A, B and C in a current-biased scheme. The DC bias current is provided by a voltage source in series with a 10 MΩ resistor. The curves are measured at the same gate voltages used for photodetection: V_g =-0.620 V for device A, V_g =-0.566V for device B, and V_g =-0.8257 V for device C. **(d)-(f)** *I-V* curves measured for device A, B and C in a voltage-biased scheme, at the same doping. The bias voltage is provided by a voltage source in series with a 1/1000 voltage divider. The load resistor is much smaller than the residual resistance ($R_2 << R_{res}$). The specific values are: $R_1 = 1$ MΩ, $R_2 = 1$ kΩ for device A and B, $R_1 = 100$ kΩ, $R_2 = 100$ Ω for device C. Adapted from [P1].

photons. The experiment works as follows: the MATBG turns resistive upon photon absorption, we record a spike in photovoltage (V_{ph}), and ultimately the detector resets itself. This setup allows us to study the photon counting statistics and explore it under different bias voltages, laser powers, and temperatures.

The first interesting observation comes from analyzing the click heights. By overlaying the average click height as a function of the bias voltage, V_{bias} (top inset in Fig. 6.2.3c), we find that the photovoltage generated by the absorbed photon equals the normal state voltage, when the whole device has transitioned into the normal state. This occurs for all explored V_{bias}: $V_{\mathrm{ph}}(V_{bias}) \approx V(V_{bias})$. This observation indicates that the incident photons induce a complete transition of the MATBG detector from its superconducting state to the normal state [P1], confirming the idea that the absorbed photon induces an avalanche effect

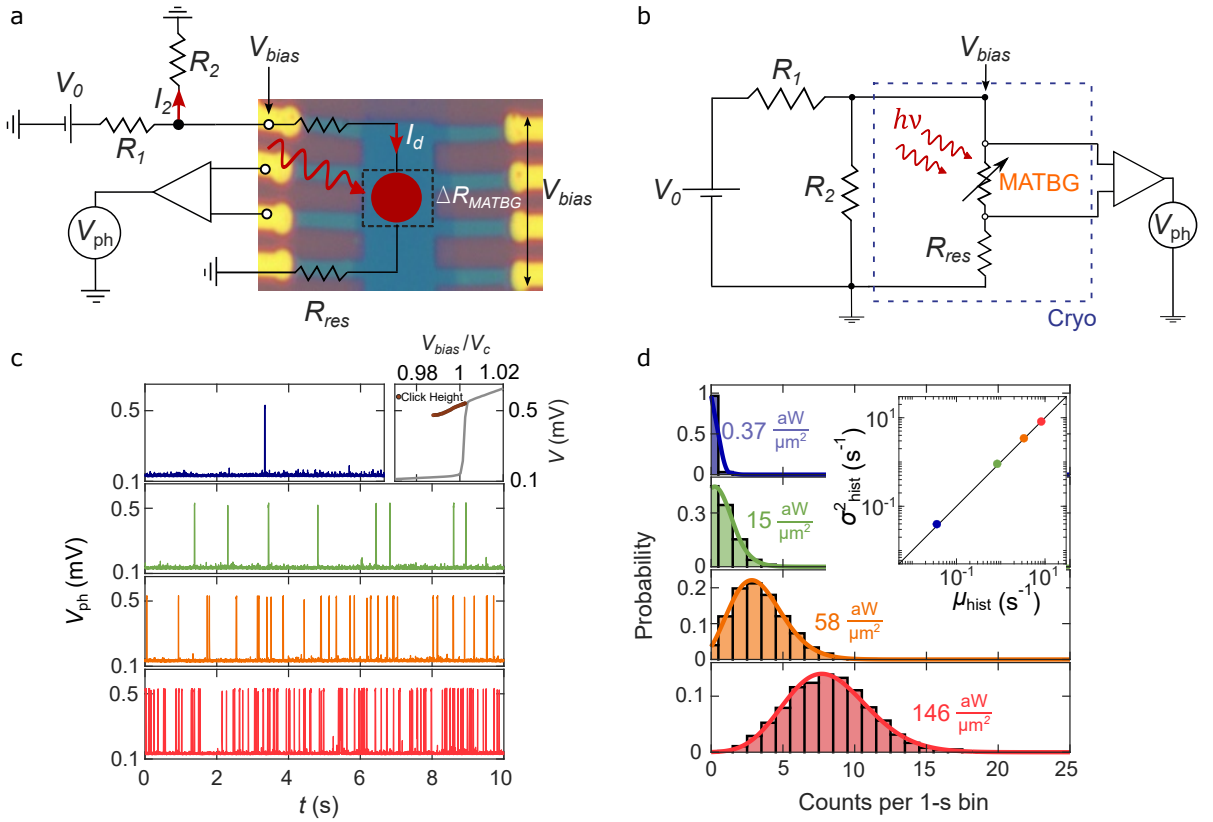

Figure 6.2.3: Photovoltage time-traces recorded with the self-reset circuitry. (a)-(b) Simplified circuit diagram used to measure the photoresponse of the MATBG detector, analogous to the one in Fig. 6.2.1. The incident photons break superconductivity across a $\sim$ 16 μm^2 device, inducing photovoltage ($V_{\rm ph}$) spikes in the MATBG detector. These spikes are recorded using an oscilloscope or an analog-to-digital converter.**(c)** Raw photovoltage time traces, $V_{\rm ph}(t)$, measured at increasing laser powers for $\lambda = 1550$ nm. In the top right inset, the average click heights vs. V_{bias} are overlaid on the I-V curve, measured in the configuration described in **(a)** and **(b)**.**(d)** Histograms of counts using 1-s time bins for the same laser powers as in **(c)**. The traces are measured over $\sim 10^3$ seconds. The extracted variance of counts, σ^2_{hist}, equals the mean, μ_{hist}, for all explored laser powers, as expected from photon shot noise. The solid lines overlaid on the histograms are the Poisson distribution with the extracted μ_{hist} and σ^2_{hist}, confirming agreement with the photon counting statistics.Adapted from [P1]

leading to a complete breaking of superconductivity across the entire $\sim$ 16 μm^2 device.

Fig. 6.2.3c presents the photovoltage traces $V_{\rm ph}(t)$, recorded over time across the MATBG detector when exposed to laser beam radiation, as described in Fig. 6.2.3a. We observe that the voltage spikes increase with the incident laser power. In section 1.1, we demonstrated that the photon counting statistic follows the Poisson distribution. Consequently, if the detected voltage spikes, or 'clicks', originate from photons emitted by the dim laser source, they should obey this statistical distribution. We generate histograms of counts with 1-second bins and calculate the mean ($\mu_{\rm hist}$) and variance ($\sigma^2_{\rm hist}$) of the

sampling distribution, in order to investigate their stochastic nature. As shown in the inset of Figure 6.2.3d, the mean equals the variance for all histograms, consistently with a Poisson process. Using the extracted μ_{hist} and σ^2_{hist}, we also calculate the Poisson distribution and overlay it on the histograms (solid lines). The experimental counts show excellent agreement with the statistical model, confirming the hypothesis that the 'clicks' are given by the photon shot noise originated by the highly attenuated CW laser source[P1].

6.3 Single-photon sensitivity by superconducting MATBG

In this section, we carefully analyze the MATBG's photoresponse and use the statistics of the light-induced counts to demonstrate that the detector is sensitive to single near-infrared photons.

6.3.1 Single-photon sensitivity with continuous wave excitation

First, we measure the PCR (photon count rate) as a function of V_{bias} with a CW excitation wavelength of $\lambda = 1550$ nm, for different laser powers (filled dots in Fig. 6.3.1a). Then, we compare the PCR under illumination with that in the dark (empty dots in Fig. 6.3.1a). We observe that the PCR under illumination is orders of magnitude higher than in the dark when the detector is operated at a bias voltage far from the critical voltage ($V_{bias} << V_c$). Conversely, when the detector is biased close to the transition, there is an abrupt increase in false-positive (dark) counts, which dominates the detector's response for $V_{bias} \sim V_c$.

Interestingly, by fitting the PCR vs. V_{bias} traces under illumination with a sigmoid function (solid line in Fig. 6.3.1a lower panel), we observe that the experimental data tend to saturate at $V_{bias} \approx 0.997 V_c$. In section 6.4.3, we demonstrate that these saturations are intrinsic to the SPD mechanism and not extrinsic, given by the limited bandwidth of the measurement circuitry. The agreement with a sigmoidal shape combined with the presence of saturation plateaus is interesting as it suggests similarities between the photoresponse observed in MATBG and the photon counts in SNSPDs [18].

In the specific case of SNSPDs, the saturation of the PCR as a function of current bias has been widely investigated and indicates that the internal detector efficiency, without coupling, reaches unity [18, 184]. In SNSPDs, the detector efficiency is given by the product of the photon coupling efficiency and the intrinsic quantum efficiency. In the saturation region, the photon coupling efficiency does not depend on the bias, indicating that the intrinsic efficiency of the device cannot be further improved by approaching closer to the transition[18, 184]. Conversely, in our experiment, the PCR curve does not exhibit complete saturation, indicating that the intrinsic efficiency of the process is not 100%. In section 6.3.4, we discuss in detail the possible reasons for the limited detector efficiency in our experiment.

Following the approach described in section 1.1.2, we can demonstrate that the registered counts are triggered by single near-infrared photons. For this purpose, we attenuate the laser power such that the number of incident photons per μm^2 in a time window τ is $\langle N_{photon} \rangle < 1$. In this scenario, the probabilities of having single photons in a time bin will be higher than having two or more photons, according to Eq. 1.1.42.

Using the approximation of a Gaussian beam, we can quantitatively estimate the density of photons incident on the MATBG detector, as previously discussed in section 4.3: $\langle N_{photon} \rangle = \tau \cdot P_L / h\nu$, where $h\nu = 1.28 \times 10^{-19}$ J is the energy of a single photon at

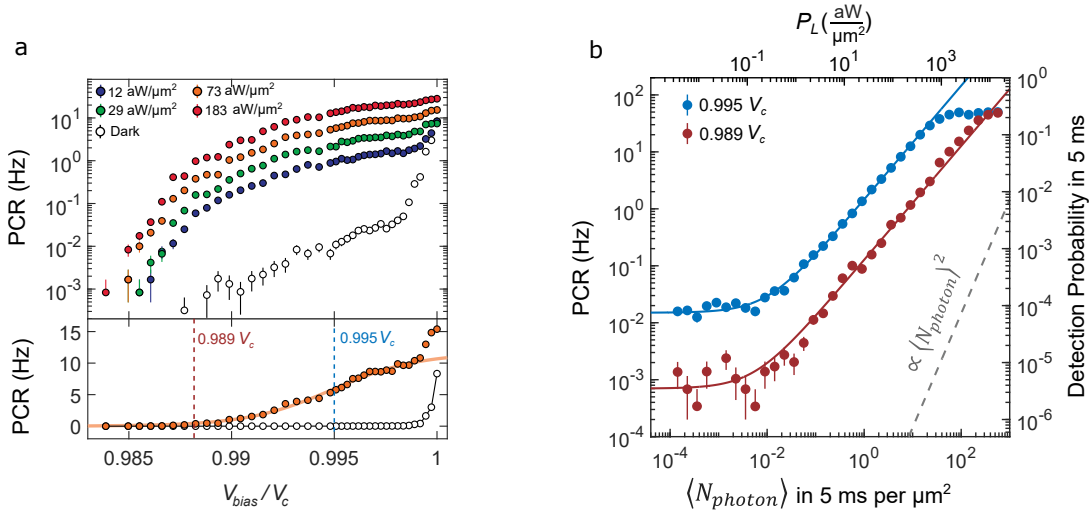

Figure 6.3.1: Single-photon sensitivity by superconducting MATBG. (a) Top panel: Photon count rate, PCR as a function of voltage bias V_{bias} for four different laser powers (filled dots) and in the dark (empty dots). Bottom panel: PCR vs. V_{bias} for $P_L = 73$ aW/μm^2 on a linear scale. The orange line is a fit with a sigmoid function. The PCR tends to saturation at $\sim 0.997\ V_c$. The vertical dashed lines are the bias points at which we performed the PCR vs. P_L measurements reported in **(b)**. **(b)** PCR versus the average incident photon number $\langle N_{photon} \rangle$ in a 5-ms time window per μm^2 for two different bias points ($V_{bias} = 0.995\ V_c$ and $V_{bias} = 0.989\ V_c$). On the top x-axis, the corresponding incident CW power density $P_L = \langle N_{photon} \rangle \cdot \frac{h\nu}{\tau}$ and on the right y-axis, the corresponding detection probability in a 5-ms time window (PCR$\cdot\tau$). The solid lines are linear fits (with an offset due to dark counts), showing that the detection probability evolves linearly with $\langle N_{photon} \rangle$. The gray dashed line depicts a quadratic power dependence. Adapted from [P1].

$\lambda = 1550$ nm. With $\tau = 5$ ms as the typical detector recovery time, a laser power density of $P_L = 10$ aW/μm^2 corresponds to $\langle N_{photon} \rangle = 0.4$ photons incident per μm^2 in a time window of 5 ms. For this range of powers, the probability of detecting m photons in a detection time window reduces to $\sim \langle N_{photon} \rangle^m / m!$.

We can prove SPD by demonstrating the linear scaling of the PCR with the average number of photons. For this purpose, we explore the PCR as a function of laser power over several orders of magnitude and different bias points. In Fig. 6.3.1b, we plot the PCR and the derived detection probability (PCR $\cdot\tau$) as a function of $\langle N_{photon} \rangle$. The measured detection probability increases linearly with $\langle N_{photon} \rangle$ over more than three orders of magnitude, demonstrating the single-photon sensitivity of the MATBG superconducting detector [16].

As reported for other SPDs [5], the PCR deviates from the linear dependence at both low and high photon fluxes. The offset observed at low photon fluxes is due to dark counts, while the saturation at high photon fluxes is due to the limited bandwidth of the measurement circuitry [P1]. In Fig. 6.3.1b, we plot two traces: one measured closer to

the transition, at $0.995V_c$, and one measured slightly further away, at $0.989V_c$. Both traces show the same overall behavior, except for efficiency. As expected, the trace measured closer to the transition exhibits a higher detection probability and dark count rate due to the increase in intrinsic quantum efficiency as we approach V_c [P1]. In section 6.4.2, we show the raw photovoltage time traces measured at different V_{bias} and P_L, used to extract the PCR reported in Fig. 6.3.1.

6.3.2 Single-photon sensitivity with pulsed light excitation

As already discussed in section 1.1.2, we repeat the SPD experiment with pulsed light excitation to provide an independent measurement and cross-check the single-photon sensitivity observed under CW illumination. The employed laser source provides pulses with a duration of approximately 50 ps, at $\lambda = 1550$ nm, with a repetition rate (f_{RR}), tunable across a broad range of frequencies. Using the pulsed laser source, we independently control the number of photons carried on average by each pulse (μ) and the rate at which these pulses are directed onto the device (inset of Fig. 6.3.2a). Similar to the CW experiment, we set $\mu < 1$ to ensure that most pulses incident on the device area A carry 0 or 1 photon, making multi-photon events negligible.

This experiment is not only a complementary method to demonstrate SPD but also proves that the observed photoresponse is due to the instantaneous absorption of single photons rather than a steady-state bolometric effect, similar to the one investigated in Chapter 5. In the scenario of a steady-state bolometric effect, the absorbed laser power could reduce the bias current, bringing the device closer to the superconducting transition, and increasing the dark counts probability. This would effectively lead to an increase of the count rate with laser power that is not due to single photons. The pulsed experiment can completely rule out this scenario.

Unlike the CW experiment, where there is no control over the exact time at which a photon is absorbed (since the CW source provides a continuous stream of photons), the pulsed experiment allows to control the time window in which a single photon can be absorbed ($\sim$ 50 ps). By sufficiently reducing the repetition rate, we ensure that a certain time ($\sim 1/f_{RR}$) elapses between two absorption events, ensuring that the MATBG detector is completely thermalized before another photon is absorbed, and that no steady-state bolometric effect can occur.

In Fig. 6.3.2a, we explore the detection efficiency for different f_{RR}, ranging from 10 Hz to 1 MHz. In this experiment, we fix $\mu = \frac{P_L}{h\nu f_{RR}} = 0.62 < 1$ by simultaneously tuning f_{RR} and P_L. The detection efficiency is defined as the ratio of counts detected per second to photons incident per second in the area $A \sim 16$ µm^2 and is plotted against the laser repetition rate. We observe a clear plateau in the range 100 Hz $< f_{RR} <$ 30 kHz, indicating that the detection efficiency is unaffected by the time distance between the pulses and that the absorbed photon rate is lower than the detector recovery time [P1]. Within this range of repetition rates, we exclude steady-state heating and still observe linear scaling of the PCR with $\langle N_{photon} \rangle$ (inset in Fig. 6.3.2a), confirming that the observed photoresponse in MATBG is due to instantaneous absorption of single photons [P1]. We observe a deviation from the plateau for $f_{RR} < 100$ Hz, where dark counts dominate the count rate, and for $f_{RR} > 30$ kHz, where the incident photon rate saturates the MATBG detector, consistently to what observed in the CW experiment for $P_L > 300$ aW/µm^2.

In Fig. 6.3.2b, we fix the repetition rate in the middle of the plateau ($f_{RR} \sim 5$ kHz) and measure the PCR for the same bias points explored in Fig. 6.3.1b by changing the

number of photons carried on average by each pulse. As expected, when $\mu < 1$, the PCR evolves linearly for both bias points, further demonstrating SPD under pulsed excitation.

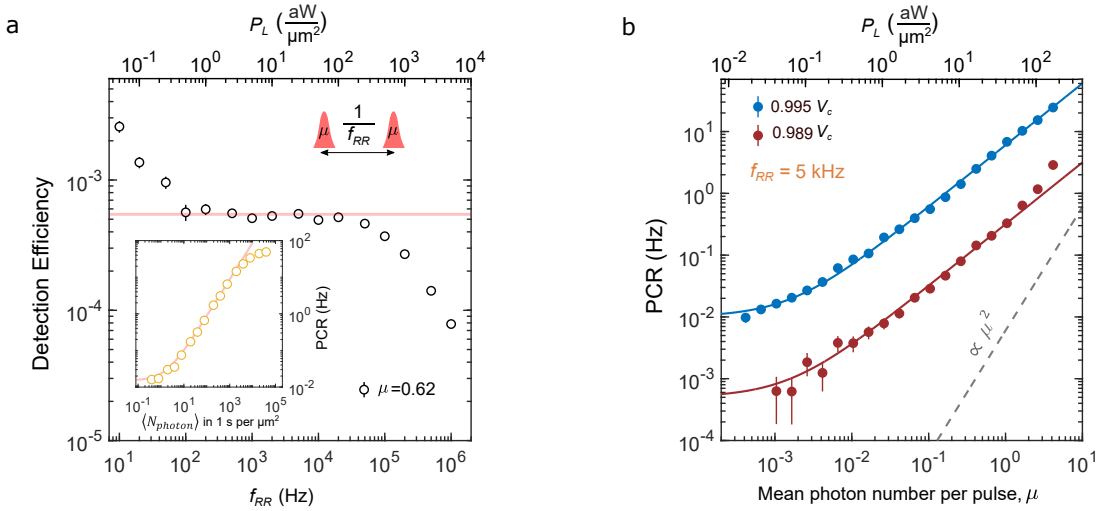

Figure 6.3.2: Single-photon sensitivity with pulsed light excitation. **(a)** Detection efficiency vs. laser repetition rate, f_{RR} measured for $\mu = 0.62$ and $V_{bias} = 0.995\ V_c$. The detection efficiency is defined as counts detected per second over photons incident per second in the area $A \sim 16\ \mu m^2$ for device A. On the top x-axis, the average incident power density P_L corresponding to each f_{RR}. The solid line highlights the plateau observed for 100 Hz $< f_{RR} <$ 30 kHz. Inset: photon count rate, PCR vs. average incident photon number $\langle N_{photon} \rangle$ in 1-s time window per μm^2. The solid line is a linear fit with an offset due to dark counts. **(b)** PCR versus μ for the same bias points measured in Fig. 6.3.1b, for a fixed $f_{RR} = 5$ kHz. The solid lines are linear fits (with an offset due to dark counts), showing that the PCR evolves linearly with μ. Adapted from [P1].

6.3.3 Detector behavior at higher temperatures

Having demonstrated SPD, we investigate the photodetection mechanism in MATBG by examining the photoresponse at higher temperatures. We measure the PCR versus V_{bias} for temperatures ranging from 35 mK to 800 mK, both with laser excitation and in the dark (filled and empty dots, respectively, in Fig. 6.3.3a). By fitting the PCR traces using a sigmoidal shape, analogous to what was done in Fig. 1.1.2a, we observe that all the PCR traces tend to saturate at $V_{bias} \sim 0.997V_c$. In our experiment, we observe SPD in our MATBG device up to approximately 0.7 K (see Fig. 6.4.9), while SPD eventually vanishes at 0.8 K, where the dark count dominates the PCR[P1].

In Fig. 6.3.3b, we compare the SPD efficiency and the dark count rate as a function of V_{bias} for all explored temperatures on a semi-logarithmic plot. The dark count rate (right-hand side of the y-axis) exhibits a similar behavior for all temperatures and shows two distinct V_{bias} dependencies. For $V_{bias} > 0.998V_c$, there is a sharp increase in dark counts, responsible for the abrupt rise in PCR under illumination when $V_{bias} \sim V_c$. These dark counts are potentially intrinsic to the MATBG photodetector, given the instabilities when the device is biased close to the transition. Conversely, for $V_{bias} < 0.998V_c$, the dark counts exhibit a more gradual rise with V_{bias}. This behavior is similar to previous reports on other SPDs[185] and points towards an extrinsic origin of these dark counts, i.e., due to background photons coupling to the device through the optical fiber[185]. This argument is further confirmed by the fact that the dark counts exhibit the same V_{bias} dependence at all temperatures.

Conversely, the detection efficiency (defined as the ratio of counts detected per second to photons incident per second in the area $A \sim 16\ \mu m^2$), has a clear temperature dependence: it is maximum at the lowest temperatures and gradually decreases as the temperature rises, similar to observations in other SPDs [184, 185]. In Fig. 6.3.3c, we plot the detector efficiency versus temperature extracted at three different V_{bias} from the sigmoid fit in Fig. 6.3.3a. As anticipated, the efficiency abruptly drops as the temperature rises. This behavior is critical to understanding the detection mechanism. A possible explanation for this trend can be the increase in thermal conductance. As measured in Chapter 5, the thermal conductance in the superconducting state of MATBG shows a rapid, power-law increase within the temperature range of 35 mK $< T <$ 800 mK. In our proof-of-concept experiment, the detection events are driven by an avalanche effect sustained by self-heating, originating from the hotspot formation within the hysteresis loop. Therefore, the increase in thermal conductance at elevated temperatures could enhance the heat leak out of the electronic ensemble, ultimately reducing the probability of transitioning into the resistive state by a self-heating effect [P1]. As we discuss in the following section 6.3.4, heat dissipation could be a limiting factor for MATBG efficiency in our experiment, and future applications may explore different readout mechanisms that do not rely on self-heating.

In Fig. 6.3.3d, we plot the detector efficiency against the dark count rate to identify the optimal operating point of the MATBG detector at various temperatures. The best trade-off between SPD efficiency and dark count rate is obtained in the plateau region,

where the efficiency is at its maximum value while the dark count rate remains below 0.05 Hz.

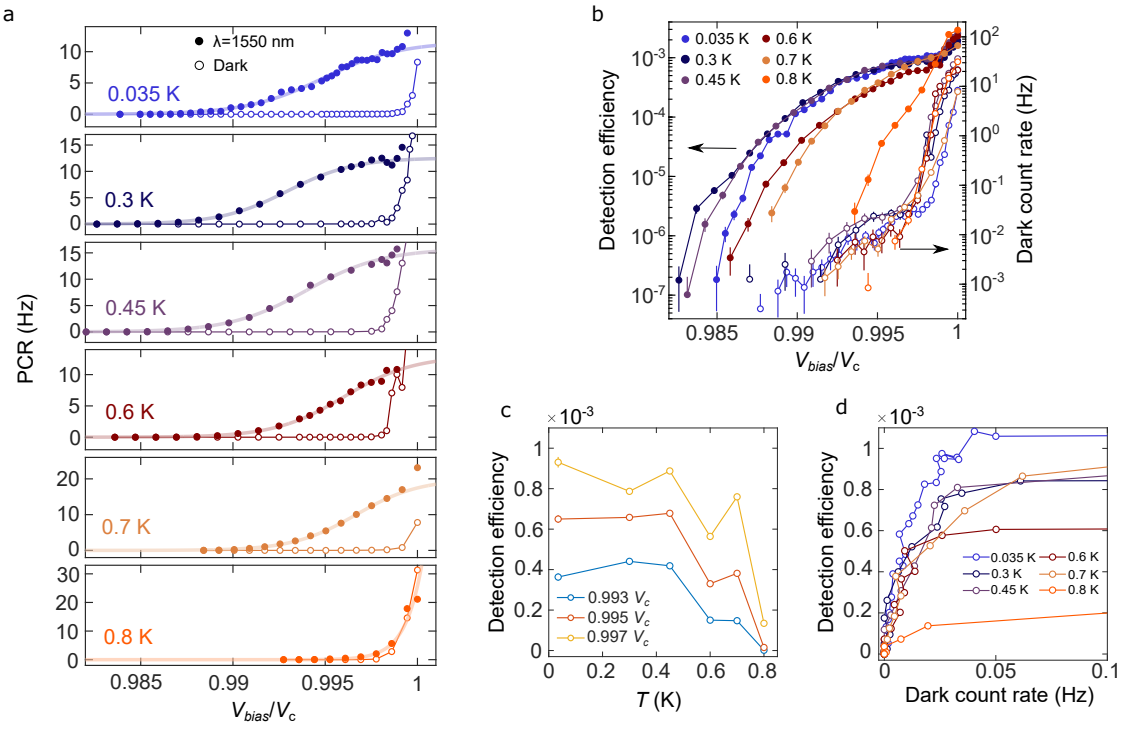

Figure 6.3.3: Detector performance at higher temperatures. **(a)** Photon count rate, PCR as a function of voltage bias V_{bias} for different temperatures T upon illumination (filled dots) and in the dark (empty dots). The solid lines are fit with the sigmoid function. **(b)** Filled markers: detection efficiency vs. V_{bias} at different temperatures. Empty markers: dark count rate vs. V_{bias} at different temperatures. The detection efficiency is defined as the ratio of counts detected per second to photons incident per second in the measured area. **(c)** Detection efficiency vs. T extracted from the sigmoidal fit in **(a)** for three different bias points. **(d)** Detection efficiency vs. dark count rate for all the explored temperatures, showing the optimal operation point of the detector. Adapted from [P1].

6.3.4 Discussion of the detector's efficiency

In this section, we estimate the internal efficiency of the MATBG detector and discuss the possible factors limiting it in our experiment. As discussed in section 5.1, the incident photon energy is significantly larger than the widths of the flat bands and the superconducting gap, allowing us to approximate the MATBG's absorption to be the same as bilayer graphene. In addition, employing the optical transfer matrix formalism, we have calculated the effects on absorption of the additional layers in the heterostructure and found them to be negligible (section 5.1.1). Therefore, assuming MATBG's absorption to be approximately 4.6%, we estimate the internal efficiency of our SPD at the saturation plateau to be $\sim 10^{-3}/0.046 \approx 0.022$.

The first factor limiting the efficiency could be the twist angle inhomogeneity. As anticipated in section 3.3.2, due to the relaxation of the lattice structure during the fabrication process, there might be local variations in the twist angle, resulting in a narrower superconducting area in MATBG. Therefore, the effective area of MATBG contributing to the photoresponse could be much smaller than the entire device area [P1]. This would be consistent with previous studies of twist angle inhomogeneity using local probe techniques on MATBG [135, 136, P7]. Even though the fabrication method developed in Chapter 3 allows us to achieve high-quality MATBG devices, local twist angle disorder significantly limits the size of the superconducting area.

We can use this argument to get insights into the superconducting area of MATBG via its interaction with photons. Supposing that the internal efficiency is close to unity at the saturation plateau (analogous to SNSPDs [18]), in that case, we can estimate a lower limit for the effective superconducting area: $A_{eff} \sim 0.022 \cdot A \approx 0.35\ \mu m^2$. Following this argument, we could also estimate the channel's width. If the resistance measured across the two voltage probes (spaced 3 µm apart) is zero, it implies that there is full percolation of the superconducting path across that length [P1, 135]. In this scenario, we could estimate the channel's width as approximately 120 nm. Interestingly, this would indicate that our MATBG detector effectively behaves as a superconducting nanowire defined by the twist angle inhomogeneities. This could explain the observed similarities in the photoresponse between the MATBG and SNSPDs.

However, while in SNSPDs the absorbed photon generates a local resistive domain to produce a readout signal [81], our detection mechanism relies on a hotspot expanding with self-sustained Joule heating, leading to a complete breakdown of superconductivity across the whole device area, as suggested by the pulse shape of all three devices (section 6.3.5). As indicated by the behavior of the detector efficiency with temperature (Fig. 6.3.3c), heat dissipation could be an additional factor limiting the detection efficiency. If the heat can easily leak out of the electronic ensemble, as pointed out by the thermal conductance measurement in Chapter 5, the probability of transitioning into the resistive state via a self-sustained heating effect, is strongly reduced and the efficiency of this process is limited.

Possible ways to overcome this issue include employing different probes that are more sensitive to changes in voltage and not relying on the complete breaking of superconduc-

tivity [P1].

6.3.5 Photovoltage generation and pulse shape

In this section, we examine the pulse shapes to understand the origin of the photovoltage generated in MATBG devices. We argue that the observed photoresponse results from the breaking of superconductivity across the entire device upon photon absorption. To support this claim, we measure the photovoltage spikes when MATBG devices are exposed to laser beam radiation at a wavelength of $\lambda = 1550$ nm, using a single-shot oscilloscope, as described in Fig. 6.2.3a, b. We compare the click heights with the oscilloscope traces recorded while sweeping the bias voltage across the transition from the superconducting to normal state and vice versa (Fig. 6.3.4d-f). The voltage output induced by the photons matches the voltage generated by manually sweeping the device across the transition, confirming our initial hypothesis of a complete breaking of superconductivity in the device [P1].

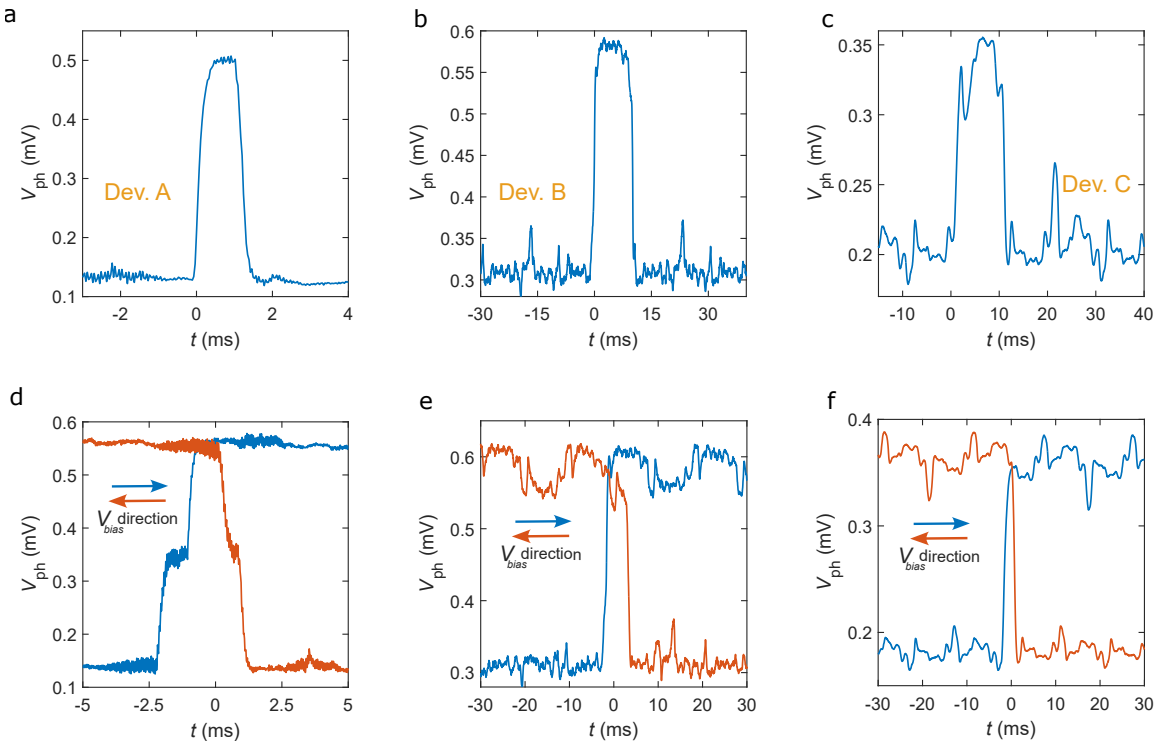

Figure 6.3.4: Photovoltage generation and pulse shape for all devices. (a)-(c) Pulse shape measured with a single-shot oscilloscope (using a room-temperature low-pass filter with 10 kHz cut-off) upon photo-absorption for all the measured devices. The bias voltage used are $V_{bias} = 0.989\ V_c$ for device A, $V_{bias} = 0.991\ V_c$ for device B, and $V_{bias} = 0.9994\ V_c$ for device C. **(d)-(f)** Single-shot oscilloscope traces recorded while sweeping the bias voltage across the transition in both directions from the superconducting to normal state (blue) and vice-versa (red). Adapted from [P1].

We also compare the measured pulse shapes in MATBG devices with those typically observed in other superconducting SPDs. In our experiment, when the MATBG detector turns resistive upon photon absorption, it remains in the normal state for a few milliseconds before returning to the superconducting state. This behavior is substantially different from other superconducting SPDs, such as SNSPDs or TES. As briefly discussed in section 1.3.1, in typical superconducting SPDs, the pulse shape is characterized by a fast increase in the photovoltage, followed by a much slower decay. For SNSPDs, the characteristic time of such decay depends on the ratio between the kinetic inductance of the superconducting circuit and the shunt resistance [80, 186]: $\tau \sim L_k/R_s$; while for TES or hot electron bolometers, it depends on the intrinsic thermalization time of the electrons in the material [15, 187], given by the ratio of electronic heat capacity and thermal conductance: $\tau = C_e/G_{th}$. In section 6.4.3, we provide a careful investigation of the detector's timescale and propose possible ways to improve the detector's speed.

Additionally, we measure the photovoltage time traces for two different excitation wavelengths ($\lambda = 1550$ nm and $\lambda = 633$ nm) and plot them in Fig. 6.3.5. The traces measured at $\lambda = 1550$ nm are shown in red, while those measured at $\lambda = 633$ nm are in blue. We extract the click heights and overlay them on the I-V curve (Fig. 6.3.5a). Interestingly, there is no appreciable difference in the click heights measured at 1550 nm and 633 nm. This observation suggests once more, that the observed photoresponse is due to a complete breaking of superconductivity, regardless of the excitation energy [P1].

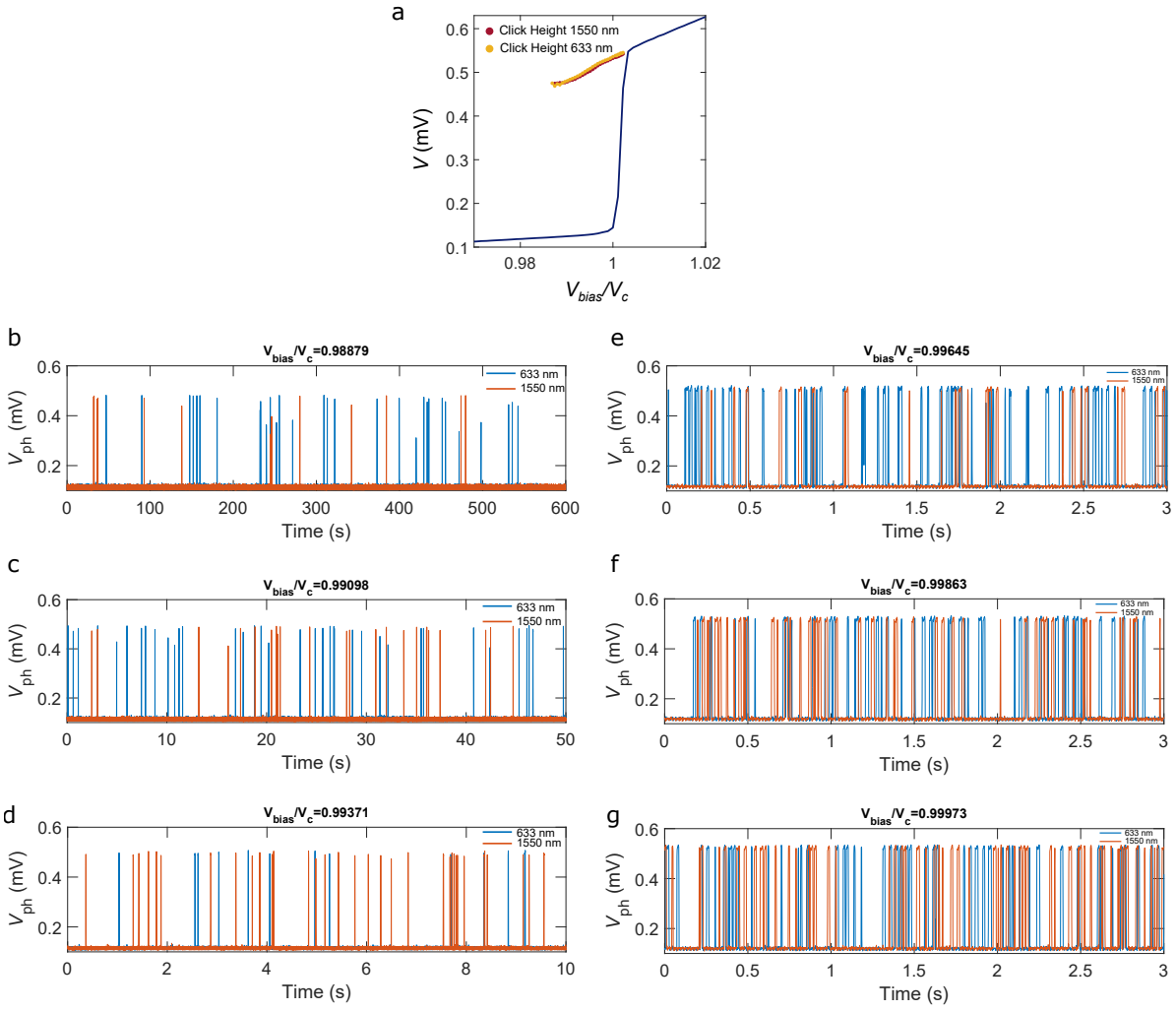

Figure 6.3.5: Raw photovoltage time traces for different excitation energies. (a) Average click height measured as a function of V_{bias} for $\lambda = 1550$ nm and $\lambda = 633$ nm. The click heights are overlaid on the I-V curve. **(b)-(g)** Raw photovoltage traces measured over time for six different bias voltages and for two different excitation wavelengths: $\lambda = 1550$ nm (red) and $\lambda = 633$ nm (blue). To make the plots more readable we reduce the time duration of the traces as we approach closer to the transition. Adapted from [P1].

6.4 Further analysis

In this section, we perform additional analysis on the technical aspects of the MATBG detector, which can be useful for improving its performance. Specifically, we quantitatively analyze the implemented self-reset circuitry and investigate the detector's timescale. Additionally, we present and discuss the photoresponse of the additional devices B and C and detail the method used to register the counts in the detector.

6.4.1 Detailed analysis of the reset circuitry

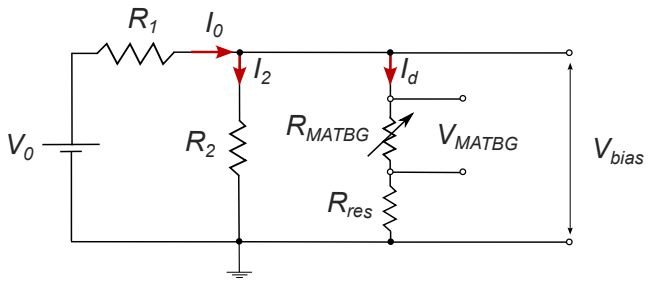

Figure 6.4.1: Schematics of the reset circuit. V_0 is the external voltage applied by the source meter. R_1 and R_2 are the two resistors constituting the voltage divider. For the photodetection experiment we used $R_1 = 1$ MΩ and $R_2 = 1$ kΩ. R_{MATBG} is the resistance of the MATBG which changes from the superconducting state to the normal state. V_{MATGB} is the 4 probe voltage generated across the MATBG device and V_{bias} the applied bias voltage across the source and drain contacts of the device. $R_{res} = 54.5$ kΩ is is the residual resistance arising from the contact resistance and the metallic leads.

Fig. 6.4.1 illustrates the schematics of the circuit implemented to reset the MATBG detector upon photon absorption. From the schematics, we can write the system of equations that fully describes the reset circuit developed in our experiment:

$$\begin{cases} V_{bias} = V_{MATBG} + R_{res} I_d \\ I_0 = I_d + \frac{V_{bias}}{R_2} \\ V_0 = I_0 R_1 + V_{bias} \end{cases} \tag{6.4.1}$$

Isolating I_0 in the second and third equations, we get:

$$\begin{cases} I_d = \frac{V_{bias} - V_{MATBG}}{R_{res}} \\ \\ V_{bias} = \frac{R_2}{R_1+R_2} V_0 - I_d \frac{R_1 R_2}{R_1+R_2} \end{cases} \tag{6.4.2}$$

To verify that the equations accurately describe the experiment, we perform a linear fit on the measured V_{bias} vs. V_0. As shown in the second expression of Eq. 6.4.2, the slope

of this curve is given by $\frac{R_2}{R_1+R_2}$. The slope extracted from the fit, 0.00099 (Fig. 6.4.2a), matches the value expected from the resistors used ($R_1 = 1$ kΩ and $R_2 = 1$ MΩ).

We also independently measure the residual resistance ($R_{res} = 54.5$ kΩ), the voltage bias V_{bias} applied across the source and drain contacts, and the 4-probe voltage generated across the MATBG, V_{MATBG}. Using the first expression of Eq. 6.4.2, we can extract I_d as a function of the applied bias voltage V_{bias} and observe that the current flowing in the MATBG is reduced by ~ 5 nA for $V_{bias} = V_c$, as reported in Fig. 6.4.2b. This indicates that when the detector transitions into the normal state, the current flowing in the MATBG detector is reduced by $\Delta I_d \sim 5$ nA, allowing the reset of the MATBG detector upon photon absorption.

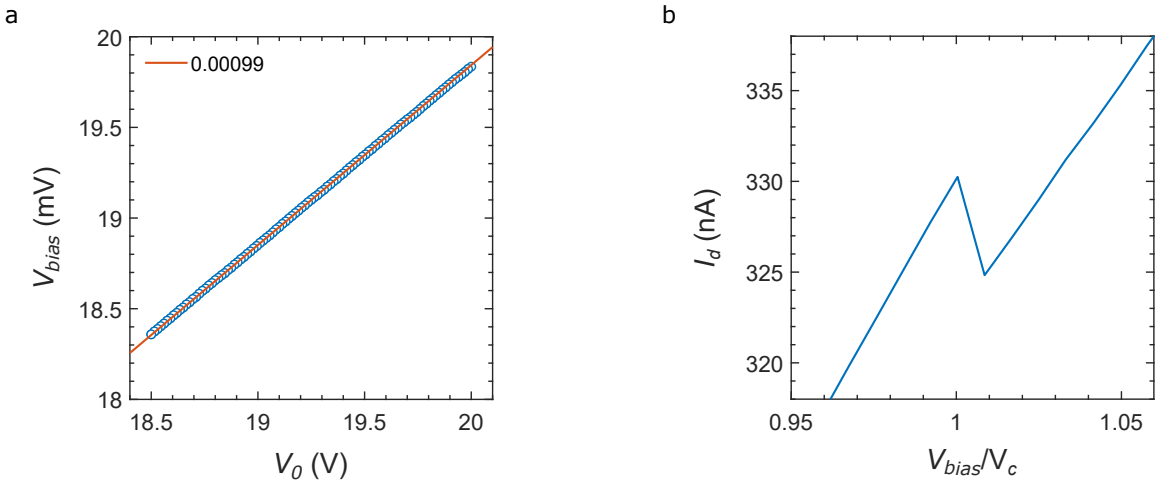

Figure 6.4.2: Analysis of the reset circuit. (a) Measured V_{bias} vs. V_0 while sweeping across the superconducting transition. The slope extracted from the fit is 0.00099, which matches the one expected from $\frac{R_2}{R_1+R_2}$ considering the resistors used in the experiment: $R_1 = 1$ kΩ and $R_2 = 1$ MΩ. **(b)** Extracted device current as a function of the applied bias voltage. The device current is calculated from Eq. 6.4.2 as: $I_d = \frac{V_{bias}-V_{MATBG}}{R_{res}}$, where V_{MATGB} is the 4 probe voltage generated across the MATBG device and V_{bias} the applied bias voltage. I_d drops by ~ 5 nA at the transition.

To investigate this further, we solve the system in Eq. 6.4.2 and calculate the reduction of critical current as a function of the parallel resistor R_2, comparing it with the experimental data. In our experiment, we tried several parallel resistors before finding the optimal configuration and measured the I-V characteristic, as shown in Fig. 6.4.3. We notice that the hysteresis loop ΔI_{hyst} is reduced when the parallel resistor R_2 is reduced and completely disappears for $R_2 = 1$ kΩ. By reducing the value of R_2, we observe that the circuit transitions from a purely current-bias (I_d is not reduced when the device turns to the normal state) to a voltage-bias, in which there is a reduction of I_d, closing the hysteresis loop.

We extract the expression for I_d as a function of R_2:

$$I_d = \frac{V_0 R_2 - (R_1 + R_2) V_{MATBG}}{R_{res}(R_1 + R_2) + R_1 R_2} \tag{6.4.3}$$

From this, we can calculate the variation of current flowing into the MATBG device (ΔI_d) when the device transitions into the normal state as a function of R_2:

$$\Delta I_d(R_2) = \frac{\Delta V_{MATBG}(R_1 + R_2)}{R_{res}(R_1 + R_2) + R_1 R_2} \tag{6.4.4}$$

Where $\Delta V_{MATBG} = V^{SC}_{MATBG} - V^{N}_{MATBG} \sim 0.44$ mV is the variation in the MATBG voltage when transitioning from the superconducting to the normal state. In Fig. 6.4.3b, we plot the extracted hysteresis loop width ΔI_{hyst} for different values of R_2 and compare it with the ΔI_{hyst} expected from the model: $\Delta I^{Model}_{hyst} = \Delta I_{hyst}(R_2 = \infty) - \Delta I_d(R_2)$.

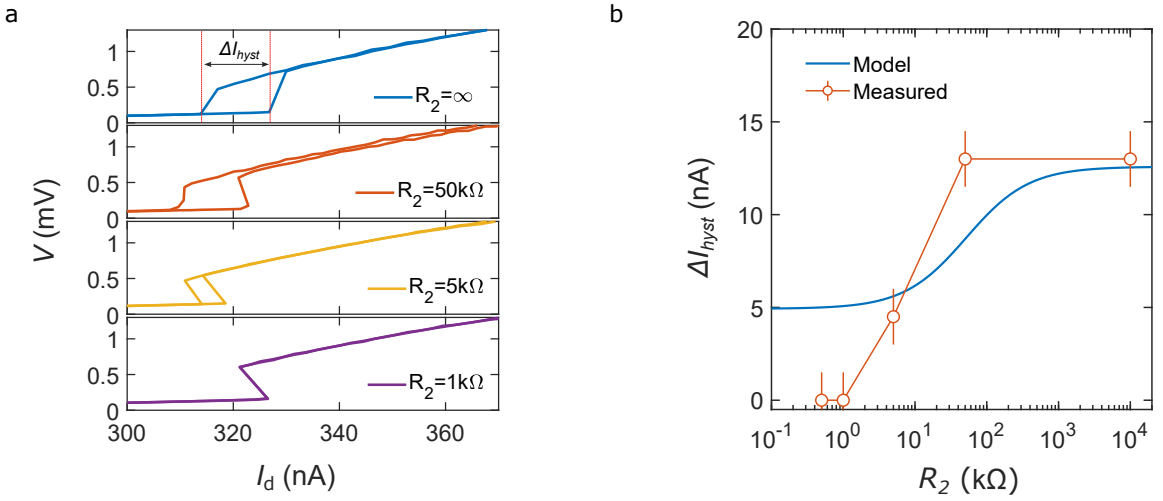

Figure 6.4.3: Closing of the hysteresis loop in the *I-V* curves. **(a)** Voltage vs. device current, I_d calculated according to Eq. 6.4.2 for different values of the parallel resistor R_2. The width of the hysteresis loop ΔI_{hyst} is progressively reduced by reducing the value of R_2. **(b)** Comparison between the ΔI_{hyst} extracted from **(a)** and the ΔI_{hyst} calculated from Eq. 6.4.4.

We notice that the model reproduces the overall experimental behavior, i.e., that the width of the hysteresis loop diminishes as R_2 decreases. However, while the model reproduces the trend well for high values of R_2, it fails for lower values, predicting a reduction in the width of the hysteresis loop but not its complete closing. This discrepancy can be explained by the fact that the reduction of I_d suppresses the Joule heating when the MATBG transitions from superconducting to the normal state: $\Delta P_J = P^N_J - P^{SC}_J = \frac{V^2_{bias}}{R_{res}+R_N} - \frac{V^2_{bias}}{R_{res}+R_{SC}} < 0$. Interestingly, the Joule heating variation is negative, similar to transition-edge sensors [15, 65]. We speculate that the mechanism restoring superconductivity in the MATBG detector after photodetection is a combination of the resetting of the device current and a negative electrothermal feedback [65].

6.4.2 Method of registering counts in the detector

Fig. 6.4.4b-g shows the raw photovoltage time traces with (red) and without illumination (blue) for six different bias points, from which we derived the PCR vs. V_{bias} in Fig. 6.4.4a. Similarly, Fig. 6.4.5b-g show the raw photovoltage time traces measured for different laser powers (colored dots) at a fixed bias $V_{bias} = 0.995\ V_c$, from which we derived the PCR vs. P_L in Fig. 6.4.5a. In this section, we present the raw photovoltage time traces used for deriving the plots in Fig. 6.3.1 and detail the method employed to extract the counts of the MATBG detector. As described earlier, the raw traces are measured using an analog-to-digital converter or an oscilloscope. We use a MATLAB script to count the number of detected events by setting a threshold ($V_{\mathrm{ph}} > 0.4$ mV for device A) and a minimum time interval between clicks to avoid double-counting. The minimum time interval is defined by the detector's recovery time, which is the period immediately following an event during which the detector is unable to record another event. As shown in Fig. 6.4.6, the recovery time ranges from approximately 1 ms to 17 ms. Therefore, we set the minimum interval between counts to 17 ms. This choice limits the maximum measurable count rate to approximately 60 Hz. For the PCR vs. P_L traces, the minimum interval between clicks is set to 13 ms.

Fig. 6.4.4b-g shows the raw photovoltage time traces with (red) and without illumination (blue) for six different bias points, from which we derived the PCR vs. V_{bias} in Fig. 6.4.4a. Similarly, Fig. 6.4.5b-g show the raw photovoltage time traces measured for different laser powers (colored dots) at a fixed bias $V_{bias} = 0.995\ V_c$, from which we derived the PCR vs. P_L in Fig. 6.4.5a.

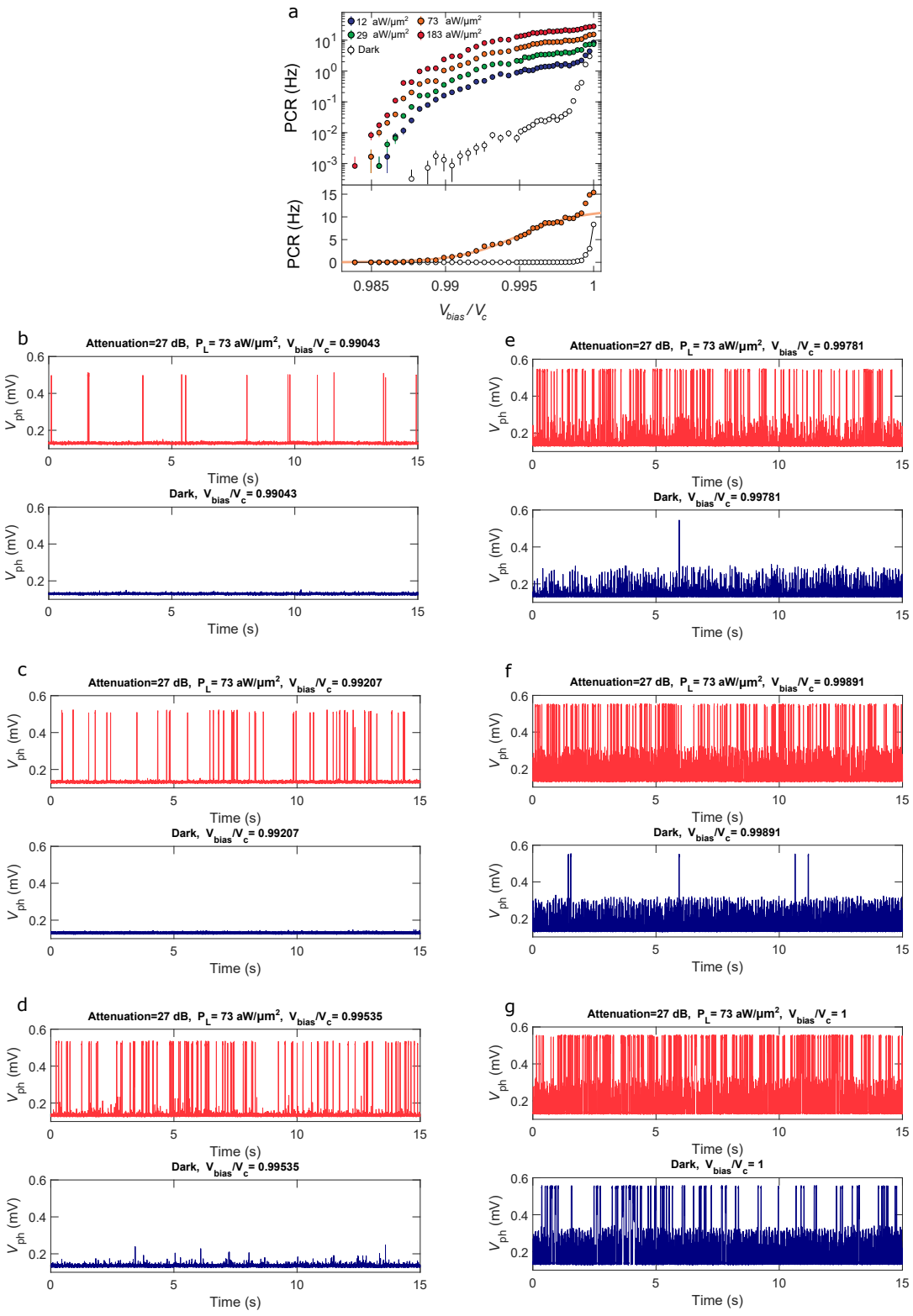

Figure 6.4.4: Raw photovoltage time traces for different bias points. **(a)** Photon count rate (PCR) vs. V_{bias} measured for different laser powers as in Fig. 6.3.1a. **(b)-(g)** Raw photovoltage time traces with and without 1550 nm laser-illumination for different bias points. Adapted from [P1].

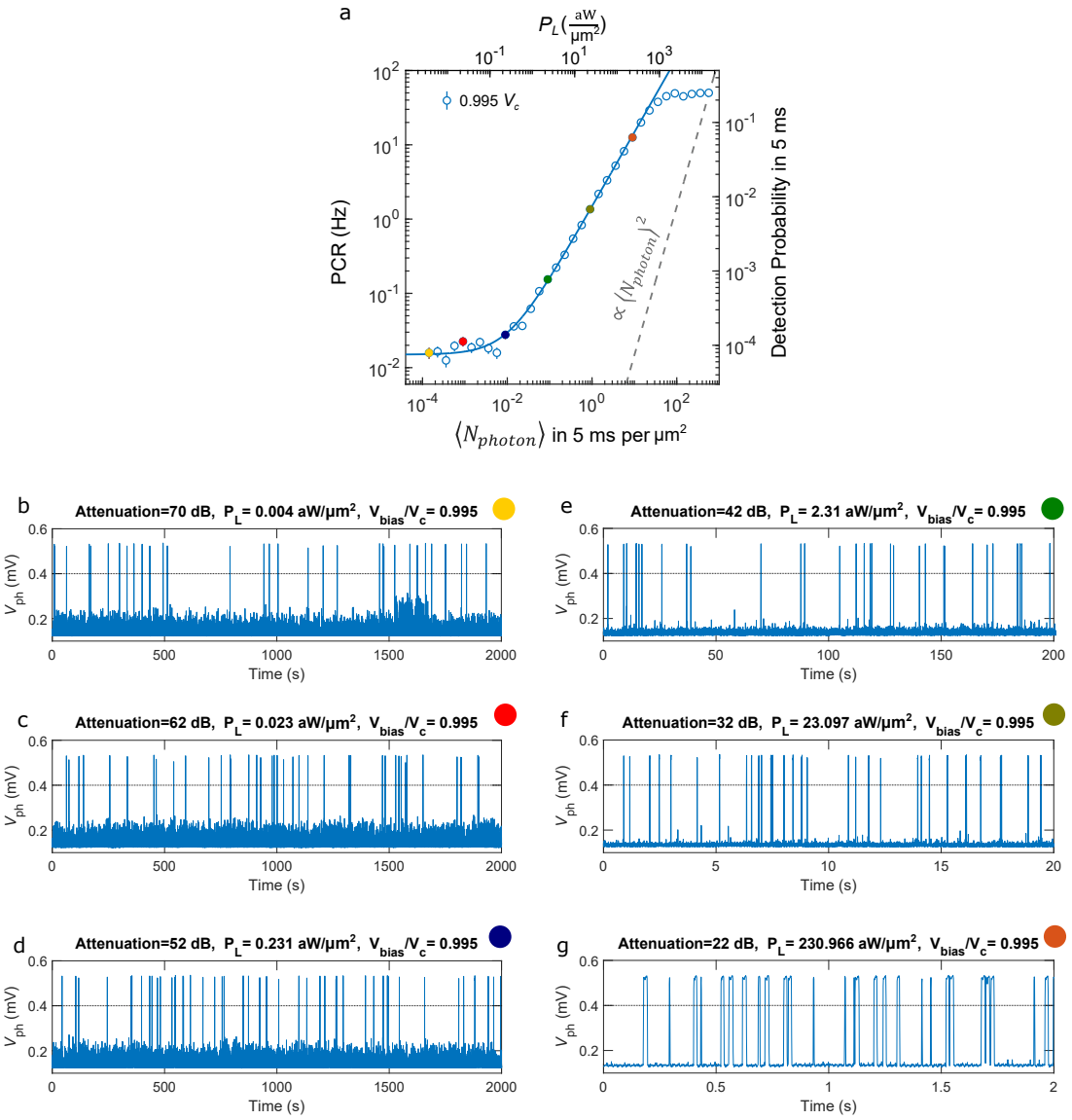

Figure 6.4.5: Raw photovoltage time traces for different laser powers. **(a)** Extracted photon count rate, PCR vs. laser power for $V_{bias} = 0.995\ V_c$. The colored dots are the selected laser powers for which we show the raw photovoltage time traces. **(b)-(d)** Raw photovoltage time traces measured for three different laser powers (attenuations of 70, 62 and 52 dB) over 2000 seconds. In this range, the PCR (< 0.02 Hz) is mostly due to dark counts as the count rate does not significantly scale with the laser power. **(e)-(g)** Raw photovoltage time traces measured for three different laser powers (attenuations of 42, 32 and 22 dB). In these plots the time duration of the traces is scaled inversely with the laser attenuation to facilitate the direct counting of the 'clicks' (200, 20 and 2 seconds respectively). The threshold used for counting the 'clicks' is $V_{\rm ph} > 0.4$ mV (black line). The PCR scales linearly with the incident power: 42 dB (PCR ~ 0.15 Hz), 32 dB (PCR ~ 1.5 Hz) 22 dB (PCR ~ 14 Hz). Adapted from [P1].

6.4.3 Detector's timescale

In this section, we study in detail the timescale of the 'clicks' and how this affects the experimental observations. Specifically, in Fig. 6.4.6, we compare the average 'clicks' timescale, τ_{av} (top panels), with the PCR (bottom panels) for different bias points.

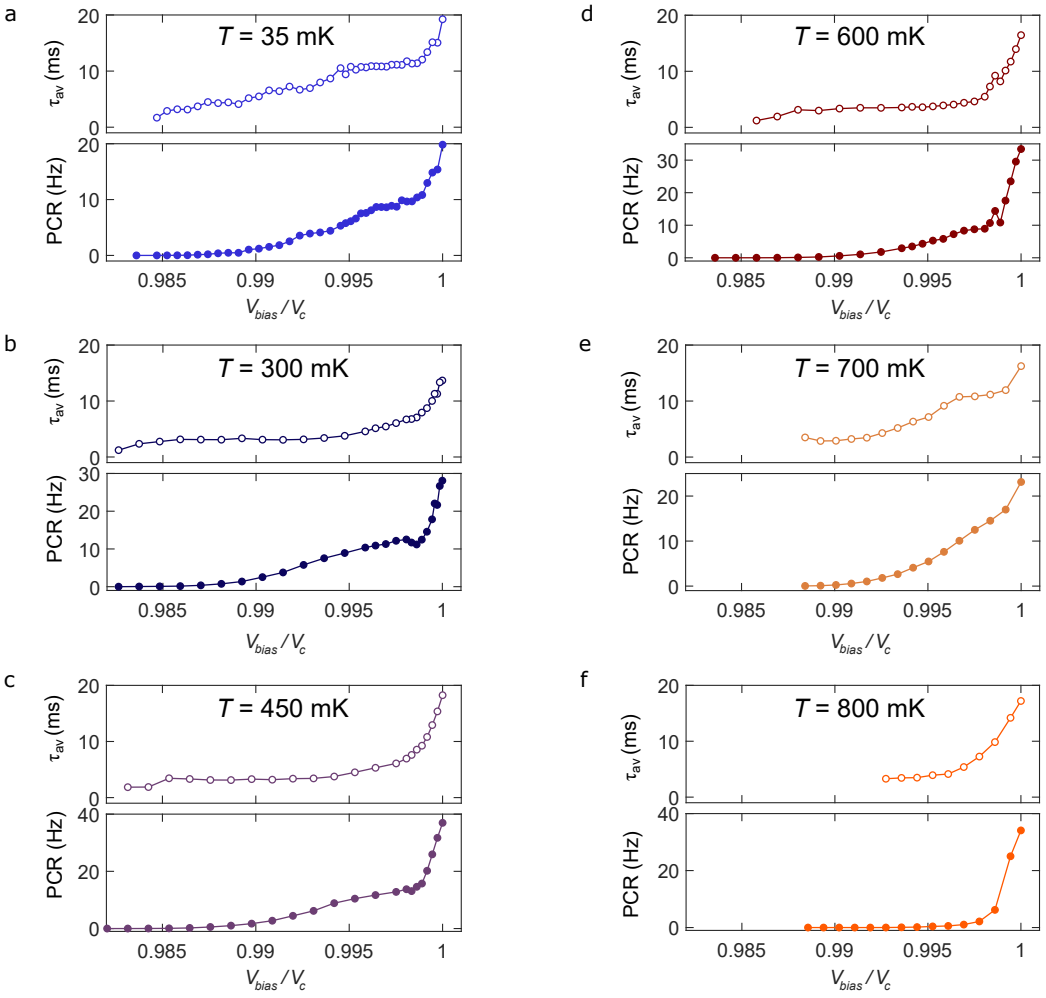

Figure 6.4.6: Detector timescale for different bias voltages. (a)-(f) Top panel: Average 'clicks' timescale, τ_{av} vs. V_{bias} extracted from the raw photovoltage time traces for different temperatures. Bottom panel: PCR vs. V_{bias} for the same temperatures.

We observe that the 'clicks' become slower as we approach V_c. This comparison is important to understand whether the origin of the saturation plateau observed in Fig. 6.4.4a at $\sim 0.997V_c$ and in Fig. 6.4.5a is intrinsic to the MATBG or extrinsic, i.e., due to a limited bandwidth of the reset circuitry. From the top panels in Fig. 6.4.6, we observe that at $V_{bias} \sim 0.997V_c$, the average time duration of the pulses is $\tau_{av} \sim 10$ ms, which

translates into a maximum count rate of ~ 100 Hz. From the bottom panels in Fig. 6.4.6, we see that the saturation plateau in the PCR vs. bias at $V_{bias} \sim 0.997$ occurs at a smaller rate (approximately 10 Hz) than the maximum bandwidth. Similar saturation plateau were also observed for lower laser powers at ~ 1 Hz. From this analysis, we conclude that the saturation behavior observed in the PCR vs. V_{bias} traces is intrinsic to the MATBG detector and not limited by the reset circuitry.

To support this argument, in Fig. 6.4.8b, we plot the PCR vs. P_L corresponding to these saturation plateaus and demonstrate that they evolve linearly with laser power and are not limited by the constrained bandwidth. Conversely, the saturation behavior of the PCR vs. P_L observed in Fig. 6.3.1b at high powers ($\sim 10^3$ aW/µm^2, which is roughly 50-60 Hz) is purely extrinsic due to the limited bandwidth.

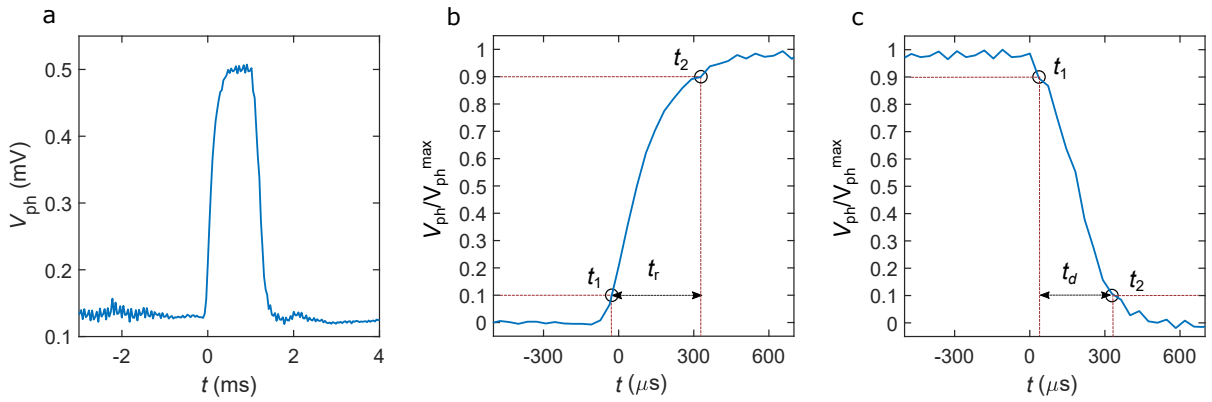

Figure 6.4.7: Pulse shape, rise time, and decay time for device A. (a) Photovoltage pulse $V_{\rm ph}$ measured in the MATBG photodetector at $V_{bias}/V_c \approx 0.989$ and $\lambda = 1550$ nm with a single-shot oscilloscope. **(b)** Rise time $t_r = 356$ µs measured from the pulse in **(a)**, resulting in an overall bandwidth of the electronic readout of < 1 kHz. **(c)** The decay time t_d is similar to the rise time. Adapted from [P1].

Analyzing the pulse shape measured with the oscilloscope allows us to extract the rise time and decay time of the voltage pulses (Fig. 6.4.7) and compare them to those expected from the effective bandwidth discussed in section 4.1.4. We find that the measured pulse rise time ($t_r = 356$ μs) is extrinsically limited by the restricted bandwidth and aligns with the one measured using the 10 kΩ resistor. The same applies to the decay time: $t_d \approx t_r$. Despite the limited bandwidth in our experiment, we are able to accurately study the statistics of the photo-induced counts and demonstrate the single-photon sensitivity of the MATBG detector.

The timescale of our MATBG detector is quite poor compared to the stat-of-the-art

SPDs[4, 5]. A possible way to improve the detector's speed is to design a resonator-based readout, in which the kinetic inductance is part of the resonator. When an absorbed photon generates quasiparticles inside MATBG, its kinetic inductance increases, suppressing the resonance frequency. This concept is similar to the kinetic inductance detector[21], which has proven to provide a fast readout of SPD.

6.4.4 Additional photoresponse data

For completeness, we report additional photoresponse data measured on device A and the full dataset measured on device B and C.

Additional photoresponse data of device A

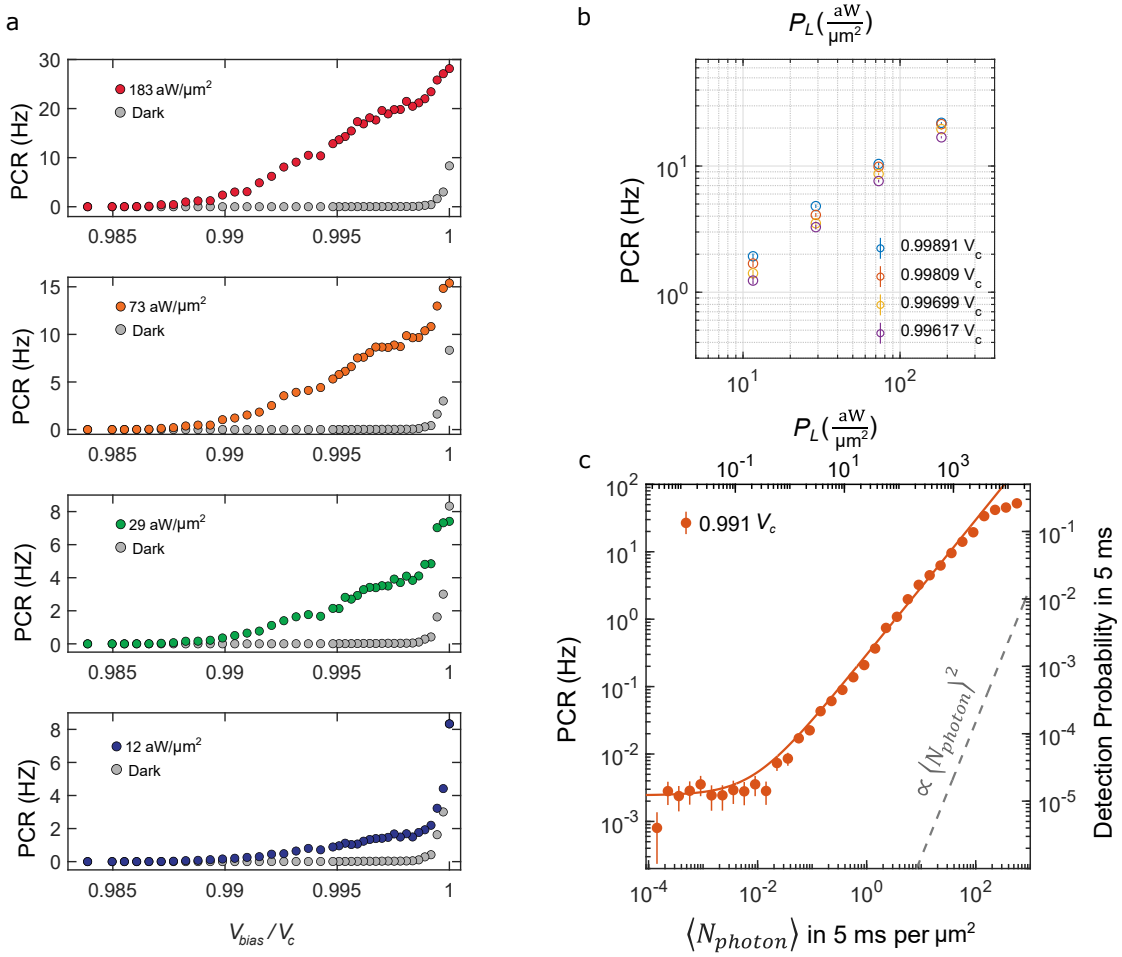

Figure 6.4.8: Additional photoresponse data of device A. **(a)** Extracted photon count rate (PCR) vs. V_{bias} measured at various laser powers and plotted in linear scale. **(b)** PCR vs. P_L in correspondence of the saturation plateaus $\sim 0.997\,V_c$. **(c)** PCR vs. P_L measured at $V_{\text{bias}} = 0.991\,V_c$. The MATBG detector shows single-photon sensitivity even at this bias point. Adapted from [P1].

In Fig. 6.4.8a, we present the PCR vs. V_{bias} measured at various laser powers on a linear

scale. This linear scale highlights the sigmoidal shape across all laser powers. In Fig. 6.4.8b, we also show the PCR vs. P_L corresponding to the saturation plateaus, demonstrating that they scale linearly with laser power. As mentioned in section 6.4.3, we can exclude the possibility that the plateaus are artifacts of limited bandwidth. Additionally, in Fig. 6.4.8c, we plot the PCR vs. P_L measured at a different bias point ($V_{bias} = 0.991V_c$) compared to those reported in Fig. 6.3.1b. Even at this bias point, the MATBG detector exhibits single-photon sensitivity. We also measure the PCR vs. P_L at $T = 700$ mK and $V_{bias} = 0.996V_c$ (Fig. 6.4.9), observing a linear scaling of the PCR with P_L, confirming single-photon sensitivity up to this temperature.

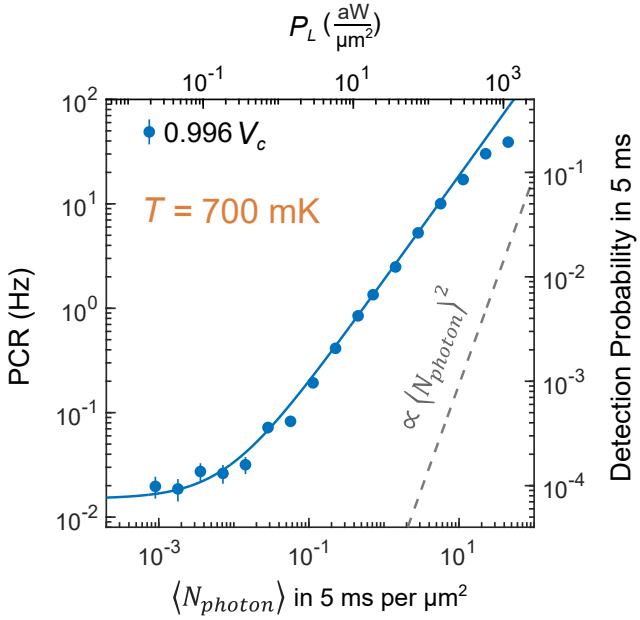

Figure 6.4.9: Single-photon sensitivity at 700 mK. PCR vs. P_L or $\langle N_{photon} \rangle$ measured at 0.996 V_c for device A at $T = 700$ mK. Adapted from [P1].

Photoresponse of device B

In this section, we summarize the photoresponse measurements performed on device B. As anticipated in the transport characterization, while the hysteresis loop in the I-V curve of device B is similar to that of device A, its superconducting state is not fully developed and does not reach zero resistance (Fig. 6.2.2e). This observation is consistent with twist angle inhomogeneity [135].

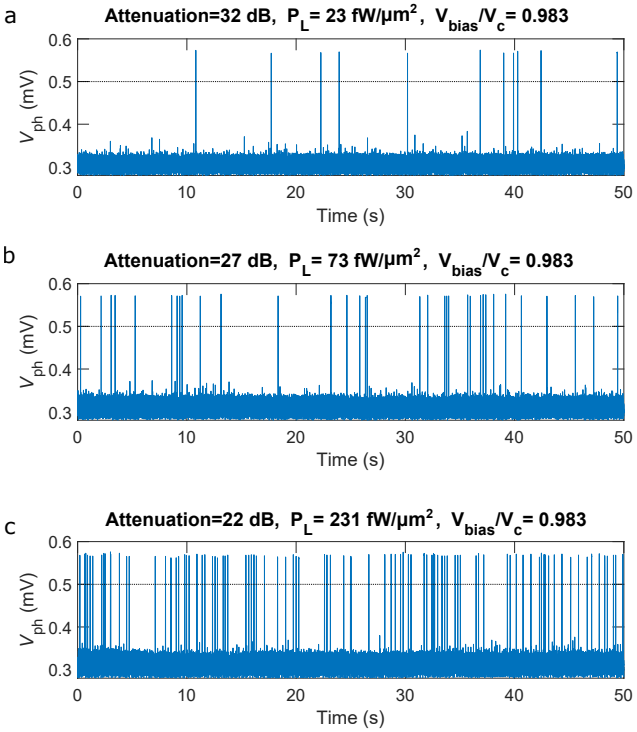

Figure 6.4.10: Raw photovoltage time traces for device B. (a)-(c) Photovoltage traces over 50 seconds time window measured at three different laser power for device B. Adapted from [P1].

In Fig. 6.4.10, we plot the raw photovoltage time traces measured with the same setup and circuit described above and observe voltage spikes that increase with the incident laser power. Notably, we observe a substantial increase in the dark count rate in device B compared to device A. Specifically, at $V_{\text{bias}} \sim 0.990\, V_c$, device A exhibits a dark count rate of approximately 10^{-3} Hz, while device B shows around 3×10^{-1} Hz (see Fig. 6.4.11a). A possible explanation for this behavior could be the non-fully developed superconducting state. In SPDs, the superconducting gap typically protects against external excitations that cause the superconductor to become normal, leading to dark counts [P1]. Therefore, we can expect the non-zero resistive state observed in the transport characterization to be responsible for this increase in the dark count rate.

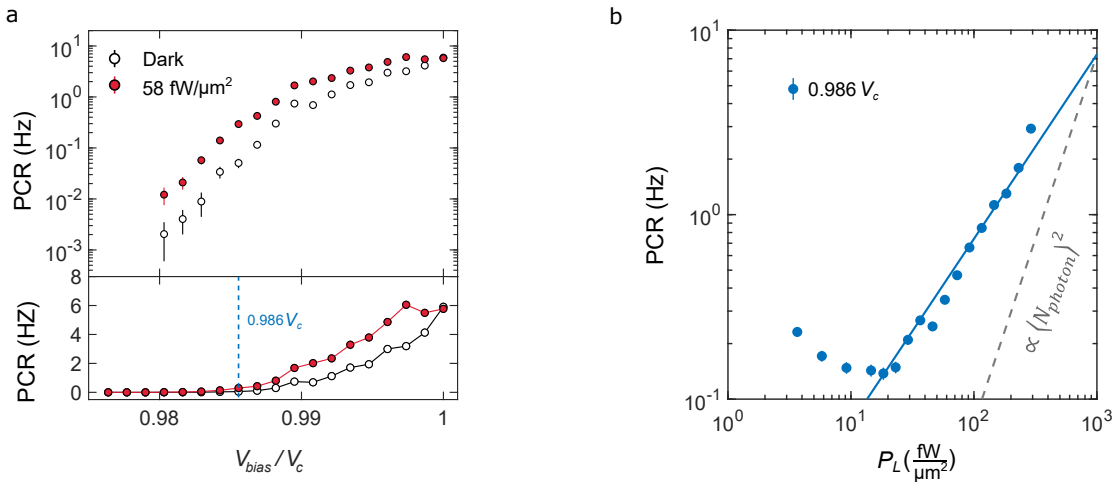

Figure 6.4.11: Photon counting statistics for device B. (a) PCR vs. V_{bias} and PCR vs. P_L extracted for device B. Adapted from [P1].

Photoresponse of device C

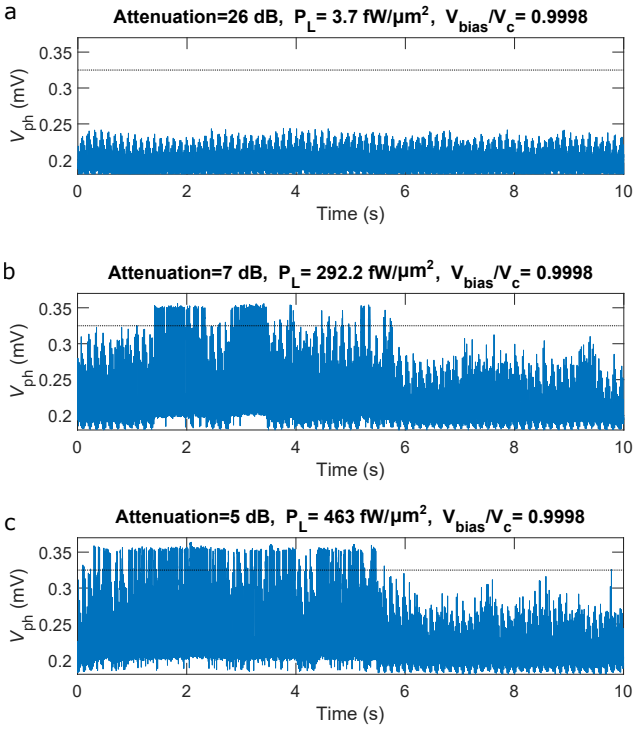

Figure 6.4.12: Raw photovoltage time traces for device C. (a)-(c) Photovoltage traces over 10 seconds time window measured at three different laser power for device C. Adapted from [P1].

The I-V characteristic for device C features a smaller hysteresis loop ($\sim$ 2-3 nA). Additionally, device C exhibits a smoother transition from the superconducting to the normal state. In Fig. 6.4.12, we plot the raw photovoltage time traces measured on device C, and in Fig. 6.4.11, we summarize the PCR against V_{bias} and P_L.

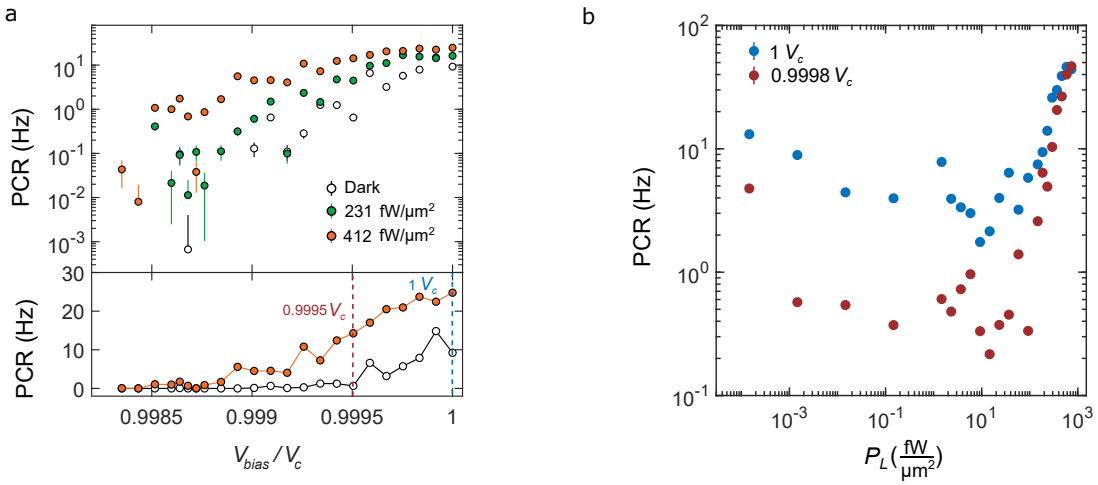

Figure 6.4.13: Photon counting statistics for device C. (a) PCR vs. V_{bias} and PCR vs. P_L extracted for device C. Adapted from [P1].

7

Towards Terahertz photodetection with superconducting MATBG

The work presented in this chapter results from a collaboration with Leon Schubert [188] and Carl Hudeczek [189]. My contributions included conceptualizing and designing the experimental setup, as well as supervising the simulation and realization of the Terahertz antennas.

7.1 Terahertz optoelectronic setup at millikelvin temperatures

Following the successful demonstration of SPD in the near-infrared range (Chapter 6), our long-term objective is to extend superconducting SPD to longer wavelengths, specifically targeting the terahertz (THz) range where SPDs remain significantly underdeveloped [19, 26]. The THz range is of considerable interest not only for technological applications as the THz SPD proposed in this study, but also for fundamental research, as many correlated phenomena in condensed matter systems exhibit energy gaps or excitations accessible via THz radiation [190–192]. For both fundamental and technological purposes, it is crucial to combine THz excitation with low temperatures, which are necessary to observe superconductivity and other correlated phenomena. However, integrating a THz source with low-temperature cryostats, such as dilution refrigerators, presents a significant challenge. Recent studies have proposed various methods to implement a THz source at millikelvin temperatures, either by incorporating the THz source within the cryostat [193, 194] or by

coupling room-temperature external optics through a diamond window[195]. Both strategies have successfully delivered relatively high radiation power to the sample stage while maintaining low temperatures. In our experiment, which aims to detect faint THz light fluxes, high laser powers are not required. Therefore, we employ a THz photomixer located within the dilution refrigerator, thermally anchored to the still plate, and coupling THz radiation in free space to the sample at millikelvin temperatures. THz photomixers are well-established THz sources with applications in various research fields, particularly spectroscopy[196–199]. The primary advantage of this technique is that the THz photomixer dissipates less power than typical lasers[193], thereby requiring lower cooling power for proper thermalization, allowing it to be placed closer to the sample stage[194]. The main heat source for this setup is the near-infrared lasers used to pump the photomixers, which can be located outside the cryostat and coupled to the photomixer through cryo-compatible optical fibers. A similar setup was utilized for photon-assisted shot-noise measurements[200], with the THz photomixer positioned at the 4K stage of a wet dilution refrigerator. In our experiment, we embed the THz photomixer in a closed-cycle dilution refrigerator (BlueFors SD250). This chapter details the design and realization of this millikelvin THz setup, as well as the implementation and simulation of THz antennas required for efficient coupling of the THz radiation to the sample.

7.1.1 Terahertz generation by continuous-wave photomixing

The source we aim to use in our experiment is based on continuous-wave (CW) photomixing, a technique that generates THz radiation by mixing two CW lasers with slightly different optical frequencies $\nu_{1,2} = \nu_0 \pm f_{THz}/2$. As illustrated in Fig. 7.1.1, a CW photomixer typically consists of two CW lasers (with powers P_1 and P_2) illuminating a semiconductor (typically GaAs or InGaAs)[196]. The working principle involves the absorption of photons from the two lasers by the semiconductor. As the optical frequencies are larger than the energy gap of the semiconducting material $h\nu_{1,2} > E_{gap}$ ($E_{gap} = 1.42$ eV for GaAs) they create electron-hole pairs. When the semiconductor is integrated into a biased antenna, this process generates a photocurrent at the THz frequency, with the emission of THz radiation.

In the following we explain the underlying physics of CW photomixing using a simple formalism. The total electric field given by two detuned optical lasers mixed in a beam splitter or an optical fiber is (see Fig. 7.1.1)[196]:

$$\vec{E}(t) = \vec{E}_1(t) + \vec{E}_2(t) = \vec{E}_{1,0}e^{i(\omega+\omega_{THz}/2)t} + \vec{E}_{2,0}e^{i(\omega-\omega_{THz}/2)t-i\varphi} \tag{7.1.1}$$

Where we have defined φ as a the relative phase between the two electrical fields and $\omega_i = 2\pi\nu_i$. After calculating the optical intensity $I_L(t) \sim |\vec{E}(t)|^2$, Eq. 7.1.1 can be expressed in terms of powers as[196]:

$$P_L(t) = P_1 + P_2 + 2\sqrt{P_1 P_2}\cos\beta \cdot \cos\left(\omega_{THz}t + \varphi\right) \tag{7.1.2}$$

Where β is the relative angle between the polarizations of the two electrical fields. This equation shows that due to interference effect the total power of the mixed detuned lasers

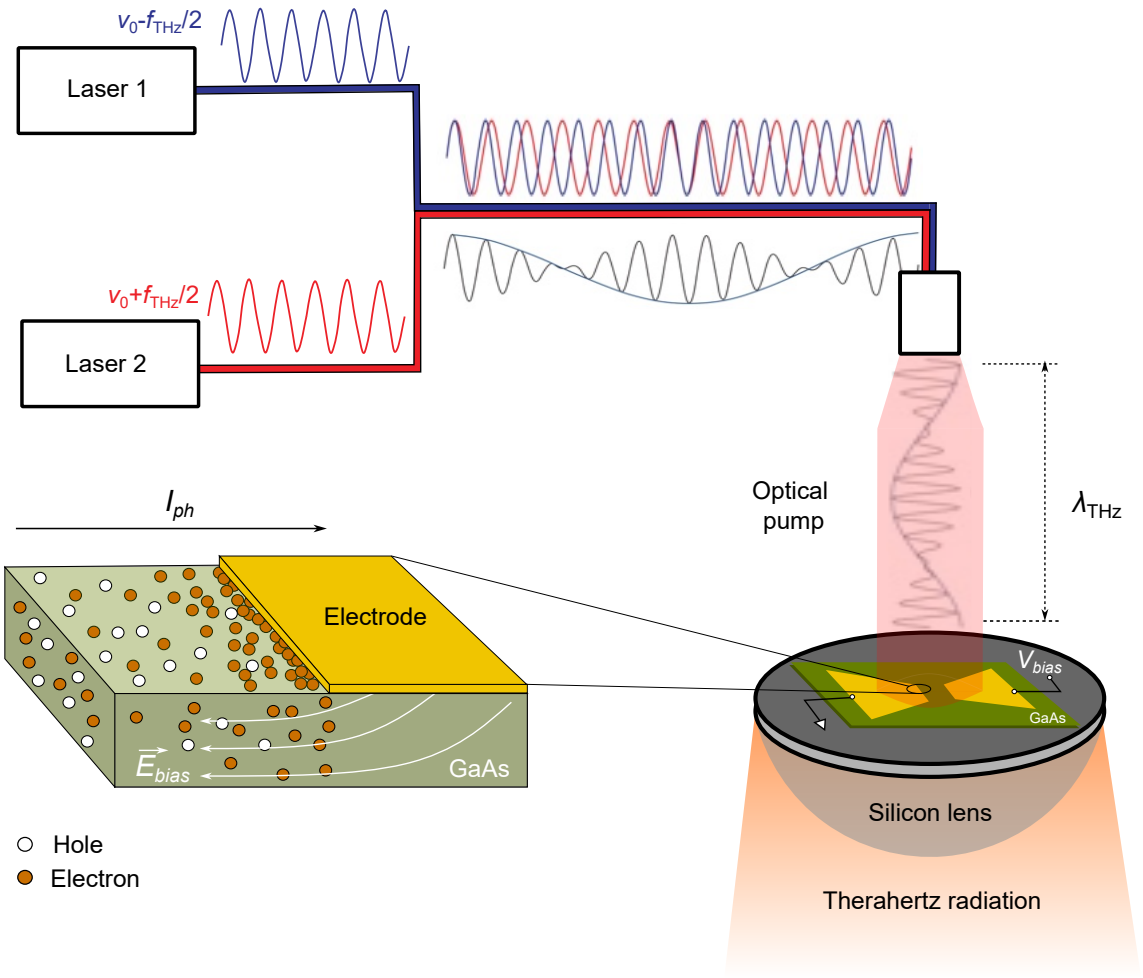

Figure 7.1.1: Schematic of the photomixing process. Two CW lasers with slightly different optical frequencies $\nu_{1,2} = \nu_0 \pm f_{THz}/2$ couple into a mixing fiber. Due to interference the total power of the mixed detuned lasers has a long-wavelength envelope that oscillates at THz frequency (λ_{THz}). The radiation impinges in a semiconducting layer (typically GaAs) generating free carriers (electrons-holes). The electrical field ($\vec{E}_{bias}$) induced by external biasing of the antenna results in a photocurrent, I_{ph}. The acceleration of free carriers generates electromagnetic radiation at THz frequency.

has a long-wavelength envelope that oscillates at THz frequency. When this oscillating optical radiation impinges on the semiconductor, it generates a time-dependent population of free charge carriers (electron-hole pairs) $n_{e-h}(t) \propto P_L(t)$ which also oscillates at THz frequencies[201]. As skecthed in Fig. 7.1.1, a metallic antenna is lithographically designed on top of the GaAs substrate[196]. By applying an external bias to the antenna, it is possible to generate an electric field $\vec{E}_{bias}$ that moves electrons and holes in opposite

directions. This spatial motion results in a periodic photocurrent $I_{ph}(t)$ of the form[196]:

$$I_{ph}(t) = \frac{eP_L(t)}{h\nu_0} = \underbrace{\frac{e(P_1+P_2)}{h\nu_0}}_{\text{DC component}} + \underbrace{2\frac{e\sqrt{P_1P_2}}{h\nu_0}\cos\beta\cdot\cos\left(\omega_{THz}t+\varphi\right)}_{\text{AC component}} \tag{7.1.3}$$

Where we have assumed for simplicity an ideal semiconductor with 100% absorption efficiency. Therefore, the photomixer acts as a THz-frequency switch: without external illumination, the semiconductor prevents current flow across the biased antenna; however, when illuminated with light above the semiconductor's bandgap, a current of free carriers flows across the antenna at the THz frequency. Here the photocurrent consists of a time-independent component (DC) and a time-dependent component oscillating at THz frequency (AC). Assuming the two lasers to have same power $P_1 = P_2 = P_L$ and polarization $\cos\beta = 1$, the photocurrent reads[196]:

$$I_{ph}(t) = \underbrace{2\frac{eP_L}{h\nu_0}}_{I_0}[1+\cos\left(\omega_{THz}t+\varphi\right)] \tag{7.1.4}$$

According to Larmor formula, the acceleration and deceleration of charge carriers leads to electromagnetic emissions $E_{THz}(t) \propto \partial I_{ph}(t)/\partial t$. Therefore, the antenna generates THz radiation according to[196]:

$$P_{THz} = \frac{1}{2}R_A I_0^2 = \frac{1}{2}R_A\left(\frac{2e}{h\nu_0}\right)^2 P_L^2 \tag{7.1.5}$$

Where R_A is the resistance of the antenna. This equation demonstrates that the THz beating generated by mixing two detuned lasers can be absorbed by a semiconducting material embedded in an antenna to produce THz radiation. While the above equation assumes ideal conditions, such as 100% efficiency and perfect polarization, experimental realizations may exhibit losses that suppress THz generation. However, even with these limitations, this technique is suitable for SPD experiments where only faint light fluxes are required.

This technique provides several advantages. First of all it provides easy tunability of the THz signal. The output THz frequency is given by:

$$f_{THz} = c\left(\frac{1}{\lambda_0} - \frac{1}{\lambda_0+\Delta\lambda}\right) \tag{7.1.6}$$

Where c is the speed of light, λ_0 is the central wavelength of the laser source, and $\Delta\lambda$ is the wavelength difference between the two lasers. To achieve an output radiation of 1 THz, a wavelength difference of $\Delta\lambda = 8$ nm is required with a laser source of $\lambda_0 = 1550$ nm, or $\Delta\lambda = 2$ nm with a laser source of $\lambda_0 = 780$ nm. As CW lasers are tunable from one tenth of nanometer to few nanometers, this technique provides an intrinsically widely tunable THz source. The linewidth of the THz radiation depends on the linewidth of

the used CW lasers, which is typically a few MHz to a few tens of MHz[196]. Finally, this technique can be easily operated at room temperature and is also versatile for low-temperature environments, making it a suitable solution for providing THz radiation in cryostats such as dilution refrigerators.

Spectral range of the THz source

As previously discussed, one of the key advantages of CW photomixing is the high tunability of the THz emission wavelength. To measure the spectral range of the THz source, which is crucial to design the experiment, we place a second GaAs photomixer below the emitter, acting as a receiver and measure the photocurrent generated in the receiver by sweeping the frequency of THz emission (Fig. 7.1.2). Due to their operational principle, THz photomixers can function interchangeably as emitters and receivers[197, 202, 203]. Specifically, the THz radiation absorbed by a photomixer, pumped with a near-infrared optical beating (with frequency ω_{THz}), induces a photocurrent which enables it to be used as a THz detector. The photocurrent recorded in the receiver has two components at ω_{THz}: one is the power of the lasers $P_L(t)$ used to pump the receiver, and the other is the THz radiation absorbed, which generates an electric field $U_{\mathrm{THz}}(t)$:

$$I_{\mathrm{ph}}(t) \propto P_L(t)U_{\mathrm{THz}}(t) \propto \cos(\omega_{\mathrm{THz}}t)\cos(\omega_{\mathrm{THz}}t + \Delta\phi) \tag{7.1.7}$$

Where $\Delta\phi$ is the phase difference between the two signals originating from the path difference between the two optical fibers transporting the mixed laser (ΔL) and the gap between the emitter and the receiver (d). The phase difference can therefore be expressed as[188]:

$$\Delta\phi = \frac{\omega_{\mathrm{THz}}}{c}\left(\Delta L \cdot n_{\mathrm{Fiber}} + d \cdot n_{\mathrm{Air}}\right) \tag{7.1.8}$$

Where n_{Fiber} and n_{Air} are the refractive indices of the optical fiber and air, respectively. Since ΔL, d, n_{Fiber}, and n_{Air} are fixed in our experimental setup, sweeping ω_{THz} generates oscillations in the photocurrent measured in the receiver due to this phase difference, as shown in Fig. 7.1.2c. Therefore, by sweeping ω_{THz} and analyzing the amplitude of the oscillations, we can determine the intensity of the THz signal generated by the emitter across the entire frequency range (Fig. 7.1.2d). We observe that the spectral range of our THz sources ranges from about 500 GHz to 1.6 THz[188].

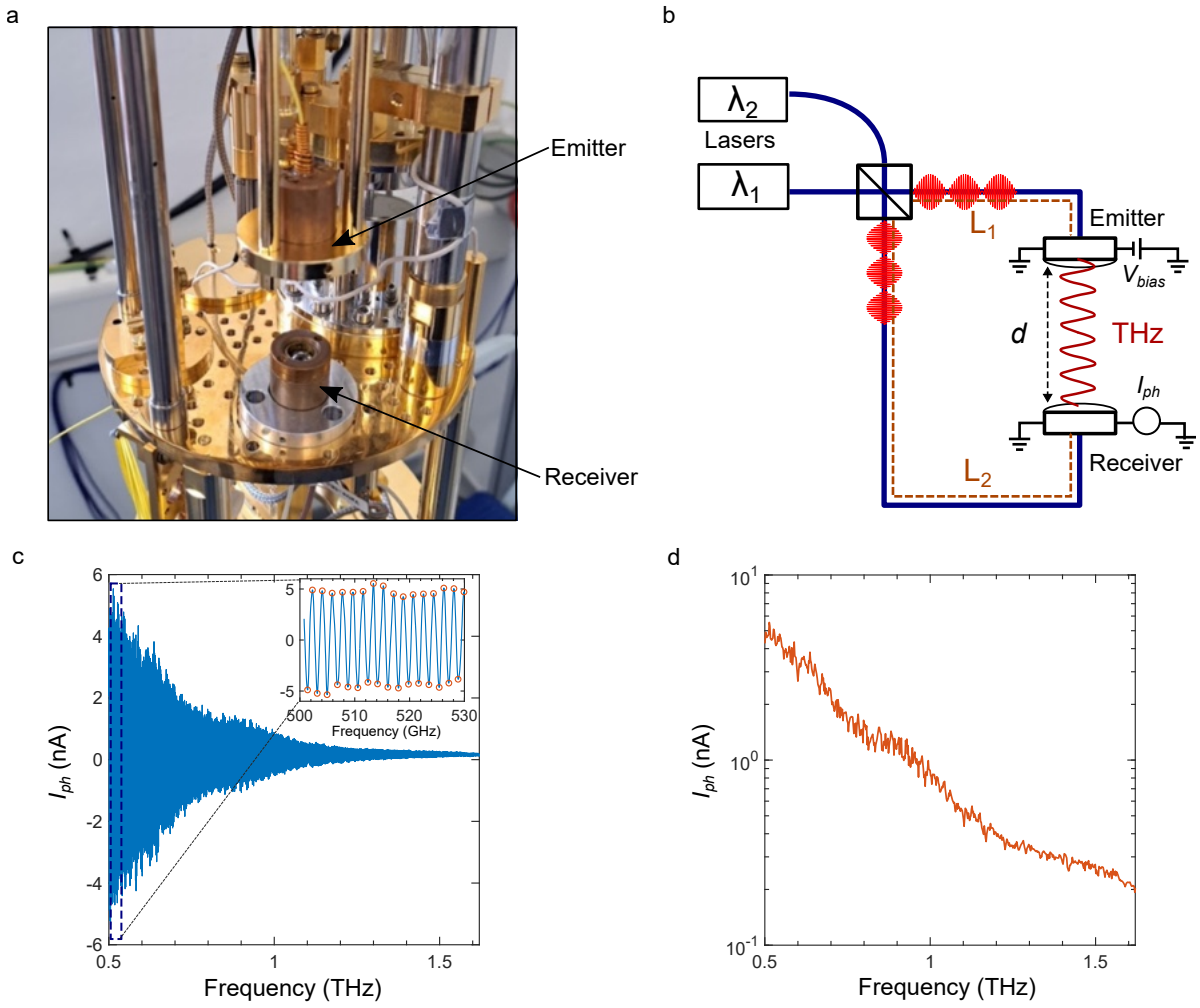

Figure 7.1.2: Measurement of the spectral range of the THz source. **(a)** Optical image of the setup implemented to measure the spectral range of the THz source. **(b)** Schematic of the measurement process. The two photomixers (emitter and receiver) are positioned facing each other. The photomixed signal from the lasers illuminates both the emitter and receiver. The THz signal generated by the emitter induces a measurable photocurrent in the receiver. As described in Eq. 7.1.1, the path difference between the emitter and receiver results in a phase shift in the photocurrent measured at the receiver. **(c)** Photocurrent measured in the receiver, I_{ph} while sweeping the beating frequency, ω_{THz}. The inset is a zoom in the frequency range 500 GHz to 530 GHz, showing the oscillations in photocurrent given by the phase difference $\Delta\phi$. The red dots indicate the amplitude of the oscillations. **(d)** Amplitude of the oscillations plotted for all the frequency range explored. We measure a THz signal from the emitter in the range between 500 GHz and 1.6 THz. The measurements were performed by Leon Schubert [188] under my supervision.

7.1.2 Design of the experimental setup

The primary experimental challenge in implementing a THz setup at millikelvin temperatures is ensuring proper thermalization of the components to maintain a low sample temperature.

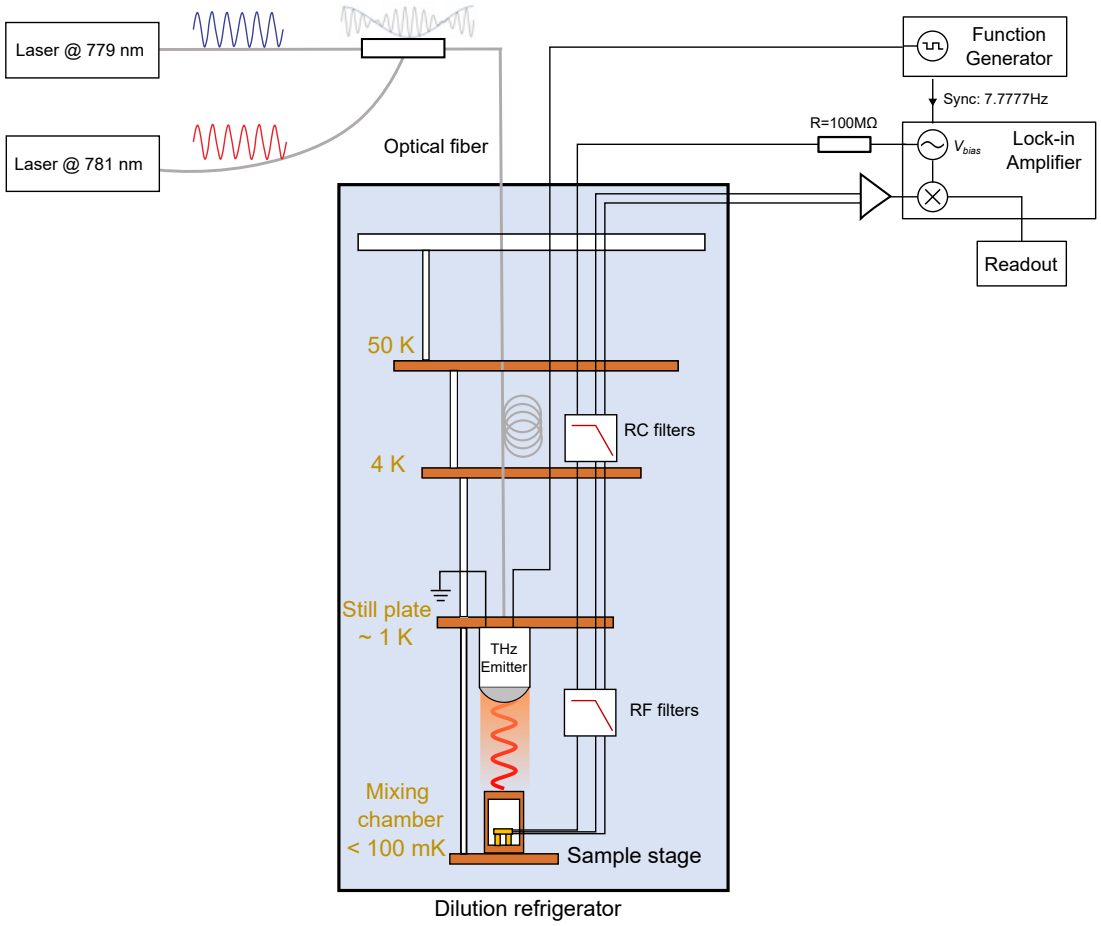

Figure 7.1.3: Schematic of the millikelvin THz setup. The millikelvin THz setup is adapted from the near-infrared optoelectronic setup shown in Fig. 4.2.2. The two detuned CW lasers are located at room-temperature outside of the cryostat.The mixed signal is couple to the GaAs photomixer through a cryo-compatible optical fiber. The GaAs THz photomixer is thermally anchored at the 1 K still plate to ensure proper thermalization and externally biased via an arbitrary wave-function generator. The emitted THz radiation is coupled in free space to the sample stage located at the mixing chamber plate.

When placed within the dilution refrigerator, the THz photomixer introduces an additional heat source that must be adequately cooled. Based on the working principle described above and the schematics in Fig. 7.1.1, the power dissipated by the photomixer (P_{ph}) has two contributions: the Joule heating generated by the photocurrent flowing

through the antenna ($I_{ph}^2 R_A$) and the near-infrared optical radiation (P_L) that pumps the GaAs photomixer. Thus:

$$P_{ph} = P_J + P_L = I_{ph}^2 R_A + P_L \tag{7.1.9}$$

In our experiment, the power provided by the external CW lasers is $P_L \sim 20$ mW, while the Joule heating dissipated by the photomixer is estimated to be $P_{ph} \sim 1$ mW (considering $R_A \sim 100$ kΩ and $I_{ph} \sim 100$ µA). From this estimation, it is evident that the majority of the power dissipated by the photomixer originates from the optical radiation of the near-infrared lasers: $P_{ph} \approx P_L$. As discussed in Chapter 4, the cooling power of a dilution refrigerator at the millikelvin stage depends on the He^3 flow rate. In our setup, the typical flow rate is approximately 300 µmol/s, resulting in a cooling power of $\dot{Q} \simeq 250$ µW at $T = 100$ mK. Given that the cooling power of the mixing chamber is significantly lower than the tens of mW of power dissipated by the photomixer, we designed custom components to ensure proper thermalization of the photomixer at the still plate of the dilution refrigerator[188]. A general schematic of the setup is shown in Fig. 7.1.3. The two near-infrared CW lasers are located outside the cryostat and connected to the THz photomixer via cryo-compatible optical fiber and a vacuum-compatible feedthrough mounted on the top of the cryostat. The THz photomixer, thermally anchored at the still plate, is connected with this optical fiber and requires a separate biasing line. The coupling of radiation to the sample stage located at the mixing chamber occurs in free space.

Fig. 7.1.4 illustrates the design and realization of the custom components fabricated to integrate the photomixer into the dilution refrigerator. The main components are the optical stage and the sample stage. The optical stage mounts the THz photomixer on top of the sample stage and has three rods to ensure proper thermal connection to the still plate. It has three set screws allowing movement in the z-direction, to adjust the focus. The sample stage is shielded to protect against thermal radiation from the top stage, which irradiates at around 1 K. The stage also features a small hole (1 cm diameter) to enable THz radiation to reach the sample stage. All parts are fabricated from high-purity oxygen-free copper and coated with 1 µm of gold to ensure high thermal conductivity required for proper thermalization [204].

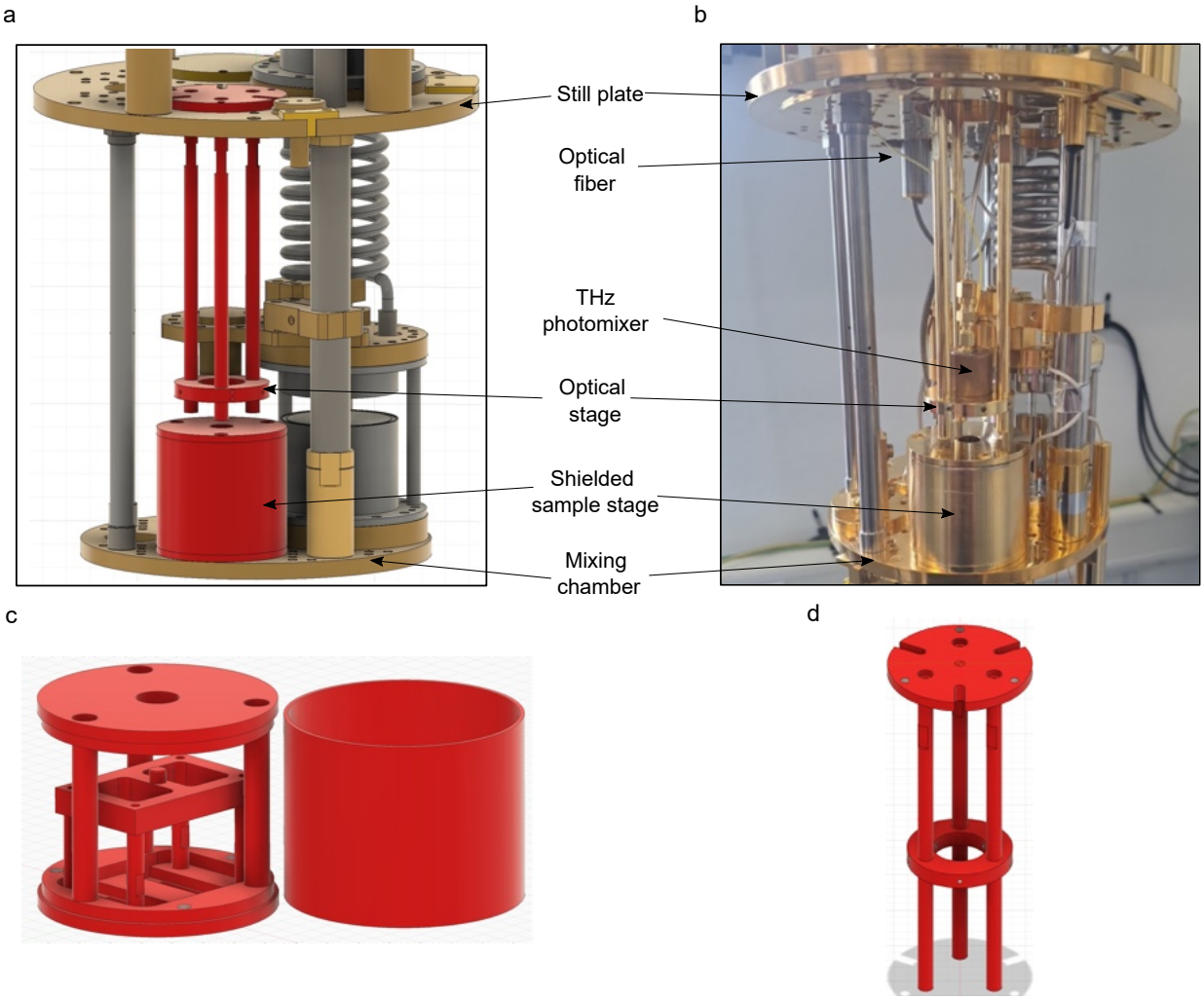

Figure 7.1.4: Custom designed components. **(a)** In red the designed custom components. The shielded sample stage is thermally anchored to the mixing chamber stage while the optical stage is thermally anchored to the still plate. **(b)** Custom oxygen-free copper components, gold-coated and integrated into the BlueFors dilution refrigerator. **(c)-(d)** Detailed design of the sample stage **(c)** and of the optical stage **(d)**. The CAD design of the custom parts was performed by Leon Schubert [188] under my supervision.

7.1.3 Testing of the Experimental Setup

To confirm that our experimental setup achieves proper thermalization, we conducted a test cool-down while monitoring the temperatures of the still plate and the mixing chamber [188]. In Fig. 7.1.5, we plot the temperature over time measured at the still plate (blue) and the mixing chamber (red). Without switching on the laser radiation or the photomixer bias, the temperatures stabilize at 1.166 K and 66 mK for the still plate and mixing chamber, respectively. Upon pumping the photomixer optical radiation at the highest power, which corresponds to dissipating power P_L at the still plate, we observe an increase in temperature at both the mixing chamber (74 mK) and the still plate (1.199 K). We also record the temperature while applying the external bias necessary to generate THz radiation in the photomixer. At this stage, a photocurrent flows through the photomixer, adding an additional heat source ($I_{ph}^2 R_A$) to the still plate as described in Eq. 7.1.2, resulting in a further increase in the still plate temperature (1.204 K).

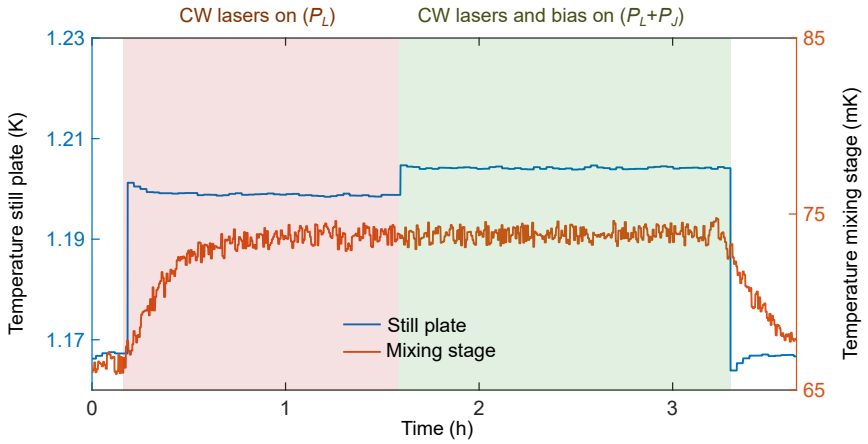

Figure 7.1.5: Test cooldown of the THz optoelectronic setup. The still plate temperature (blue) and mixing plate temperature (red) measured during the test cooldown and photomixer operation. The red shaded region indicates the period when the photomixer is pumped with optical radiation at maximum power. The green shaded region indicates the period when the photomixer is both pumped with optical radiation and biased. The measurements were performed by Leon Schubert [188] under my supervision.

Notably, the temperature increase induced by the Joule heating of the photomixer is significantly lower than that caused by the near-infrared laser radiation alone. This indicates that the primary source of heat is the optical radiation rather than the Joule heating, as we have roughly predicted from Eq. 7.1.2. The temperature of the mixing chamber increases by a few mK when the lasers are switched on but does not change appreciably when the DC bias is applied. While the increase in base temperature at the still plate can be attributed to the increased heat load, the temperature rise at the mixing chamber may be explained by enhanced thermal radiation from the still plate due to its elevated temperature. Therefore, the insertion of the THz photomixer into the dilution

refrigerator causes a slight temperature increase of approximately 8 mK. The additional heat source does not interfere with the dilution process, allowing us to shine THz radiation while maintaining the sample at millikelvin temperatures (< 100 mK) which are well below the typical critical temperatures of MATBG devices.

7.2 Development of THz antennas for efficient light coupling

A significant challenge when dealing with THz radiation, is the large wavelengths of photons of these energies (1 THz corresponds approximately to 300 µm) which are much larger than the typical size of MATBG devices, resulting in a very small cross-section for the absorption process[34]. One potential strategy to address this issue is to integrate the device into an antenna structure. Due to strong field enhancement, the antenna concentrates the incident THz light around the gap region, funneling the incident radiation to the active area. Various types of antennas have been extensively implemented in photodetectors based on 2D materials to enhance radiation coupling[92, 205–208]. Our approach is similar to those followed by these other research groups. In its simplest definition, an antenna is a transition device between a free-space wave and a guided wave, and vice versa[209]. It can act as an emitter of radiation which converts a current into photons or as receiver which operates in the opposite way. In both cases the antenna acts as a boundary condition for the electric field and consequently, the behavior of an antenna is strongly dependent on its geometry.

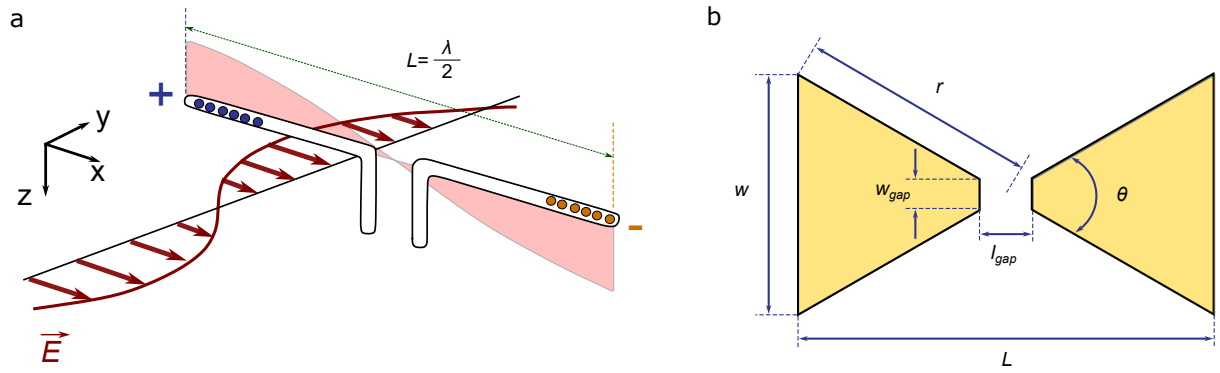

Figure 7.2.1: Dipole and bow-tie antennas. **(a)** Schematics illustrating the general working principle of a dipole antenna in the receiving configuration. The incoming electric field $\vec{E}$ moves the carriers in the conductor, transforming the incident photon into a current. Notably the length of the antenna L determines the resonant condition according to $\lambda/2 = L$. **(b)** Schematics of all the geometrical parameters constituting a bow-tie antenna. In this geometry the resonance condition is not given by Eq. 7.2, but it has to be calculated according to these geometrical parameters.

Dipole and bow-tie antennas

The simplest type of antenna is the half-wave dipole antenna as the one illustrated in Fig. 7.2.1a, which consists of two infinitely thin metallic wires[209]. In the transmitting scenario, given the geometry of the dipole antenna, the movement of charge carriers within

the conductor generates an electric field polarized along the direction of the dipole (Fig. 7.2.1a). Similarly, in the receiving scenario, it funnels the incident radiation along this direction. The length of the antenna determines the resonance condition, denoted as λ^*. At this specific condition, the imaginary part of the dipole's impedance, or reactance, is zero, resulting in a purely resistive impedance. This condition simplifies impedance matching with the transmission line, ensuring maximum power transfer by minimizing reflections and losses. For a dipole antenna, the resonance condition occurs when its length is half the wavelength of the operating frequency:

$$\lambda^* = 2L \tag{7.2.1}$$

A more versatile geometry is represented by the bow-tie antenna. Bow-tie antennas provide more broadband absorption compared to dipole antennas. However, the resonance condition is not as straightforward as in the dipole case (Eq. 7.2) and depends on more parameters than just the length[210] (see Fig. 7.2.1b). There is a large range of antennas available other than the dipole and bow-tie, such as log-spiral, log periodic etc.[196]. In our experiment, we chose a bow-tie antenna design, which is a notably simpler geometry compared to the others and makes the fabrication and design easier. To properly design the antenna geometry, we use COMSOL Multiphysics to simulate the spectral response of the bow-tie antennas, exploring different geometrical parameters.

Design of THz antennas for photovoltage experiment with superconducting MATBG

To properly design the THz antennas required for the photodetection experiment with superconducting MATBG, we consider the physical parameters involved in the photodetection process, which will also reflect on the antenna geometry. The primary energy scale is defined by the superconducting gap of MATBG. As discussed in Chapter 1, to break Cooper pairs and generate quasiparticles, the THz photon energy must exceed the superconducting gap of approximately 1 meV $\sim$ 0.24 THz ($E_{THz} > \Delta_{SC}$). The photon excitation energies in the experiments are determined by the spectral range of the THz source, which spans approximately 0.5-1.5 THz, corresponding to an energy range of 2-6 meV. Considering that the source power is greater at the lower end of the spectrum (Fig. 7.1.2d), we designed the antenna geometry to achieve resonance at approximately $f^* = 0.5$ THz. This frequency represents the optimal balance between having a photon energy higher than the MATBG superconducting gap and the available power delivered to the sample.

Another crucial aspect of the antenna's geometry is the antenna gap size (l_{gap}) and the angle of the bow-tie arms (θ). The l_{gap} must be carefully selected to match the spatial dimensions of typical MATBG devices. In all our simulations, we have used $l_{gap} = 25$ µm, which is compatible with the size of our MATBG devices. Regarding the angle of the bow-tie arms, a larger angle increases radiation coupling. However, this conflicts with the experimental requirement of having electrodes perpendicular to the MATBG device for electrical connection. Therefore, in both simulations and experimental realizations, we use angles between 60° and 90°. Taking these considerations into account, we first simulate

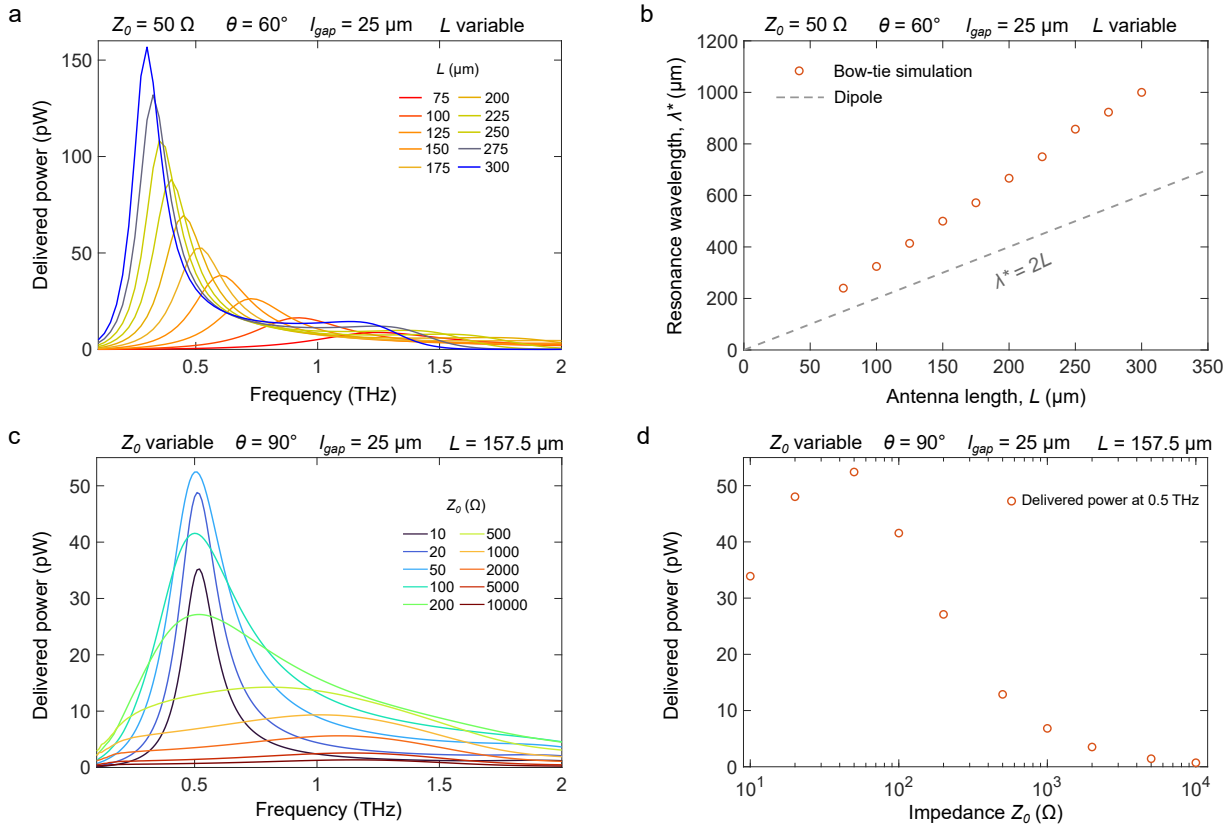

Figure 7.2.2: Frequency response simulation of a bow-tie antenna. **(a)** Simulation of the delivered power at the antenna feed versus the frequency of incident THz radiation for various bow-tie antenna lengths, L using COMSOL. The other geometrical parameters are: $l_{gap} = 25$ µm, $\theta = 60°$, thickness $d = 60$ nm and feed impedance $Z_0 = 50$ Ω. **(b)** Resonance wavelengths λ^* for the bow-tie antennas simulated in **(a)**, extracted from the peaks in delivered power. The gray dashed line indicates the resonance condition for an ideal dipole antenna, $\lambda^* = 2L$. **(c)** Simulation of the delivered power for different values of feed impedance, Z_0 for a bow-tie antenna of length $L = 157.7$ µm, designed be resonant at approximately 0.5 THz. The other geometrical parameters are: $l_{gap} = 25$ µm, $\theta = 90°$, thickness $d = 60$ nm and $L = 157.7$ µm. **(d)** Delivered power at 0.5 THz for the antennas simulated in **(c)**. The simulations were performed by Carl Hudeczek[189] under my supervision.

the behavior of the bow-tie antennas for different lengths L, while keeping fixed the other experimental parameters, specifically $l_{gap} = 25$ µm, $\theta = 60°$, thickness $d = 60$ nm, and feed impedance $Z_0 = 50$ Ω. In Fig. 7.2.2a, we simulate the power delivered at the antenna's feed vs. frequency for L ranging from 75 µm to 300 µm. We observe that at some specific frequencies, there is a maximum of transferred power which corresponds to the resonance frequency. By increasing the antenna length, the resonance frequency shifts towards lower values. In Fig. 7.2.2b, we plot the resonance condition extracted from the simulation for different antenna lengths and compare it to the expected values for a dipole antenna. We observe that the resonance wavelength for the bow-tie antennas is larger than the length

of the antenna: $\lambda^* > 2L$.

Another major challenge in the integration of this material into an antenna structure is represented by the high input impedance. As the fabrication of low-resistance ohmic contacts in 2D materials is challenging[150], there is a large impedance mismatch between the metallic antenna and the 2D material which substantially limits the maximum power transferable. Recent works have shown imporvements in the fabrication protocol to minimize this effects on another 2D superconductor, NbSe2 [92]. Using the fabrication protocol described in Chapter 3, we expect a contact resistance of our MATBG devices of approximately a few kΩ/µm. In Fig. 7.2.2c, we simulate the delivered power for an antenna designed for resonance frequency $f^* = 0.5$ THz, for different values of input impedance Z_0, and in Fig. 7.2.2d, we plot the delivered power at 0.5 THz for different values of Z_0. We notice that the maximum power delivery is achieved at 50 Ω and progressively drops at higher impedance values. This simulation suggests that improvements in our fabrication protocol might be required to reduce the contact resistance and maximize the power transfer.

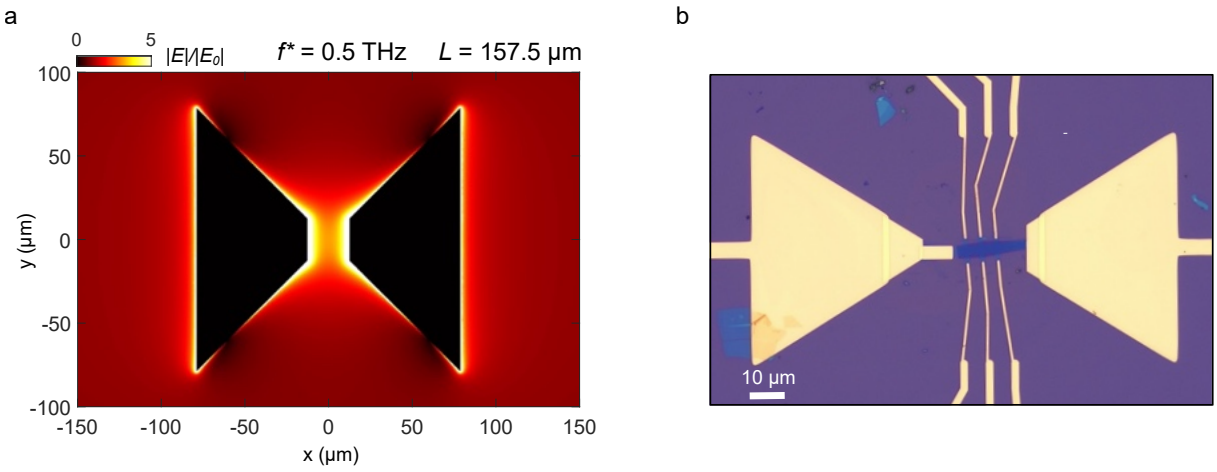

Figure 7.2.3: Simulation and realization of THz bow-tie antennas. (a) Simulation of the electric field enhancement $|E|/|E_0|$ for a bow-tie antenna. Experimental parameters are: $\lambda^* = 587.8$ µm, $L = 157.5$ µm, $l_{gap} = 25$ µm, $\theta = 90°$ and thickness $d = 60$ nm. In this simulation, the antenna arms are assumed to be perfect conductors. This boundary condition in COMSOL sets the electric field perpendicular to the conductor's surface. The simulation was performed by Carl Hudeczek[189] under my supervision. **(b)** Experimental realization of a single-layer graphene sample embedded in a bow-tie antenna. The experimental parameters of the antenna are: $L = 164.4$ µm, $l_{gap} = 40$ µm and $\theta = 60°$. The device was fabricated by Leon Schubert[188] under my supervision.

In Fig. 7.2.3a, we present a COMSOL simulation of the spatial distribution of the electric field enhancement for a bow-tie antenna with a resonance frequency of 0.5 THz ($L = 157.7$ µm). Notably, the central region of the antenna exhibits the highest radiation

intensity, which is where the sample is positioned. Following insights from the simulations, we proceed with the fabrication of test samples. Given the challenges of the stacking process of twisted bilayers described in Chapter 3, we fabricate the test samples using single-layer graphene encapsulated in hBN. Our approach is as follows: first, we pre-fabricate the antenna arms using a photolithography technique and evaporate chromium/gold (5 nm/50 nm), leaving an antenna gap of approximately 50-60 µm. Then, we stack a single-layer graphene sample encapsulated with hBN using the standard van der Waals technique described in Chapter 3 and deposit it within the antenna gap, where the electric field enhancement is maximal. In the final fabrication step, the antenna arms are electrically connected to the sample using electron-beam lithography and evaporating chromium/gold (5 nm/50 nm). Fig. 7.2.3b shows an optical image of a chromium/gold (5 nm/50 nm) antenna fabricated on a silicon chip with similar geometrical parameters as those used for the simulation in Fig. 7.2.3a. This test sample will be used as a calibration for the cryogenic THz setup described in Section 7.1.

Conclusion and Perspectives

The superconducting state formed by twisting two graphene layers at the magic-angle of 1.1° (MATBG) leads to a novel superconducting phase with a carrier density of only 10^{11} electrons per cm^2. The utilization of ultra-low carrier density moiré superconductors represents a novel concept from the material perspective to enable far-infrared SPD, which is notoriously underdeveloped. In this thesis, we have taken a major step towards exploiting MATBG for infrared SPD, investigating both the fundamental physics of this unconventional superconducting phase[P2] and demonstrating, for the first time, near-infrared SPD[P1]. Since the discovery of MATBG in 2018 [114], researchers worldwide have begun investigating these captivating materials, discovering an entire family of graphene-based superconductors that share these unique superconducting properties [95–97, 145]. As a result, the scope of this thesis extends beyond MATBG to include the entire family of graphene-based superconductors.

Given the novelty and sensitivity of two-dimensional moiré superconductors, significant effort has been dedicated to the experimental aspects of this research. Firstly, in optimizing the fabrication of twisted bilayer graphenes, which is extremely challenging due to low yield. In Chapter 3, we have carefully described the most recent progress and detailed the fabrication protocol perfected over the years for MATBG samples. This protocol guarantees high fabrication yield and quality[P6]. Achieving highly reproducible and high-quality MATBG samples is crucial for obtaining a sharp superconducting transition, necessary for the SPD applications presented here. Similarly, in Chapter 4, we have described the implementation of a custom-made optoelectronic setup for SPD, which combines optics and electronics and constitutes a major experimental undertaking.

The following chapters focused on the experimental results achieved. In Chapter 5 we have described the first optoelectronic experiment in which we illuminated the superconducting state of MATBG with a near-infrared source while monitoring the electronic transport. By measuring the bolometric response upon light illumination, we were able to investigate the thermal properties of the superconducting state. This work provided the first measurement of the thermal conductivity in the superconducting state of MATBG, a fundamental thermal property important for photodetection applications. This represents the first optoelectronic study to examine the thermal properties and light-matter interac-

tion in the superconducting state of MATBG, and one of the first optoelectronic studies in MATBG overall. This work constitutes an important contribution to understanding the fundamental physics of the superconducting state of MATBG.

More importantly, in Chapter 6, we performed a proof-of-concept experiment in which, by voltage-biasing MATBG close to the superconducting transition and illuminating it with a highly attenuated laser source, we successfully demonstrated near-infrared SPD. This exciting result marks the first major step towards our long-term vision of extending superconducting SPD to long-wavelength photons and constitutes a major achievement in this PhD thesis.

In the endeavor of extending detection to lower energy photons, in Chapter 7, we discussed the most recent progress in extending SPD to the far-infrared and THz range. Specifically, we have discussed the implementation of a novel optoelectronic THz setup capable of operating at millikelvin temperatures while providing tunable THz excitation. Simultaneously, we have shown recent advances in designing and fabricating THz antennas to couple radiation to the sample efficiently.

Perspectives

This PhD thesis opens up several promising avenues for future research. The most immediate and promising follow-up is using MATBG as a far-infrared SPD. Initial steps in this direction are encouraging (see Chapter 7). One approach could be to replicate the proof-of-principle experiment conducted in the near-infrared, described in Chapter 6, using far-infrared radiation. In the near-infrared experiment, incident single photons caused a complete disruption of the superconducting state, resulting in a large voltage output [P1]. However, given that the superconducting gap of MATBG is approximately 1 meV, a single THz photon ($\sim$ 4 meV) may not generate enough quasiparticles to break superconductivity fully. Therefore, alternative detection mechanisms that offer greater sensitivity could also be explored. Bolometric detection, as proposed in [34], remains a viable option for THz SPD. Another promising detection scheme could involve a kinetic inductance readout, where the absorbed photon shifts the resonance frequency, δf, proportional to the ratio of generated quasiparticles (δn_{qp}) to Cooper pairs (n_s): $\delta f \sim \delta n_{qp}/n_s$. Given MATBG's record-low carrier density of 10^{11} electrons per cm^2, a significant change in kinetic inductance is expected even with the absorption of a low-energy photon[P1]. Additionally, implementing nanostructures similar to superconducting nanowire SPDs could be another viable direction.

Beyond SPD, the THz millikelvin setup presents an intriguing experimental probe for studying correlated phases in 2D materials. Previous optoelectronic studies on MATBG, such as those described in this thesis, have used excitation wavelengths much larger than the flatband bandwidth, targeting high-energy dispersive bands [P2, P8]. However, the investigation of flatbands with far-infrared radiation remains largely unexplored[P9]. Specifically, the correlated band gaps with energies below 1 meV (Chapter 2), typically measured in transport, could be studied by applying THz radiation at low temperatures. This direc-

tion is of notable interest, as evidenced by recent works that have attempted to explore interactions in MATBG using THz photocurrent [211] and spectroscopy [212], as well as the development of far-infrared spectroscopy tools at millikelvin temperatures [195].

Another follow-up research direction, building on Chapter 5, could involve investigating the thermal properties of MATBG. In the experiment described in Chapter 5, the bolometric response of MATBG electrons was probed using near-infrared radiation. Future experiments could employ configurations where local micro-heaters induce the temperature gradient [213, 214], enabling more efficient heating of the electronic ensemble and providing directional heat flows in sample geometries that are easier to model and investigate. A limitation of our previous experiment was the restricted range of electronic temperatures we could explore, which was well below the critical temperature. To address this, alternative temperature readout mechanisms, such as Johnson noise thermometry, could be utilized to offer more sensitive and broader readout schemes [175, 179, 215].

In conclusion, the experimental work presented in this thesis has successfully demonstrated the potential of the superconducting state of MATBG for infrared SPD. These findings strongly encourage further exploration to extend SPD capabilities to lower energies using MATBG and other low-carrier density graphene-based superconductors. This seminal work paves the way for the development and design of innovative quantum devices and sensors that exploit the unique characteristics of moiré superconductors, ultimately advancing the field of quantum sensing.

Bibliography

[1] Planck, M. On the improvement of Wien's equation for the spectrum. *Verh. Dtsch Phys. Ges.* **2,** 237–45 (1900).

[2] Lewis, G. N. The conservation of photons. *Nature* **118,** 874–875 (1926).

[3] Einstein, A. On a heuristic point of view about the creation and conversion of light. *Annalen der Physik* **17,** 132–48 (1905).

[4] Morozov, D. V., Casaburi, A. & Hadfield, R. H. Superconducting photon detectors. *Contemporary Physics* **62,** 69–91 (2021).

[5] Hadfield, R. H. Single-photon detectors for optical quantum information applications. *Nat. Photonics* **3,** 696–705 (2009).

[6] Yin, J., Li, Y.-H., Liao, S.-K., Yang, M., Cao, Y., Zhang, L., Ren, J.-G., Cai, W.-Q., Liu, W.-Y., Li, S.-L., Shu, R., Huang, Y.-M., Deng, L., Li, L., Zhang, Q., Liu, N.-L., Chen, Y.-A., Lu, C.-Y., Wang, X.-B., Xu, F., Wang, J.-Y., Peng, C.-Z., Ekert, A. K. & Pan, J.-W. Entanglement-based secure quantum cryptography over 1,120 kilometres. *Nature* **582,** 501–505 (2020).

[7] Knill, E., Laflamme, R. & Milburn, G. J. A scheme for efficient quantum computation with linear optics. *Nature* **409,** 46–52 (2001).

[8] Battersby, C., Armus, L., Bergin, E., Kataria, T., Meixner, M., Pope, A., Stevenson, K. B., Cooray, A., Leisawitz, D., Scott, D., Bauer, J., Bradford, C. M., Ennico, K., Fortney, J. J., Kaltenegger, L., Melnick, G. J., Milam, S. N., Narayanan, D., Padgett, D., Pontoppidan, K., Roellig, T., Sandstrom, K., Su, K. Y. L., Vieira, J., Wright, E., Zmuidzinas, J., Staguhn, J., Sheth, K., Benford, D., Mamajek, E. E., Neff, S. G., Carey, S., Burgarella, D., De Beck, E., Gerin, M., Helmich, F. P., Moseley, S. H., Sakon, I. & Wiedner, M. C. The origins space telescope. *Nat. Astron.* **2,** 596–599 (2018).

[9] Karasik, B. S., Sergeev, A. V. & Prober, D. E. Nanobolometers for THz Photon Detection. *IEEE Trans. Terahertz Sci. Technol.* **1,** 97–111 (2011).

[10] Benford, D. J. & Moseley, S. H. Cryogenic detectors for infrared astronomy: the Single Aperture Far-InfraRed (SAFIR) Observatory. *Nucl. Instrum. Methods Phys. Res. A* **520,** 379–383 (2004).

[11] Marsh, D. J. E., Fong, K. C., Lentz, E. W., Šmejkal, L. & Ali, M. N. Proposal to detect dark matter using axionic topological antiferromagnets. *Phys. Rev. Lett.* **123,** 121601 (2019).

[12] Schütte-Engel, J., Marsh, D. J. E., Millar, A. J., Sekine, A., Chadha-Day, F., Hoof, S., Ali, M. N., Fong, K. C., Hardy, E. & Šmejkal, L. Axion quasiparticles for axion dark matter detection. *J. Cosmol. Astropart. Phys.* **2021,** 066 (2021).

[13] Tinkham, M. *Introduction to Superconductivity* 2nd ed. (McGraw-Hill, New York, NY, 1995).

[14] Cabrera, B., Clarke, R. M., Colling, P., Miller, A. J., Nam, S. & Romani, R. W. Detection of single infrared, optical, and ultraviolet photons using superconducting transition edge sensors. *Appl. Phys. Lett.* **73,** 735–737 (1998).

[15] Irwin, K. D. & Hilton, G. C. Transition-Edge Sensors. *Topics Appl. Phys.* **99.** ISBN: 3540201130, 63–149 (2005).

[16] Gol'tsman, G. N., Okunev, O., Chulkova, G., Lipatov, A., Semenov, A., Smirnov, K., Voronov, B., Dzardanov, A., Williams, C. & Sobolewski, R. Picosecond superconducting single-photon optical detector. *Applied Physics Letters* **79,** 705–707 (2001).

[17] Semenov, A. D., Gol'tsman, G. N. & Korneev, A. A. Quantum detection by current carrying superconducting film. *Physica C Supercond.* **351,** 349–356 (2001).

[18] Marsili, F., Verma, V. B., Stern, J. A., Harrington, S., Lita, A. E., Gerrits, T., Vayshenker, I., Baek, B., Shaw, M. D., Mirin, R. P. & Nam, S. W. Detecting single infrared photons with 93% system efficiency. *Nat. Photonics* **7,** 210–214 (2013).

[19] Verma, V. B., Korzh, B., Walter, A. B., Lita, A. E., Briggs, R. M., Colangelo, M., Zhai, Y., Wollman, E. E., Beyer, A. D., Allmaras, J. P., Vora, H., Zhu, D., Schmidt, E., Kozorezov, A. G., Berggren, K. K., Mirin, R. P., Nam, S. W. & Shaw, M. D. Single-photon detection in the mid-infrared up to 10 μm wavelength using tungsten silicide superconducting nanowire detectors. en. *APL Photonics* **6,** 056101 (2021).

[20] Karasik, B. S., Pereverzev, S. V., Soibel, A., Santavicca, D. F., Prober, D. E., Olaya, D. & Gershenson, M. E. Energy-resolved detection of single infrared photons with $\lambda = 8$ μm using a superconducting microbolometer. *Appl. Phys. Lett.* **101,** 052601 (2012).

[21] Day, P. K., LeDuc, H. G., Mazin, B. A., Vayonakis, A. & Zmuidzinas, J. A broadband superconducting detector suitable for use in large arrays. *Nature* **425,** 817–821 (2003).

[22] Walsh, E. D., Efetov, D. K., Lee, G.-H., Heuck, M., Crossno, J., Ohki, T. A., Kim, P., Englund, D. & Fong, K. C. Graphene-based Josephson-junction single-photon detector. *Phys. Rev. Appl.* **8** (2017).

[23] Walsh, E. D., Jung, W., Lee, G.-H., Efetov, D. K., Wu, B.-I., Huang, K.-F., Ohki, T. A., Taniguchi, T., Watanabe, K., Kim, P., Englund, D. & Fong, K. C. Josephson junction infrared single-photon detector. *Science* **372,** 409–412 (2021).

[24] Lee, G.-H., Efetov, D. K., Jung, W., Ranzani, L., Walsh, E. D., Ohki, T. A., Taniguchi, T., Watanabe, K., Kim, P., Englund, D. & Fong, K. C. Graphene-based Josephson junction microwave bolometer. *Nature* **586,** 42–46 (2020).

[25] Kokkoniemi, R., Girard, J.-P., Hazra, D., Laitinen, A., Govenius, J., Lake, R. E., Sallinen, I., Vesterinen, V., Partanen, M., Tan, J. Y., Chan, K. W., Tan, K. Y., Hakonen, P. & Möttönen, M. Bolometer operating at the threshold for circuit quantum electrodynamics. *Nature* **586,** 47–51 (2020).

[26] Lau, J. A., Verma, V. B., Schwarzer, D. & Wodtke, A. M. Superconducting single-photon detectors in the mid-infrared for physical chemistry and spectroscopy. *Chem. Soc. Rev.* **52,** 921–941 (2023).

[27] Johnson, B. R., Reed, M. D., Houck, A. A., Schuster, D. I., Bishop, L. S., Ginossar, E., Gambetta, J. M., DiCarlo, L., Frunzio, L., Girvin, S. M. & Schoelkopf, R. J. Quantum non-demolition detection of single microwave photons in a circuit. *Nat. Phys.* **6,** 663–667 (2010).

[28] Kono, S., Koshino, K., Tabuchi, Y., Noguchi, A. & Nakamura, Y. Quantum non-demolition detection of an itinerant microwave photon. *Nat. Phys.* **14,** 546–549 (2018).

[29] Komiyama, S., Astafiev, O., Antonov V, V., Kutsuwa, T. & Hirai, H. A single-photon detector in the far-infrared range. en. *Nature* **403,** 405–407 (2000).

[30] Komiyama, S. Single-photon detectors in the terahertz range. *IEEE J. Sel. Top. Quantum Electron.* **17,** 54–66 (2011).

[31] Echternach, P. M., Pepper, B. J., Reck, T. & Bradford, C. M. Single photon detection of 1.5 THz radiation with the quantum capacitance detector. *Nat. Astron.* **2,** 90–97 (2017).

[32] Du, L., Molas, M. R., Huang, Z., Zhang, G., Wang, F. & Sun, Z. Moiré photonics and optoelectronics. *Science* **379,** eadg0014 (2023).

[33] Cao, Y., Fatemi, V., Demir, A., Fang, S., Tomarken, S. L., Luo, J. Y., Sanchez-Yamagishi, J. D., Watanabe, K., Taniguchi, T., Kaxiras, E., Ashoori, R. C. & Jarillo-Herrero, P. Correlated insulator behaviour at half-filling in magic-angle graphene superlattices. *Nature* **556,** 80–84 (2018).

[34] Seifert, P., Lu, X., Stepanov, P., Durán Retamal, J. R., Moore, J. N., Fong, K.-C., Principi, A. & Efetov, D. K. Magic-angle bilayer graphene nanocalorimeters: Toward broadband, energy-resolving single photon detection. *Nano Lett.* **20,** 3459–3464 (2020).

[35] Fox, M. *Quantum Optics: An Introduction* (Oxford University Press, London, England, 2006).

[36] Schiff, L. I. *Quantum mechanics,3rd edition* (McGraw-Hill, 1958).

[37] Glauber, R. J. Coherent and incoherent states of the radiation field. *Phys. Rev.* **131,** 2766–2788 (1963).

[38] Walsh, E. D. *Detecting Single Photons with Graphene-Based Josephson Junctions* (PhD Thesis, Harvard University, Boston, USA, 2020).

[39] Loudon, R. *Quantum Theory of Light 3rd Edn* (Oxford University Press, New York, 2000).

[40] Jackson, J. D. *Classical Electrodynamics* 3rd ed. (John Wiley & Sons, Nashville, TN, 1998).

[41] Becher, C., Gao, W., Kar, S., Marciniak, C. D., Monz, T., Bartholomew, J. G., Goldner, P., Loh, H., Marcellina, E., Goh, K. E. J., Koh, T. S., Weber, B., Mu, Z., Tsai, J.-Y., Yan, Q., Huber-Loyola, T., Höfling, S., Gyger, S., Steinhauer, S. & Zwiller, V. 2023 roadmap for materials for quantum technologies. *Mater. Quantum Technol.* **3,** 012501 (2023).

[42] Oliver, W. D. & Welander, P. B. Materials in superconducting quantum bits. *MRS Bulletin* **38,** 816–825 (2013).

[43] Polini, M., Giazotto, F., Fong, K. C., Pop, I. M., Schuck, C., Boccali, T., Signorelli, G., D'Elia, M., Hadfield, R. H., Giovannetti, V., Rossini, D., Tredicucci, A., Efetov, D. K., Koppens, F. H. L., Jarillo-Herrero, P., Grassellino, A. & Pisignano, D. Materials and devices for fundamental quantum science and quantum technologies. *arXiv:* 2201.09260 (2022).

[44] Onnes, H. K. The Superconductivity of Mercury. *Comm. Phys. Lab. Univ.* **29,** 122–124 (1911).

[45] Andrews, D. H. *American PhilisophicalYearbook,* 132 (1938).

[46] Goetz, A. The possible use of superconductivity for radiometric purposes. *Phys. Rev.* **55,** 1270–1271 (1939).

[47] Andrews, D. H., Brucksch Jr, W. F., Ziegler, W. T. & Blanchard, E. R. Attenuated superconductors I. for measuring infra-red radiation. *Rev. Sci. Instrum.* **13,** 281–292 (1942).

[48] Andrews, D. H., Fowler, R. D. & Williams, M. C. The effect of alpha-particles on a superconductor. *Phys. Rev.* **76,** 154–155 (1949).

[49] Gross, R., Marx, A. & Deppe, F. *Applied superconductivity* (De Gruyter, Berlin, Germany, 2019).

[50] Gross, R. & Marx, A. *Applied superconductivity,Josephson Effect and Superconducting Electronics* Garching, Germany, 2005.

[51] Tinkham, M., Free, J. U., Lau, C. N. & Markovic, N. Hysteretic I-V curves of superconducting nanowires. *Phys. Rev. B Condens. Matter* **68** (2003).

[52] Shakeripour, H., Petrovic, C. & Taillefer, L. Heat transport as a probe of superconducting gap structure. *New Journal of Physics* **11,** 055065 (2009).

[53] Behnia, K., Taillefer, L., Flouquet, J., Jaccard, D., Maki, K. & Fisk, Z. Thermal conductivity of superconducting UPt3. *J. Low Temp. Phys.* **84,** 261–278 (1991).

[54] Lussier, B., Ellman, B. & Taillefer, L. Anisotropy of heat conduction in the heavy fermion superconductor UPt3. *Phys. Rev. Lett.* **73,** 3294–3297 (1994).

[55] Lussier, B., Ellman, B. & Taillefer, L. Determination of the gap structure in UPt3 by thermal conductivity. *Phys. Rev. B Condens. Matter* **53,** 5145–5148 (1996).

[56] Löfwander, T. & Fogelström, M. Low-temperature thermal conductivity of superconductors with gap nodes. *Phys. Rev. Lett.* **95,** 107006 (2005).

[57] Guruswamy, T., Goldie, D. J. & Withington, S. Nonequilibrium superconducting thin films with sub-gap and pair-breaking photon illumination. *Supercond. Sci. Technol.* **28,** 054002 (2015).

[58] Semenov, A. D., Gol tsman, G. N. & Sobolewski, R. Hot-electron effect in superconductors and its applications for radiation sensors. *Supercond. Sci. Technol.* **15,** 1–16 (2002).

[59] Rothwarf, A. & Taylor, B. N. Measurement of recombination lifetimes in superconductors. *Phys. Rev. Lett.* **19,** 27–30 (1967).

[60] Kozorezov, A. G., Volkov, A. F., Wigmore, J. K., Peacock, A., Poelaert, A. & den Hartog, R. Quasiparticle-phonon downconversion in nonequilibrium superconductors. *Phys. Rev. B Condens. Matter* **61,** 11807–11819 (2000).

[61] Zehnder, A. Response of superconductive films to localized energy deposition. *Phys. Rev. B Condens. Matter* **52,** 12858–12866 (1995).

[62] Massicotte, M., Soavi, G., Principi, A. & Tielrooij, K.-J. Hot carriers in graphene - fundamentals and applications. *Nanoscale* **13,** 8376–8411 (2021).

[63] Tielrooij, K. J., Song, J. C. W., Jensen, S. A., Centeno, A., Pesquera, A., Zurutuza Elorza, A., Bonn, M., Levitov, L. S. & Koppens, F. H. L. Photoexcitation cascade and multiple hot-carrier generation in graphene. *Nat. Phys.* **9,** 248–252 (2013).

[64] Fukuda, D. Single-photon measurement techniques with a superconducting transition edge sensor. *IEICE Trans. Electron.* **E102.C,** 230–234 (2019).

[65] Irwin, K. D. An application of electrothermal feedback for high resolution cryogenic particle detection. *Appl. Phys. Lett.* **66,** 1998–2000 (1995).

[66] Karasik, B. S., Pereverzev, S. V., Olaya, D., Gershenson, M. E., Cantor, R., Kawamura, J. H., Day, P. K., Bumble, B., LeDuc, H. G., Monacos, S. P., Harding, D. G., Santavicca, D., Carter, F. & Prober, D. E. *Development of the nano-HEB array for low-background far-IR applications* in *Millimeter, Submillimeter, and Far-Infrared Detectors and Instrumentation for Astronomy V* (SPIE, San Diego, California, USA, 2010).

[67] Gershenson, M. E., Gong, D., Sato, T., Karasik, B. S. & Sergeev, A. V. Millisecond electron–phonon relaxation in ultrathin disordered metal films at millikelvin temperatures. *Appl. Phys. Lett.* **79,** 2049–2051 (2001).

[68] Wei, J., Olaya, D., Karasik, B. S., Pereverzev, S. V., Sergeev, A. V. & Gershenson, M. E. Ultrasensitive hot-electron nanobolometers for terahertz astrophysics. *Nat. Nanotechnol.* **3,** 496–500 (2008).

[69] Richards, P. L. Bolometers for infrared and millimeter waves. *J. Appl. Phys.* **76,** 1–24 (1994).

[70] Mather, J. C. Bolometer noise: nonequilibrium theory. *Appl. Opt.* **21,** 1125–1129 (1982).

[71] Fukuda, D., Fujii, G., Numata, T., Amemiya, K., Yoshizawa, A., Tsuchida, H., Fujino, H., Ishii, H., Itatani, T., Inoue, S. & Zama, T. Titanium-based transition-edge photon number resolving detector with 98% detection efficiency with index-matched small-gap fiber coupling. *Opt. Express* **19,** 870–875 (2011).

[72] Lita, A. E., Miller, A. J. & Nam, S. W. Counting near-infrared single-photons with 95% efficiency. *Opt. Express* **16,** 3032–3040 (2008).

[73] Morozov, D., Mauskopf, P. D., Ade, P., Ridder, M., Khosropanah, P., Bruijn, M., van der Kuur, J., Hoevers, H., Gao, J.-R. & Griffin, D. Ultrasensitive TES Bolometers for Space-Based FIR Astronomy. *IEEE Trans. Appl. Supercond.* **21,** 188–191 (2011).

[74] Il'in, K. S., Milostnaya, I. I., Verevkin, A. A., Gol'tsman, G. N., Gershenzon, E. M. & Sobolewski, R. Ultimate quantum efficiency of a superconducting hot-electron photodetector. *Appl. Phys. Lett.* **73,** 3938–3940 (1998).

[75] Gershenzon, E. M. Millimeter and submillimeter range mier based on electronic heating of superconducting films in the resistive state. *Sov Phys Supercond.* **3,** 1582–1597 (1990).

[76] Wellstood, F. C., Urbina, C. & Clarke, J. Hot-electron limitation to the sensitivity of the dc superconducting quantum interference device. *Appl. Phys. Lett.* **54,** 2599–2601 (1989).

[77] Wellstood, F. C., Urbina, C. & Clarke, J. Hot-electron effects in metals. *Phys. Rev. B Condens. Matter* **49,** 5942–5955 (1994).

[78] Prober, D. E. Superconducting terahertz mixer using a transition-edge microbolometer. *Appl. Phys. Lett.* **62,** 2119–2121 (1993).

[79] Natarajan, C. M., Tanner, M. G. & Hadfield, R. H. Superconducting nanowire single-photon detectors: physics and applications. *Supercond. Sci. Technol.* **25,** 063001 (2012).

[80] Kerman, A. J., Yang, J. K. W., Molnar, R. J., Dauler, E. A. & Berggren, K. K. Electrothermal feedback in superconducting nanowire single-photon detectors. *Physical Review B* **79,** 100509 (2009).

[81] Holzman, I. & Ivry, Y. Superconducting nanowires for single-photon detection: Progress, challenges, and opportunities. *Adv. Quantum Technol.* **2,** 1800058 (2019).

[82] Semenov, A., Engel, A., Hübers, H.-W., Il'in, K. & Siegel, M. Spectral cut-off in the efficiency of the resistive state formation caused by absorption of a single-photon in current-carrying superconducting nano-strips. *Eur. Phys. J. B* **47,** 495–501 (2005).

[83] Divochiy, A., Marsili, F., Bitauld, D., Gaggero, A., Leoni, R., Mattioli, F., Korneev, A., Seleznev, V., Kaurova, N., Minaeva, O., Gol'tsman, G., Lagoudakis, K. G., Benkhaoul, M., Lévy, F. & Fiore, A. Superconducting nanowire photon-number-resolving detector at telecommunication wavelengths. *Nat. Photonics* **2,** 302–306 (2008).

[84] Allmaras, J. P., Wollman, E. E., Beyer, A. D., Briggs, R. M., Korzh, B. A., Bumble, B. & Shaw, M. D. Demonstration of a Thermally Coupled Row-Column SNSPD Imaging Array. *Nano Letters* **20,** 2163–2168 (2020).

[85] Demonstration of sub-3 ps temporal resolution with a superconducting nanowire single-photon detector. *Nat. Photonics* **14,** 250–255 (2020).

[86] Hadfield, R. H. Superfast photon counting. *Nat. Photonics* **14,** 201–202 (2020).

[87] Gao, J., Vissers, M. R., Sandberg, M. O., da Silva, F. C. S., Nam, S. W., Pappas, D. P., Wisbey, D. S., Langman, E. C., Meeker, S. R., Mazin, B. A., Leduc, H. G., Zmuidzinas, J. & Irwin, K. D. A titanium-nitride near-infrared kinetic inductance photon-counting detector and its anomalous electrodynamics. *Appl. Phys. Lett.* **101,** 142602 (2012).

[88] Saito, Y., Nojima, T. & Iwasa, Y. Highly crystalline 2D superconductors. *Nat. Rev. Mater.* **2** (2016).

[89] Charaev, I., Bandurin, D. A., Bollinger, A. T., Phinney, I. Y., Drozdov, I., Colangelo, M., Butters, B. A., Taniguchi, T., Watanabe, K., He, X., Medeiros, O., Božović, I., Jarillo-Herrero, P. & Berggren, K. K. Single-photon detection using high-temperature superconductors. *Nat. Nanotechnol.* **18,** 343–349 (2023).

[90] Merino, R. L., Seifert, P., Duran Retamal, J., Mech, R., Taniguchi, T., Watanabe, K., Kadowaki, K., Hadfield, R. H. & Efetov, P. D. D. K. Two-dimensional cuprate nanodetector with single telecom photon sensitivity at T = 20 K. *2d Mater.* (2023).

[91] Seifert, P., Retamal, J. R. D., Merino, R. L., Sheinfux, H. H., Moore, J. N., Aamir, M. A., Taniguchi, T., Watanabe, K., Kadowaki, K., Artiglia, M., Romagnoli, M. & Efetov, D. K. A high-T c van der Waals superconductor based photodetector with ultra-high responsivity and nanosecond relaxation time. *2d Mater.* **8,** 035053 (2021).

[92] Shein, K., Zharkova, E., Kashchenko, M., Kolbatova, A., Lyubchak, A., Elesin, L., Nguyen, E., Semenov, A., Charaev, I., Schilling, A., Goltsman, G., Novoselov, K. S., Gayduchenko, I. & Bandurin, D. A. Fundamental limits of few-layer NbSe2 microbolometers at terahertz frequencies. *Nano Lett.* **24,** 2282–2288 (2024).

[93] Orchin, G. J., De Fazio, D., Di Bernardo, A., Hamer, M., Yoon, D., Cadore, A. R., Goykhman, I., Watanabe, K., Taniguchi, T., Robinson, J. W. A., Gorbachev, R. V., Ferrari, A. C. & Hadfield, R. H. Niobium diselenide superconducting photodetectors. *Appl. Phys. Lett.* **114,** 251103 (2019).

[94] Park, J. M., Cao, Y., Watanabe, K., Taniguchi, T. & Jarillo-Herrero, P. Tunable strongly coupled superconductivity in magic-angle twisted trilayer graphene. *Nature* **590,** 249–255 (2021).

[95] Park, J. M., Cao, Y., Xia, L.-Q., Sun, S., Watanabe, K., Taniguchi, T. & Jarillo-Herrero, P. Robust superconductivity in magic-angle multilayer graphene family. *Nat. Mater.* **21,** 877–883 (2022).

[96] Zhou, H., Holleis, L., Saito, Y., Cohen, L., Huynh, W., Patterson, C. L., Yang, F., Taniguchi, T., Watanabe, K. & Young, A. F. Isospin magnetism and spin-polarized superconductivity in Bernal bilayer graphene. *Science* **375,** 774–778 (2022).

[97] Zhou, H., Xie, T., Taniguchi, T., Watanabe, K. & Young, A. F. Superconductivity in rhombohedral trilayer graphene. *Nature* **598,** 434–438 (2021).

[98] Kang, W. N., Jung, C. U., Kim, K. H. P., Park, M.-S., Lee, S. Y., Kim, H.-J., Choi, E.-M., Kim, K. H., Kim, M.-S. & Lee, S.-I. Hole carrier in MgB2 characterized by Hall measurements. *Appl. Phys. Lett.* **79,** 982–984 (2001).

[99] Gozar, A., Logvenov, G., Kourkoutis, L. F., Bollinger, A. T., Giannuzzi, L. A., Muller, D. A. & Bozovic, I. High-temperature interface superconductivity between metallic and insulating copper oxides. *Nature* **455,** 782–785 (2008).

[100] Saveskul, N. A., Titova, N. A., Baeva, E. M., Semenov, A. V., Lubenchenko, A. V., Saha, S., Reddy, H., Bogdanov, S. I., Marinero, E. E., Shalaev, V. M., Boltasseva, A., Khrapai, V. S., Kardakova, A. I. & Goltsman, G. N. Superconductivity behavior in epitaxial TiN films points to surface magnetic disorder. *Phys. Rev. Appl.* **12** (2019).

[101] Stangl, A., Palau, A., Deutscher, G., Obradors, X. & Puig, T. Ultra-high critical current densities of superconducting YBa2Cu3O7-δ thin films in the overdoped state. *Sci. Rep.* **11,** 8176 (2021).

[102] Ge, H., Jin, Y.-R. & Song, X.-H. High quality NbTiN films fabrication and rapid thermal annealing investigation. *Chin. Physics B* **28,** 077402 (2019).

[103] Novoselov, K. S., Geim, A. K., Morozov, S. V., Jiang, D., Zhang, Y., Dubonos, S. V., Grigorieva, I. V. & Firsov, A. A. Electric field effect in atomically thin carbon films. *Science* **306,** 666–669 (2004).

[104] Ferrari, A. C., Bonaccorso, F., Fal'ko, V., Novoselov, K. S., Roche, S., Bøggild, P., Borini, S., Koppens, F. H. L., Palermo, V., Pugno, N., Garrido, J. A., Sordan, R., Bianco, A., Ballerini, L., Prato, M., Lidorikis, E., Kivioja, J., Marinelli, C., Ryhänen, T., Morpurgo, A., Coleman, J. N., Nicolosi, V., Colombo, L., Fert, A., Garcia-Hernandez, M., Bachtold, A., Schneider, G. F., Guinea, F., Dekker, C., Barbone, M., Sun, Z., Galiotis, C., Grigorenko, A. N., Konstantatos, G., Kis, A., Katsnelson,

M., Vandersypen, L., Loiseau, A., Morandi, V., Neumaier, D., Treossi, E., Pellegrini, V., Polini, M., Tredicucci, A., Williams, G. M., Hong, B. H., Ahn, J.-H., Kim, J. M., Zirath, H., van Wees, B. J., van der Zant, H., Occhipinti, L., Di Matteo, A., Kinloch, I. A., Seyller, T., Quesnel, E., Feng, X., Teo, K., Rupesinghe, N., Hakonen, P., Neil, S. R. T., Tannock, Q., Löfwander, T. & Kinaret, J. Science and technology roadmap for graphene, related two-dimensional crystals, and hybrid systems. *Nanoscale* **7,** 4598–4810 (2015).

[105] Randviir, E. P., Brownson, D. A. C. & Banks, C. E. A decade of graphene research: production, applications and outlook. *Mater. Today* **17,** 426–432 (2014).

[106] Castro Neto, A. H., Guinea, F., Peres, N. M. R., Novoselov, K. S. & Geim, A. K. The electronic properties of graphene. *Rev. Mod. Phys.* **81,** 109–162 (2009).

[107] Wallace, P. R. The band theory of graphite. *Phys. Rev.* **71,** 622–634 (1947).

[108] Cohen, M. L. & Louie, S. G. *Fundamentals of condensed matter physics* (Cambridge University Press, Cambridge, England, 2016).

[109] Novoselov, K. S., Geim, A. K., Morozov, S. V., Jiang, D., Katsnelson, M. I., Grigorieva, I. V., Dubonos, S. V. & Firsov, A. A. Two-dimensional gas of massless Dirac fermions in graphene. *Nature* **438,** 197–200 (2005).

[110] Lopes Dos Santos, J. M. B., Peres, N. M. R. & Castro Neto, A. H. Graphene bilayer with a twist: electronic structure. *Phys. Rev. Lett.* **99,** 256802 (2007).

[111] Bistritzer, R. & MacDonald, A. H. Moiré bands in twisted double-layer graphene. *Proc. Natl. Acad. Sci. U. S. A.* **108,** 12233–12237 (2011).

[112] Bernevig, B. A. & Efetov, D. K. Twisted bilayer graphene's gallery of phases. *Phys. Today* **77,** 38–44 (2024).

[113] Li, G., Luican, A., Lopes dos Santos, J. M. B., Castro Neto, A. H., Reina, A., Kong, J. & Andrei, E. Y. Observation of Van Hove singularities in twisted graphene layers. en. *Nat. Phys.* **6,** 109–113 (2010).

[114] Cao, Y., Fatemi, V., Fang, S., Watanabe, K., Taniguchi, T., Kaxiras, E. & Jarillo-Herrero, P. Unconventional superconductivity in magic-angle graphene superlattices. *Nature* **556,** 43–50 (2018).

[115] Andrei, E. Y. & MacDonald, A. H. Graphene bilayers with a twist. *Nat. Mater.* **19,** 1265–1275 (2020).

[116] Lopes dos Santos, J. M. B., Peres, N. M. R. & Castro Neto, A. H. Continuum model of the twisted graphene bilayer. *Phys. Rev. B Condens. Matter Mater. Phys.* **86** (2012).

[117] Tarnopolsky, G., Kruchkov, A. J. & Vishwanath, A. Origin of magic angles in twisted bilayer graphene. *Phys. Rev. Lett.* **122,** 106405 (2019).

[118] Carr, S., Fang, S., Zhu, Z. & Kaxiras, E. Exact continuum model for low-energy electronic states of twisted bilayer graphene. *Phys. Rev. Res.* **1** (2019).

[119] Nam, N. N. T. & Koshino, M. Lattice relaxation and energy band modulation in twisted bilayer graphene. *Phys. Rev. B.* **96** (2017).

[120] Luican, A., Li, G., Reina, A., Kong, J., Nair, R. R., Novoselov, K. S., Geim, A. K. & Andrei, E. Y. Single-layer behavior and its breakdown in twisted graphene layers. *Phys. Rev. Lett.* **106,** 126802 (2011).

[121] Currle, M. *Theoretical and Experimental Study of the Electronic Structure of Graphene-based Systems with the Quantum Twisting Microscope* Master Thesis, Ludwig Maximilians University of Munich. 2024.

[122] Lu, X., Stepanov, P., Yang, W., Xie, M., Aamir, M. A., Das, I., Urgell, C., Watanabe, K., Taniguchi, T., Zhang, G., Bachtold, A., MacDonald, A. H. & Efetov, D. K. Superconductors, orbital magnets and correlated states in magic-angle bilayer graphene. *Nature* **574,** 653–657 (2019).

[123] Das, I., Lu, X., Herzog-Arbeitman, J., Song, Z.-D., Watanabe, K., Taniguchi, T., Bernevig, B. A. & Efetov, D. K. Symmetry-broken Chern insulators and Rashba-like Landau-level crossings in magic-angle bilayer graphene. *Nat. Phys.* **17,** 710–714 (2021).

[124] Zhang, Y.-H., Po, H. C. & Senthil, T. Landau level degeneracy in twisted bilayer graphene: Role of symmetry breaking. *Phys. Rev. B.* **100** (2019).

[125] Hejazi, K., Liu, C. & Balents, L. Landau levels in twisted bilayer graphene and semiclassical orbits. *Phys. Rev. B.* **100** (2019).

[126] Ashcroft, N. W. & Mermin, N. *Solid State Physics* (Saunders College Publishing, 1976).

[127] Cao, Y., Rodan-Legrain, D., Park, J. M., Yuan, N. F. Q., Watanabe, K., Taniguchi, T., Fernandes, R. M., Fu, L. & Jarillo-Herrero, P. Nematicity and competing orders in superconducting magic-angle graphene. *Science* **372,** 264–271 (2021).

[128] Datta, S. *Electronic transport in mesoscopic systems* (Cambridge University Press, Cambridge, England, 2013).

[129] Cao, Y., Luo, J. Y., Fatemi, V., Fang, S., Sanchez-Yamagishi, J. D., Watanabe, K., Taniguchi, T., Kaxiras, E. & Jarillo-Herrero, P. Superlattice-induced insulating states and valley-protected orbits in twisted bilayer graphene. *Phys. Rev. Lett.* **117** (2016).

[130] Yankowitz, M., Chen, S., Polshyn, H., Zhang, Y., Watanabe, K., Taniguchi, T., Graf, D., Young, A. F. & Dean, C. R. Tuning superconductivity in twisted bilayer graphene. *Science* **363,** 1059–1064 (2019).

[131] Balents, L., Dean, C. R., Efetov, D. K. & Young, A. F. Superconductivity and strong correlations in moiré flat bands. en. *Nat. Phys.* **16,** 725–733 (2020).

[132] Stepanov, P., Das, I., Lu, X., Fahimniya, A., Watanabe, K., Taniguchi, T., Koppens, F. H. L., Lischner, J., Levitov, L. & Efetov, D. K. Untying the insulating and superconducting orders in magic-angle graphene. *Nature* **583,** 375–378 (2020).

[133] Arora, H. S., Polski, R., Zhang, Y., Thomson, A., Choi, Y., Kim, H., Lin, Z., Wilson, I. Z., Xu, X., Chu, J.-H., Watanabe, K., Taniguchi, T., Alicea, J. & Nadj-Perge, S. Superconductivity in metallic twisted bilayer graphene stabilized by WSe2. *Nature* **583,** 379–384 (2020).

[134] Serlin, M., Tschirhart, C. L., Polshyn, H., Zhang, Y., Zhu, J., Watanabe, K., Taniguchi, T., Balents, L. & Young, A. F. Intrinsic quantized anomalous Hall effect in a moiré heterostructure. *Science* **367,** 900–903 (2020).

[135] Uri, A., Grover, S., Cao, Y., Crosse, J. A., Bagani, K., Rodan-Legrain, D., Myasoedov, Y., Watanabe, K., Taniguchi, T., Moon, P., Koshino, M., Jarillo-Herrero, P. & Zeldov, E. Mapping the twist-angle disorder and Landau levels in magic-angle graphene. *Nature* **581.** Publisher: Springer US, 47–52 (2020).

[136] Benschop, T., de Jong, T. A., Stepanov, P., Lu, X., Stalman, V., van der Molen, S. J., Efetov, D. K. & Allan, M. P. Measuring local moiré lattice heterogeneity of twisted bilayer graphene. *Phys. Rev. Res.* **3** (2021).

[137] Kazmierczak, N. P., Van Winkle, M., Ophus, C., Bustillo, K. C., Carr, S., Brown, H. G., Ciston, J., Taniguchi, T., Watanabe, K. & Bediako, D. K. Strain fields in twisted bilayer graphene. *Nat. Mater.* **20,** 956–963 (2021).

[138] Choi, Y., Kemmer, J., Peng, Y., Thomson, A., Arora, H., Polski, R., Zhang, Y., Ren, H., Alicea, J., Refael, G., von Oppen, F., Watanabe, K., Taniguchi, T. & Nadj-Perge, S. Electronic correlations in twisted bilayer graphene near the magic angle. en. *Nat. Phys.* **15,** 1174–1180 (2019).

[139] Castellanos-Gomez, A., Buscema, M., Molenaar, R., Singh, V., Janssen, L., van der Zant, H. S. J. & Steele, G. A. Deterministic transfer of two-dimensional materials by all-dry viscoelastic stamping. *2d Mater.* **1,** 011002 (2014).

[140] Huang, Y., Sutter, E., Shi, N. N., Zheng, J., Yang, T., Englund, D., Gao, H.-J. & Sutter, P. Reliable exfoliation of large-area high-quality flakes of graphene and other two-dimensional materials. *ACS Nano* **9,** 10612–10620 (2015).

[141] Dean, C. R., Young, A. F., Meric, I., Lee, C., Wang, L., Sorgenfrei, S., Watanabe, K., Taniguchi, T., Kim, P., Shepard, K. L. & Hone, J. Boron nitride substrates for high-quality graphene electronics. *Nat. Nanotechnol.* **5,** 722–726 (2010).

[142] Miyazaki, H., Odaka, S., Sato, T., Tanaka, S., Goto, H., Kanda, A., Tsukagoshi, K., Ootuka, Y. & Aoyagi, Y. Inter-Layer Screening Length to Electric Field in Thin Graphite Film. *Applied Physics Express* **1,** 034007 (2008).

[143] Han, E., Yu, J., Annevelink, E., Son, J., Kang, D. A., Watanabe, K., Taniguchi, T., Ertekin, E., Huang, P. Y. & van der Zande, A. M. Ultrasoft slip-mediated bending in few-layer graphene. *Nat. Mater.* **19,** 305–309 (2020).

[144] Kim, K., Yankowitz, M., Fallahazad, B., Kang, S., Movva, H. C. P., Huang, S., Larentis, S., Corbet, C. M., Taniguchi, T., Watanabe, K., Banerjee, S. K., LeRoy, B. J. & Tutuc, E. Van der Waals heterostructures with high accuracy rotational alignment. *Nano Lett.* **16,** 1989–1995 (2016).

[145] Park, J. M., Cao, Y., Watanabe, K., Taniguchi, T. & Jarillo-Herrero, P. Flavour Hund's coupling, Chern gaps and charge diffusivity in moiré graphene. *Nature* **592,** 43–48 (2021).

[146] Zomer, P. J., Guimarães, M. H. D., Brant, J. C., Tombros, N. & van Wees, B. J. Fast pick up technique for high quality heterostructures of bilayer graphene and hexagonal boron nitride. *Appl. Phys. Lett.* **105,** 013101 (2014).

[147] D´ıez M´erida, J. *Probing Magic-Angle Twisted Bilayer Graphene with Monolithic Gate-Defined Josephson Junctions* Master Thesis, Ludwig Maximilians University of Munich. 2024.

[148] Sharpe, A. L., Fox, E. J., Barnard, A. W., Finney, J., Watanabe, K., Taniguchi, T., Kastner, M. A. & Goldhaber-Gordon, D. Emergent ferromagnetism near three-quarters filling in twisted bilayer graphene. *Science* **365,** 605–608 (2019).

[149] Zhang, Y.-H., Mao, D. & Senthil, T. Twisted bilayer graphene aligned with hexagonal boron nitride: Anomalous Hall effect and a lattice model. *Phys. Rev. Res.* **1** (2019).

[150] Wang, L., Meric, I., Huang, P. Y., Gao, Q., Gao, Y., Tran, H., Taniguchi, T., Watanabe, K., Campos, L. M., Muller, D. A., Guo, J., Kim, P., Hone, J., Shepard, K. L. & Dean, C. R. One-dimensional electrical contact to a two-dimensional material. *Science* **342,** 614–617 (2013).

[151] Pizzocchero, F., Gammelgaard, L., Jessen, B. S., Caridad, J. M., Wang, L., Hone, J., Bøggild, P. & Booth, T. J. The hot pick-up technique for batch assembly of van der Waals heterostructures. *Nat. Commun.* **7,** 11894 (2016).

[152] Khestanova, E., Guinea, F., Fumagalli, L., Geim, A. K. & Grigorieva, I. V. Universal shape and pressure inside bubbles appearing in van der Waals heterostructures. *Nat. Commun.* **7,** 12587 (2016).

[153] Haigh, S. J., Gholinia, A., Jalil, R., Romani, S., Britnell, L., Elias, D. C., Novoselov, K. S., Ponomarenko, L. A., Geim, A. K. & Gorbachev, R. Cross-sectional imaging of individual layers and buried interfaces of graphene-based heterostructures and superlattices. *Nat. Mater.* **11,** 764–767 (2012).

[154] Purdie, D. G., Pugno, N. M., Taniguchi, T., Watanabe, K., Ferrari, A. C. & Lombardo, A. Cleaning interfaces in layered materials heterostructures. *Nat. Commun.* **9,** 5387 (2018).

[155] Pobell, F. *Matter and methods at low temperatures* 3rd ed. (Springer, Berlin, Germany, 2006).

[156] Frossati, G. Experimental techniques: Methods for cooling below 300 mK. *J. Low Temp. Phys.* **87,** 595–633 (1992).

[157] Sydoriak, S. G. & Roberts, T. R. Vapor Pressures of ^{3}He-^{4}He Mixtures. *Phys. Rev.* **118,** 901–912 (1960).

[158] Thalmann, M., Pernau, H.-F., Strunk, C., Scheer, E. & Pietsch, T. Comparison of cryogenic low-pass filters. *Rev. Sci. Instrum.* **88,** 114703 (2017).

[159] Glattli, D. C., Jacques, P., Kumar, A., Pari, P. & Saminadayar, L. A noise detection scheme with 10 mK noise temperature resolution for semiconductor single electron tunneling devices. *J. Appl. Phys.* **81,** 7350–7356 (1997).

[160] Stremler, F. G. *Introduction to Communication Systems* 3rd ed. (Pearson, Upper Saddle River, NJ, 1990).

[161] Principles of lock-in detection and the state of the art, White Paper, Zurich Instrument (2016).

[162] User Manual UHF 600 MHz Lock-in Amplifier, Zurich Instruments (2016).

[163] Svelto, O. *Principles of Lasers* 5th ed. (Springer, New York, NY, 2010).

[164] Oh, M., Nuckolls, K. P., Wong, D., Lee, R. L., Liu, X., Watanabe, K., Taniguchi, T. & Yazdani, A. Evidence for unconventional superconductivity in twisted bilayer graphene. *Nature* **600,** 240–245 (2021).

[165] Ohta, T., Bostwick, A., Seyller, T., Horn, K. & Rotenberg, E. Controlling the electronic structure of bilayer graphene. *Science.* **313,** 951–954 (2006).

[166] Lisi, S., Lu, X., Benschop, T., de Jong, T. A., Stepanov, P., Duran, J. R., Margot, F., Cucchi, I., Cappelli, E., Hunter, A., Tamai, A., Kandyba, V., Giampietri, A., Barinov, A., Jobst, J., Stalman, V., Leeuwenhoek, M., Watanabe, K., Taniguchi, T., Rademaker, L., van der Molen, S. J., Allan, M. P., Efetov, D. K. & Baumberger, F. Observation of flat bands in twisted bilayer graphene. *Nat. Phys.* **17,** 189–193 (2021).

[167] Gierz, I., Petersen, J. C., Mitrano, M., Cacho, C., Turcu, I. C. E., Springate, E., Stöhr, A., Köhler, A., Starke, U. & Cavalleri, A. Snapshots of non-equilibrium Dirac carrier distributions in graphene. *Nat. Mater.* **12,** 1119–1124 (2013).

[168] Tielrooij, K. J., Piatkowski, L., Massicotte, M., Woessner, A., Ma, Q., Lee, Y., Myhro, K. S., Lau, C. N., Jarillo-Herrero, P., van Hulst, N. F. & Koppens, F. H. L. Generation of photovoltage in graphene on a femtosecond timescale through efficient carrier heating. *Nat. Nanotechnol.* **10,** 437–443 (2015).

[169] Nair, R. R., Blake, P., Grigorenko, A. N., Novoselov, K. S., Booth, T. J., Stauber, T., Peres, N. M. R. & Geim, A. K. Fine structure constant defines visual transparency of graphene. *Science* **320,** 1308 (2008).

[170] Burkhard, G. F., Hoke, E. T. & McGehee, M. D. Accounting for interference, scattering, and electrode absorption to make accurate internal quantum efficiency measurements in organic and other thin solar cells. *Adv. Mater.* **22,** 3293–3297 (2010).

[171] Furchi, M., Urich, A., Pospischil, A., Lilley, G., Unterrainer, K., Detz, H., Klang, P., Andrews, A. M., Schrenk, W., Strasser, G. & Mueller, T. Microcavity-integrated graphene photodetector. *Nano Lett.* **12,** 2773–2777 (2012).

[172] Efetov, D. K., Shiue, R.-J., Gao, Y., Skinner, B., Walsh, E. D., Choi, H., Zheng, J., Tan, C., Grosso, G., Peng, C., Hone, J., Fong, K. C. & Englund, D. Fast thermal relaxation in cavity-coupled graphene bolometers with a Johnson noise read-out. *Nat. Nanotechnol.* **13,** 797–801 (2018).

[173] Fetter, A. & J. D. Walecka. *Quantum theory of many-particle systems* (McGraw-Hill, 1971).

[174] Aamir, M. A., Moore, J. N., Lu, X., Seifert, P., Englund, D., Fong, K. C. & Efetov, D. K. Ultrasensitive calorimetric measurements of the electronic heat capacity of graphene. *Nano Lett.* **21,** 5330–5337 (2021).

[175] Fong, K. C., Wollman, E. E., Ravi, H., Chen, W., Clerk, A. A., Shaw, M. D., Leduc, H. G. & Schwab, K. C. Measurement of the electronic thermal conductance channels and heat capacity of graphene at low temperature. *Phys. Rev. X.* **3,** 041008 (2013).

[176] Banerjee, A., Hao, Z., Kreidel, M., Ledwith, P., Phinney, I., Park, J. M., Zimmerman, A. M., Watanabe, K., Taniguchi, T., Westervelt, R. M., Jarillo-Herrero, P., Volkov, P. A., Vishwanath, A., Fong, K. C. & Kim, P. Superfluid stiffness of twisted multilayer graphene superconductors. *arXiv,* 2406.13742 (2024).

[177] Tanaka, M., Wang, J. Î.-J., Dinh, T. H., Rodan-Legrain, D., Zaman, S., Hays, M., Kannan, B., Almanakly, A., Kim, D. K., Niedzielski, B. M., Serniak, K., Schwartz, M. E., Watanabe, K., Taniguchi, T., Grover, J. A., Orlando, T. P., Gustavsson, S., Jarillo-Herrero, P. & Oliver, W. D. Kinetic inductance, quantum geometry, and superconductivity in magic-angle twisted bilayer graphene. *arXiv,* 2406.13740 (2024).

[178] Portolés, E., Perego, M., Volkov, P. A., Toschini, M., Kemna, Y., Mestre-Torà, A., Zheng, G., Denisov, A. O., de Vries, F. K., Rickhaus, P., Taniguchi, T., Watanabe, K., Pixley, J. H., Ihn, T. & Ensslin, K. Quasiparticle and superfluid dynamics in Magic-Angle Graphene. *arXiv,* 2405.06793 (2024).

[179] Fong, K. C. & Schwab, K. C. Ultrasensitive and wide-bandwidth thermal measurements of graphene at low temperatures. *Phys. Rev. X.* **2,** 031006 (2012).

[180] Fong, K. C. Impact of contact resistance in Lorenz number measurements. *arXiv,* 1711.04005 (2024).

[181] Matula, R. A. Electrical resistivity of copper, gold, palladium, and silver. *J. Phys. Chem. Ref. Data* **8,** 1147–1298 (1979).

[182] Mehew, J. D., Merino, R. L., Ishizuka, H., Block, A., Mérida, J. D., Carlón, A. D., Watanabe, K., Taniguchi, T., Levitov, L. S., Efetov, D. K. & Tielrooij, K.-J. Ultrafast Umklapp-assisted electron-phonon cooling in magic-angle twisted bilayer graphene. *Sci. Adv.* **10** (2024).

[183] Skocpol, W. J., Beasley, M. R. & Tinkham, M. Self-heating hotspots in superconducting thin-film microbridges. *J. Appl. Phys.* **45,** 4054–4066 (1974).

[184] Baek, B., Lita, A. E., Verma, V. & Nam, S. W. Superconducting a-W_xSi_{1-x} nanowire single-photon detector with saturated internal quantum efficiency from visible to 1850 nm. *Appl. Phys. Lett.* **98,** 251105 (2011).

[185] Yamashita, T., Miki, S., Qiu, W., Fujiwara, M., Sasaki, M. & Wang, Z. Temperature dependent performances of superconducting nanowire single-photon detectors in an ultralow-temperature region. *Appl. Phys. Express* **3,** 102502 (2010).

[186] Annunziata, A. J., Quaranta, O., Santavicca, D. F., Casaburi, A., Frunzio, L., Ejrnaes, M., Rooks, M. J., Cristiano, R., Pagano, S., Frydman, A. & Prober, D. E. Reset dynamics and latching in niobium superconducting nanowire single-photon detectors. *Journal of Applied Physics* **108,** 084507 (2010).

[187] Du, X., Prober, D. E., Vora, H. & McKitterick, C. B. Graphene-based Bolometers. *Graphene and 2D Materials* **1,** 1–22 (2014).

[188] Schubert, L. G. *Development of a milli-Kelvin THz Setup for Photovoltage Experiments on 2D Materials* Master Thesis, Ludwig Maximilians University of Munich. 2024.

[189] Hudeczek, C. A. *Finite Element Analysis and Fabrication of a Bow-tie Antenna for Terahertz Detection* Bachelor Thesis, Ludwig Maximilians University of Munich. 2024.

[190] Pinczuk, A., Dennis, B. S., Pfeiffer, L. N. & West, K. Observation of collective excitations in the fractional quantum Hall effect. *Phys. Rev. Lett.* **70,** 3983–3986 (1993).

[191] Basov, D. N., Averitt, R. D., van der Marel, D., Dressel, M. & Haule, K. Electrodynamics of correlated electron materials. en. *Rev. Mod. Phys.* **83,** 471–541 (2011).

[192] Basov, D. N. & Timusk, T. Electrodynamics of high-tcsuperconductors. *Rev. Mod. Phys.* **77,** 721–779 (2005).

[193] Vaughan, M., Michailow, W., Salih, M., Li, L., Beere, H., Ritchie, D. A., Linfield, E. H., Davies, A. G. & Cunningham, J. E. Directed delivery of terahertz frequency radiation from quantum cascade lasers within a dry 3He dilution refrigerator. *Rev. Sci. Instrum.* **93,** 113906 (2022).

[194] Vaughan, M., Michailow, W., Tan, M., Salih, M., Li, L., Beere, H., Ritchie, D. A., Linfield, E. H., Davies, A. G. & Cunningham, J. E. Enhanced delivery and detection of terahertz frequency radiation from a quantum cascade laser within dilution refrigerator. *J. Low Temp. Phys.* **213,** 306–316 (2023).

[195] Onyszczak, M., Uzan-Narovlansky, A. J., Tang, Y., Wang, P., Jia, Y., Yu, G., Song, T., Singha, R., Khoury, J. F., Schoop, L. M. & Wu, S. A platform for far-infrared spectroscopy of quantum materials at millikelvin temperatures. *Rev. Sci. Instrum.* **94** (2023).

[196] Carpintero, G., Garcia-Munoz, E., Hartnagel, H., Preu, S. & Raisanen, A. *Semiconductor Terahertz technology* (eds Carpintero, G., Garcıa Muñoz, L. E., Hartnagel, H. L., Preu, S. & Räisänen, A. V.) (John Wiley & Sons, Nashville, TN, 2015).

[197] Roggenbuck, A., Thirunavukkuarasu, K., Schmitz, H., Marx, J., Deninger, A., Mayorga, I. C., Güsten, R., Hemberger, J. & Grüninger, M. Using a fiber stretcher as a fast phase modulator in a continuous wave terahertz spectrometer. *J. Opt. Soc. Am. B* **29,** 614 (2012).

[198] Shimizu, N., Ikari, T., Kikuchi, K., Matsuyama, K., Wakatsuki, A., Kohjiro, S. & Fukasawa, R. *Remote gas sensing in full-scale fire with sub-terahertz waves* in *2011 IEEE MTT-S International Microwave Symposium* (IEEE, Baltimore, MD, USA, 2011).

[199] Reschke, S., Farkas, D. G., Strinić, A., Ghara, S., Guratinder, K., Zaharko, O., Prodan, L., Tsurkan, V., Szaller, D., Bordács, S., Deisenhofer, J. & Kézsmárki, I. Confirming the trilinear form of the optical magnetoelectric effect in the polar honeycomb antiferromagnet Co2Mo3O8. *Npj Quantum Mater.* **7** (2022).

[200] Parmentier, F. D., Serkovic-Loli, L. N., Roulleau, P. & Glattli, D. C. Photon-assisted shot noise in graphene in the terahertz range. *Phys. Rev. Lett.* **116** (2016).

[201] Gregory, I. S., Baker, C., Tribe, W. R., Bradley, I. V., Evans, M. J., Linfield, E. H., Davies, A. G. & Missous, M. Optimization of photomixers and antennas for continuous-wave terahertz emission. *IEEE J. Quantum Electron.* **41,** 717–728 (2005).

[202] Deninger, A. J., Roggenbuck, A., Schindler, S. & Preu, S. 2.75 THz tuning with a triple-DFB laser system at 1550 nm and InGaAs photomixers. en. *J. Infrared Millim. Terahertz Waves* **36,** 269–277 (2015).

[203] Stanze, D., Deninger, A., Roggenbuck, A., Schindler, S., Schlak, M. & Sartorius, B. Compact cw Terahertz Spectrometer Pumped at 1.5 μm Wavelength. *J. Infrared Millim. Terahertz Waves* **32,** 225–232 (2011).

[204] Valois, J. J., Nellis, G. F. & Pfotenhauer, J. M. Characterization of the thermal properties of OFHC copper at cryogenic temperature. *IOP Conf. Ser. Mater. Sci. Eng.* **1301,** 012167 (2024).

[205] Castilla, S., Terrés, B., Autore, M., Viti, L., Li, J., Nikitin, A. Y., Vangelidis, I., Watanabe, K., Taniguchi, T., Lidorikis, E., Vitiello, M. S., Hillenbrand, R., Tielrooij, K.-J. & Koppens, F. H. L. Fast and sensitive terahertz detection using an antenna-integrated graphene pn junction. *Nano Lett.* **19,** 2765–2773 (2019).

[206] Vicarelli, L., Vitiello, M. S., Coquillat, D., Lombardo, A., Ferrari, A. C., Knap, W., Polini, M., Pellegrini, V. & Tredicucci, A. Graphene field-effect transistors as room-temperature terahertz detectors. *Nat. Mater.* **11,** 865–871 (2012).

[207] Viti, L. & Vitiello, M. S. Tailored nano-electronics and photonics with two-dimensional materials at terahertz frequencies. *J. Appl. Phys.* **130,** 170903 (2021).

[208] Guo, Z., Ma, C., Ou, H., Wang, X., Liu, S., Chen, H., Zheng, S. & Deng, S. Room–temperature terahertz detector based on monolayer graphene integrated with an asymmetric bowtie antenna. *Photonics* **10,** 576 (2023).

[209] Kraus, J. D. *Antennas* 2nd ed. (McGraw-Hill, New York, NY, 1988).

[210] Wen-jun, C., Bin-hong, L. & Tao, X. A resonant frequency formula of bow-tie antenna and its application. *IEEE Antennas and Propagation Society Symposium* (2004).

[211] Kumar, R. K., Li, G., Bertini, R., Chaudhary, S., Nowakowski, K., Park, J. M., Castilla, S., Zhan, Z., Pantaleón, P. A., Agarwal, H., Battle-Porro, S., Icking, E., Ceccanti, M., Reserbat-Plantey, A., Piccinini, G., Barrier, J., Khestanova, E., Taniguchi, T., Watanabe, K., Stampfer, C., Refael, G., Guinea, F., Jarillo-Herrero, P., Song, J. C. W., Stepanov, P., Lewandowski, C. & Koppens, F. H. L. Terahertz photocurrent probe of quantum geometry and interactions in magic-angle twisted bilayer graphene. *arXiv,* 2406.16532 (2024).

[212] Li, G., Kumar, R. K., Stepanov, P., Pantaleón, P. A., Zhan, Z., Agarwal, H., Bercher, A., Barrier, J., Watanabe, K., Taniguchi, T., Kuzmenko, A. B., Guinea, F., Torre, I. & Koppens, F. H. L. Infrared spectroscopy for diagnosing superlattice minibands in magic-angle twisted bilayer graphene. *arXiv,* 2404.05716 (2024).

[213] Zuev, Y. M., Chang, W. & Kim, P. Thermoelectric and magnetothermoelectric transport measurements of graphene. *Phys. Rev. Lett.* **102,** 096807 (2009).

[214] Song, T., Jia, Y., Yu, G., Tang, Y., Wang, P., Singha, R., Gui, X., Uzan-Narovlansky, A. J., Onyszczak, M., Watanabe, K., Taniguchi, T., Cava, R. J., Schoop, L. M., Ong, N. P. & Wu, S. Unconventional superconducting quantum criticality in monolayer WTe2. *Nat. Phys.* **20,** 269–274 (2024).

[215] Waissman, J., Anderson, L. E., Talanov, A. V., Yan, Z., Shin, Y. J., Najafabadi, D. H., Rezaee, M., Feng, X., Nocera, D. G., Taniguchi, T., Watanabe, K., Skinner, B., Matveev, K. A. & Kim, P. Electronic thermal transport measurement in low-dimensional materials with graphene non-local noise thermometry. *Nat. Nanotechnol.* **17,** 166–173 (2022).

Author's publications

[P1] Di Battista, G., Fong, K. C., Dıez-Carlón, A., Watanabe, K., Taniguchi, T. & Efetov, D. K. Infrared single-photon detection with superconducting magic-angle twisted bilayer graphene. *Sci. Adv.* **10,** eadp3725 (2024).

[P2] Di Battista, G., Seifert, P., Watanabe, K., Taniguchi, T., Fong, K. C., Principi, A. & Efetov, D. K. Revealing the thermal properties of superconducting magic-angle twisted bilayer graphene. *Nano Lett.* **22,** 6465–6470 (2022).

[P3] Di Battista, G. & Efetov, D. K. Active element for single photon detection, single photon detector and method of manufacturing an active element for single photon detection. *European patent application* **24,** 160, 614.4 (2024).

[P4] Yang, S. Y., Dıez-Carlón, A., Dıez-Mérida, J., Jaoui, A., Das, I., Battista, G. D., Luque-Merino, R., Mech, R. & Efetov, D. K. Plethora of many body ground states in magic angle twisted bilayer graphene. *Low Temp. Phys.* **49,** 631–639 (2023).

[P5] Jaoui, A., Das, I., Di Battista, G., Dıez-Mérida, J., Lu, X., Watanabe, K., Taniguchi, T., Ishizuka, H., Levitov, L. & Efetov, D. K. Quantum critical behaviour in magic-angle twisted bilayer graphene. *Nat. Phys.* **18,** 633–638 (2022).

[P6] Diez-Merida, J., Das, I., Di Battista, G., Diez-Carlon, A., Lee, M., Zeng, L., Watanabe, K., Taniguchi, T., Olsson, E. & Efetov, D. K. High-yield fabrication of bubble-free magic-angle twisted bilayer graphene devices with high twist-angle homogeneity. *arXiv,* 2405.11323 (2024).

[P7] Grover, S., Bocarsly, M., Uri, A., Stepanov, P., Di Battista, G., Roy, I., Xiao, J., Meltzer, A. Y., Myasoedov, Y., Pareek, K., Watanabe, K., Taniguchi, T., Yan, B., Stern, A., Berg, E., Efetov, D. K. & Zeldov, E. Chern mosaic and Berry-curvature magnetism in magic-angle graphene. *Nat. Phys.* **18,** 885–892 (2022).

[P8] Hubmann, S., Di Battista, G., Dmitriev, I. A., Watanabe, K., Taniguchi, T., Efetov, D. K. & Ganichev, S. D. Infrared photoresistance as a sensitive probe of electronic transport in twisted bilayer graphene. *2d Mater.* **10,** 015005 (2023).

[P9] Hubmann, S., Soul, P., Di Battista, G., Hild, M., Watanabe, K., Taniguchi, T., Efetov, D. K. & Ganichev, S. D. Nonlinear intensity dependence of photogalvanics and photoconductance induced by terahertz laser radiation in twisted bilayer graphene close to magic angle. *Phys. Rev. Mater.* **6** (2022).